Metal Clusters on Surfaces: Morphology, Stability and Reactivity

THÈSE N^O 4901 (2010)

PAR

Michael HUGENTOBLER

ÉCOLE POLYTECHNIQUE
FÉDÉRALE DE LAUSANNE

Suisse
2010

Résumé

La morphologie, la stabilité et la réactivité des particules de taille nanométrique (Au, Pt) sont étudiées sur trois supports différents: HOPG, YSZ et TiO_2 .

Dans le premier cas, des nanoparticules d'or avec un diamètre compris entre 4 et $6nm$ sont stabilisées dans des trous d'une profondeur bien définie dans du HOPG (higly ordered pyrolytic graphite). Ces trous sont produits par la création de défauts artificiels, suivie d'un agrandissement (etching) à température élevée sous une pression contrôlée d'oxygène. À des faibles taux de recouvrement, les nanoparticules d'or se trouvent dans les coins des trous hexagonaux afin de maximiser les contacts avec les liaisons pendantes des multicouches de graphite. Pour des taux de recouvrement plus élevés, les particules d'or forment des chaînes avec une taille bien définie et une distribution uniforme le long des marches. Le résultat le plus remarquable est la stabilité de ces nanostructures dans des conditions ambiantes. Des températures aussi élevées que $650K$ ne modifient pas la morphologie des nanoparticules d'or. Au-dessus de $700K$, les nanoparticules d'or montrent un pouvoir catalytique qui permet de faire un etching dans des couches de graphite lorsque ce système est chauffé sous conditions atmosphériques. La profondeur du canal ainsi produit est définie par la profondeur du trou qui est à l'origine du canal et sa largeur du canal est donnée par la taille de la particule d'or. Hydrogène, oxygène et l'eau se dissocient sur les particules d'or à basse température $(> 400K)$. Du CO et du CO_2 sont produits au-dessus de $700K$ ce qui confirme l'etching des multicouches de graphène. La réaction du "water-gas shift" a été observée dans laquelle l'oxygène et l'eau se dissocient sur les particules d'or à basse température.

Des mesures de spectroscopie par désorption thermique (TDS) ont été effectuées sur du platine Pt déposé sur YSZ. Les pics de désorption de CO et O_2 ont été mis en évidence. Le monoxyde de carbone désorbe de la surface à une température de $535K$ et l'oxygène à $705K$, en accord avec les valeurs présentes dans la littérature. Des mesures catalytiques ont confirmé la forte activité catalytique du Pt. L'oxydation du CO s'effectue à des températures comprises entre $450K$ et $700K$. Les températures d'adsorption et de désorption des deux gaz ont été confirmées lors de la mesure de la catalyse.

Des particules d'or triées en taille Au_n ($n = 5, 7$) sont déposées à partir de la phase gazeuse à température ambiante avec une énergie cinétique bien contrôlée sur du TiO_2. Deux reconstructions de surface différentes ont été utilisées comme support: $TiO_2(110) - (1 \times 1)$ et $TiO_2(110) - (1 \times 2)$. Des études systématiques de la morphologie, de la stabilité et des sites d'adsorption ont été effectuées en utilisant la microscopie à effet tunnel (STM). La taille moyenne des nanoparticules d'or est maintenue en cours de dépôt à une énergie cinétique de $7.1 eV$ par atome, ce qui indique qu'il n'y a pas de fragmentation. Les nanoparticules d'or ne sont pas stables sur les deux reconstructions lors du recuit jusqu'à $800 K$, ni sur le $TiO_2(110) - (1 \times 1)$ ni sur le $TiO_2(110) - (1 \times 2)$. Une transition progressive des structures bidimensionnelles vers des particules tridimensionnelles est observée. La distribution en taille des particules est petite et le mode de croissance (mûrissement d'Ostwald) est indépendant de la reconstruction de surface. La rugosité élevée de la reconstruction $TiO_2(110) - (1 \times 2)$ résulte en une stabilité marquée des particules sur les terrasses, contrairement à la reconstruction $TiO_2(110) - (1 \times 1)$ où 90% des particules se trouvent sur les bords des terrasses à des températures élevées. L'activité catalytique des particules d'or commence au moment où la structure des agrégats passe de deux à trois dimensions. Ces mesures doivent être confirmées et une compréhension complète du processus doit encore être trouvée.

Mots-clés: catalyse, agrégats metalliques, stabilité des agrégats, TiO_2, HOPG, YSZ, STM, TDS

Abstract

The morphology, stability and reactivity of nanometre-sized particles (Au, Pt) is investigated on three different supports. Gold nanoparticles with a diameter comprised between 4 and $6nm$ are stabilized in nanosized pits of well defined depth in highly oriented pyrolytic graphite (HOPG). These pits are produced by creation of artificial defects, followed by etching under a controlled oxygen atmosphere. At low Au coverage, clusters are found on the edges of the hexagonal pits maximizing the contact to dangling bonds on graphite multisteps. Larger coverage results in Au beads of well defined shape and with a constant bead density per unit length. Most remarkable is the stability of these nanostructures under ambient conditions. Temperatures as high as $650K$ do not alter the morphology of the gold clusters. Above $700K$, the gold clusters catalyze the etching of graphite layers when heated under atmospheric conditions. The depth of the etching channel is defined by the depth of the pit and the channel width can be controlled by the cluster size. Hydrogen, oxygen and water are dissociated on the Au clusters at low temperatures $(> 400K)$. CO and CO_2 is produced above $700K$ which confirms the etching of the multilayer graphene sheets. The so-called water-gas shift reaction has been observed where oxygen and water dissociate on the Au clusters at low temperatures.

Thermal desorption spectroscopy (TDS) measurements on the Pt/YSZ system have been performed and the desorption peaks of CO and O_2 have been evidenced. Carbon monoxide desorbs from the surface at a temperature of $535K$ and oxygen at $705K$, in good agreement with values reported in literature. Catalytic measurements have confirmed the known strong catalytic activity of Pt. The CO oxidation takes place at temperatures between $450K$ and $700K$. The adsorption and desorption temperature of the two educts have been confirmed during the catalysis measurements.

Size-selected Au_n clusters ($n = 5, 7$) are deposited from the gas phase at room temperature with well-controlled kinetic energy on rutile TiO_2 . Two different surface reconstructions have been used as support: $TiO_2(110) - (1 \times 1)$ and $TiO_2(110) - (1 \times 2)$. Systematic studies of morphology, stability and adsorption sites have been performed using scanning tunnelling

microscopy (STM). The mean size of the clusters is maintained during deposition at a kinetic energy of $7.1eV$ per atom, indicating that there is no fragmentation. Au clusters are not stable neither on the $TiO_2(110) - (1 \times 1)$ nor on the $TiO_2(110) - (1 \times 2)$ reconstruction during annealing of the substrate to $800K$. A progressive transition into a pronounced 3-d formation is observed. The size distribution of the particles is small and the growth mode (Ostwald ripening) independent of the surface reconstruction. The higher corrugation of the $TiO_2(110) - (1 \times 2)$ reconstruction results in a pronounced stabilization of the clusters on terraces, in contrast to the $TiO_2(110) - (1 \times 1)$ reconstruction where 90% of the clusters are found on step edges at elevated temperatures. The catalytic activity of the Au clusters sets in during the 2d - 3d transition. These measurements have to be confirmed and a full understanding of the process should be found.

Contents

Chapter 1

Introduction

The expression "nano" is a prefix in the metric system denoting a factor of 10^{-9}. It is mostly used for the size of objects, i.e. nanometres. Nowadays, nano is widely used for fancy objects that possess properties in relation with particles of this specific size range. The first hits on Google for example show links to Apple (for their iPod Nano), an Indian car company with a homonymous car model or a computer processor company. All these examples have in common that their products distinguish themselves from their competitors by their small size.

Research in nanotechnology has significantly increased in the last decades. There are different motivations: the first one (in relation with the above cited examples) is to minimize the size of objects, e.g. in computer chips, for storage devices or nanometre-sized engines for drug transport and release in human bodies. Second, the properties on nanometre-sized objects vary strongly with their size. A historical example from the middle age is the optical properties of metallic nanoparticles in stained glasses. Figure 1.1 shows a window in the Cathedral of Canterbury from the 12th century, where the colours are due to the different size of gold nanoparticles inside the glass. Of course, at this time glass workers had no idea of the origin of the magnificent colours in stained glass, but they knew the recipes to produce it. It was only at the beginning of the last century when Gustav Mie provided an explanation based on electromagnetic theory [1]. This is not the only example that nanotechnology has been of benefit. The famous Damascus sabres, well known for their strength contain carbon nanotubes [2]. To benefit from the elaborated properties of nanosize materials beyond accidental discoveries as cited above, a more detailed knowledge of physical and chemical properties of nanometre sized materials is necessary.

Figure 1.1: Stained glass window in the Cathedral of Canterbury from the 12th century.

Besides the optical and mechanical properties presented above, also chemical, magnetic and electronic properties strongly depend on particle size. The change of properties is not necessarily smooth, as it is illustrated in Figure 1.2. Here, G denotes a physical property such as the melting point, the ionization potential or the band gap. It is shown as a function of particle size. The property G varies from the bulk value $G(\infty)$ to $G(1)$, the value for a single atom. For large cluster size, G increases smoothly but with smaller cluster sizes, the change can vary strongly with each atom that is missing.

The size of nanoparticles ranges from a few to a million atoms and especially very small particles present strong variation of their properties. Very small nanoparticles are also called clusters. Our study focuses on this size range (from one to thousands of atoms), where one sentence gives a good summary: *small is different - each atom counts!* This is particularly true for the cluster abundance. The stability of clusters or, more precisely, metal clusters is due to their confinement of the electronic shells. The valence electrons are delocalized and form a shell-like structure [4, 5]. If one looks at the mass spectrum of sodium studied by Knight *et. al.*, the abundance drops above precise cluster sizes: $8, 20, 40, 58, ...$ These
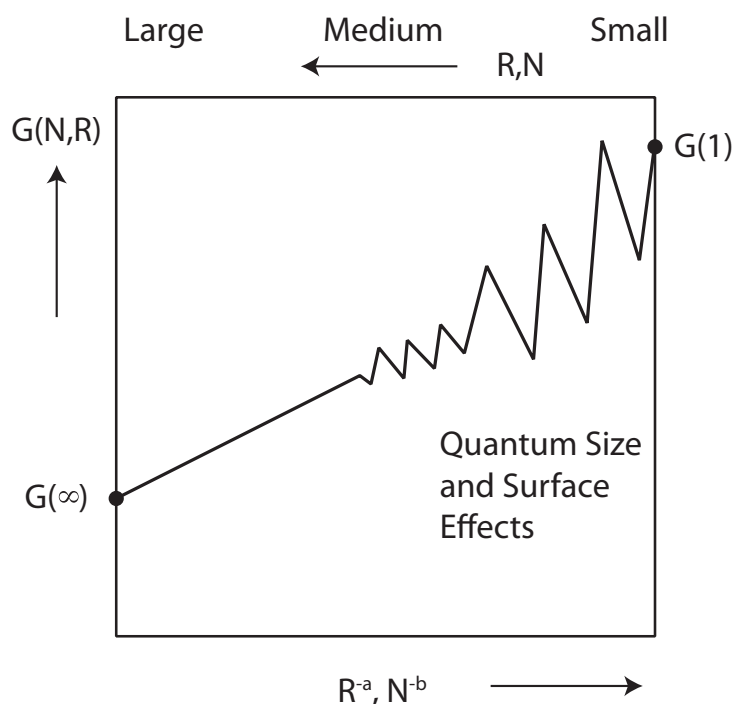
Figure 1.2: Physical or chemical properties as a function of size [3].

so-called magic numbers are clusters with completely filled electron shells. An example to be cited for a magic-number cluster is the beautiful tetrahedral geometrical structure of Au_{20} clusters, studied by Li *et. al.* [6] (see Figure 1.3).

Nanoparticles can be created in different ways, but two fundamentally different approaches exist: top-down and bottom-up. The first (top-down) cuts a piece of material to smaller and smaller sizes. It is limited by mechanical constraints and one cannot reach very small sizes. The second (bottom-up) goes the other way. Starting from a single atom, atoms are added one by one and the cluster size can be precisely controlled. This is the way employed in almost all studies of clusters including this one.

Many results have been obtained for clusters in the gas phase, also called free clusters. Geometric structures of free clusters have been determined by ion mobility measurements [7–10] and electron diffraction methods [11–16]. A more indirect way to determine the geometry has become available with the invention of free electron lasers [17, 18].

Some studies of clusters require that they are deposited and stabilized on surfaces. Thus, clusters have to be deposited in a way that they adhere but do not decompose on the surface.
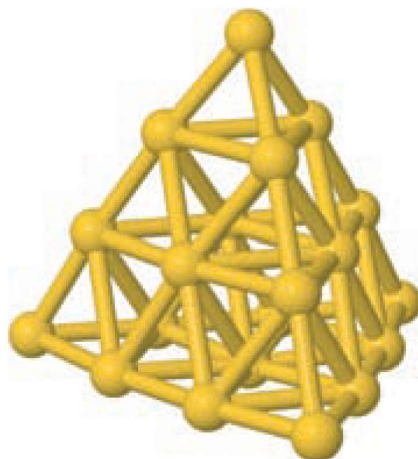
Figure 1.3: Tetrahedral structure of a Au_{20} cluster [6].

One can also imagine assembling such structures one by one. Atoms can be added to and moved on the surface by means of an STM (scanning tunnelling microscope) tip. On the other hand, self-organization is also possible. Deposited atoms and nanoparticles can organize themselves under energetically favourable conditions. A simple energy supply by heating the surface is sometimes sufficient to enhance the mobility and the arrangement of particles.

One of the fascinating discoveries in the last years is the catalytic activity of metallic nanoparticles with a countable number of atoms, in particular Au clusters. Gold, which is an inert material in the bulk phase becomes catalytically active when the size of the nanoparticles drops below $10nm$ approximately. This pioneering work of Haruta [19–22] has led to an intense research effort on the catalysis of gold [23]. The size dependence was thoroughly studied and it was generally agreed that the activity increases with decreasing cluster size, as shown by the work of Goodman and co-workers [24]. However, the smallest sizes active for specific reaction were badly defined because of experimental imperfections. It was the seminal work of Heiz *et. al.* [25, 26] and some years later Anderson [27–29] who used mass selected deposition of Au clusters. These investigations clearly showed that Au clusters containing as few as 7 atoms are already active. To be more precise we should state that the first catalytic measurements on size selected clusters have been performed by Wöste and co-workers in Lausanne [30, 31]. They showed that Ag clusters containing at least 4 atoms were necessary to develop $AgBr$ grains in the photographic process.

Later work by Turner [32] showed, using high resolution, aberration corrected electron
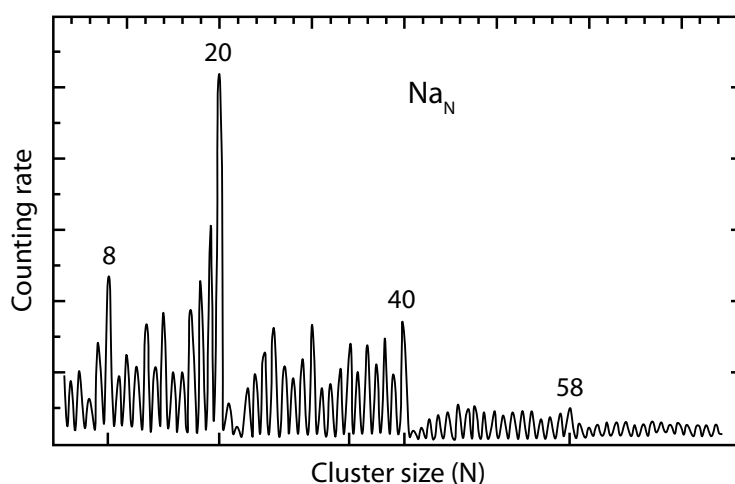
Figure 1.4: Spectrum of sodium clusters. The so-called magic numbers $8, 20, 40, 58$ show higher abundance than neighbouring clusters, due to their closed shell structure. The stability of such closed-shell is elevated [4].

microscopy, that the active clusters in samples with a broad size distribution are the very small ones. Vajda *et. al.* extended these studies with mass selected clusters to real catalysis conditions [33, 34]. One of the key issues in this research, however, is the question on morphology and stability. So far very few is known on the morphology change of such small clusters under reaction conditions, i.e. temperature and gas exposure.

This work focuses on different properties of clusters, deposited on surfaces: their morphology, stability and the catalytic activity. The morphology describes the above mentioned arrangement of particles, their location on surfaces and evolution at high temperatures. The stability gives information about how strong particles are bound to the surface. Catalysis is the change in rate of a chemical reaction due to the participation of a substance called a catalyst. The understanding of catalytic properties of nanoparticles is related to stability and morphology which is itself related to stability. Unlike other reagents that participate in the chemical reaction, a catalyst is not consumed by the reaction itself. The industrial applications of effective catalysts are huge, going from exhaust gas catalysers in cars to the industrial production of ammonia-based fertilizers. This fertilizer production is an excellent example of how important catalysts can be for our live and society and what impact they have on the economy: the worldwide production of ammonia-based fertilizers is huge, the total production in 2009

was at 133 million tons[1]! The impact on nature, i.e. the energy consumption is not negligible. In fact, the energy used in ammonia production alone equals 2% of the total energy consumed globally[2]. It has been shown that the use of catalysts can reduce the required energy by an important factor and its impact on economy as well as ecology would be drastic. The only drawback is that such catalysts exist in laboratories but are not yet ready for the application in the industry.

One of the purposes of this work is to evidence the catalytic activity of clusters in an environment, which could be of interest in industrial applications. Different supports (substrates where clusters are deposited) and different cluster materials have been used for cluster deposition but all pursue the same goal: to show a catalytic activity of metal nanoparticles.

This work is structured in several chapters. Chapter 2 gives an overview of theory regarding the present work. In Chapter 3 the different supports that have been used in order to study the properties of metal clusters are described. The following Chapter (4) introduces the experimental setup to the reader. One of the achievements of this thesis is the development of a new, highly sensitive detector for reaction products. The setup and performance tests are presented in this part. The results of the different systems (clusters on different supports) are divided into three chapters (5 to 7) in order to facilitate the reading of this manuscript. The review of results in literature in relation with this work and parts of the discussion are summarized in Chapters 2 and 3. Finally, Chapter 8 summarizes the results and gives some final conclusions.

---

[1]`http://minerals.usgs.gov/minerals/pubs/commodity/nitrogen/`
[2]`http://www.qsinano.com/apps_ammonia.php`

Chapter 2

Clusters on surfaces and their catalytic properties

Contents

This Chapter presents the theoretical aspects of physical processes with an interest for the present work. As this study concentrates on morphology, stability and chemical reactivity of clusters, we focus also in the fundamentals on these points. In a first part (Section 2.1) cluster deposition process, evolution and structure of clusters on surfaces are presented. General remarks as cluster deposition on surfaces or evolution of clusters are true for clusters of different

7

materials. Different models have been proposed in literature that describe cluster growth. We are able to identify the growth of our metal clusters with one of the presented growth models. The detailed structure of gold clusters as well as their diffusion properties are shown in Sections 2.1.4 and 2.1.5, as gold is the material we used predominantly in this work.

In a second part (Section 2.2) we discuss catalytic processes in general and their fundamental characterization. Moreover, catalytic reactions by clusters are presented. Finally, we go more into detail and explain the different catalytic activities of gold clusters (in Section 2.2.5).

2.1 Clusters - systems with reduced dimensions

Clusters ($n = 2$ to 10^6 atoms) bridge the gap between atomic and molecular physics on one side and solid state physics on the other. These small objects are inherently interesting from a fundamental point of view, i.e. how the transition to the bulk is formed, as well as for possible applications [35]. Small particles are defined as objects that behave as one unit in terms of chemical, electronic, optical, magnetic or mechanical properties. They are classified according to their size: small particles of 100 to some thousands nanometres of diameter mark the upper limit of fine particles. Ultrafine particles, also called nanoparticles, are sized between one and 100 nanometres. They consist of one to several thousands of atoms. They may (but do not have to) show size-related properties that differ strongly from those observed in bulk material.

Our knowledge of the electronic and geometric structure as well as of material properties has been considerably improved over the last two decades. Spectacular discoveries in particular on carbon clusters (fullerenes and nano-tubes) have led to the development of proper research fields. The discovery that small gold clusters are catalytically active and efficient has emerged into a field today known as nanocatalysis [25, 36]. Metal clusters have attracted much interest for different reasons. Alkaline metals are "the" model system for free electron metals which allows a relatively simple theoretical description. The free electron nature of the valence electrons and their formation into electronic shells has been discovered already 15 years ago [5]. Coinage metals are much more resistant to a satisfying understanding of their electronic structure since the d-electrons have to be taken into consideration in any theoretical modeling. A large amount of experimental data has been collected in particular for their optical properties [37]. The calculation of the electronic structure of small silver, gold and copper clusters ($n < 15$) using sophisticated ab initio methods is state of the art and in the focus of several research groups. Gold clusters have gained considerable interest not only for their optical properties but also for their catalytic properties as will be further outlined below. The geometric structure of small gold anions have been found planar [8] in experiments against theoretical predictions which have been corrected now showing the importance of relativistic effects in the electronic structure [38]. A prominent example for a geometrical structure is

the beautiful tetrahedron of the free Au_{20} cluster which has been found by a comparison of photoelectron spectroscopy (PES) and state of the art density functional theory [6].

The electronic structure of the "true" transition metal clusters like Platinum, Palladium or Nickel is even more complicated. These materials are interesting in particular for their magnetic, ferroelectric and catalytic properties. Intense research on these systems is actually underway [25, 33, 39, 40].

The study of free clusters are the key to understand the evolution of the electronic and geometric structure with size. This is also true for reactive collisions of gas phase clusters with specific gases. These experiments can be considered as the precursor experiments to heterogenous catalysis of supported clusters. Considerable progress has been made in the last years by the group of Bernhardt [41–44]. However any imaginable application asks for the cluster to be either supported or embedded in a medium. An additional difficulty is then added in these cluster surface system since the geometrical and electronic structure of the clusters are altered. This is in particular true for small clusters and strongly interacting substrates. However, one has to be aware of the support influence on the reactivity. Recently, the group of Heiz investigated the effects of the cluster support (MgO surfaces grown on molybdenum) on the catalytic activity of deposited gold nanoparticles [45]. They found that the thickness and the composition of the substrate influence the reactivity of such gold nanoparticles.

2.1.1 Cluster deposition of surfaces

The properties of nanostructures depend strongly on their size and shape. It is therefore essential to control the precise size of the particles during the production process. Different ways have been proposed with different aims: nanolithography with a minimal size of $5nm$ is widely used in the fabrication of leading-edge semiconductor integrated circuits (nanocircuitry) or nanoelectromechanical systems [46]. Single atom manipulation, on the other end of the scale of nanostructures, can be done by moving atoms with an STM (Scanning tunnelling microscope) tip on the surface [47, 48]. In a simpler way, but with less control of the particle size, we can let nature do the work by using the thermodynamic laws. When single atoms or small clusters are deposited on a surface, they will migrate and maybe aggregate together. We will use this process for our deposition of nanoparticles. It is not possible to control the precise deposition location and the cluster shape. However, the size, still the most important

parameter, can be well controlled. Various studies in the last decades have pushed the knowledge of morphology[1] evolution forward to a point where some behaviours of nanoparticles can be forced (by carefully choosing the cluster size, the substrate and the deposition conditions). In particular, we want to mention the auto-assembly of nanostructures and its derived technological applications [49]. In the following paragraphs, we develop the basics of cluster deposition on a surface, particle evolution and finally the equilibrium structure and shape of cluster islands after their thermalization.

Collision mechanism In cluster and atom depositon, the particle collides with the surface. The collision time of an atom or a cluster with a surface is very short, in the order of some picoseconds ($10^{-12}s$) [50]. The very fast reaction time does not allow a broad dissipation of energy. The area concerned is very narrow, therefore the local temperature ($T \approx 3000K$) and pressure ($p \approx 10^7 mbar$) are high enough to enable the fusion of the support material [51]. It implies the structural change of the support and the cluster (or atom) during impact. In the case of clusters the results depend on various parameters:

- Kinetic cluster energy: $\quad 10^{-2}eV < E_{kin}^{cluster} < 10^8 eV$

- Size (number of atoms in a cluster): $\quad 2 < n < 10^5$

- Adsorption energy E_{ads} of the cluster atoms on the surface.

- Cohesion energy of the cluster (E_{coh}^{Cl}) and the surface (E_{coh}^{surf}), representing the hardness of the material.

- Angle of incidence.

- Ratio of atomic mass between cluster and surface material.

The ratio of cohesion energies of the cluster and the surface can be expressed as:

$$R = \frac{E_{coh}^{Cl}}{E_{coh}^{surf}} \tag{2.1}$$

If R is large, a hard cluster encounters a soft surface. The particle can penetrate easily into a substrate. On the other hand, a small value of R represents an impact of a soft cluster on a

---

[1]morphology is the study of form and structure without regard to function
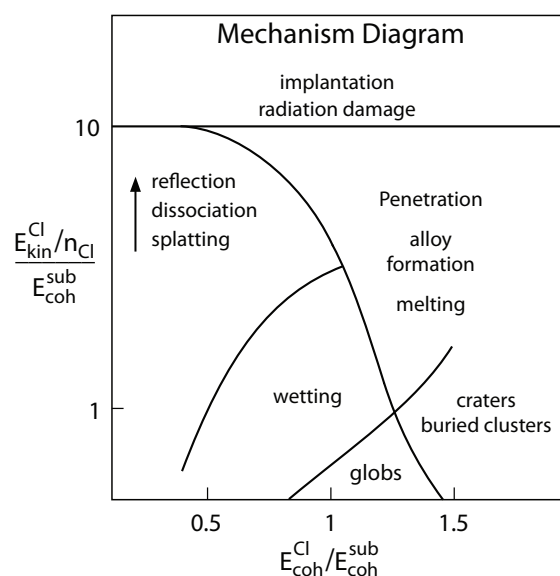
Figure 2.1: Diagram for fundamental processes at cluster impact. X-axis represents the relative hardness of cluster and surface, Y-axis the reduced kinetic energy [50].

hard surface. The impinging cluster then risks fragmenting without inducing damage to the surface.

In Figure 2.1 the different regimes of cluster impact are schematically represented. The different regimes of a cluster impact can be classified in ten subgroups, according to the above mentioned cluster and surface properties and the cluster impact energy. Figure 2.2 shows an overview of most of the possible processes. Here, we concentrate on the important ones for this study:

- **Soft landing:** the cluster lands on the surface smoothly without any damage, neither on the surface nor to the cluster itself. This is an ideal case that does not happen in reality. In fact, the adsorption energy is never zero and the surface induces deformation to the cluster. The real process is closer to a plastic deformation than a soft landing. An example hereof are hard metal clusters deposited in rare gas matrices [53, 54].

- **Plastic deformation:** the surface remains intact. The cluster undergoes a deformation but does not break into several parts. The shape of the cluster is changed, due to attracting forces between substrate and cluster.

- **Fragmentation:** the surface remains intact but the cluster breaks into several pieces.
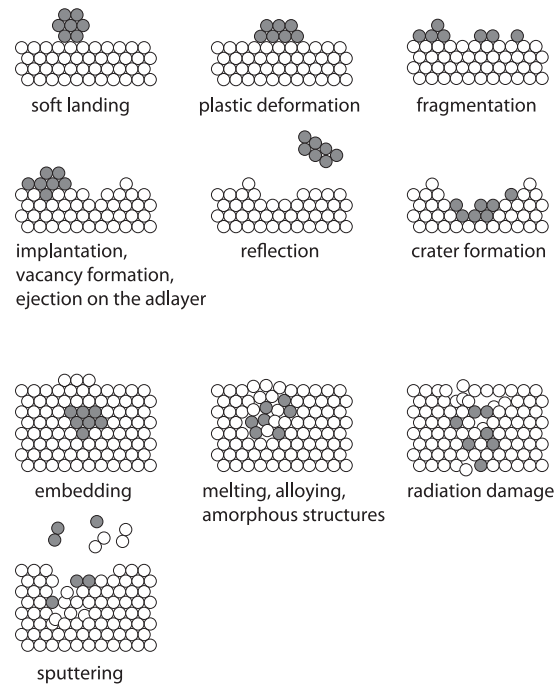
Figure 2.2: Fundamental processes for cluster deposition [52].

- **Implantation:** during impact, the cluster modifies locally the surface and creates defects. The defects can figure as anchor points for the cluster and stabilize its position.

- **Sputtering:** at very high impact energies, surface atoms or even bigger parts of the cluster are ejected. This process is used as a standard method for producing nanoparticles (made of the surface material), see Section 4.1.3.

2.1.2 Evolution of clusters and atoms on surfaces

After impact, and once the deposited particles are thermalized down to the support temperature, the system still evolves. These processes, such as surface diffusion, have different reaction rates as a function of the system temperature or activation energy. They can be seen as a random walk process. Figure 2.3 shows different possible mechanisms of cluster or atom movement on a surface: dissociation of a cluster that splits in several parts, position exchange between a cluster and a surface atom, evaporation, aggregation of single atoms or entire clusters, diffusion of atoms on terraces, at steps or at the edge of clusters. An atom diffusing on the surface can meet another atom (dimer formation) or a whole cluster (adhesion). The product of such a combination can itself diffuse on the surface, dissociate or stay immobile. In a
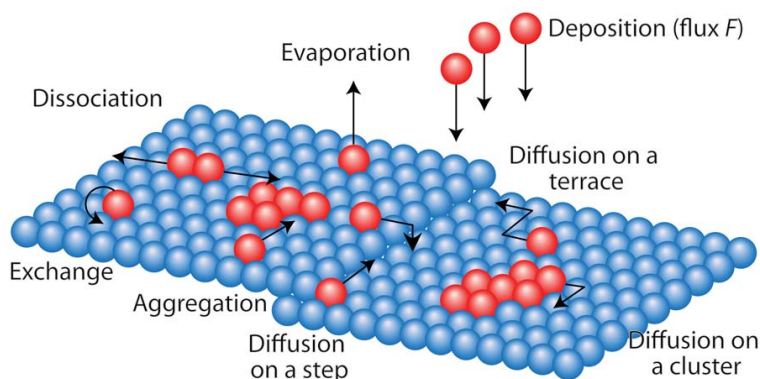
Figure 2.3: Movements of atoms and molecules on a surface.

normal case, atomic diffusion is faster than diffusion of cluster islands. The results are bigger clusters but with a lower abundance.

Cluster growth mechanisms   The case of immobile clusters where only single atoms diffuse is known as Ostwald ripening process [55]. Single surface atoms leave the cluster and migrate on the substrate. After a random walk on the surface they will meet another cluster or attachment point and adhere to it. The theory developed around this process has been applied in many studies after the discovery of electronic microscopy and scanning tunnelling microscopy (STM) [56, 57]. The Gibbs-Thompson equations require that the vapour pressure (in the present case the diffusing atoms), in equilibrium with its condensed phase (the islands), decreases with the increase of the curvature radius of the islands. As a consequence, small particles decompose more rapidly than big ones and will finally disappear. The second process is characterized by the diffusion of entire cluster or islands. They migrate as an ensemble and do not dissociate during migration. When two migrating clusters meet each other, they fuse and build a new, bigger cluster. Their growth is thus not smooth in size but increases stepwise.

The mean size evolution of islands as a function of the temperature is different for each growth mechanism. Figure 2.4 illustrates the thermal evolution of the mean island size for nucleation by cluster diffusion and Ostwald ripening. In the first case we get a growth by steps. As whole clusters diffuse, there are no intermediate sizes between multiples of the initial cluster sizes. One observes for Ostwald ripening a constant island size at low temperatures followed by an exponential growth. The plateau on the Ostwald ripening curve can be explained with the fact that the smallest particles need a certain energy to get unstable and to dissociate [59]. From this data we deduce information about the binding energies of small
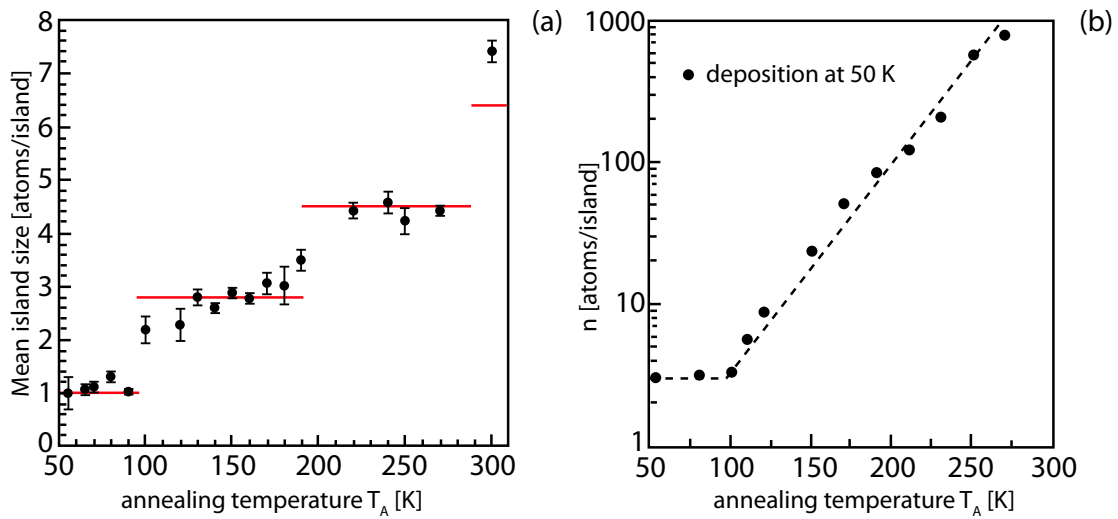
Figure 2.4: (a): nucleation by cluster diffusion (0.1ML $Co/Pt(111)$) [58]. (b): mean size evolution of clusters by Ostwald ripening (0.1ML $Ag/Pt(111)$) [59].

islands. Looking at the size distribution for Ostwald ripening and nucleation growth, one sees that the peak for Ostwald ripening is much sharper than the latter (see Fig 2.5). The diffusion of single atoms and the enhanced stability of big clusters lead to the narrower distribution. The control of island size is achieved by carefully choosing the annealing temperature of the sample.

An everyday example of Ostwald ripening is the re-crystallisation of water within ice cream which gives old ice cream a gritty, crunchy texture. Larger ice crystals grow at the expense of smaller ones within the ice cream, thereby creating a coarser texture [61]. Another gastronomical example is found when Pastis is mixed with water, the so-called ouzo effect. Droplets in the cloudy microemulsion grow by Ostwald ripening [62].

2.1.3 Equilibrium structure of islands

At thermodynamic equilibrium all diffusion processes cited above take place in both directions. On a macroscopic scale one can claim that there is neither growth nor decomposition. The growth mechanism can be re-activated by supplying additional energy (heat) to the sample. The evolution continues as before by diffusion of particles. After cooling, the system is found in the most stable state. The total energy is minimal and does not depend on the history of deposition and diffusion. The only determining factors are the surface tension $\Delta\gamma$ of the deposited material γ_{Cl}, the substrate γ_{Surf} and the free interface energy
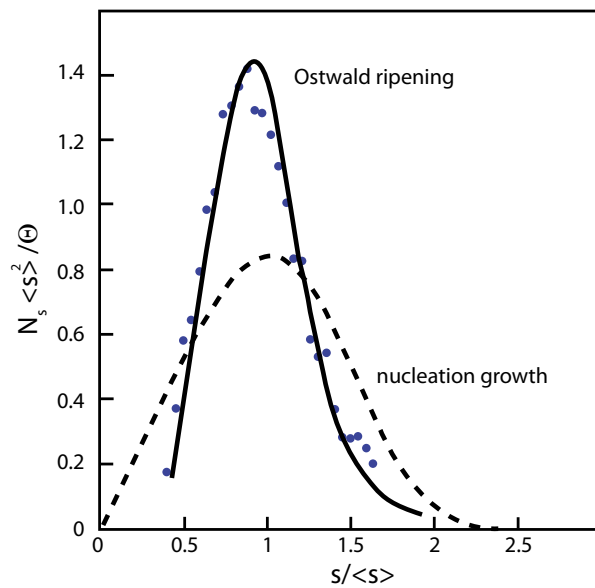
Figure 2.5: Comparison of cluster size distribution between nucleation process and Ostwald ripening. The abundance $N_s < s >^2$ is plotted against the normalized mean island size. Island size distributions for Ostwald ripening collapse with the used normalization into a single curve for all annealing temperatures and are significantly narrower than nucleation (the solid line is a guide to the eye, the dashed line a theoretical scaling curve) [60].
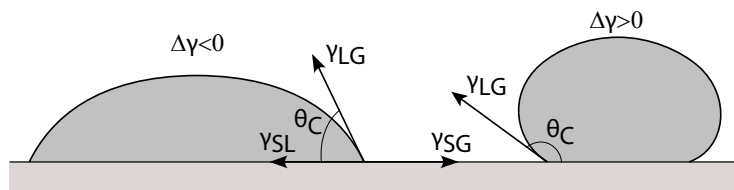
Figure 2.6: Illustration of different models of growth by means of the Bauer criterion: Angle between surface and the deposited nanoparticle.

γ_{Inter}: $\Delta\gamma = \gamma_{Cl} - \gamma_{Surf} + \gamma_{Inter}$. The Bauer criterion (see Fig. 2.6) helps to distinguish between the different models of growth [63, 64]. Depending on the sign of $\Delta\gamma$ one can distinguish between the different growth mechanism, schematically shown in Figure 2.7.

- $\Delta\gamma < 0$: The energy balance of the surface favours the complete wetting of the surface. Particles have tendency to form bidimensional layers. This growth in called Frank van der Merwe and goes layer by layer. It is the normal growth mechanism for metals deposited on metallic surfaces with similar lattice parameters and is of particular importance in the case of epitaxial growth of semiconductors.
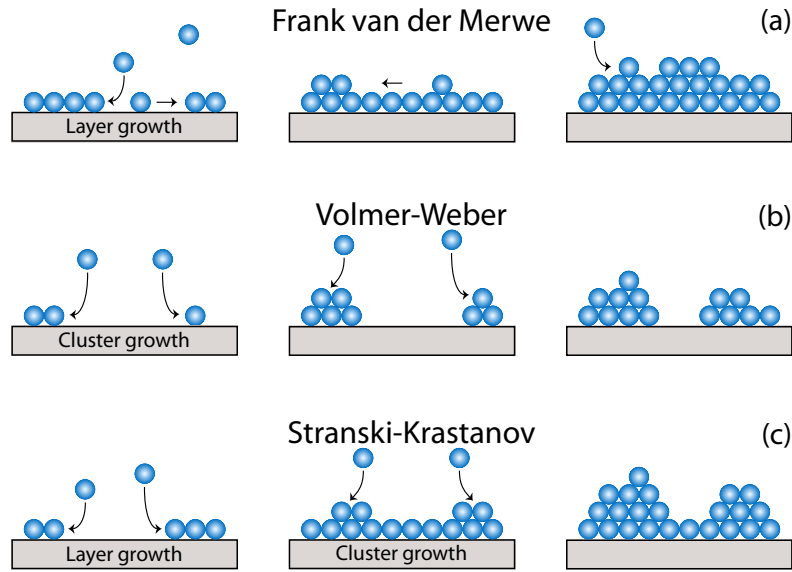
Figure 2.7: Schematic representation of different growth models: (a) Frank van der Merwe growth: clusters aggregate layer by layer. (b) Volmer-Weber: clusters grow three-dimensionally from the beginning. (c): Stransky-Krastanov mechanism: In initial layer growth is followed by 3-d aggregation and cluster formation [68].

- $\Delta\gamma > 0$: The free surface energy of the deposited material prevails over the surface and three-dimensional nanostructures will appear. It is called a Volmer-Weber growth mechanism and occurs principally for transition metals (Pt, Cu, Au,...) deposited on oxide surfaces [65–67]. Our study fits into this category.

- Intermediate case: The transition between the two growth mechanisms is smooth. Typically, two-dimensional growth is observed for a few monolayers before growth is getting three-dimensional. The change is due to a tension relaxation of the grid, caused by the different lattice parameters. This type of growth is called Stransky-Krastanov growth.

As a concrete example, we mention gold clusters on graphite. An important factor is the binding force between gold nanoparticles and the surface. Different studies on the surface tension of gold clusters on graphite have been made. The results differ significantly from each other. The values of γ vary between $1.2\frac{N}{m}\gamma < 3.1\frac{N}{m}$ [69–71]. Theoretical calculations have shown that the contact angle of liquid gold on graphite is $\theta = 146°$, independent of the cluster size. Taking this value also for considerations of single clusters, the shape of clusters would then be a truncated sphere (see Fig. 2.6).
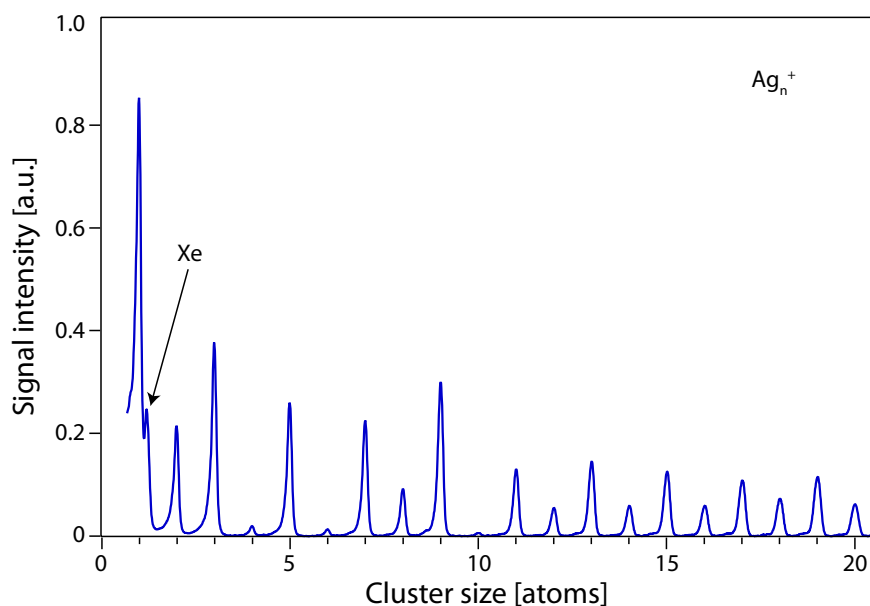
Figure 2.8: Mass spectrum for cationic silver clusters Ag_n^+ obtained during this work. Peaks for odd-numbered clusters are stronger than even-numbered ones (for cations, the number of electrons is one unit inferior to the number of protons; therefore the magic numbers are shifted by one). The peak between Ag_1^+ and Ag_2^+ is due to ionization gas in the sputtering gun (see Section 4.1.3).

2.1.4   Geometry and stability of small gold clusters

Several groups have investigated the structure of small free gold clusters (anions, cations, neutrals) during the last years. Experiment and theory (DFT) are often in a good agreement. In the present study we focus on cations and present therefore only the related results from the literature. More general publications can be found here [7, 8, 72–74].

The stability of gold clusters or, more general, of metallic clusters, is mainly due to their electronic shell structure. It is generally accepted that the electronic structure of simple metal clusters is dominated by the number of valence electrons. They are delocalized and the system shows a spherical shell structure [4, 5]. Knight *et. al.* investigated the stability of sodium clusters and showed that for certain cluster sizes, the stability is strongly increased. By adding an additional atom to these stable structures, the abundance was found to be lower. The explanation is found when looking at the shell structure of these clusters: the so-called "magic numbers" with $2, 8, 20, 40, 58, ...$ atoms stand for completely filled shells. By adding one atom, the valence electron has to occupy a state in a higher energy level and thus the stability of the cluster drops. An example is presented in Figure 2.8.
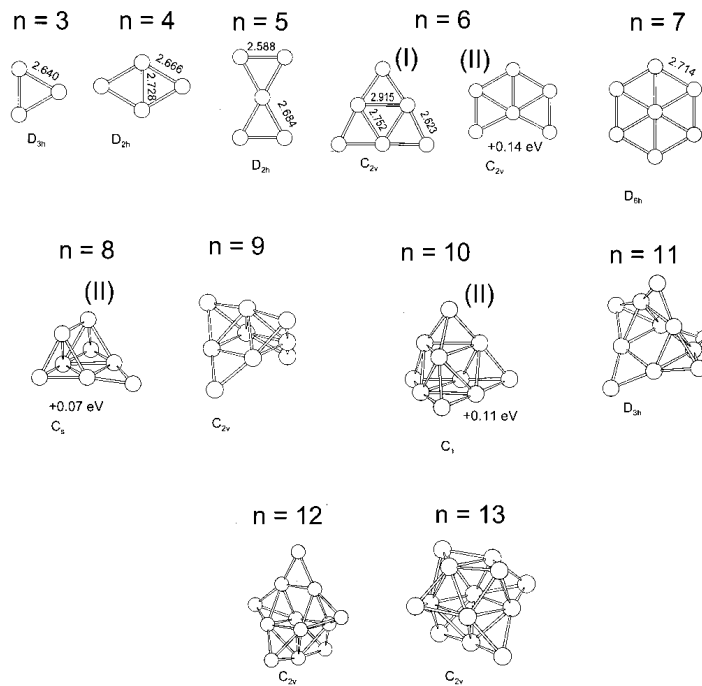
Figure 2.9: Representation of lowest energy forms of $Au_n^+(n = 3 - 13)$ from DFT calculations. The symmetry as well as bond lengths are indicated [7].

The same behaviour is also valid for gold clusters. Katakuse *et. al.* [75] showed the abundance for cationic gold clusters: at the magic numbers $(3, 9, 21, 41, 59, ...)$ the ion intensity decreased steeply (for cations, the number of electrons is one unit inferior to the number of protons; therefore the magic numbers are shifted by one). Beside the dependence on the shells they also observed an even-odd oscillation in stability. It is caused by the same effect, namely that odd-numbered cation clusters possess an even number of electrons (an entire number of pairs) and tend to be more stable than even-numbered clusters [76]. Gilb *et. al.* [7] combined experimental measurements and theoretical DFT calculations to find the geometric structure of small cationic gold clusters. In contrast to other metal cluster cations (e.g. silver), gold remains two-dimensional until a cluster size of seven atoms. The strong s-d hybridization allows small gold clusters to stay favourably in a 2-d configuration. Starting from Au_8^+, they grow in three dimensions. Figure 2.9 shows the computed cluster cation shapes.

2.1.5 Structure and diffusion of Au on $TiO_2(110) - (1 \times 1)$

This Section ends with a brief summary of the results of gold on rutile $TiO_2(110) - (1 \times 1)$. Titanium dioxide ($TiO_2$) is one of the supports we used for our measurements. The properties

of the substrate are described in detail in Section 3.2. Particularly in systems like metal oxides, bias voltage and the polarity for scanning tunnelling microscopy play important roles on the measured contrast (see Section 4.3.4). This has to be taken into account when data are compared.

A nominal $Au(111)$ monolayer has an effective thickness of $0.235nm$ [67]. However, the association of an apparent height to gold mono- and multilayer on the surface is not unambiguous. Spiridis *et. al.* [77] have measured height distributions of thermally grown gold clusters at a bias potential of $+1.7V$. They find an apparent height of $0.2nm$ for 2-d and $0.4nm$ for 3-d gold clusters. Much smaller values have been found by Buratto *et. al.* [78]. In their work mass selected Au atoms and clusters are deposited and observed at room temperature. They found that deposited gold atoms sinter very rapidly and lead to formation of particles with an average height of four atomic layers. In contrast to atoms, gold dimers, trimers and tetramers show almost no sintering. They remain isolated and lay flat on the surface, showing 2-d structures. Bigger clusters $Au_n(n > 4)$ all exhibit two-layer, i.e. three-dimensional structures. They associate an apparent height of $0.15nm$ to these flat clusters and $0.25nm$ to gold double layers $Au_n(n > 4)$. The observed transition from flat to 3-d structures between Au_4 and Au_5 is in contradiction to theoretical calculations and results in the gas phase, see Section 2.1.4. Buratto *et. al.* explain their observation with the ability of the surface to bind the cluster. For them, the binding sites are such that the tetramer is the smallest cluster able to span across two adjacent rows. The transition from 4 to 5 atoms suggests that the fifth atom is not needed for maximal binding and a second layer can be created. The cluster thus grows in three dimensions. Matthey *et. al.* [79] conducted a careful study on the stability of Au monomers on $TiO_2(110) - (1 \times 1)$ in different surface preparation states (reduced, hydroxilated and oxygen rich). They used the same tunnelling parameters as we used in this work. The isolated gold atom has a measured height of $0.23nm$, compared to the monolayer height of $0.25nm$. Both Au_5^+ and Au_7^+ are two-dimensional in the gas phase in their neutral as well as cationic charge state [7, 73]. From the above presented results we assume that Au_5^+ and Au_7^+ deposited on $TiO_2(110) - (1 \times 1)$ are two-dimensional.
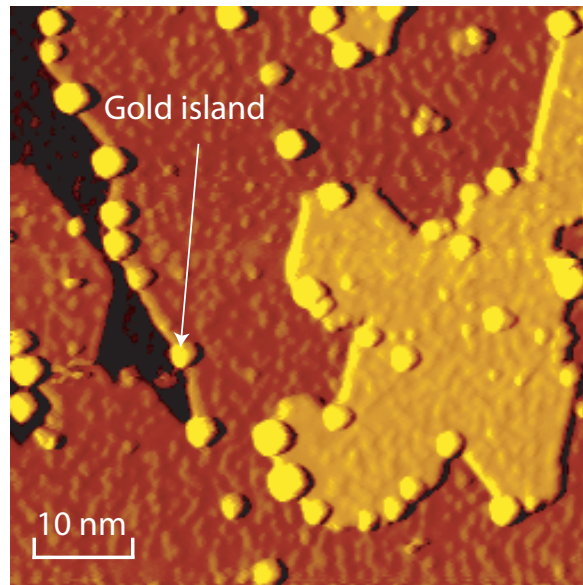
Figure 2.10: STM image of gold atoms deposited on $TiO_2(110) - (1 \times 1)$ at room temperature. Clusters are located almost exclusively on steps. $V_{gap} = 1.2\,V$, $I_T = 100\,pA$. Image size: $60nm \times 60nm$ [80].

Former workers in our group made systematic investigations of deposited Au clusters on $TiO_2(110) - (1 \times 1)$ at different kinetic energies [80]. They studied the influence of cluster size and deposition kinetic energy on the morphology, adsorption sites and defects created by the impact. They concluded that on defect-poor surfaces, gold particles have the tendency to accumulate on steps, in agreement with many other groups [81–84]. An example is shown in Figure 2.10. Large terraces are barely covered with Au clusters, they are principally connected to steps. The key point for the stabilization of cluster on terraces is the presence of oxygen vacancies on the surface.

The group of Egdell realized a study on the mobility of gold atoms deposited on $TiO_2(110)$ [81]. They observed that the size of gold islands increases at higher temperature ($750K$). The principal growth is due to Ostwald ripening. Diffusion of small islands at $750K$ in the [001] direction has been observed, but not for bigger islands. They do not migrate and thus remain stable for several hours. Above $873K$ the gold particles leave the surface. The cluster diffusion can be explained with the surface structure. In fact, TiO_2 is composed of parallel rows of Ti and O atoms (see Section 3.2). If the crystal is not perfectly stoichiometric, some of the oxygen atoms are missing and create oxygen vacancy sites. The mobility of these vacancy sites is not zero, even at room temperature, and thus the surface cannot be re-

garded as temporal stable. The group of Besenbacher [82] related the diffusion of gold atom and vacancy sites for temperatures between $150K$ and $300K$. They have measured a decrease of the number of vacancy sites with increasing gold quantities deposited on the surface and thus concluded that a vacancy stabilizes three to five gold atoms. If the islands get too big for the number of vacancies, the whole gold-vacancy complex diffuses on the surface until it captures a sufficient number of vacancy sites.

Density functional theory (DFT) calculations have shown that a monolayer of gold binds very poorly to the clean surface [85] but connects to the oxygen vacancy sites ($1.6eV$ binding energy per vacancy) [86]. Big gold particles can only be stabilized on vacancy sites or at steps which can be considered as ensemble of vacancies [87, 88].

The mobility of thermally deposited atoms or clusters creates problems for the fabrication of commercial catalysers containing small gold particles ($d < 4nm$). They have to be stable up to temperatures of $600K$ which is apparently not the case. Their mobility leads to an assembly of particles with size larger than the critical size (see Section 2.2.5).

2.2   Catalysis

The word "catalyst" originates from the Greek word "$\kappa\alpha\tau\alpha\lambda\upsilon\epsilon\iota\nu$", meaning "to annul" or "to untie" or "to pick up". It was Berzelius in 1836 who defined a catalysed process: "to awaken affinities, which are asleep at a particular temperature, by their mere presence and not by their own affinity". Ostwald started in the 1880s a systematic investigation on catalysis. He introduced the concept of reaction velocity as a criterion of a catalytic process. He proposed the following definition: "Catalysts are substances which change the velocity of a reaction without modification of the energy factors of the reaction" [89]. Unlike other chemical reactants, the catalyst is not consumed during the reaction, it is thus available in principle for unlimited cycles.

Chemical reactions are characterized by a certain activation energy, denoted by E_A (Figure 2.11). Free reactants possess a characteristic potential energy E_{pot}. Almost any reaction between these active parts needs additional energy, for example adsorption energy E_{ads}. We are confronted with an energy barrier which has to be exceeded to launch the
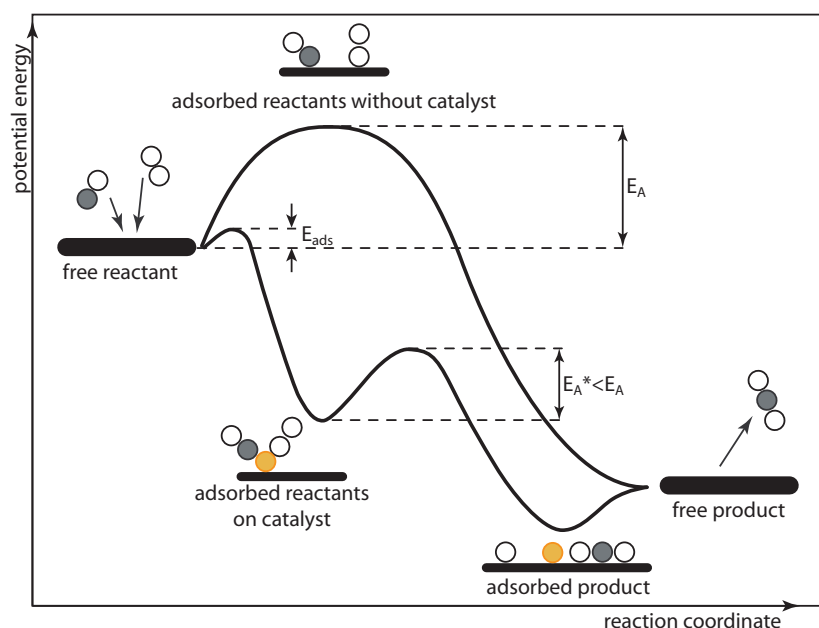
Figure 2.11: Activation energy barrier E_A for a chemical reaction. The presence of a catalyst reduces the energy barrier E_A^* and increases the reaction rate [90].

reaction. This barrier can be high, even for strongly exothermic reactions [1]. The presence of a catalyst can reduce this energy barrier and increase the speed of the reaction. The main catalysts are transition metals such as $Fe, Co, Ni, Cu, Rh, Ag, Pt, Ru, Ir, Os$ or Au. Each catalyst has its own efficiency rate for different reactions. The efficiency of a catalyst is also influenced by the number of available adsorption sites on the catalyst. It is important to note that catalysis is a process which happens on surfaces and not in the bulk. It is thus favourable to increase the catalytically active surface instead of the volume. This is where nanostructures enter the discussion. Their accumulated surface, due to the isolated structures as particles, ribbons or patterns, exceed conventional surfaces by a factor of several thousands. For illustration, Pt particles with a diameter of $1mm$ have a total surface of $1.4 \cdot 10^{-1} \frac{m^2}{kg}$. If the diameter is reduced to $1nm$, the actual dimension of nanoparticles, the active surface increases to $1.4 \cdot 10^5 \frac{m^2}{kg}$, a difference of a factor of 10^6!

In the industry, catalysts are widely used. One of the most common examples is the exhaust gas catalyser in motorized vehicles. They use metal coated ceramics (platinum, palladium and rhodium) as catalyst because they are amongst the most efficient (but not cheapest) catalysts.

---

[1]An exothermic reaction is a chemical reaction which releases energy, mostly delivered as heat. The final potential energy is lower than the potential energy of the reactants. In contrast, an endothermic reaction has a higher final potential energy than the reactants, it thus needs external energy to launch the reaction.

In nature, many processes use catalysts, for example to produce ammonia which can be used as a natural fertilizer. The bacteria Azobacer vinelandii is able to synthesize ammonia out of nitrogen and hydrogen at ambient conditions (this is not yet possible in industry. Industrial production of ammonia needs very high temperature and pressure and thus a huge amount of energy). It possesses an enzyme, called Nitrogenase, that, thanks to an iron complex in the inner part, breaks apart the very strong nitrogen bonds [91, 92]. Many other examples could be cited.

Catalytic reactions can take place either in one phase (homogeneous reaction) or in different phases (heterogeneous reactions). We concentrate on the second one, as it is the actual process taking place in our study. Heterogeneous catalysis typically involves a solid catalyst and the reactants being in a liquid or gaseous phase. Different types of mechanisms exist, as presented in the following.

2.2.1   Dissociation

The simplest process is a dissociation by adsorption on a surface [90]. A molecule (AB) in the gas phase (denoted with a g) adsorbs on an adsorption site $(*)$ at the catalyst. The presence of a catalyst leads to a dissociation of the molecule and a subsequent desorption of the products:

$$AB\left(g\right) + * \rightleftharpoons AB^* \rightarrow A^* + B\left(g\right) \rightarrow A\left(g\right) + B\left(g\right) \tag{2.2}$$
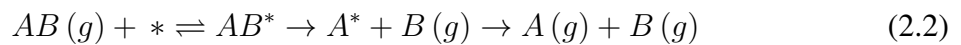
We define the reaction speed r as a function of the partial rate constants for adsorption (k_1), desorption (k_{-1}) and reaction (k). Lets C_{AS} denote the number of occupied sites, C_A the number of available molecules, θ the surface coverage and C_S the total number of available sites:

$$r = -\frac{dC_{AS}}{dt} = kC_{AS} = k\theta C_S \tag{2.3}$$

Consider now a steady state condition. The balance of reactants and products remains constant and Equation 2.3 becomes:

$$\frac{dC_{AS}}{dt} = 0 = k_1 C_A (1 - \theta) C_S - k_{-1} \theta C_S - k \theta C_S \tag{2.4}$$

The first term on the right side of Equation 2.4 represents the quantity of adsorbed and the second of desorbed molecules. Molecules taking part in the reaction are expressed by the last term. Solving the equation for θ we get the coverage of the surface and the reaction speed r:

$$\theta = \frac{k_1 C_A}{k_1 C_A + k_{-1} + k} \tag{2.5}$$

$$r = \frac{k_1 k C_A C_S}{k_1 C_A + k_{-1} + k} \tag{2.6}$$

For $k \gg k_1 C_A$, i.e. when the reaction is limited by adsorption or desorption, the Equation 2.6 becomes:

$$r \approx k_1 C_A C_S \tag{2.7}$$

for $k \ll k_1 C_A$, representing a reaction rate limitation, we get

$$r \approx \frac{\frac{k_1}{k_{-1}} k C_A C_S}{\frac{k_1}{k_{-1}} C_A + 1} \tag{2.8}$$

2.2.2 Bimolecular reaction: Langmuir-Hinshelwood mechanism

In contrast to a simple dissociation of one molecule, a Langmuir-Hinshelwood-driven catalytic reaction involves two different molecules which have both to adsorb on the surface. Figure 2.12 shows schematically the chemical process of the reaction.

$$A + * \rightleftharpoons A^*$$
$$B + * \rightleftharpoons B^* \tag{2.9}$$
$$A^* + B^* \rightarrow AB^* \rightarrow AB(g)$$
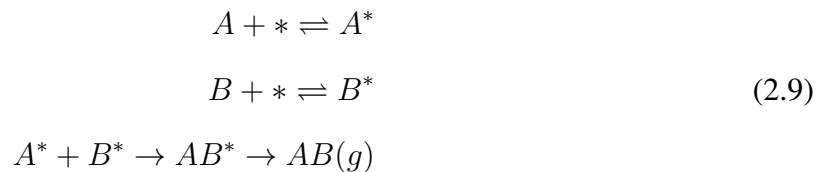
The rate constants are now k_1, k_{-1}, k_2 and k_{-2} for the adsorption and desorption of A (concentration C_A) and B (concentration C_B) respectively and k for the reaction rate. The
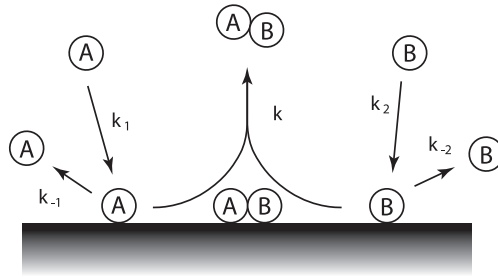
Figure 2.12: Reaction of the Langmuir-Hinshelwood type. Both molecules A and B are adsorbed on the surface and react together.

reaction speed can thus be written as $r = k\theta_A\theta_B C_S^2$. We proceed identically for A and B as before and get

$$\frac{dC_{AS}}{dt} = 0 = k_1 C_A(1 - \theta_A - \theta_B)C_S - k_{-1}\theta_A C_S - k\theta_A\theta_B C_S^2$$

$$\frac{dC_{BS}}{dt} = 0 = k_2 C_B(1 - \theta_A - \theta_B)C_S - k_{-2}\theta_B C_S - k\theta_A\theta_B C_S^2 \quad (2.10)$$

Similarly to the case of dissociation:

$$\theta_A = \frac{k_1 C_A(1 - \theta_A - \theta_B)}{k_{-1} + kC_S\theta_B} \quad (2.11)$$

The limiting step for a Langmuir-Hinshelwood mechanism is the reaction between the adsorbed reactants: the probability that two different adsorbed molecules meet each other on a surface is much smaller than the probability that one molecule desorbs off the catalyst. We can assume that $k_{-1} \gg k_A C_A \theta_A$. The expressions for θ_a and θ_B becomes:

$$\theta_A = \frac{k_1 C_A(1 - \theta_A - \theta_B)}{k_{-1}}$$

$$\theta_B = \frac{k_2 C_B(1 - \theta_A - \theta_B)}{k_{-2}} \quad (2.12)$$

Knowing that the reaction speed is given by $r = k\theta_A\theta_B C_S^2$, Equations 2.12 can be combined:

$$r = kC_S^2 \frac{\frac{k_1}{k_{-1}}C_A\frac{k_2}{k_{-2}}C_B}{\left(1 + \frac{k_1}{k_{-1}}C_A + \frac{k_2}{k_{-2}}C_B\right)^2} \tag{2.13}$$

Consider now three scenarios:

- **Both molecules have a low adsorption probability:** $1 \gg k_1C_A \sim k_2C_B$

$$r = kC_S^2 \frac{k_1}{k_{-1}}C_A\frac{k_2}{k_{-2}C_B} \tag{2.14}$$

The order is one respect to both reactants.

- **One molecule (B) has an adsorption probability close to zero:** In this case, only one part can be neglected: $1 \gg k_2C_B$ and the reaction rate is:

$$r \approx kC_S^2 \frac{\frac{k_1}{k_{-1}}C_A\frac{k_2}{k_{-2}}C_B}{(1 + \frac{k_1}{k_{-1}}C_A)^2} \tag{2.15}$$

At low concentrations of A, the reaction has the order one with respect to A. At high concentrations, the order gets minus one with A. The higher the concentration of A, the slower the reaction takes place and one says that A inhibits the reaction.

- **One molecule (B) has an adsorption probability close to one:**

$$r = kC_S^2 \frac{\frac{k_2}{k_{-2}}C_B}{\frac{k_1}{k_{-1}}C_A} \tag{2.16}$$

The reaction order is one respect to B and minus one respect to A. Molecule B dominates all the adsorption sites and molecule A cannot adsorb. It inhibits the reaction at any concentration. This scenario is also called surface poisoning. We will discuss the adsorption properties of molecules on substrates (especially for TiO_2) in Section 3.2.7.

2.2.3 Bimolecular reaction: Eley-Rideal mechanism

In this model (Figure 2.13), only one of the two reactants (A) adsorbs on the surface of the catalyst. The second part of the catalytic reaction (B) does not adsorb on the surface but react directly with the adsorbed species (A). We can write the process as the following:
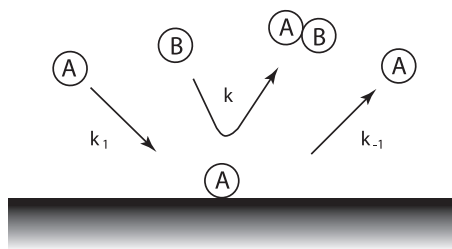
Figure 2.13: Sketch of an Eley-Rideal type reaction. Only one type of molecule adsorbes on the surface and reacts with the other, remaining in the gas phase.

$$A + * \rightleftharpoons A^*$$

$$A^* + B(g) \rightarrow AB(g) \tag{2.17}$$

The reaction speed in this case is

$$r = C_S C_B \frac{\frac{k_1}{k_{-1}} C_A}{\frac{k_1}{k_{-1}} C_A + 1} \tag{2.18}$$

The reaction has the order one regarding the molecule in the gas phase. We can, similar to the preceding process, distinguish different cases:

- **Low concentration of** A**:** The reaction is of the order 1 with respect to A.

$$r = C_S \frac{k_1}{k_{-1}} \frac{k_2}{k_{-2} C_A C_B} \tag{2.19}$$

- **High concentration of** A**:** The order of the reaction with respect to A is zero:

$$r = C_S \frac{k_2}{k_{-2}} C_B \tag{2.20}$$

An example of a catalytic reaction following the Eley-Rideal mechanism is the oxidation of CO on free gold clusters [93]. It is not always evident to identify the catalytic mechanism. Gold nanoparticles Au_8 on a metal oxide surface show a Langmuir-Hinshelwood-like behaviour during the oxidation of carbon monoxide if the CO molecule sits on the top of the gold particle. If the CO is attached elsewhere on the Au_8 cluster, the process follows an Eley-Rideal mechanism [94]. This example shows how minor changes in the setup of the sys-
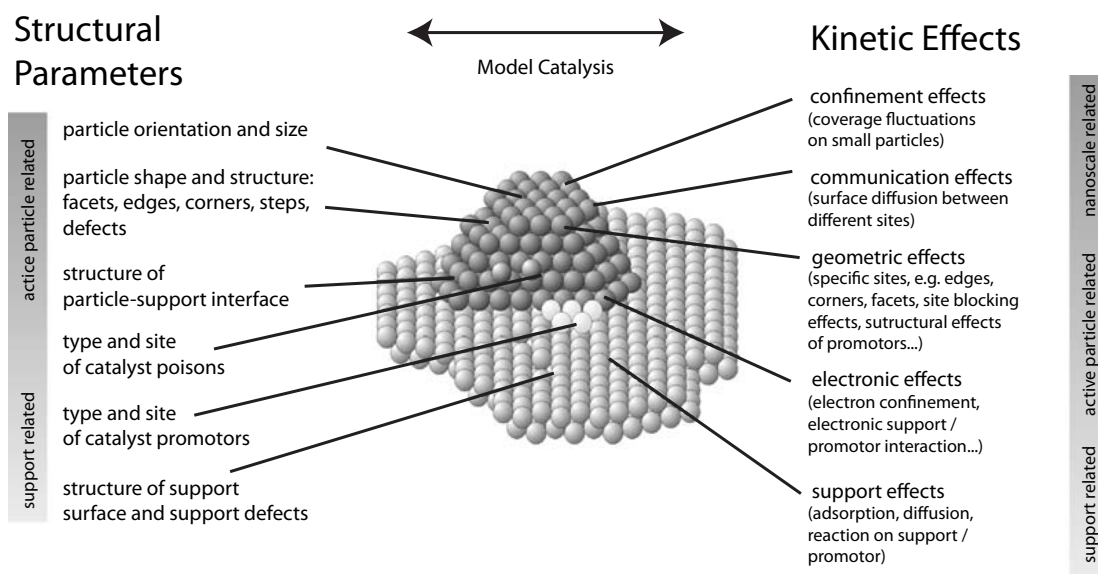
Figure 2.14: Structural parameters and kinetic effects on supported metal catalysts [95].

tem (in the particular case the support and the adsorption site) can change the whole catalytic mechanism.

2.2.4 Catalysis by clusters

The catalytic properties of clusters on surfaces are basically defined by their size and their geometric and electronic configuration. Additionally, it is also important to understand the dynamics of the reaction. Gas molecules are able to move during the catalytic process and the cluster itself can change its geometrical and electronic properties during the cycle. But, as the definition of a catalyst requests a cyclic behaviour, the catalyst has to find its original configuration before the reaction ends. Figure 2.14 summarizes the aspects one has to take into account to describe the fundamentals of catalysis. Freund and co-workers presented a model study in heterogeneous catalysis in their reviews [95, 96]. The parameters can be split into different categories:

1. Support-related effects (a schematic representation is given in Figure 2.15): The capture zone limits the perimeter wherein the molecule can reach the catalyst before it desorbs to the gas phase. The capture zone depends on the temperature, the adsorption and desorption coefficients as well as the cluster density. Schwab and Pietsch proposed in 1929 that catalytic reactions often take place at the interface between catalyst and the
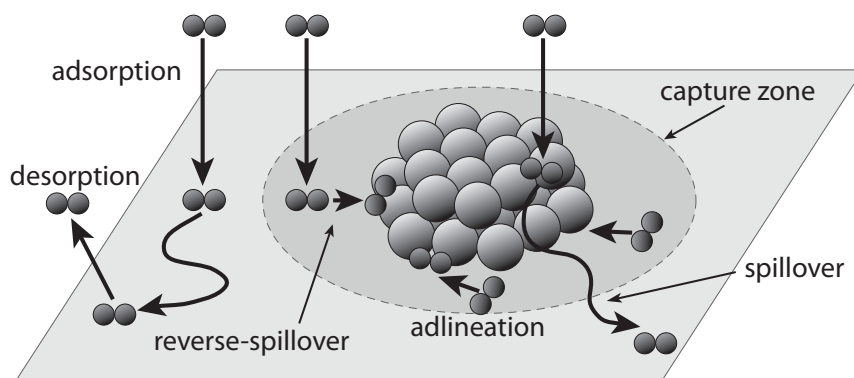
Figure 2.15: Schematic representation of the collection zone, adlineation and reverse spillover (graphics adapted from [36].

surface [97]. This effect is known as adlineation and is similar to reverse-spillover. In reverse-spillover, the molecule adsorbs on the surface of the support and diffuses towards the catalyst. Spillover is the opposite effect. It describes compounds which are formed on the catalyst surface and which migrate then from the catalyst to the support surface where they desorb from the surface. In addition to the mentioned support-related process, one can also imagine chemical reactions involving support components.

2. Effects related to the electronic structure of the active particle: in small particles, electron confinement due to lattice distortion plays an important role. Electronic interaction with the support can also influence the catalytic (and other) properties.

3. Effects due to the geometric structure of the particle: metal particles expose specific sites, edges and corners which do not occur in the bulk material. Their density depends on the particle size and is substantial in the practically relevant size range of a few nanometers. Additional irregular sites such as steps may occur, in particular if the equilibrium shape of the particle is not fully established.

4. Communication effects: these can result from the coupling of small surface regions with different adsorption and reaction properties via surface diffusion. The behaviour of the coupled system may differ a lot from that of a simple superposition of the individual regions.

5. Confinement phenomena: modifications of the kinetics can arise as a result of the fact that the mobility of reactants is limited due to the structure of the catalyst. Reactants
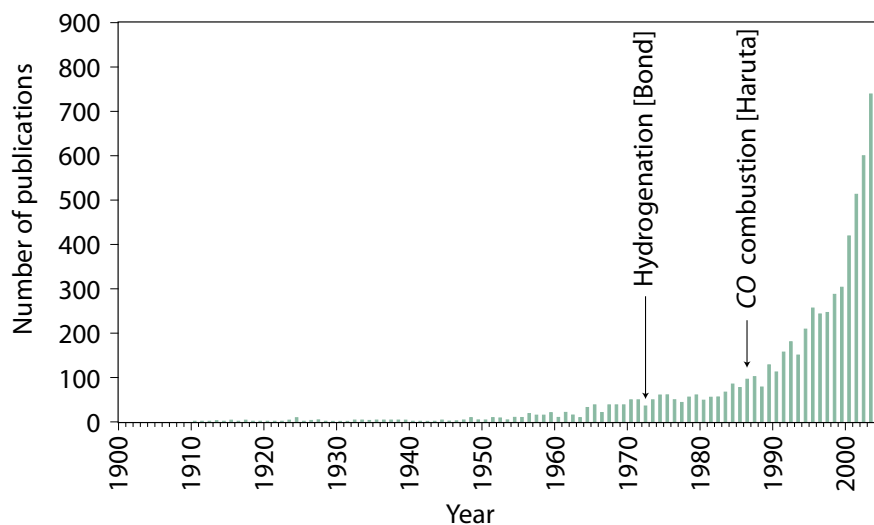
Figure 2.16: Publications of the catalytic activity of gold from 1900 to 2005 [100].

may, for example, be confined to the active metal particles, with surface diffusion to other parts of the surface being inhibited. There are different consequences of this effect: for example, bulk diffusion of hydrogen, may be restricted, leading to changes in the related kinetics.

2.2.5 Catalytic activity of gold

Bulk gold is chemically inert and was for a long time considered as a very poor catalyst [98]. It was in 1973 when Bond reported the hydrogenation of supported gold clusters [99]. Other publications have been submitted during the following years, but it was only in the '90s when Haruta and co-workers showed that, under certain conditions, gold clusters can catalyze the oxidation of CO [19–22]. In the following years, many groups started to investigate different catalytic systems and the number of publications increased almost exponentially. Figure 2.16 shows the evolution of publications about catalytic activity of gold from 1900 to 2005. Knowing that the rush of research on this topic did not stop yet, we estimate that the number of publications in 2010 is still increasing.

Nowadays gold is known as a catalyst with a huge chemical potential. Various catalytic processes have been studied: the most studied reaction is the oxidation of CO and H_2 [19, 22, 101, 107–112]. Haruta *et. al.* also reported the reduction of NO [113] on gold, deposited on supported metal oxides and the methanol synthesis from CO_2 [114, 115]. The

Bond and Thompson, 1999	Preparation and characterization of active gold catalysts, CO and H_2 oxidation and reactions involving hydrogen and nitrogen	[101]
Haruta, 2002	Summary of the catalysis of Au nanoparticles deposited on metal oxides	[102]
Cortie, 2002	Phenomenology of heterogeneous catalysis by Au nanoparticles	[103]
Daniel and Astruc, 2004	Chemical properties, application towards biology, catalysis and nanotechnology	[104]
Meyer *et. al.* , 2004	Reaction on single gold crystals, model catalyst systems regarding the relationship between gold and the support	[105]
Heiz and Bullock, 2004	Role of oxide support defects, cluster size dependence, cluster structure fluxionality and impurity doping on the catalytic properties of size-selected metal clusters	[25]
Hashmi and Hutchings, 2006	Chemical transformation, homogeneous and heterogeneous catalysis	[100]
Thompson, 2006	Overview of gold-catalyzed oxidation processes	[106]

Table 2.1: Review articles about the catalytic activity on Au nanoparticles.

water-gas shift reaction, as one of the oldest known catalytic reactions, has been investigated by Andreeva *et. al.* and other groups [116–120] (Section 2.2.6). Many researchers have published review articles regarding the catalytic activity of Au nanoparticles during the last decade. They focussed on different parts of this very broad field, summarized in Table 2.1. The mentioned catalytic reactions in the text above are by far not the only ones known for Au nanoparticles. References are given in the Table.

Two requirements for a powerful industrial catalytic system are reliability at ambient conditions and a high efficiency. The experimental development is not yet at a point to produce samples which fulfil the standards of industry. Depositions on surfaces still have to be done under controlled conditions, the particle size is a very sensitive parameter and setups able to produce reasonable quantities of clusters do not exist so far. But the research on these systems is progressing and applications are becoming reality.

(a) Valden *et. al.* [24, 122]

(b) Haruta *et. al.* [123]

(c) Lee *et. al.* [27]
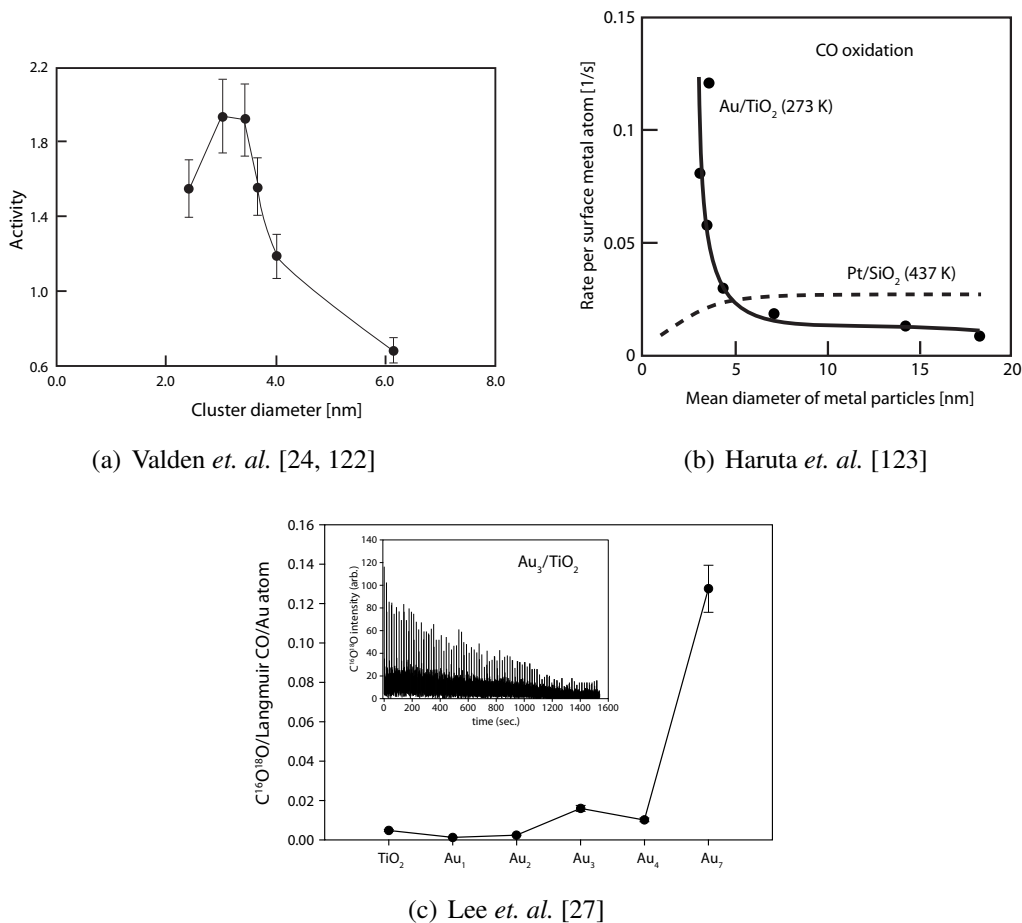
Figure 2.17: Catalytic activity of CO oxidation as a function of cluster diameter (a) Results of Valden show a maximum in activity for cluster size of $3nm$ diameter [24, 122]. (b) Haruta observed a maximal activity at $3nm$ but did not investigate on smaller particles [123]. (c) Lee showed that the activity drops drastically below a critical cluster size of 8 atoms [27].

Studies have shown that an important factor for the oxidation of CO is the production of size-selected particles. Only particles with a certain size exhibit catalytic activity, shown by Valden [24, 121, 122] and Haruta [123]. These authors highlighted the maximum of activity for particles with a diameter of $3nm$ (see Figure 2.17(a)). For particles below a specific barrier ($n < 8$ atoms) the catalytic activity drops and is almost inexistent, as shown by Lee and Heiz *et. al.* [27, 94]. The drawback of this measurement is that no morphological confirmation of the clusters has been done and thus no information about an eventual aggregation is available. This statement is supported by Convers in his PhD thesis [80]. He deposited low energetic $Au_n(n = 2...8)$ clusters on $TiO_2(110) - (1 \times 1)$ at low energy ($2eV/atom$) and showed that small gold clusters migrate on the surface even at room temperature which leads to bigger islands [80, 81]. This diffusion is strongly influenced by the saturation of defects with

OH-groups as confirmed by Besenbachers group. Moreover, oxygen vacancies are the active nucleation sites for Au clusters on $TiO_2(110)$ [82]. Theoretical calculations by Lopez and Nørskov [85] confirm this statement. Their DFT calculations showed that bonding at the interface depends on Au coverage. At low coverage, protruding oxygen atoms are the preferred adsorption sites and are responsible for the reactivity. No strong interaction exists for defect free supports.

2.2.6   Water-gas shift reaction (WGS)

The water-gas shift reaction (WGS) is one of the oldest catalytic processes employed in chemical industry. Details of the processes are described below. Its principle application is the production of hydrogen:

$$CO + H_2O \rightarrow CO_2 + H_2 \tag{2.21}$$

Hydrogen is one of the primary ingredients to produce ammonia-based fertilizers. The catalysts used for WGS are basically iron-based at high temperature and copper-based at low temperature. Many authors have studied the catalytic activity of other metals in the WGS. Grenoble *et. al.* studied the reaction details of several noble metals on alumina [124]. He presented a rating of the reaction activity for different metals, noting that gold has the lowest activity of all studied metals. He also pointed out that the substrate on which the particles are deposited plays a crucial role. For instance, the activity of platinum on alumina is a factor of 90 higher than the reactivity of the same metal on carbon. Ovesen *et. al.* [125] presented a kinetic model of the water-gas shift reaction, based on a description of its elementary steps at the atomic level, as shown in Table 2.2. A gaseous water molecule adsorbs on the surface (the asterisk ($*$) signifies an adsorption site) (1) and dissociates into an OH group and a hydrogen atom (2). If two hydroxyl groups are close enough, the can recombine to form water, leaving a single oxygen atom on one of the adsorption site (3). Alternatively, if free adsorption sites are present around a hydroxyl group, it dissociates (4). The thus obtained hydrogen atoms form a hydrogen molecule that leaves the surface (5) and gaseous CO adsorbs on one of the free adsorption site (6). It combines with an oxygen atom (7) to form gaseous CO_2 (8).

Reaction steps			Reaction number
$H_2O\,(g) + \ *$	$\rightleftarrows$	H_2O^*	1
$H_2O^* + \ *$	$\rightleftarrows$	$OH^* + H^*$	2
$2OH^*$	$\rightleftarrows$	$H_2O^* + O^*$	3
$OH^* + \ *$	$\rightleftarrows$	$O^* + H^*$	4
$2H^*$	$\rightleftarrows$	$H_2\,(g) + 2\ *$	5
$CO\,(g) + \ *$	$\rightleftarrows$	CO^*	6
$CO^* + O^*$	$\rightleftarrows$	$CO_2^* + \ *$	7
CO_2^*	$\rightleftarrows$	$CO_2\,(g) + \ *$	8

Table 2.2: Different steps in the water-gas shift reaction [125]. The asterisk $(*)$ stands for an adsorption site.

After the publications of Haruta *et. al.* (mentioned above), the perception of gold changed drastically. Several groups investigated WGS reactions of gold nanoparticles on various surfaces. Andreeva *et. al.* showed that the essential mechanisms are the dissociative adsorption of water on gold particles and the spillover of active hydroxyl groups onto adjacent sites on the surfaces (Al_2O_3 and $\alpha - Fe_2O_3$) [117, 118]. Boccuzzi and his group showed by FTIR (Fourier Transform Infrared Spectroscopy) measurements that H_2 dissociates already at room temperature on the catalyst and that it reacts with adsorbed oxygen atoms [120]. Schumacher [126] studied the catalytic activity of WGS for various transition metals by estimating the reaction rate with the use of a micro kinetic model. One of the conclusion of his work is that Cu is close to the optimum rate but no quantitative results have been presented for Au. A review of Andreeva summarizes the results reported in literature for the WGS reaction over gold-containing catalysts [119].

Chapter 3

Cluster supports

Contents

This Chapter treats the support materials for these investigations. We basically worked with three different substrates, highly ordered pyrolytic graphite (HOPG), titanium dioxide TiO_2 and yttria-stabilized zirconia YSZ. Each system has its own properties but all have in common that they are basically inert for catalytic reactions. Once the metal particles are deposited on the surfaces, one can observe catalytic reactions. Hence, the catalytic activity is related to the particle itself and the interaction between particles and substrate.

Highly ordered pyrolytic graphite (in the following named HOPG or graphite) is one of the supports used in this thesis for catalytic measurements. Its main advantage are that it does not need complex surface preparation and that it can be handled at ambient conditions. It is also known as one of the simplest surfaces for STM measurements. In Section 3.1, we will point out the most important features and processes on HOPG in relation to this work. It is catalytically inert which makes it an ideal support for such studies. Thus, many groups studied catalytic reactions and particle-enhanced catalytic etching of graphite. These investigations deal with almost all catalytic active metals such as Ni, Pt, Rh, Co or Ag. Gold on graphite has only been studied in very few publications, the results are presented in Section 3.1.4.

Titanium dioxide is another support we used for the studies. It is an interesting surface for the investigation of mobility and evolution of clusters because it presents natural defects that can figure as anchor points for clusters. On the other side, it is known as inert for catalytic measurements. We present the crystallographic structure and different surface reconstructions in Section 3.2.1. The chemical properties, i.e. adsorption of gas molecules, are shown in Section 3.2.7.

YSZ, yttria-stabilized zirconia is used for platinum deposition. An interesting property of YSZ is the conductance of ions rather than electrons. Widely used in chemistry, this support is an ideal candidate for electrochemical promotion. The support as well as the properties of platinum films on YSZ are presented in Section 3.3.

3.1 Highly ordered pyrolytic graphite (HOPG)

3.1.1 Atomic structure

●	A	Carbons	a : 2.456 Å
○	B	Carbons	c : 6.696 Å

(a) side view

● Upper layer (A)

○ Lower layer (B)
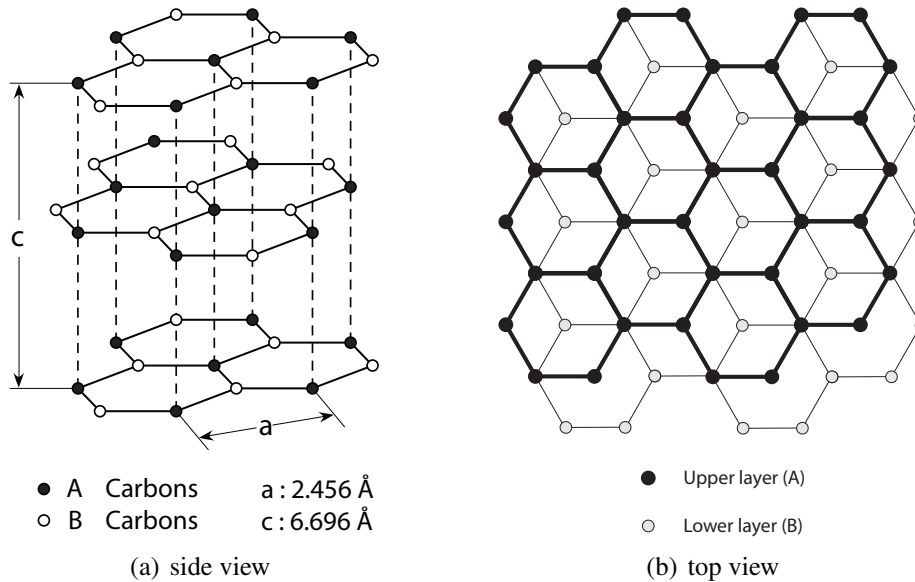
(b) top view

Figure 3.1: Atomic lattice of highly ordered pyrolytic graphite (HOPG). Side view (a): The planes are constituted of sp^2 carbon atoms which form a hexagonal two-dimensional lattice. Van der Waals forces act between the layers. Top view (b) shows the hexagonal lattices of two neighbouring layers that are shifted by 1.42 Å. [127]

Graphite is a layered semi-metal with very strong covalent carbon-carbon bonds within its basal plane and relatively weak Van der Waals interlayer forces. The planes composed of sp^2 carbon atoms, each forming a hexagonal two-dimensional lattice, are stacked in a AB or Bernal structure (Fig. 3.1) [127]. An A atom is placed above an underlying A atom. An atom B in the upper layer is located above the centre (hollow site) of the hexagon in the adjacent lower layer. There are four atoms per unit cell, two of the inequivalent A and B carbon atoms (Fig. 3.1(a)). Theoretical calculations and experimental results agree for the distances between atoms: the lattice constant is 2.456 Å, the interlayer distance 3.348 Å [127]. An STM image of a clean HOPG surface with atomic resolution taken in our laboratory is shown in Fig. 3.2.

A clean surface of HOPG presents large atomically flat terraces separated by steps ($< 5\%$, according to the quality). These single crystalline surfaces can cover distances up to the mi-
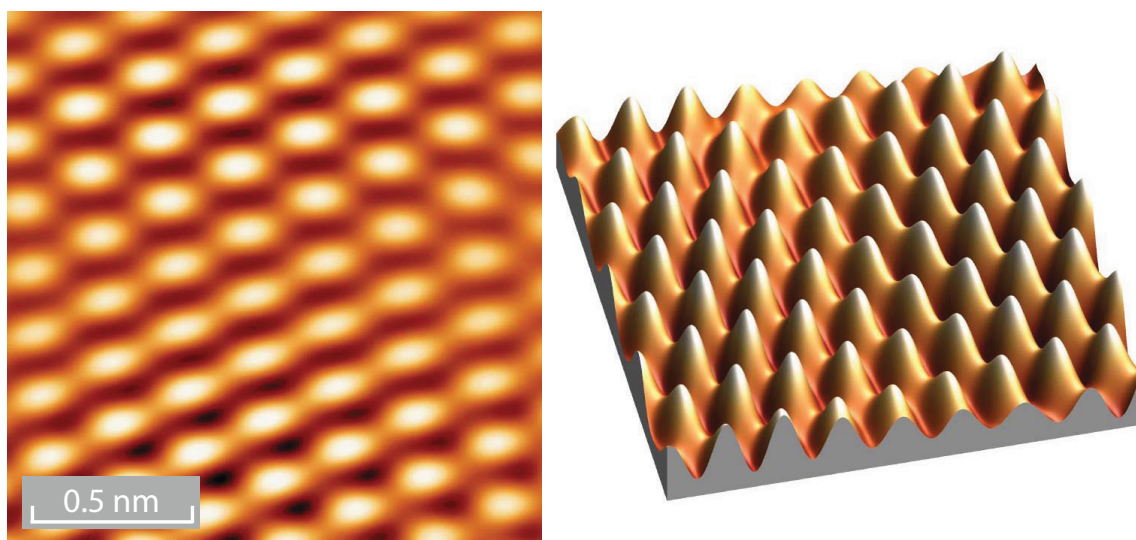
Figure 3.2: STM image of a clean HOPG surface in a 2-d (a) and 3-d representation (b). One can see the hexagonal pattern of the atom alignment in a plane. $V_{gap} = 0.6\,V$, $I_T = 4\,nA$, $T = 77K$. Image size: $1.65nm \times 1.65nm$.

crometer scale. Naturally, monolayer as well as multilayer step edges occur. The orientation of the steps follows the atomic alignment of the HOPG structure. Natural defects on the surface or atoms at step edges contain dangling bonds, unoccupied sp^2 orbitals. These free orbitals are highly reactive and responsible for molecule adsorption on the surface, for example O_2.

3.1.2 Etching process

In order to obtain a structured HOPG surface, local defects can be enlarged by an etching process. The defect induced etching mechanism or oxidation of graphite is driven by an exothermic dissociation of the oxygen molecule. Two different models have been proposed for the etching mechanism: oxidation from direct interaction of gas-phase O_2 molecules with reactive carbon sites (Eley-Rideal mechanism) and adsorption of oxygen on a non-active site on graphite. The chemisorbed oxygen has to migrate on the surface towards an active site. The reaction pathway to produce CO and CO_2 gases is shown in Fig. 3.3 [128]. An O_2 molecule dissociates and adsorbs either on top sites or on bridge sites of HOPG. Due to adsorption, there is an energy gain of $5.5eV$ and $10.1eV$ for the two different adsorption sites respectively. Since the C-O bond is more stable at the bridge site than at the top site, C-O at the top site is more liable to be etched away to form CO gas at typical temperatures. During this
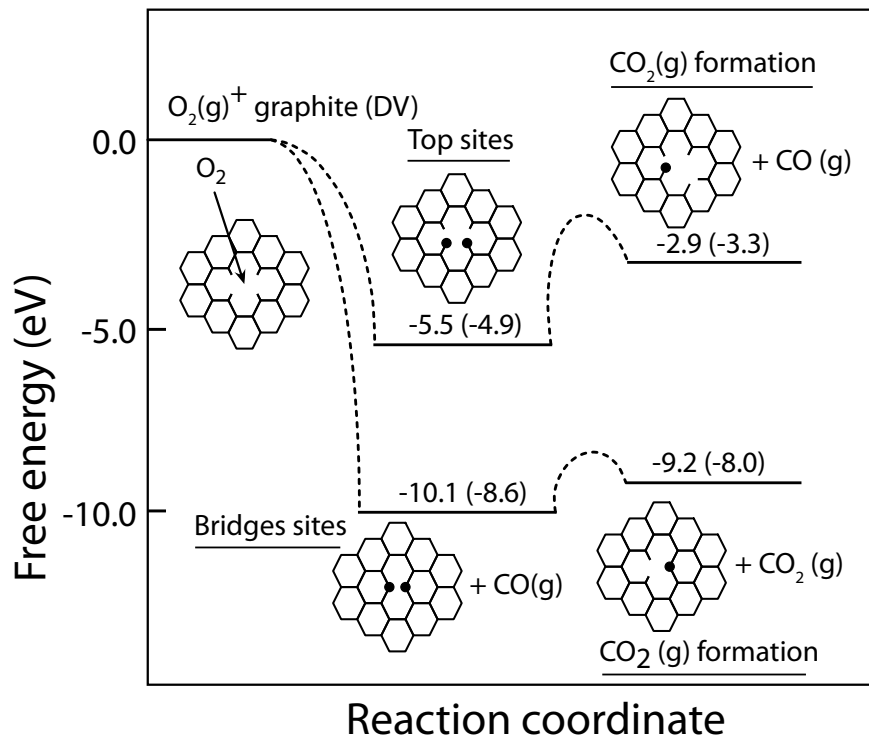
Figure 3.3: Reaction pathway for the etching mechanism of HOPG with the presence of O_2 [128].

reaction, the free energy is increased by $2.6eV$ at the top sites, however it is still lower than that in the initial state before the reaction. The reaction we are describing is thus exothermic, following an Eley-Rideal mechanism. Unlike at the top sites, the C-O bond at the bridge site is much stronger linked and its etching is unlikely. Under assistance of an energetic CO molecule from another etching process, the reaction can be enhanced and lead to formation of CO_2. The free energy is increased in this process by $0.9eV$ but is still much lower than that of the initial stage of an O_2 molecule.

The oxidation of HOPG depends on the temperature during the process. At temperatures below $1000K$, the carbon-oxygen reaction is highly dependent on the nature of the carbon sites on the HOPG. Oxidation is basically initiated at defects, vacancies or step edges, due to their unoccupied sp^2 orbital, following the mechanisms described above [129, 130]. At temperatures above $1000K$, the energy of the oxygen molecules is sufficiently high to attack basal planes of the HOPG and create additional defects in the surface [131].

Thermal oxidation of graphite is a widely used technique to prepare samples with different properties, i.e. nanopits or channels in the graphite layer. First measurements of gasification

reactions of carbon have been made by Hennig, Thomas, Yang and others [132–134] in the middle of the last century. In the '80s, the invention of the scanning tunnelling microscopy (STM) opened new doors to investigate the etching process.

Rabe *et. al.* [129] studied the etching rate of monolayer pits. They showed that the diameter of the pit during etching grows with a constant velocity.

Beebe *et. al.* [135] compared the etching speed of monolayer and multilayer pits. At a given temperature ($920K$), multilayer pits grew up to four times faster than monolayer pits. They stated that the pit growth rate of multilayer pits increases with increasing depth up to four or five layers and then levels off and stays constant for deeper pits. Additionally, they found that the pit growth rate is dependent on the pit density. The growth rate for both monolayer and multilayer pits decreases with increasing pit density [136].

Kang *et. al.* [137] confirmed the results on etching speed vs. pit depth. They studied oxygen adsorption energies and thus the desorption process that leads to gaseous CO and CO_2 with DFT calcualtion. According to their results, the pit grows along the graphite lattice directions, i.e. $\langle 1100 \rangle$, $\langle 1010 \rangle$ and $\langle 0110 \rangle$ directions ($< 30nm$). For such small dimensions, the pits grow first hexagonally but at a certain size, these shapes are blurred. The dangling bonds of atoms on straight rims get randomly attacked and the pit shapes become circular.

Kappes and co-workers [138, 139] exposed their graphite surface to energetic carbon clusters. They presented the first results on the relation between cluster (or ion) impact energy and the induced pit depths.

The group of Palmer was the first to investigate experimentally and theoretically the impact of energetic metal clusters (in their case silver) into HOPG. Their DFT calculations show in details the physical process during impact and give information about the deformation of the graphite substrate [140–142].

A more detailed investigation was made in our group [143–145]. Seminara proposes in her PhD thesis a universal scaling law which relates the momentum of the impinging particle and the pit depth. She showed a linear behaviour between the scaled momentum and the depth for different cluster sizes and cluster materials. Creating artificial defects in HOPG became a standard method to prepare samples for different applications.

Hövel [146] and Kappes [147] use the technique for nanolithography and increased the number of defects per surface unit.

3.1.3   Metal atom and cluster deposition on graphite

Nanopits can be used to control the stability of atoms or molecules deposited on the surface. Hövel and Barke presented a review on morphology and electronic structure of gold clusters on graphite [148]. They prepared the HOPG surface in order to create artificial pits and observed the formation of individual gold clusters along the rim of these pits. The key role of the nanometer sized pits in HOPG is to provide condensation centres which capture the metal atoms and hence serve as starting locations for subsequent nucleation processes. Once a critical nucleus has developed, it is favourable for additional atoms to adhere to existing nanoparticles than to form further nuclei. With increasing Au coverage, the mean cluster size increases but the quantity of particles remains constant. So created small gold clusters show a three-dimensional growth with a ratio of diameter to height $d/h \approx 1.4$. With increasing gold coverage the cluster size grows, and they observed facets on top of the clusters. The growth of these larger clusters is basically lateral [149, 150]. Furthermore, they are oriented in the (111) plane parallel to the (0001) HOPG surface. Without fixation, the clusters do not show a preferred orientation and diffuse at elevated temperatures on the surface, which will lead to very large gold particles [151].

Very recently, the group of Beebe prepared bigger nanopits in the range of $100\,nm$. They deposited different gold and silicon clusters on the surface and reported that the evaporation and subsequent annealing of various amounts of gold onto these molecule corral templates result in the formation of metal nanostructures. It was found that by varying the total amount of metal evaporated, different types of nanostructures (rings, disks and mesas) appear. Sufficiently large gold structures such as mesas (which fill up the pits) are nearly atomically flat with a (111) surface orientation on the top [152].

Theoretical calculations using density functional theory (DFT) were made by Akola and Häkkinen [153]. They studied the adsorption energies of gold atoms and small gold clusters (Au_6) on graphite. The calculated adsorption energies for both gold atoms and the gold cluster Au_6 on HOPG ($0.3\,eV$) are slightly lower than the experimental values found by Anton *et. al.* ($0.39 \pm 0.04 eV$) [154, 155].

3.1.4 Catalytic reactions on graphite and particle-enhanced etching by various metals

Catalytic reactions on graphite were investigated for the first time already in the '60s by Hennig and Tomita. Hennig [156] deposited colloidal metal particles on single crystals and studied the oxidation of graphite. He stated that the oxidation only occurs at the metal-carbon interface. The graphite layers are attacked parallel to the cleavage surfaces and channels are produced. This was explained by the force maintaining a maximum contact area between the catalyst and the graphite surface.

Other publications highlight the catalytic role of transition metal particles such as nickel, platinum or rhodium for the hydrogenation of carbon (CH_x) [157, 158]. Various groups investigated the catalytic properties of nanoparticles deposited on graphite and the channel formation [159–172]. Common to all is that they observed local particle-enhanced etching.

Tomita [173] examined the mechanism at an atomic scale. He found a large number of straight channels in presence of iron, nickel and cobalt particles. Channels are parallel to the $\langle 11\bar{2}0 \rangle$ and the $\langle 10\bar{1}0 \rangle$ direction. Small particles ($< 0.5\mu m$) generally produce straight channels whereas channels from bigger particles bend at specific angles. The etching follows the crystallographic structure of graphite and the bending is consequently $120°$ and, less frequently, $60°$ [169, 170].

Baker [159] related the channel length to the channel depth. He showed that the propagation rate is inversely proportional to the channel depth. It is also very interesting to note that the channel depth is always identical to the step height, i.e. the local catalyst enhances etching even for multilayer steps [171]. This clearly means that the nanoparticle lies on the bottom of the pit or the step and no vertical etching across the graphene layers take place. Additionally, Goethel and Yang claimed that the channelling speed is also dependent on the crystallographic orientation. The underlying atomic configuration and the edge structure (zigzag or armchair) influences the etching speed [162]. The same group investigated the C-NO reaction enhanced by alkali, alkaline earth and transition metal catalysts. All catalysts follow the established modes of channelling at high temperature ($900K$) and under gas pressure ($1\% NO$ and $99\% He$).

The group of Takasu [164] deposited cobalt nanoparticles and observed straight channel

formation above $900K$ in a mixture stream of hydrogen and nitrogen gas. The channels are oriented along specific crystallographic directions.

The research of Rabe *et. al.* [168] related the cluster size of silver particles on graphite and the etching speed in ambient environment and at elevated temperatures. According to their results, the speed of particle channelling through graphite is proportional to the particle diameter.

A contradiction with most of the presented results has been observed in the publication of Boxley [174]. He suggests that gold nanoparticles in the same size range as other groups (diameter of $10nm$) are preferably found on top of the steps. This would mean that the particles cannot be responsible for the local etching of multilayer steps.

Possible explanations for the detailed mechanism of local etching were given recently. Strongly bound metal atoms (Pt, Ni, Ru) break the carbon-carbon bonds at the interface with the nanoparticle. Carbon atom transport through the nanoparticle leads finally to the reaction with the gas. Weakly bound nanoparticles as copper or gold are not able to break the strong carbon bonds. In contrary to platinum or nickel, the oxygen atoms dissociate on the nanoparticle and are transferred to the metal-carbon interface, leading to the etching of graphite [162, 170–172].

3.1.5 Catalytic activity of Au_n clusters on graphite (HOPG)

The only indication of a catalytic activity of gold nanoparticles was studied by Watanabe [165]. He deposited small gold particles (2-$3nm$) on graphite and annealed the sample to $700K$. Gold particles coagulate to form particles with a diameter of 10 to $100nm$. During the coagulation process, etching of the HOPG graphite substrate was observed. On the other hand, no etching phenomenon was observed for a diamond surface[1].

The water-gas shift reaction on HOPG has not been investigated so far. The presented results of Section 2.2.6 were made on different surfaces (Al_2O_3, α-Fe_2O_3 and TiO_2) and are thus not comparable with HOPG surfaces. There are indications that gold exhibits the

---

[1]Like HOPG, diamond is also built of carbon atoms but has a different crystallographic structure (sp^3).

same channel etching capacity as other metals. Namely Beebe [175] deposited gold nanostructures on HOPG and showed that oxygen can adsorb molecularly on gold clusters. This is the first step to a particle enhanced etching. We clearly see a dissociation as it will be shown in Section 5.6.

3.2   Titanium dioxide (TiO_2)

Titanium dioxide is a metal oxide, that is not only widely used in scientific research, but it is also used in our daily life. A summary of different applications can be found in online encyclopedias:

TiO_2 is the most widely used white pigment because of its brightness and very high refractive index, in which it is surpassed only by a few other materials. Approximately 4 million tons of pigmentary TiO_2 are consumed annually worldwide. When deposited as a thin film, its refractive index and colour make it an excellent reflective optical coating for dielectric mirrors and some gemstones. TiO_2 is also an effective opacifier in powder form, where it is employed as a pigment to provide whiteness and opacity to products such as paints, coatings, plastics, papers, inks, foods, medicines (i.e. pills and tablets) as well as most toothpastes. In paint, it is often called "the perfect white", "the whitest white", or other similar terms. Opacity is improved by optimal sizing of the titanium dioxide particles.

Titanium dioxide is used to mark the white lines on the tennis courts of The All England Lawn Tennis and Croquet Club, best known as the venue for the annual grand slam tennis tournament The Wimbledon Championships.

In cosmetic and skin care products, titanium dioxide is used as a pigment, sunscreen and a thickener. It is also used as a tattoo pigment and in styptic pencils. Titanium dioxide is produced in varying particle sizes, oil and water dispersable, and with varying coatings for the cosmetic industry. This pigment is used extensively in plastics and other applications for its UV resistant properties where it acts as a UV absorber, efficiently transforming destructive UV light energy into heat.

Titanium dioxide is found in almost every sunscreen with a physical blocker because of its high refractive index, its strong UV light absorbing capabilities and its resistance to discolouration under ultraviolet light. This advantage enhances its stability and ability

to protect the skin from ultraviolet light. Sunscreens designed for infants or people with sensitive skin are often based on titanium dioxide and/or zinc oxide, as these mineral UV blockers are believed to cause less skin irritation than chemical UV absorber ingredients. The titanium dioxide particles used in sunscreens have to be coated with silica or alumina, because titanium dioxide creates radicals in the photocatalytic reaction. These radicals are carcinogenic, and could damage the skin.

Recently, Graetzel received the Millennium Technology Prize (2010) and the Prix Balzan (2009) for the invention of dye-sensitised solar cells, based on TiO_2 nanoparticles [176, 177]. Its hydrophilic properties are used in coatings of front shields in cars. Even though titanium dioxide is a semiconductor, scanning tunnelling microscopy is widely used because the low quantity of defects makes the surface sufficiently conducting.

TiO_2 is one of the most used metal oxide surfaces in fundamental research, if not the most common one. The number of scientific publications is countless and there is no decrease in sight, due to its huge field of applications and the many techniques it is suitable for. A rather detailed review article on the properties of titanium dioxide has been written by Diebold [178]. Many presented facts have been taken from this review.

3.2.1 Bulk structure: types and mobility of defects

The intrinsic defects of TiO_2 are the most interesting in order to understand the properties of the material. They can be found on the surface as well as in the bulk, where they are created during annealing cycles at temperatures superior to $850 K$. Different species of defects can be found: oxygen vacancies, interstitial titanium atoms, linear defects or even crystallographic shear planes [179, 180]. The oxygen vacancies influence strongly the electronic properties (Section 3.2.3) as they are situated in the gap. This gives the crystal a bluish colour with variable intensity, depending on the defect concentration in the bulk [181]. Therefore they are named *F-centres* where *F* comes from the German word "Farbe" (colour). We notice that atoms, both titanium and oxygen, can migrate in the bulk and on the surface. They show different migration behaviours, as it will be discussed in the following:

Oxygen atoms: An atom neighbouring an oxygen vacancy can migrate onto the free position. In the following, another neighbour can occupy the new free position and so on. The movement of oxygen can thus be regarded as a migration of oxygen vacancies [87].

Titanium atoms: In the case of a rutile crystallographic structure (Section 3.2.3) the interstitial titanium atoms migrate with preference in the $[001]$ crystallographic direction [182].

Just as it is possible to reduce the crystal, we can also oxidize it in order to regain the original stoichiometric structure. This happens under oxygen atmosphere at elevated temperatures. However, if the concentration of defects is too high, the perturbation in the crystalline structure is too important and no recovery is possible. Nowadays, it is also widely accepted that the oxidation process implies the movement of interstitial titanium rather than oxygen atoms [183, 184]. A detailed description of the different crystallographic structures follows in Sections 3.2.2 and 3.2.3.

3.2.2   Crystallographic structure

TiO_2 crystals can be found in different crystallographic configurations. Figure 3.4 shows the most abundant structures:

Brookite: this form is of no interest neither for research nor for industrial application. It consists of a rhombohedra structure.

Cotunnitte: Ti atoms are nine-fold coordinated to oxygen. It is known as one of the hardest existing oxides [185].

Anatase: Commercial powders are made of anatase TiO_2 , having a tetragonal structure, representing almost 75% of the annual production of TiO_2 . It is extremely difficult to obtain monocrystals of large dimensions and therefore only few studies are dedicated to anatase TiO_2.

Rutile: This is the most stable structure and is easier to produce than anatase. Details of the rutile structure are presented in the following Section.
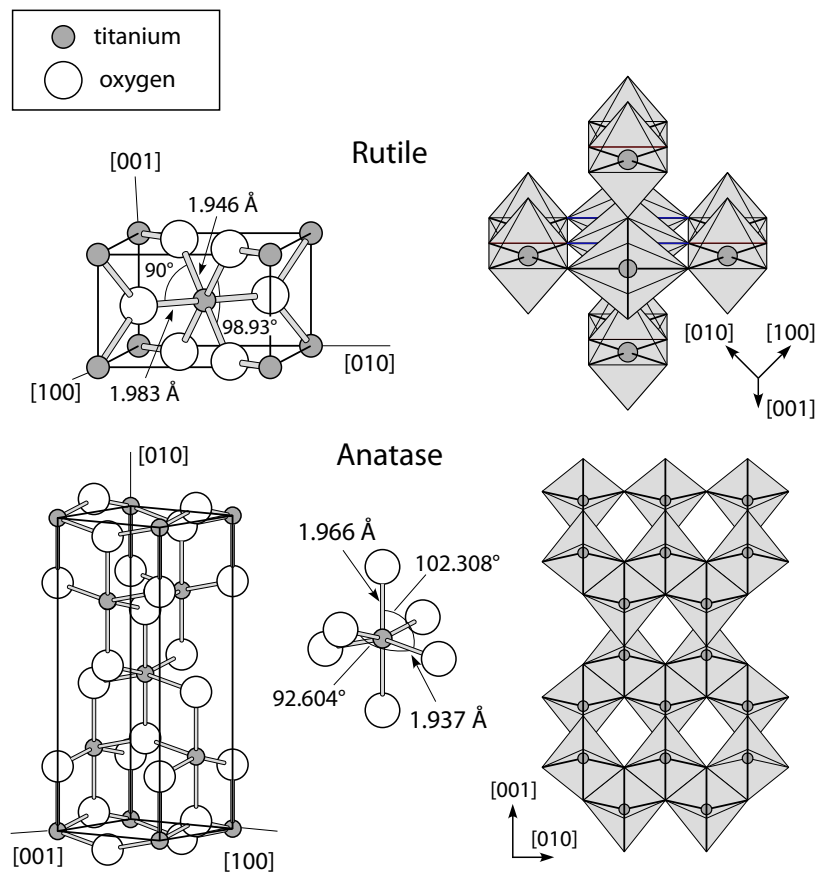
Figure 3.4: Bulk structure of rutile and anatase TiO_2. In both structures, slightly distorted octahedrons are the basic building units. The bond lengths and angles of the Ti atoms are indicated and the stacking of the octahedra in both structures is shown on the right side [178].

The chemical, electronic and physical properties of these crystal structures are different. Anatase for example has a lower activity for oxidation of CO than rutile in presence of gold nanoparticles [186]. In the following, we always talk about the rutile structure when TiO_2 is mentioned, as this is the surface used in this work.

3.2.3 Rutile $TiO_2(110) - (1 \times 1)$

In our study we used the rutile (110) surface of TiO_2. This plane cuts the crystal in a direction where different reconstructions are possible, as a function of annealing temperature and defect density. We concentrate on two reconstructions with the unit cell (1×1) and (1×2).
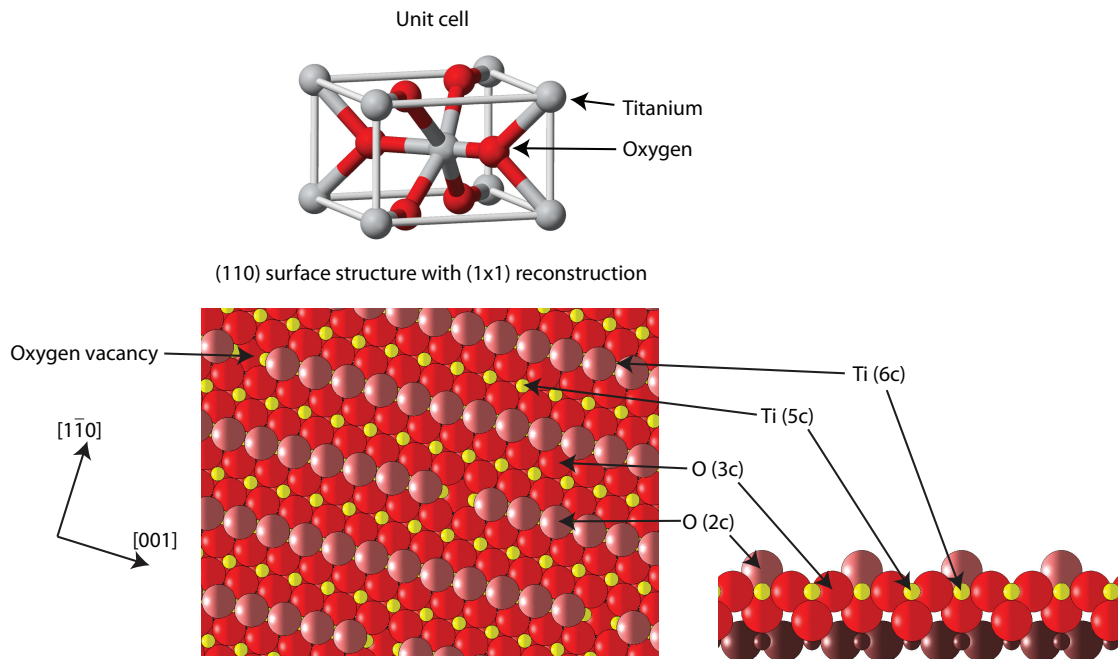
Figure 3.5: Cut through the (110) surface with (1×1) reconstruction. One can see on the top view (left) the oxygen vacancies or F-centres.

The (1×1) reconstruction presents alternately rows of oxygen and titanium in the $[001]$ and the $[1\bar{1}0]$ directions. It does not possess modifications or deformations of the interatomic bonds and is similar to bulk structure. It is used as a model system for investigations on other surface reconstructions of TiO_2 [178]. Atoms with different coordinations can be found on the surface, as illustrated in Fig. 3.5.

- **Ti(6c):** Identical coordination as bulk atoms.
- **Ti(5c):** No connections to the superior plane. The electronic orbital perpendicular to the surface is of type d.
- **O(3c):** In-plane atoms with no particular properties.
- **O(2c):** The rows of superficial oxygen atoms build a kind of bridge between the titanium rows. Their attachment to the surface is reduced due to the present dangling bond. That is why they can easily be removed from the surface by annealing, leading to the formation of oxygen vacancies. The occurrence of vacancies varies between 1% and 15% depending on the annealing procedure. Their presence (or absence) changes chemical and physical properties of the surface [178].
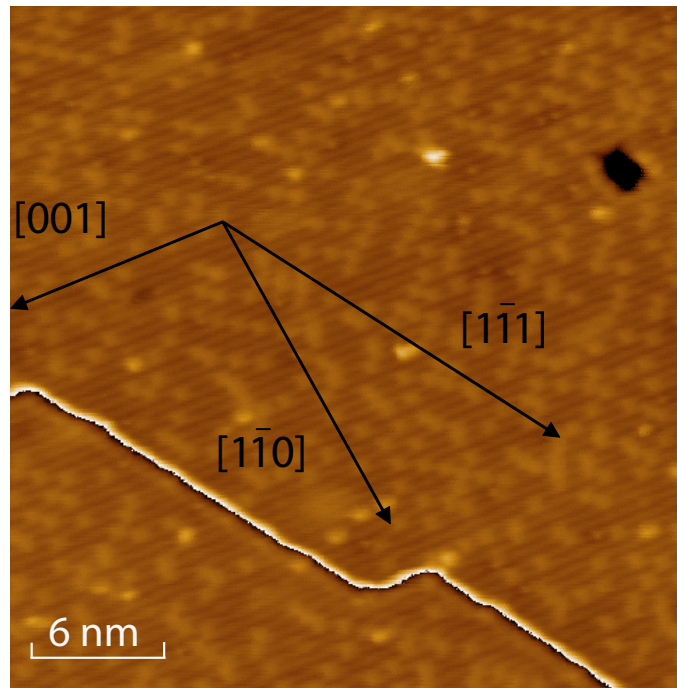
Figure 3.6: STM image of rutile TiO_2 (110)-(1×1). The orientation of the steps follows the $[001]$ and the $[1\bar{1}1]$ crystallographic direction. $V_{gap} = 1.5\,V$, $I_T = 400\,pA$, $T = 77K$. Image size: $30nm \times 30nm$.

All atoms lie in the same plane with the exception of the 2-fold coordinated oxygen. The dimensions of the (1×1) unit cell are $a_{[001]} = 2.95$ Å and $a_{[1\bar{1}0]} = 6.5$ Å. The surface contains terraces of width up to $100nm$ (see Fig. 3.6). They are separated by steps of 3.2 Å, parallel to the $[001]$, $[1\bar{1}1]$ and $[11\bar{1}]$ directions. The size of the terraces depends strongly on the annealing temperature during surface preparation [187, 188]. It is proportional to $T^{1/4}$ for temperatures over $800K$. If the annealing temperature exceeds a certain value, the twofold oxygen atoms will leave the surface and the reconstruction will be changed.

3.2.4 Rutile $TiO_2(110) - (1 \times 2)$

After a strong reduction due to a high annealing temperature, the stoichiometric equilibrium is disturbed. The resulting reconstruction shows a (1×2) grid with a dimension of 13 Å in the $[1\bar{1}0]$ direction. The oxygen rows appear with a double spacing, as shown in Fig. 3.8(b). They are called double strands and have the same stoichiometry as the Ti_2O_3 surface. Their appearance in the STM is similar to bright stripes, centred on the $Ti(5c)$ atoms and not on the oxygen atoms of the bond. Different models have been proposed to explain the growth and

(a) missing row

(b) added 'Ti$_2$O$_3$' row

(c) added row
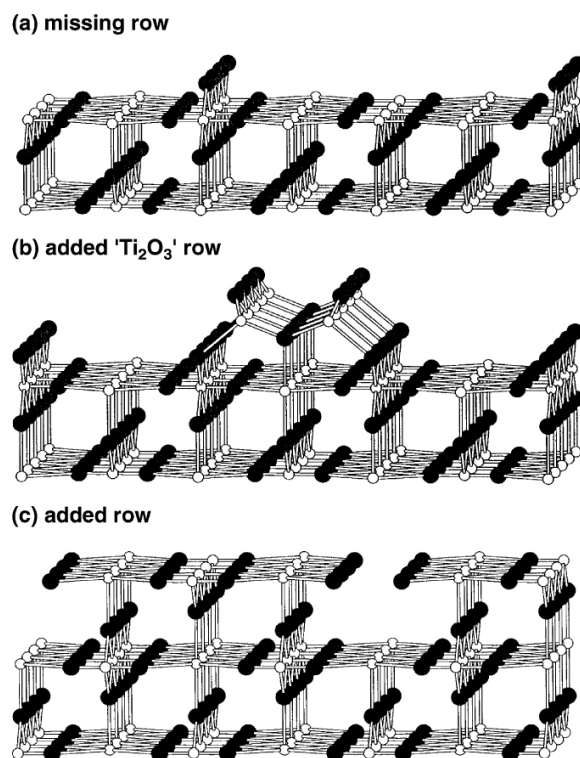
Figure 3.7: Three models to explain the structure of reconstructed surface of $TiO_2(110) - (1 \times 2)$. Small white balls: Ti, large black balls: O [194].

the organization of the surface, as shown in Figure 3.7.

a) The missing row model is obtained by removal of one row of bridging oxygen. This model is inconsistent with more recent STM images and first-principles calculations [189, 190].

b) The added Ti_2O_3 row model has Ti_2O_3 stoichiometry. It was suggested by Onishi *et. al.* [191, 192].

c) The missing unit (or added-row) model was proposed by Pang *et. al.* [193].

Recent results have shown that the two models (b) and (c) do not exclude each other. Both of them are present simultaneously in several studies on the subject. During the reoxidation of the crystal, the formation of the structure depends mainly on the sample preparation parameters and on the actual condition of the crystal [195]. Takakusagi [196] published an article where he looked at the different models and mentioned the secondary structures he observed on the reconstructions, i.e. the presence of cross-links between two rows of Ti_2O_3. The same phenomenon has been observed in our study during STM imaging at low temperature (see Fig. 3.8).
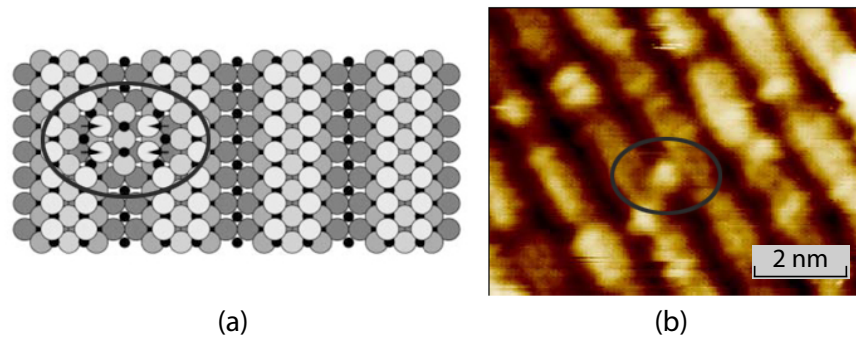
Figure 3.8: (a) Draft of the connection (circle) between the rows of TiO_2 [196]. (b) STM image showing the (1×2) reconstruction and the cross-link (circle). $V_{gap} = 1.25\,V$, $I_T = 100\,pA$, $T = 83K$. Image size: $8nm \times 6nm$.

3.2.5 Reconstruction change between (1×1) and (1×2)

A strongly reduced sample can be reoxidized as mentioned above. Additionally, the (1×2) reconstruction is more often present at high vacancy concentration. It is thus possible to vary the reconstruction in a reversible way. In the following, two important points will be discussed: the dependence of surface growth on temperature and pressure and the influence of surface temperature on the presence of different reconstructions.

McCarthy studied the way the surface grows for a slightly reduced sample as a function of temperature and partial oxygen pressure [197, 198]. He evidenced different regimes (Figure 3.9). At high temperatures, TiO_2 only grows by pushing forward the steps and without creation of new islands. If the temperature drops below a critical barrier, the gaseous oxygen combines with interstitial Ti atoms, migrating from the bulk to the surface, which lead to the formation of new small islands on the terraces. The global reconstruction is alternating periodically between the (1×1) and the (1×2) [179, 199].

3.2.6 Electronic structure and STM contrast

TiO_2 can be considered as a semiconductor of type n with a large band gap ($3eV$) or like an oxide with a small band gap [200, 201]. The band structure of both rutile and anatase TiO_2 are shown in Figure 3.10. In its stoichiometric configuration, the occupied states come principally from the oxygen atoms (2c); the unoccupied states from the titanium atoms (5c). Once the material is reduced, it contains oxygen vacancies. The two electrons occupying the $2p$ orbital have to change into the conductance band, created by the $3d$ states from Ti.
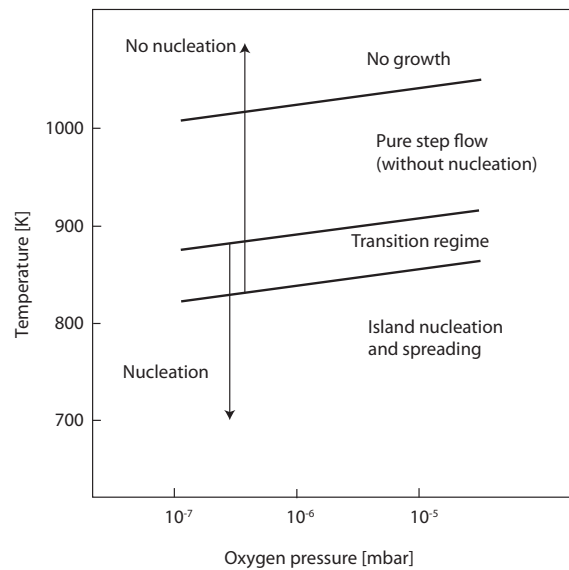
Figure 3.9: Growth regimes as a function of temperature and oxygen pressure for a slightly reduced TiO_2 crystal. The approximate boundaries between the different growth processes are shown as solid lines [197].

According to the applied voltage between sample and atoms at the tip of the STM, it is possible to map the topography of the different species on the surface, but the measured height does not correspond to the real topography, as will be described in Section 4.3.4. The principal electrons contributing to the current are the ones tunnelling from the tip to the unoccupied states of Ti. They make the Titanium rows appear brighter (or higher) than the oxygen atoms as the local density of states (LDOS) is much higher. The same effect happens for hydroxyl (OH) groups and oxygen vacancies. OH groups really protrude from the surface and appear thus very bright. However, for oxygen vacancy sites, this is not the case (since they lack an atom): the electronic orbitals from the Ti atoms underneath the vacancy are clearly visible and make them look like protrusions.

An example is shown in Figure 3.11. The bright spot (dashed circle) represents an OH group and the oxygen vacancy is marked with a continuous circle. The contrast can be completely reversed under certain scanning conditions, but this normally does not lead to good results. However, one has to keep in mind that the tip can as well change its shape by picking up single atoms from the surface. In conclusion, it is important to remember that the STM contrast is dominated by electronic effects and does not represent the real topography of the surface [203, 204].

(a) Band structures for bulk TiO_2

(b) Electronic density of states (DOS)
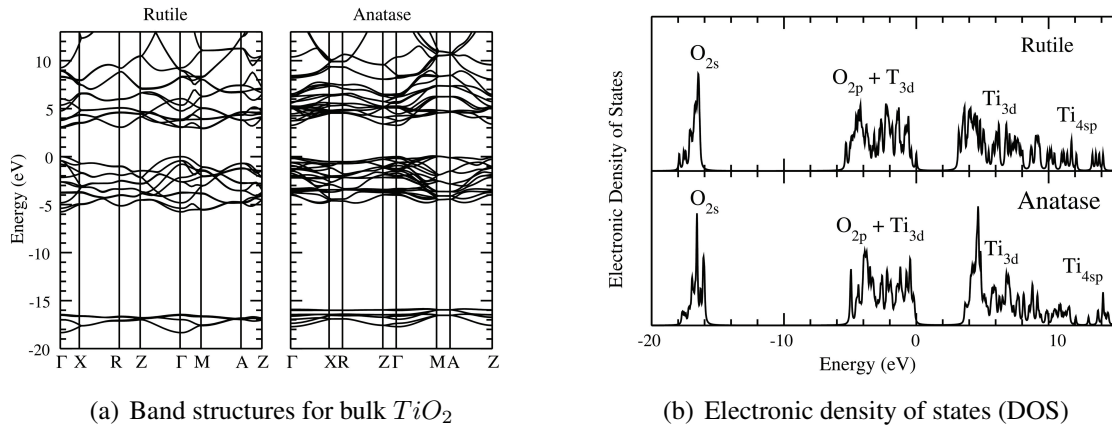
Figure 3.10: (a) Band structures for bulk TiO_2 in the rutile (left panel) and anatase (right panel) structures. The valence band maximum is taken as the zero of energy. (b) Electronic density of states (DOS) for bulk TiO_2 in the rutile (upper panel) and anatase (lower panel) structures, respectively. The valence band maximum is taken as the zero of energy [202].
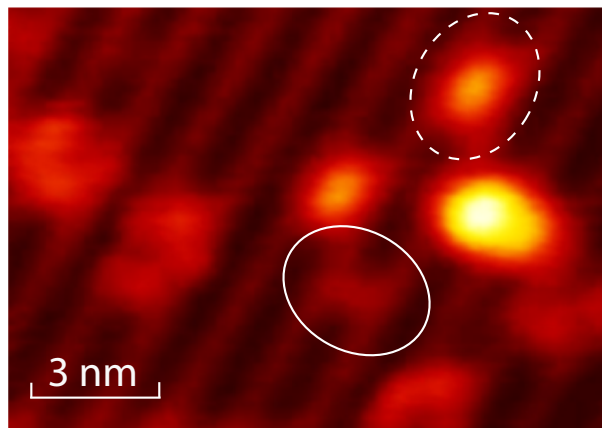
Figure 3.11: Illustration of the contrast in STM images for $TiO_2(110) - (1 \times 1)$, taken in our laboratory. Red rows represent Ti atoms, black rows O lines. The circle shows an oxygen vacancy. The Ti atom from the layer below appears as a protrusion, due to the higher local density of states (LDOS). Dashed circle marks a protruding OH group. $V_{gap} = 1.5\,V$, $I_T = 100\,pA$, $T = 79K$. Image size: $14nm \times 10nm$.

3.2.7   Chemical properties and adsorption

One of the biggest studied topic on TiO_2 is without any doubt the adsorption properties of molecules and atoms, their dissociation and reactions to form other products. We concentrate on reactions with interest for our research, including O_2, CO, CO_2 and H_2O on rutile $TiO_2(110)$.

Oxygen on $TiO_2(110)$

Titanium is a very reactive element, we could therefore expect oxygen to react with the reduced surfaces of TiO_2 , leading to the appearance of $Ti(5c)$. On a stoichiometric surface, molecular oxygen does not adsorb, at least not at temperatures higher than $100K$. On the other hand, it adsorbs with a high initial sticking probability to the oxygen vacancy sites [184]. The model proposed by Hendersson [184] suggests that the molecule benefits of a charge transfer from the substrate and stays on the surface as O_2^- next to a vacancy. Experimental studies have shown that one of the O atoms fills up the vacancy where the other adsorbs next to it on the surface [205].

Carbon monoxide on $TiO_2(110)$

Adsorption of CO has been studied for many years, both theoretically [206–208] and experimentally [209–211]. Yates *et. al.* made measurements using temperature programmed desorption spectroscopy (TPD) (see Section 4.2.1) on TiO_2 surfaces [209]. They found that CO adsorbs on oxidized TiO_2 at a temperature of $105K$ on the Ti in-plane lattice sites. On the other hand, CO completely desorbs from the surface if the temperature exceeds $225K$. When they adsorbed CO on pre-annealed surfaces (up to $900K$ with the creation of oxygen vacancy sites), a new high temperature desorption process up to $350K$ appears which is associated to the presence of oxygen vacancies. However, CO does not undergo dissociation, thermal oxidation or isotopic exchange with the lattice oxygen. Furthermore, no production of CO_2 was detected. Figure 3.12 shows the TPD spectra and the observed high temperature tail for the pre-annealed surface.

A theoretical model is proposed to explain the enhanced binding energy of CO in the vicinity of vacancy sites in which the binding of CO on Ti lattice sites is enhanced through the interaction of the oxygen moiety of CO with the vacancy site. This model is consistent
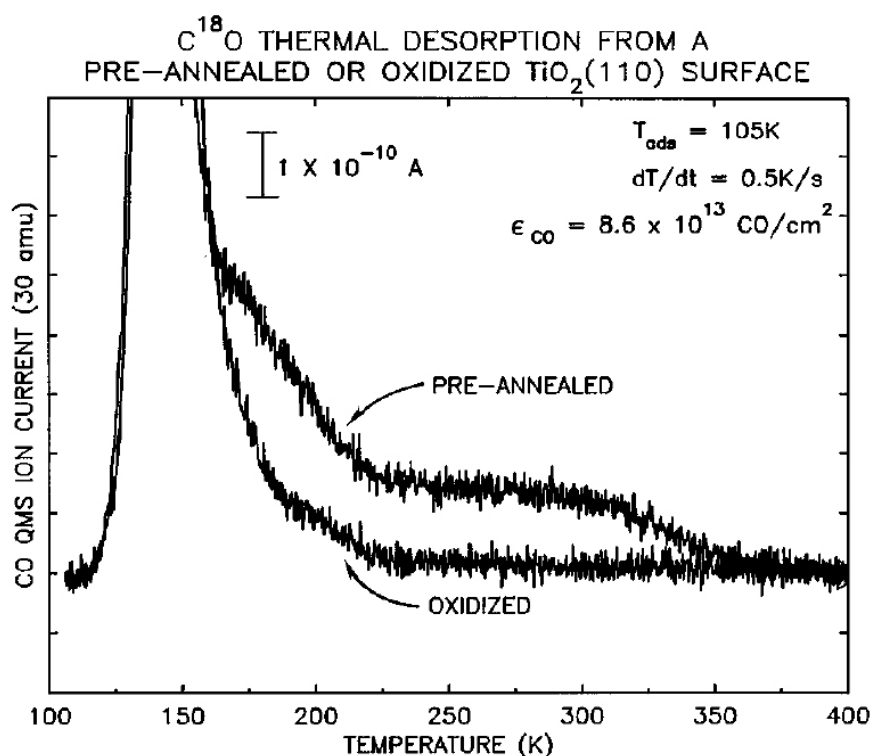
Figure 3.12: TPD spectra for CO desorption on TiO_2 $(110) - (1 \times 1)$. Desorption stops at $170K$ for oxidized surfaces but extends to $350K$ for surfaces which underwent a pre-annealing [209].

with the observation that the CO saturation coverage is not influenced by the production of vacancy sites. However, the values for the binding energy are higher than the values obtained experimentally by Yates [209].

Carbon dioxide CO_2 on $TiO_2(110)$

This molecule interacts only very weakly with TiO_2 [184, 211]. It desorbs at $137K$ from the intact surface and at $166K$ from adsorption sites on defects. Its adsorption can be blocked by the presence of water.

Water H_2O on $TiO_2(110)$

Water is probably the most important adsorbed molecule on TiO_2 . Numerous applications including photocatalysis, gas sensors and solar panels have been industrialized in aqueous environments. A complete review on water interaction with solid surfaces has been published by Henderson [212].

When the surface is exposed to water at low temperature ($100K$), the desorption peaks are located at $160K$ (multilayer) and $275K$ (monolayer) for the clean surface and around $300K$ for slightly defective surfaces. An additional peak can be observed at $500K$ (explained in the following paragraph) [213]. In the case of a clean surface, water binds molecularly to Ti^{4+} sites first (peak at $275K$). The next water molecule can bind to bridging oxygen sites and their desorption is almost identical with the multilayer peak ($170K$).

In addition to these results, Brinkley *et. al.* [214] showed another peak at $200K$, corresponding to the second water layer. He identified, as already Hugenschmidt, desorption peaks above $290K$ as recombination of hydroxyl groups.

On stoichiometric TiO_2 without defects, water is almost not present at room temperature, as described in the publication of Henrich [215]. Defects are needed for water to adsorb on the surface. Furthermore, experimental and theoretical studies have shown that water not only adsorbs on TiO_2 , but also dissociates [213, 216–221]. The *O-O* distance on $TiO_2(110)$ is too large to facilitate hydrogen bonds [212]. It was Kurtz and co-workers who, for the first time, studied the interaction of water with vacancies on TiO_2 and observed the dissociation on oxygen vacancy sites [219].

The first group using TPD for this kind of investigation was Hugenschmidt *et. al.* They detected a high-temperature state at $500K$ that was attributed to the recombination of two OH groups, generated by dissociation of H_2O [213]. This result was confirmed by Hendersons group [222, 223] and additionally they put in evidence the mobility of hydrogen atoms, generated from dissociation, along the rows of bridging oxygen. These atoms recombine in the recombinative desorption state at $500K$. The fact that vacancies do not oxidize during water dissociation is a strong sign that the OH molecules are not in an ionic state OH^-, but present as radicals $OH^{\bullet}$.

There is a contradictory topic concerning the vacancy healing: one part of the researchers suggests that water dissociation can heal the vacancies and enable desorption of H_2 [214, 216]. Other groups did observe neither healing of vacancies nor hydrogen desorption [213, 224].

Finally, Brooks [225] and Schaub [226] confirmed the water dissociation at vacancy sites for heating to $290K$, inducing creation of bridging OH groups. In their publications, they show that water also binds to five-folded Ti^{4+} sites and desorbs during heating to the mentioned temperature without dissociation.

3.2.8 Sample preparation

Several samples have been used during this work, provided by *MTI Corporation*. They are all cut out from one big crystal and are thus similar. Once the sample is mounted on the sample holder, several sputtering-annealing cycles are necessary to prepare the surface. The sputtering is made with a commercially available ion gun. Argon ions are accelerated and focussed on the sample in an incident angle of $50°$ with respect to the surface. The ion energy varies between 800 and $1000eV$ and the current attains $100nA$ (for a total surface of $25mm^2$). A typical sputtering cycle takes two hours, followed by annealing under UHV conditions at $920 - 950K$ for one hour. Subsequent STM images are necessary to control the surface shape and to decide whether or not further sputtering cycles are necessary. Between the measurements, regular cleaning (sputtering) is needed to prepare the sample for new particle depositions. These cycles are less intense and take only one hour of sputtering. The following annealing is made under UHV during 10 minutes at $950K$. For Au deposited on TiO_2 one cycle is sufficient for cleaning. However, recent experiments with Pt on TiO_2 have shown that several sputtering cycles are needed to clean the surface completely. These long sputtering cycles are done during the night (10 hours), followed by annealing and an STM control scan.

With an increasing number of annealing cycles the sample gets darker and darker, indicating that the number of defects increases. The terraces get smaller and the surface reconstruction changes to the (1×2) structure. We can partially inhibit this process by annealing the sample under oxygen pressure. We therefore anneal the sample at $900K$ and $10^{-6}mbar$ oxygen pressure.

3.3 Yttria-stabilized zirconia YSZ

3.3.1 Structure and properties of YSZ

Yttria-stabilized zirconia is a so-called ion conductor. Ion conductivity takes place because of the presence of imperfections or defects in the lattice. A review on ion and mixed conducting oxides as catalysts was presented by Gellings and Bouwmeester [227]. Defects are always present at temperatures above $0K$, arising from the Gibbs free energy and by consequence the disorder in the lattice. Following the reasoning of Gellings, the mole fraction of defects is

given by

$$x \propto \mathrm{e}^{-\frac{\Delta H_f^{defects}}{RT}} \tag{3.1}$$

where $\Delta H_f^{defects}$ is the formation enthalpy of defects. As these enthalpies are usually very different for different defects (ions, electrons), there is always one dominant type of defect, the so-called majority defect. The defect under consideration can be vacant lattice sites, ions at unoccupied sites (interstitial ions), foreign ions of dopants. In ionic lattices, the electric neutrality is required. This means that the overall charge has to be compensated by the number and charge of defects. Thus, charged defects are always present in form of pairs with opposite charge signs.

The mobility of electronic defects are in general thousand times larger than those of ionic defects. In order to overcome this difference, a minimal bandgap of $3eV$ is required for the substrate [227]. In this case, a purely ionic conducting substrate can be obtained.
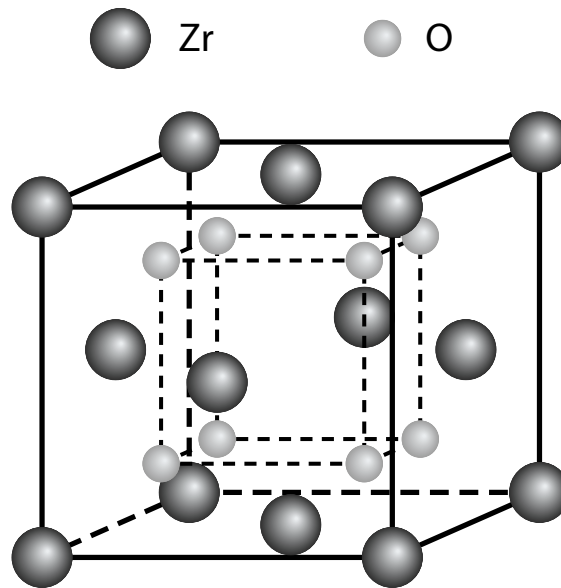
Figure 3.13: Fluorite structure of zirconia oxide ZrO_2 [227].

Yttria-stabilized zirconia (YSZ) is a zirconium oxide based ceramic, with the particular crystal structure of zirconium oxide, shown in Figure 3.13. The majority of the defects in pure zirconia (ZrO_2) are oxygen vacancies and electrons, both at low concentrations and both contributing to the conductance. Above $550K$, even pure zirconia becomes an ionic conductor
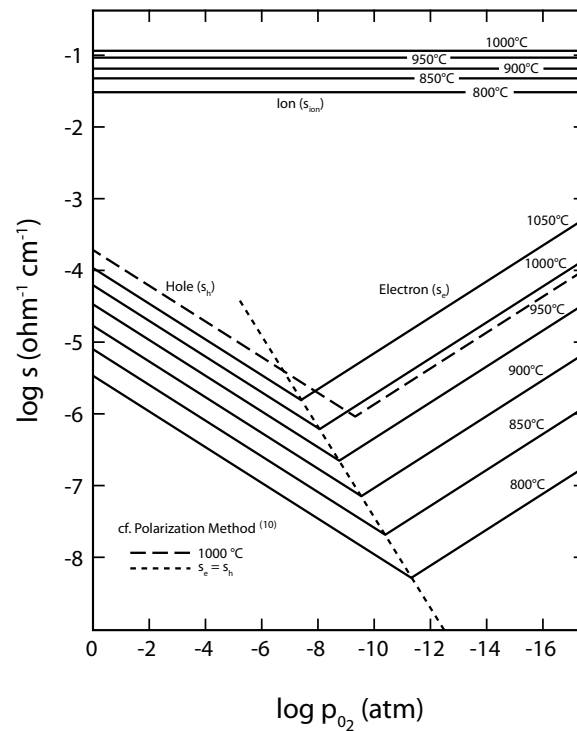
Figure 3.14: Electron, hole, and ion conductivities in yttria-stabilized zirconia for 10 mole percent (m/o) yttria-stabilized zirconia YSZ [229].

(O^{2-}-ions), but due to volume changes, pure ZrO_2 will pulverize on cooling. It is therefore stabilized with lower-valent oxides. The addition of lower-valence oxides as Yttria (Y_2O_3) or calcium (CaO) stabilizes the cubic structure and increases the number of oxygen vacancies. The ionic conductance is thus increased and dominates by far the electronic conductance. The ionic defects induced by the impurities are randomly distributed in the ceramic [228, 229]. Figure 3.14 illustrates the ionic and electron conductivity of YSZ at different temperatures and oxygen pressure. One sees that ion conductance is several magnitudes higher than conductance by electrons [229].

3.3.2 Catalytic properties of Pt films deposited on YSZ

Platinum films deposited on YSZ are frequently used as an efficient catalytic system. It is used for classical catalysis as well as for electrocatalysis and electrochemical promotion. Electrocatalysts are a specific form of catalysts that function at electrode surfaces or may be the electrode surface itself. Electrochemical promotion is a technique where small currents or potentials are applied to a solid electrolyte, i.e. Pt/YSZ. The current implies an enhanced

promotion of ions or electrons through the solid that leads to an increase of the catalytic activity of the system [230–236].

A thin, homogeneous film of platinum is deposited *ex-situ* by PVD deposition on YSZ [237]. The sample is mounted on a sample holder, equipped with a thermocouple for temperature control. We are able to heat the sample up to $1000K$ and maintain the elevated temperature during the catalytic measurements. The YSZ sample with platinum coating has a size of $1cm^2$. The reported gas quantities are all related to this surface, if not mentioned differently.
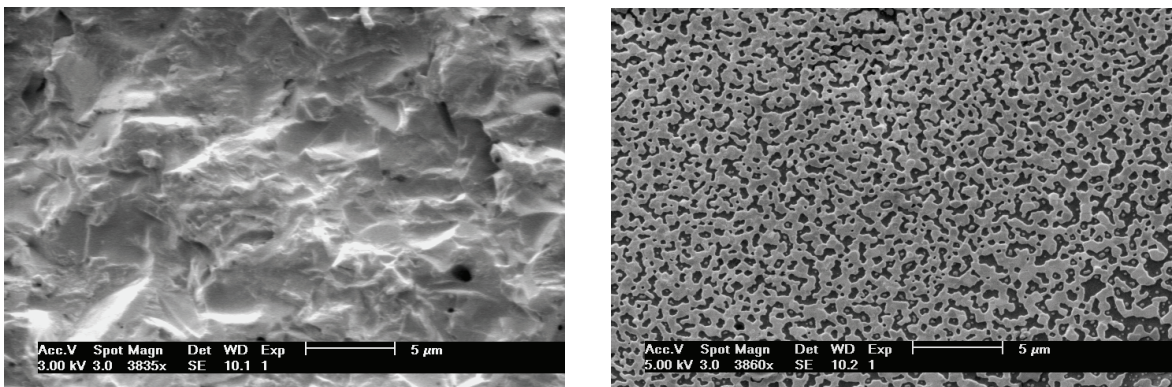
(a) SEM image before (left) and after (right) annealing at $1000K$ of platinum, deposited on YSZ. Image sizes: $31\mu m \times 21\mu m$.
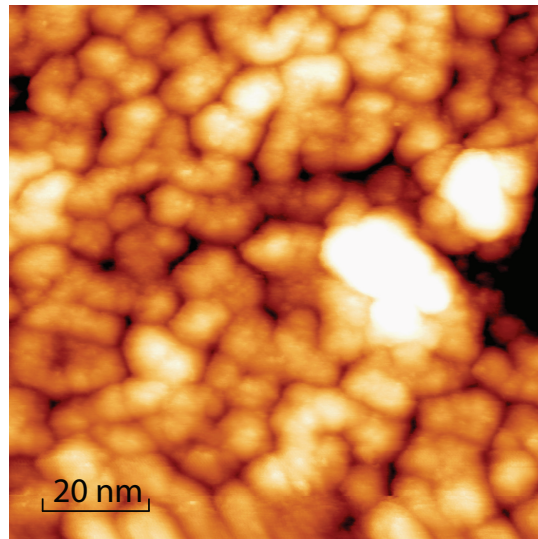
(b) STM image of a Pt film deposited on YSZ. The film is percolated and single particles isolated one from each other. $V_{gap} = 0.5\,V$, $I_T = 200\,pA$. Image size: $100nm \times 100nm$.

Figure 3.15: Images of platinum deposited on YSZ. Electron microscopy images with (a) SEM and (B) STM microscope.

Similar films have been deposited by Jaccoud. He investigated the morphology of such films before and after annealing of the sample by means of electron microscopy SEM [231]. Figure 3.15(a) shows the evolution of the sample. On the left, one sees the surface after platinum deposition. Platinum is found to form a compact amorphous film without apparent porosity. On the right, the same sample is shown after annealing at $1000K$ for 4 hours. A continuous amorphous platinum network with pores of a few hundred of nanometers is visible on the YSZ surface. A more detailed view of the platinum film can be observed by STM imaging. In Figure 3.15(b) the individual platinum particles are visible. The platinum film in not homogeneous but constitutes an ensemble of individual particles that have the same adsorption properties for gas molecules as step edges on a $Pt(111)$ surface.

The catalytic reactions of platinum films on YSZ are various. Vayenas describes in his book a wide range of oxidation reactions: ethylene C_2H_4, C_2H_6, C_3H_6, CH_4 and CO. Further, methanol dehydrogenation, H_2S dehydrogenation or NO reduction by C_2H_4 [238]. One of the most studied reactions is the oxidation of carbon monoxide. The efficiency of this system can even be enhanced when a current is applied between the substrate (YSZ) and the platinum layer [233].

3.3.3 TDS of O_2 and CO adsorbed on Pt/YSZ

Thermal desorption spectroscopy for adsorbates on Pt/YSZ films has been used by several groups. Especially the group of Vayenas made systematic measurements on these systems [239, 240]. They deposited oxygen at $673K$ during various exposure times ($1kL - 12kL^1$) and recorded the desorption spectra, as it is shown in Fig. 3.16(a).

The desorption peak of oxygen is located at $T = 718 \pm 5K$. With increasing oxygen coverage one observes a small increase in desorption temperature of $10K$, corresponding to an adsorption energy difference of $\Delta E = 30.5meV$ (see Redhead-equation 4.11). The authors explain this shift with a weak overall attractive interaction between chemisorbed atoms.

Results of CO TPD measurements on Pt/YSZ do not exist in literature. An alternative system with similar properties is presented in Figure 3.16(b). It shows the TPD spectra of CO on a platinum surface $Pt(111)$. Even though a platinum surface is not similar to a percolated

---

[1]A Langmuir L corresponds to a gas exposure of $1.33 \cdot 10^{-6}mbar$ during one second.
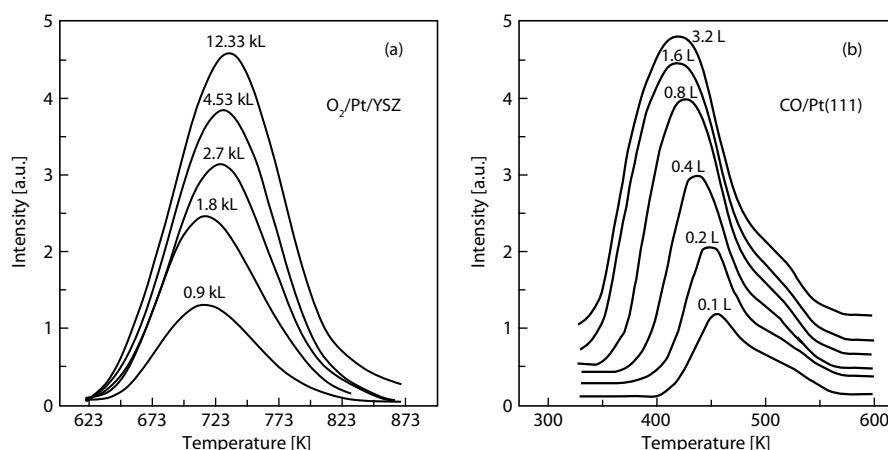
Figure 3.16: (a) Oxygen thermal desorption spectra of Pt catalyst after exposure to oxygen partial pressure. $P_{O2} = 5.3 \cdot 10^{-6} mbar$ at $673K$ for various exposure times. Exposures are expressed in kL, where $lkL = 1.3 \cdot 10^{-3} mbar \cdot s$ [239]. (b) Thermal desorption curve for CO on $Pt(111)$. Adsorption temperature: $300K$ [241].

Pt film, the properties are however comparable. Desorption peaks of this system have been studied by different groups with the same result [241–244]: the desorption peak decreases with increasing CO coverage. The peak shifts from $440K$ at low to $410K$ for high coverage. There is a high-temperature shoulder, visible in each of the curves. Collins *et. al.* relate this shoulder to defect sites (or step edges) on the platinum surface. The shoulder of the desorption spectrum seems not to shift with various oxygen exposures.

Chapter 4

Experimental Setup

Contents

This Chapter presents the different experimental setups that have been used during this work. Most of the measurements need very clean conditions. Therefore, we have to work at very low pressures ($p < 10^{-9} mbar$). These conditions are called ultra high vacuum (UHV) conditions. Two different UHV devices are used during this work. They possess equivalent equipment for the cluster production but differ in the sample analysis devices. We present the setup of the two chambers ("big chamber" for TiO_2 and "small chamber" for the HOPG measurements) in the following Section (4.1), followed by the presentation of the different equipment used in either one or both of the UHV chambers.

During this work, we used an experimental setup that has been working for a long time. Minor modifications have been done on several pieces but one key piece has been designed especially for catalytic measurements. A highly sensitive detector for reaction products of catalysis measurements, called sniffer, has been designed and constructed. Different improvements have been made on a first version in order to enhance the sensitivity. This setup is explained in detail in Section 4.2.

One of the principle measuring instruments during this work is a scanning tunnelling microscope (STM). We mention the historical background of the STM in Section 4.3.1, followed by a theoretical review (4.3.2). The actual device we used is presented in Section 4.3.

4.1 UHV chamber

4.1.1 UHV chamber for measurements on TiO_2

A schematic Figure (4.1) shows the chamber and its three parts: the main chamber (A), the cluster source (B) and the STM chamber (C). The main chamber consists of the deposition area, catalysis measurement device, the sputter gun for sample preparation and the sample storage system. In the cluster source chamber (B), the clusters are produced by a cluster ion gun and deposited on the prepared sample. The STM (Scanning tunnelling microscope) is placed in the part (C) of the chamber, that can be separated from the rest of the chamber. The vacuum is maintained in both parts by means of vacuum valves between them. The separation is necessary to avoid vibrations caused by turbomolecular pumps. The sample transfer from one chamber to the other is achieved by a cryogenic manipulator. Its four degrees of freedom (X, Y, Z and rotation) allow accessing all necessary positions with the sample.

The experimental setup was initially created with the aim to study nanometre-sized particles deposited on surfaces at variable temperatures. The total range of sample temperature reaches from $7K$ to approximately $1100K$. Low temperatures are used for STM imaging and high temperatures for the catalytic measurements and the sample preparation.

Catalysis measurements and STM scans of surfaces at nanoscale request that they remain clean without any adsorption of gas. Therefore one has, as mentioned above, to work at very low pressures ($p < 10^{-9}mbar$), called ultra high vacuum (UHV) conditions. To attain these conditions, we have a sophisticated pumping system available. 9 turbomolecular pumps are connected to the parts (A and B) of the chamber. The main chamber and the STM are the places were the highest vacuum is required, as the sample is prepared and analyzed there. Two turbopumps are connected in series to the main chamber to decrease the partial hydrogen pressure and thus the vacuum to a lower level. A cryogenic pump encases the entire main chamber. A flow of liquid nitrogen in tubes cools a copper cylinder next to the walls of the chamber to $77K$ and creates a cold wall where gas molecules stick and remain fixed until the pump is heated up again. One of the most difficult molecules to pump is hydrogen. Therefor we use so-called getter pumps. A getter is a coating applied to surfaces within the evacuated chamber. In the present chamber, we sublimate titanium on a copper cylinder. Titanium
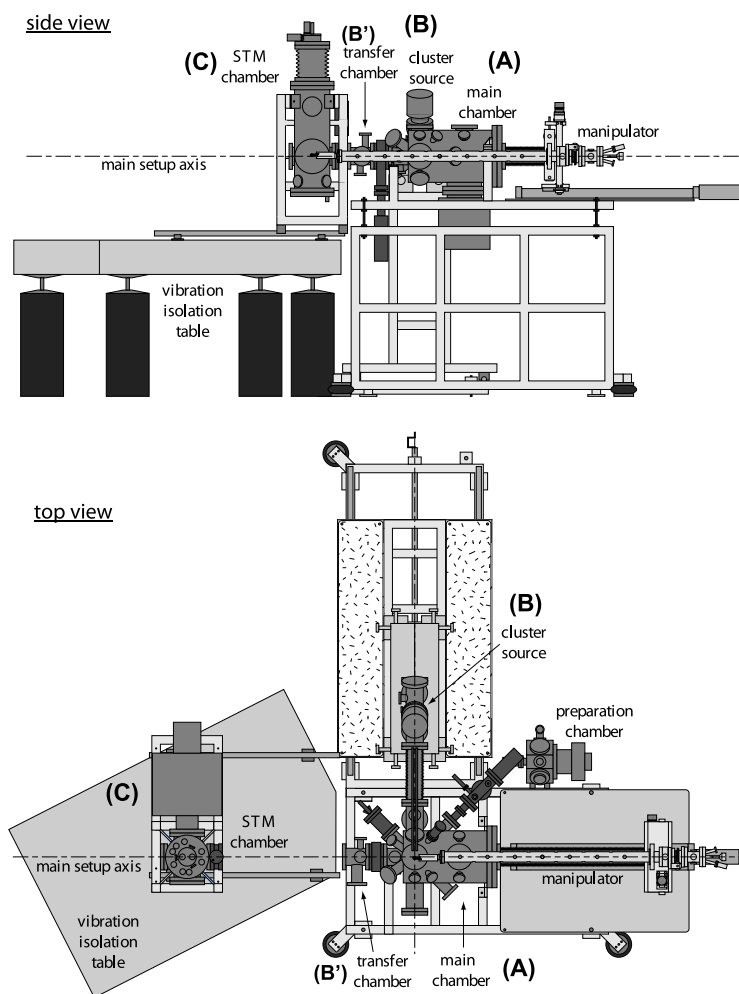
Figure 4.1: Draft of the experimental setup for TiO_2 experiments. Sample preparation, storage as well as catalytic measurements take place in the main chamber (A). Part (C) contains the STM microscope and is separable from the rest of the setup. Chamber (B) serves as hosting for the cluster source to produce the required nanoparticles. The transfer chamber (B') connects the STM part with the main chamber.

particles combine with the gas molecules present in the chamber, namely hydrogen, and form stable compounds. The drawback of these kind of pumps (cryogenic and getter pump) is that molecules are just temporarily fixed and do not leave the vacuum chamber. Sooner or later, we have to heat up the walls to liberate the gas molecules and to clean the surfaces.

Four turbomolecular pumps are connected to the cluster source chamber (B). During the cluster deposition process, the pressure is mainly due to the presence of the ionized gas (a detailed description will be presented in Section 4.1.3) and we have to decrease this pressure step by step towards the main chamber.

The STM chamber (C) does not possess mechanical pumps as their vibrations are too important and would add too much noise to the STM signal. An ionic pump assures the vacuum when the chamber is decoupled. Ion pumps ionize gases and employ a strong electrical potential to accelerate the created ions into a solid electrode. They are then trapped in a strong magnetic field.

A detailed description of the different parts of the UHV chamber (surface preparation device, sample and STM tip storage, manipulator, tip manipulation device and Faraday cup, including the development of a new UHV STM microscope) are presented in the PhD thesis of Raphaël Vallotton [90].

4.1.2 UHV chamber for HOPG sample preparation

The chamber for HOPG sample preparation is less complex than the chamber presented above. It only consists of two parts: one chamber for the CORDIS ion source (Section 4.1.3), the second for the deposition. Two turbomolecular pumps maintain the vacuum but no cryogenic or ionic pumps are connected to the chamber. The vacuum in the deposition chamber reaches $1 \cdot 10^{-8} mbar$.

4.1.3 CORDIS cluster source

Theory of sputtering

Physical sputtering is driven by momentum exchange between a high energetic ion and the atoms in the material, due to collisions [245]. The impinging charged ions start collision cascades (see the sketch concerning sputtering in Figure 2.2). When the cascade reaches the surface, the energy of cascading atoms can exceed the surface binding energy and atoms are ejected. The ratio between impinging ions and the number of ejected surface atoms is called *sputtering yield*. It depends on the ion incident angle, the energy of the ion, the masses of ion and surface atoms and the surface binding energy. To get the highest possible sputtering yield, we use rare gas ions with heavy atomic masses (Kr or Xe). Their energy is typically chosen between 20 and $30keV$. Figure 4.2 shows the sputtering yield for Xe ions on gold. For an energy of $20keV$, we find a yield of approximately $25 \frac{\text{gold atoms}}{\text{ion}}$ [246].
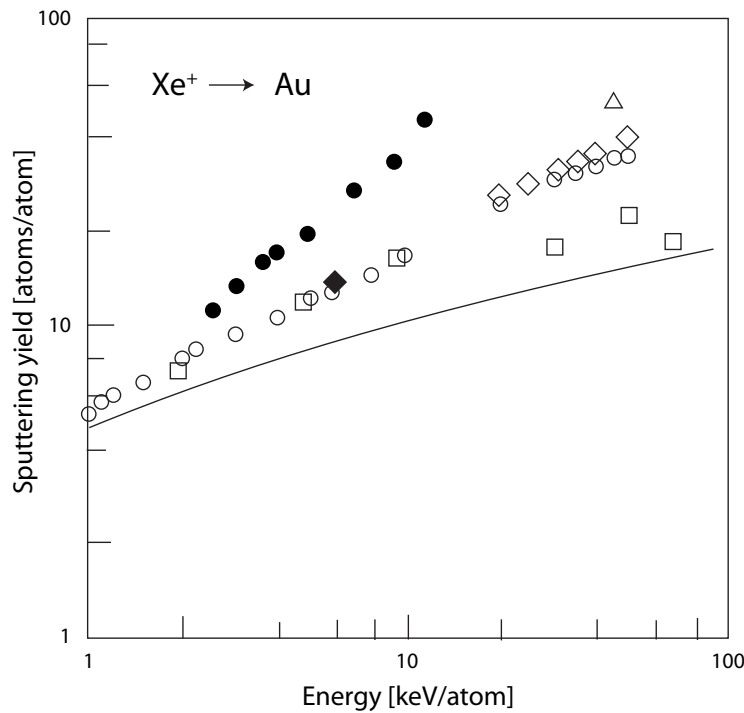
Figure 4.2: Sputtering yield of gold versus Xe^+ projectile energy [246]. Values from different experimental and theoretical studies.

Device in use

Clusters are produced using a Cold Reflex Discharge Ion Source (CORDIS) [247]. An ion plasma of rare gas, in the present case Xe or Kr, is created by emitting electrons from a hot filament. Ions are extracted, focussed through electrostatic lenses and accelerated onto a metallic target. The cluster source is equipped with a rotatable target holder where six different targets can be fixed. The high potential of $20kV$ for the acceleration of the ions implies that the cooling system of the ion gun must be isolated, i.e. that deionised water has to be used in order to avoid electrical breakthroughs. A special water circuit is installed to ensure the cooling.

The primary ion current has a magnitude of $10mA$. Ion impacts create collision cascades and hence provoke the extraction of particles from the target. Different kinds of particles are ejected: single atoms, neutral as well as charged clusters.

Note that the choice of the applied potential is crucial for the efficiency of the sputtering process. At too low energies, only few surface atoms are ejected and the yield is very low. On the other hand at high energies, the collision cascade takes place in the bulk and too far
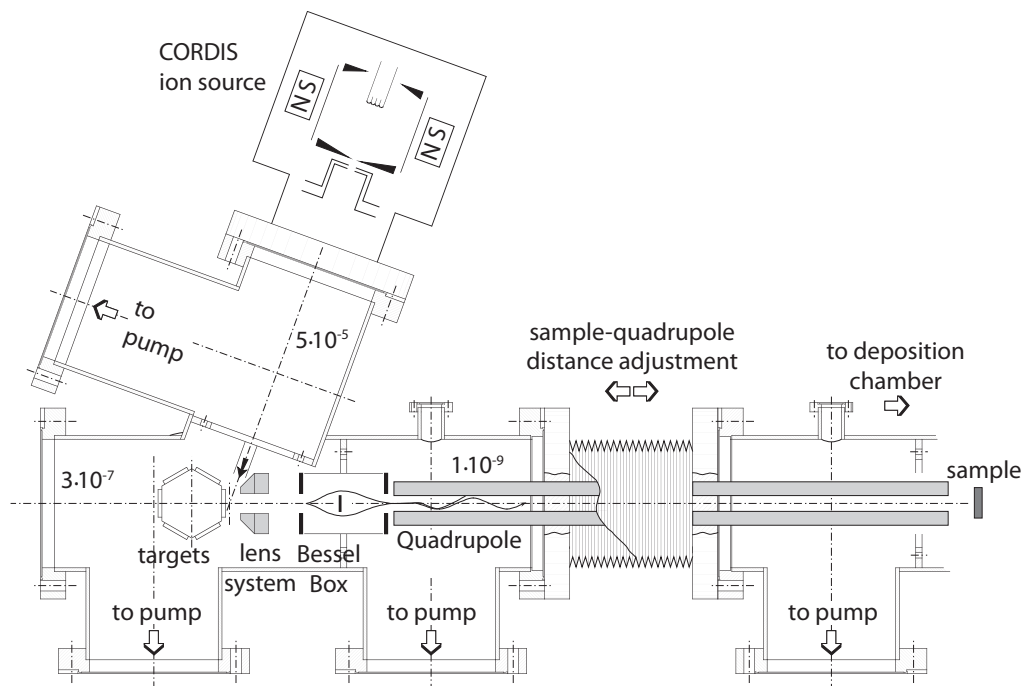
Figure 4.3: Schematic view of the production chamber. High energetic ions are produced in the CORDIS ion source and focussed on the gold target. A lens system focuses the cluster beam, the Bessel Box filters neutral and negatively charged clusters out. Mass separation is achieved in the Quadrupole. The size selected nanoparticles are deposited on the sample.

from the surface. In that case, internal collisions dominate the process and there is only a low ejection rate of particles. The energy range for maximum sputtering yield has been simulated by Samela *et. al.* [248] and is situated between 20 and $100 keV$.

4.1.4 Quadrupole and mass selection

After the ion impact on the metal target, atoms and nanoparticles are ejected and spread in a wide angle. Only a fraction of the particles move in the direction of the sample. A positive potential is applied to the target to define the extraction energy of the particle on the one hand and to create repulsion between positively charged clusters and the target on the other. It thus privileges the positively charged clusters to leave the target. Electrostatic lenses guide and focus the clusters into a Bessel Box (see Fig. 4.3). It works as an energy and charge filter. The axis of the Bessel Box is aligned with the cluster beam, but a central electrode prevents neutral clusters to pass the filter. Lateral electrodes create an electric field in order to guide the positively charged clusters around the central electrode and to guided them into the quadrupole. The quadrupole figures itself as cluster guide but also as the mass selection
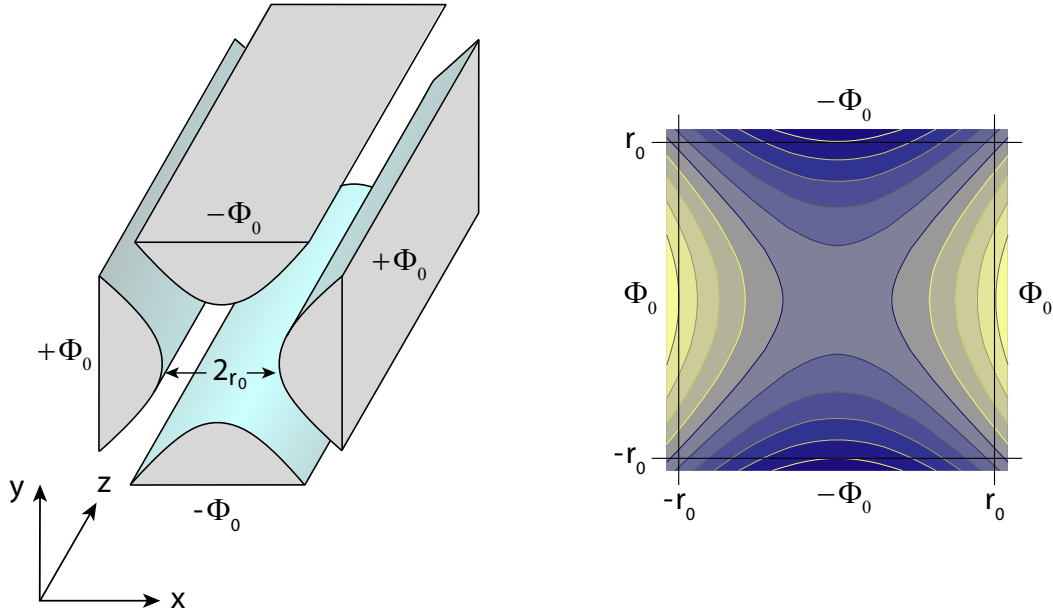
Figure 4.4: (a) Metal rods of the quadrupole with the applied potentials Φ_0 and $-\Phi_0$. Cluster propagate through the quadrupole in the z-direction. (b) Equipotential lines show the stability zone in the quadrupole. The sign of the potential changes with radio frequency which leads to an alternate confinement in X and Y-direction.

device. Four circular rods (Figure 4.4) are placed parallel to the axis of the cluster beam and opposed potentials are applied to the rods. Inverting the potentials periodically with radio frequency between the rods gives oscillating potentials:

$$U(t) = U_0 + V \cos(\omega t) \tag{4.1}$$

where the voltages U_0, V and the frequency ω are predefined parameters. They are adjusted so that the clusters with the required ratio $r = \frac{m}{q}$ of mass over charge stay on a stable trajectory. Clusters with a different ratio leave the quadrupole and collide with the chamber wall. The potential V basically defines the authorized mass and $\frac{U}{V}$ is responsible for the mass resolution $\frac{m}{\Delta m}$ [249].

4.1.5   Cluster current measurement devices

The cluster current is measured with a Faraday cup. A Faraday cup is a metal plate, grid or cup designed to catch the charged particles escaping from the quadrupole. The created current

can be measured and used to determine the quantity of particles in the cluster beam [250].

Two different setups have been used in the different vacuum chambers. In the big chamber, the Faraday cup measures the total cluster current with an insulated metal plate. The device is moved into the cluster beam to adjust the power of beam before the deposition on the sample. During deposition no current measurement is possible. In the small chamber, the cluster current is measured even during deposition. At the exit of the quadrupole, a metallic grid with a well known transmission coefficient (60%) is placed in the cluster beam. It allows to control in situ the cluster current and to adjust the power of the source.

4.1.6   Sample and tip storage

The UHV chamber is in possession of storage devices for tips and samples. The sample storage system is similar to a drawer, where the samples are parked and remain under UHV conditions. It has a capacity of three samples and the exchange of samples is rapid. STM tips are stored simply on a magnet fixed on a linear feedthrough. As it will be shown in Section 4.3, the tip holder is made of iron and is thus magnetic.

4.2   Gas measurement systems - Development of a new sniffer setup

4.2.1   Theoretical aspects of thermal desorption spectroscopy (TDS)

Different methods exist for studying the adsorption energy on molecules on surfaces. Temperature-programmed desorption techniques are important methods to determine the kinetic or thermodynamic parameters of a desorption process, also known under the term thermal desorption spectroscopy (TDS). Besides the determination of the adsorption energy, these methods contribute also to the identification of different adsorption sites for a molecule on the surface.

From a theoretical point of view, the desorption rate is expressed as

$$r(t) = -\frac{d\theta}{dt} = k_n \theta^n \tag{4.2}$$

where k_n is in an Arrhenius-type form: $k_n = \nu_n \exp{-\frac{E}{RT}}$. n is the order of the reaction, θ the surface coverage, ν the activation frequency and E the activation energy of desorption. This relation is known as the Polanyi-Wigner equation. In the case where the surface coverage is high enough for an interaction between the particles, the desorption parameters depend on the surface coverage, i.e. $E = E(\theta)$ and $\nu = \nu(\theta)$.

In a first approximation the reaction order depends on the surface coverage. If the layer desorbs in the same configuration as it was adsorbed, the reaction rate is of order one. If a recombination precedes the desorption, i.e. it needs two parts to form a compound that desorbs, the reaction rate is two.

Several methods have been proposed in the last decades in order to obtain information of the adsorbed molecules out of the desorption spectra. De Jong published an article where he applied all methods to a simulated spectrum [251]. They can be classified in two principal categories:

Complete methods: based on the Polanyi-Wigner equation and without any additional hypotheses. Their analysis require a huge number of desorption spectra but they allow to determine all parameters. These methods have the disadvantage to be long both in acquisition time and data treatment. Examples are published by King and others [252, 253].

Simplified methods: these methods are faster than the complete analysis and need only one single desorption spectrum. The necessary information are desorption peak temperature, the full width at half maximum (FWHM) and the peak shape. Nevertheless it is sometimes necessary to make some hypotheses. Among the methods are the one of Redhead [254], Chan-Aris-Weinberg [255, 256] or Konvalinka and Scholten [257].

In the following, two methods are presented: the complete analysis of King and the Redhead method. The second one has been used during this work.

Complete method (after King)

This is certainly the method requiring the most time to acquire data. The large number of desorption spectra makes it possible to identify activation energies, the pre-factors ν and
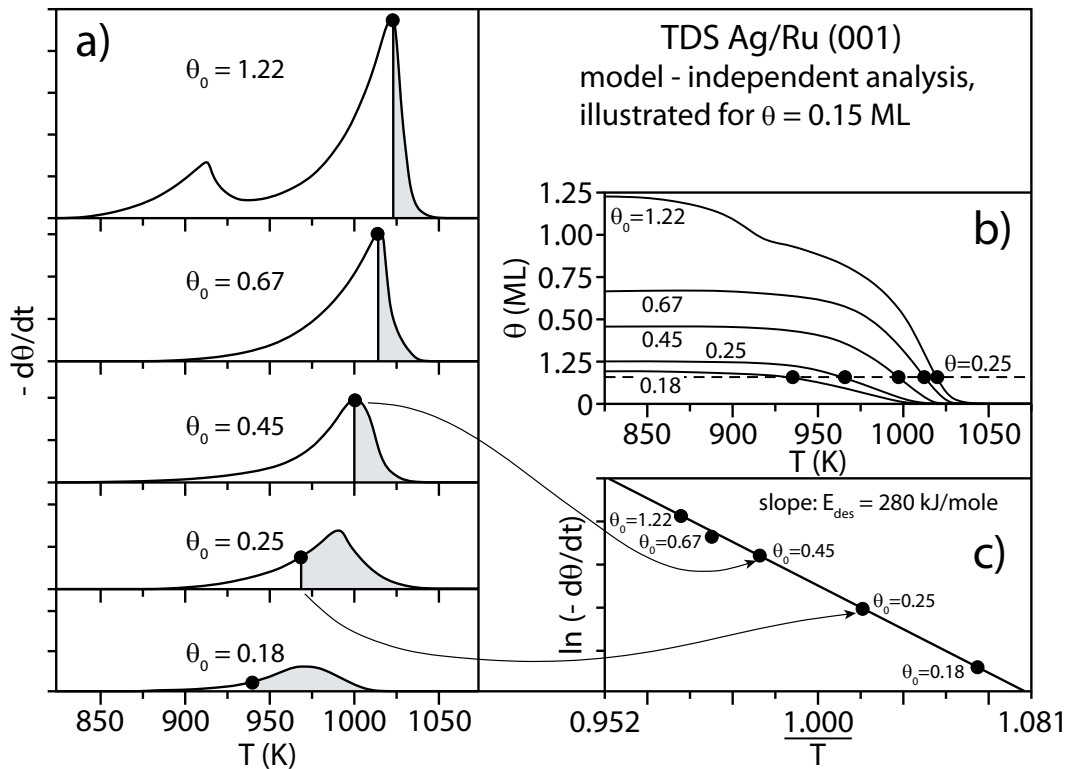
Figure 4.5: Principles of the method after King [252].

the desorption order. However, as the pre-factor as well as the desorption energy depend on the surface coverage, they have to be determined separately. The method will be explained with the support of Figure 4.5. (a) represents several desorption spectra for different surface coverages θ_0. At high temperatures, the curves drop due to complete desorption. Plot (b) represents the integral $\left(- \int_{\infty}^{T} f_\theta \left(T^* \right) dT^* \right)$ of the surfaces of (a). They represent the surface coverage as a function of temperature. The dotted line represents 15% of effective surface coverage. With decreasing coverage this temperature drops, too. Finally, (c) shows the slope of the curve at $\theta = 0.15$. If the curve is drawn on a logarithmic scale, we find:

$$ln(r) = ln(-\frac{d\theta}{dt}) = ln(\nu_n \theta^n) - \frac{E}{R} \cdot \frac{1}{T} \qquad (4.3)$$

The desorption energy corresponds now directly to the slope of the right side. The pre-factors and the order of reaction can be determined with the offset, i.e.

$$ln(\nu_n \theta^n) = n \ln \theta' + \ln \nu(\theta') \qquad (4.4)$$

If the surface coverage is low ($< 0.1ML$) the first term is negligible and the pre-factor ν is found.

Redhead method

This method, presented by Redhead [254] is based on the Polanyi-Wigner equation and includes several hypotheses:

- The energy E and pre-factor ν do not depend on the surface coverage.

- The reaction is of first order, i.e.

$$r(t) = -\frac{d\theta}{dt} = \nu_1 \theta exp(-\frac{E}{RT}) \tag{4.5}$$

- The variation of temperature is linear $\left(\beta = \frac{dT}{dt} = \text{const.}\right)$

The analysis is based on the temperature measurement of the desorption peak. The derivative of the desorption rate with respect to the temperature is thus zero. By replacing T with $T_0 + \beta t$, we get:

$$\frac{dr}{dt} = -\frac{d^2\theta}{dt^2} = 0 \tag{4.6}$$

$$\nu_1 \frac{d\theta}{dt} exp(-\frac{E}{\beta Rt}) + \frac{\nu_1 \theta E}{\beta Rt^2} exp(-\frac{E}{\beta Rt}) = 0 \tag{4.7}$$

We use Equation 4.2 and a change of variables ($t = \frac{T_{max}}{\beta}$) to bring the equation into the following form:

$$\frac{E\beta}{RT_{max}^2} = \nu_1 exp(-\frac{E}{RT_{max}}) \tag{4.8}$$

or

$$\frac{E}{RT_{max}} = \left(\frac{\nu_1 T_{max}}{\beta}\right) exp(-\frac{E}{RT_{max}}) \tag{4.9}$$

Finally the expression for desorption energy can be written as:

$$\frac{E}{RT_{max}} = ln\left(\frac{\nu_1 T_{max}}{\beta}\right) - ln\left(\frac{E}{RT_{max}}\right) \tag{4.10}$$

This equation does not give an analytical solution. One has to deduce an approximate value for the desorption energy out of the spectra and introduce it into Equation 4.10. The value $\frac{E}{RT_{max}}$ is itself inserted into the equation until the difference gets marginal. Four to six iterations are typically necessary.

For simplification, Redhead made the hypothesis $\nu_1 = 10^{13}s^{-1}$ and got the new equation:

$$\frac{E}{RT_{max}} = ln(\frac{\nu_1 T_{max}}{\beta}) - 3.64 \tag{4.11}$$

This approximation leads to an uncertainty of 1.5% on $\frac{E}{RT}$ for values of $\frac{\nu}{\beta}$ between 10^8 and $10^{13}K^{-1}$. Thus, the analysis of a single desorption spectrum gives a first estimate of the adsorption energy of a gas on a surface. Figure 4.6 represents different desorption energy traces as a function of maximal desorption temperature for different values of β.
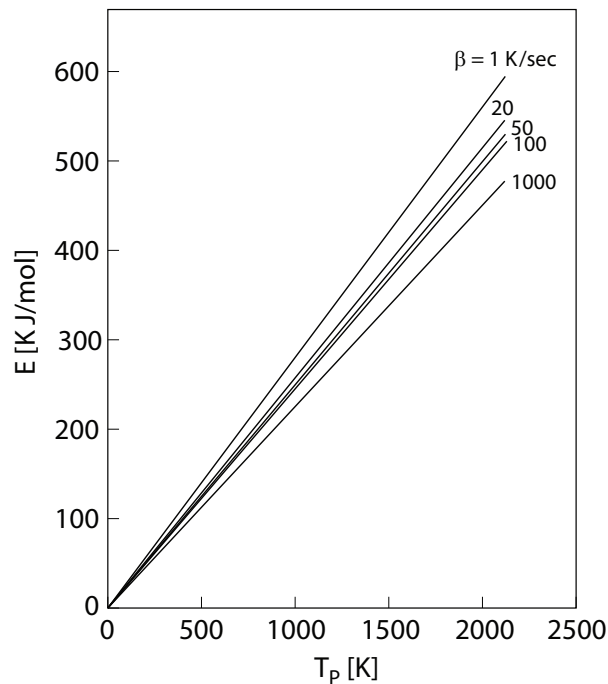
Figure 4.6: Activation energy for a desorption process as a function of maximum temperature. The lines represent different heating rates. Hypothesis: $\nu = 10^{13}s^{-1}$ [254].

4.2.2 Development of a highly sensitive detector for reaction products

During this work, a new home-built device enabling dynamic reactivity studies on surfaces with very small amounts of catalytically active material has been developed. We call this device in the following "sniffer". Besides standard measurements like TDS, the sniffer allows to expose the sample to gas pulses of well defined pressure and duration and to measure at the same time the reaction products from the sample, and this as function of sample temperature.
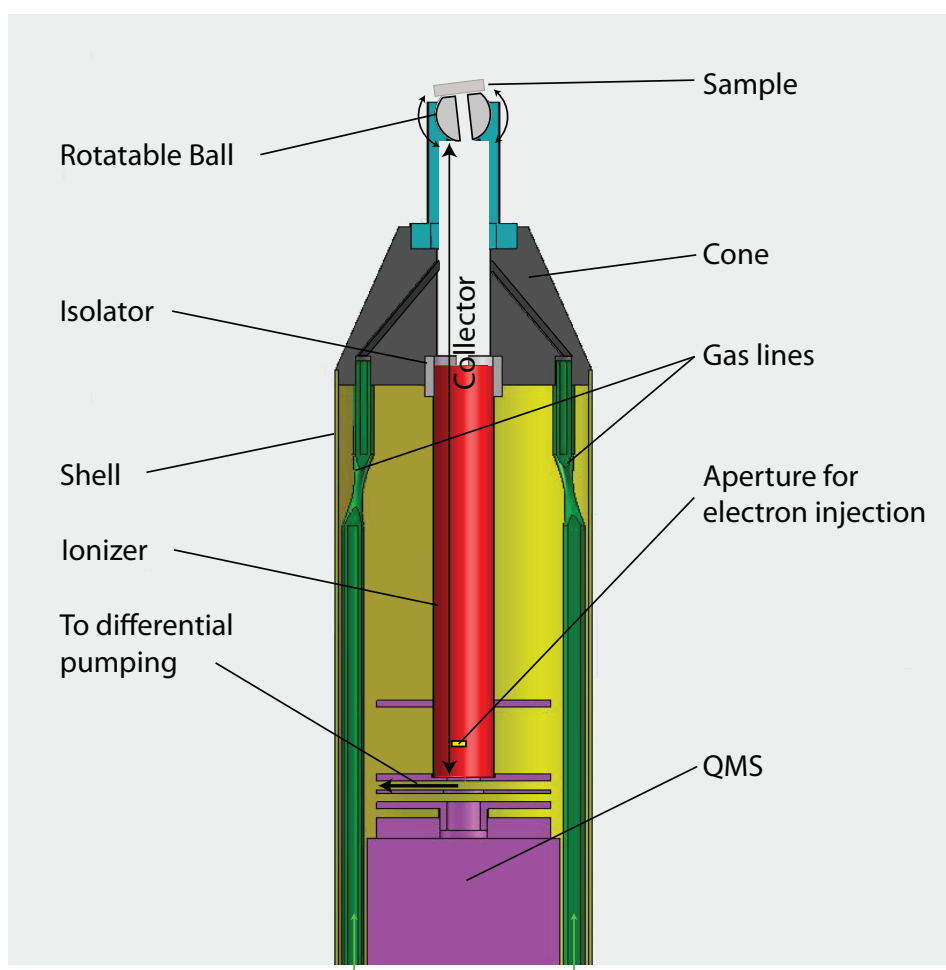
Figure 4.7: Schematic view of the sniffer.

The main idea in the design of the home-built sniffer (Fig. 4.7) is the possibility of creating an almost independent differentially pumped volume, which allows the use of rather high gas pressures. The gases desorbing from the sample get trapped in this volume labeled collector in Fig. 4.7 and are continuously analyzed by means of an integrated quadrupole mass spec-

trometer (QMS) shown in purple. In order to integrate the commercial QMS in the sniffer the ionization cage of the open ion source has been substituted by a stainless steel cylindrical tube. This tube is labeled ionizer and shown in red. It represents the main volume of the collector.

A hot yttrium filament (not shown in the Figure) is positioned outside the ionizer tube and near to an aperture in the tube. It produces electrons that are accelerated through the aperture into the ionizer by a potential of $100V$. The aperture also serves to pump the collector. The electrons ionize the gas, and a system of electrostatic lenses guides the ions through a small hole into the quadrupole, where the mass analysis is performed. Placing the filament outside the ionizer reduces the catalytic background signal produced by reactions taking place on the hot filament. The sniffer parts described above are enclosed in a stainless steel shell (yellow in Fig. 4.7) differentially pumped by a turbomolecular pump. The base pressure in the differential pumping line of the sniffer is below $2 \cdot 10^{-9} mbar$.

The injection of well defined amounts of gases in the collector is controlled by two UHV compatible electromagnetic pulsed valves, positioned outside of the UHV chamber. The cone in dark grey contains a portion of the collector volume. It also allows the gas lines to converge with a Λ shape to the principal axis of the collector. The gas tightness and electrical insulation between the cone and the ionizer is guaranteed by a Teflon ring, named isolator.

The selectivity with which one captures the reactants and the dosed gases coming off from the sample crucially depends on the vacuum separation of the collector from the preparation chamber. It also depends on the distance between the sample and the sniffer end. The parallelism of the sniffer entrance and the sample surface has been insured by a stainless steel ball mounted at the end of the collector, where it can freely rotate. The ball has a central bore of $3mm$. The ball apex facing the sample has a planar part perpendicular to the bore which can be oriented parallel to the sample surface by gently touching it. Thus, the sampled surface area is defined by this aperture, we examine a total area of $7.1mm^2$. Afterwards, the sample is retracted until the electrical contact between ball and sample is ruptured. The smallest distances obtainable this way are given by the mechanical stability of the long manipulator arm perpendicular to its axis. We achieve $0.1mm$, reducing the gas exchange between preparation chamber and collector by a factor of at least 70 with respect to the configuration with the sample far from the sniffer. The reduced gas conductance between sniffer and preparation chamber together with the differential pumping of the sniffer allow to keep a static pressure
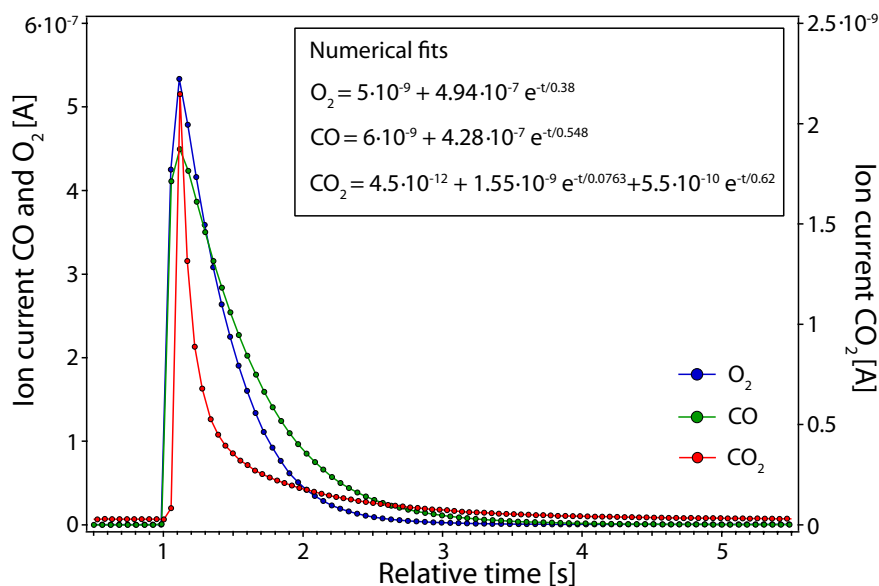
Figure 4.8: Experimental values for the temporal evolution of reactants (CO and O_2) and product (CO_2) coming off a $Pt/TiO_2(110)$ surface held at $480K$. $t = 0$ corresponds to the opening of the pulsed valves, the driving electrical pulse length has been $10ms$. The functions for a numerical fit of CO, O_2 and CO_2 peaks are indicated.

difference of three orders of magnitude between the preparation chamber and the sniffer collector while dosing gases. In addition, it enables higher exposing gas pressures compared to a more open solution.

The theoretical time constant of the collector when the entrance of the sniffer is firmly connected to the sample surface, can be estimated by considering the ratio $\tau = \frac{V}{S}$ between the volume V of the collector and the gas pumping speed S through both the aperture for electron injection and the hole for ion injection into the quadrupole can be estimated to $10ms$. In order to estimate the real temporal behavior of the sniffer we consider the catalytic oxidation of CO on Pt nanoparticles on TiO_2 [258] pre-covered with oxygen. As can be seen in Fig. 4.8, the time constants of the reactants are comparatively long and mainly given by the conductance of the gas lines from the pulsed valves to the sample. The onset times are $130ms$ for both gases, while the full width at half maximum is $550ms$ for CO and $450ms$ for O_2. The temporal decay after the maximum can be fitted for CO and O_2 by a single exponential each, yielding the time constants $\tau_{CO} = 550ms$ and $\tau_{O_2} = 380ms$. The time constant of the reaction product (CO_2) is markedly shorter. The tail can be fitted with a double exponential yielding $\tau_{CO_2,1} = 80ms$ for the main component (amplitude $1.55 \cdot 10^{-9}A$) and $\tau_{CO_2,2} = 620ms$ for the smaller component (amplitude $5.5 \cdot 10^{-10}A$). Subtracting the acquisition time of the spectrometer of

$65ms$, we find that the main component of CO_2 has a time constant of $15ms$ very close to the theoretical estimate. The fact that the time constant of this reaction comes close to the theoretical limit of the time resolution of our instrument can be explained by the main CO_2 component, corresponding to the reaction product created instantly into the collector as soon as the first CO molecules arrive at the surface. The second part is caused by the continued flux of reactants even after the valves have been closed due to the finite conductance of the gas supply and due to the finite pump speed.

Since the two electromagnetic valves can be controlled independently, the sniffer allows to perform catalytic reaction measurements in different ways. For instance, it is possible to study:

- The evolution of the reaction products as a function of the partial pressure of two dosed reactants and the sample temperature.

- The reaction between two reactants by keeping a constant pressure of one reactant (high frequency of gas pulses) and pulsing the other with a chosen (much smaller) frequency.

- The reaction dynamics by pulsing both reactants with a delay to each other (see results in Chapter 6).

The sniffer permits also to carry out TDS measurements by dosing gases onto the sample at low temperatures and measuring the initial species as function of increasing temperature. TDS performed with this new design shows two main advantages with respect to TDS measured with standard QMS-based instruments. First, the gases desorbing from the sample stagnate in the collector due to the small pump rate, and therefore the partial pressure in the collector increases to values easily detectable by the QMS, even for very small fluxes of molecules desorbing from the sample (our noise level corresponds to roughly $2 \cdot 10^{-10} \frac{molecules}{cm^2 \cdot s}$). Second, since the gases are dosed only locally on the sample, the pollution of the preparation chamber by these gases is negligible, and thus the measured TDS spectra are almost completely free of parasite peaks of gases desorbing, e.g., from the sample holder or the filament during heating.

For a quantitative analysis of the data measured by the sniffer in terms of number of gas molecules coming off the sample per unit time and surface, two calibrations have been performed. (i) We determined the relation between the partial pressure in the sniffer and the

measured ion current, which is used to calculate the amount of the dosed gas. (ii) We established the relation between the flux of molecules entering in the sniffer and the measured ion current, which is used for a quantitative analysis of the gas desorbing from the sample.

For calibration (i) no sample was positioned in front of the sniffer, the differential pumping of the sniffer was closed by a valve, and argon was introduced in the preparation chamber, and its partial pressure was increased step by step. This way the sniffer was only pumped via the preparation chamber and thus the argon pressure in the sniffer was the same as the one in the preparation chamber which has continuously been monitored by a gauge. The ion current corresponding to each argon pressure step was then measured. For calibration (ii) the sniffer was in the usual measurements configuration, i.e. it was differentially pumped and the sample was positioned in front of it, so that gas exchange between the sniffer and the preparation chamber was minimized.

4.3 Scanning tunnelling microscope (STM)

Scanning tunnelling microscopes are widely used nowadays in research as well as in industry. They give access to the morphological analysis of surfaces such as roughness or reconstructions and three-dimensional representations of prepared surfaces. Moreover, more detailed information are available such as the handling of single atoms [48] or electronic states and their confinement on specially prepared surfaces [259].

4.3.1 History

The principle of the tunnel effect is based on the quantum mechanical theory presented in the '20s by Schrödinger, Heisenberg, Bohr and de Broglie [260]. Their theory predicts that electrons can pass from one medium to another through the vacuum with a certain probability, depending amongst others on the distance between the medias. The theoretical prediction has been experimentally observed for the first time by Young *et. al.* in 1971 [261]. The real breakthrough was made by Binnig and Rohrer in 1981 at the IBM research centre in Rüschlikon, Switzerland. They realized the first STM images at atomic resolution [262–264]. They showed the famous silicon surface $Si(111)$ with its (7×7) surface reconstruction, see Figure 4.9 [265, 266]. For their design of the scanning tunnelling microscope and thus the experi-
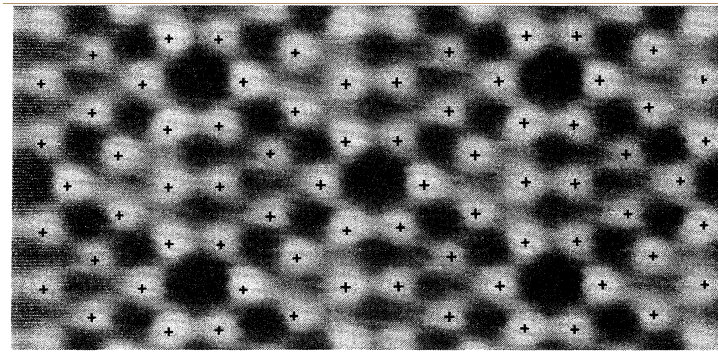
Figure 4.9: The STM image of the 7×7 reconstruction of $Si(111)$ was one of the first images with atomic resolution [266].

mental confirmation of the theoretical predictions they obtained the Nobel Prize in 1986.

The experimental techniques have been strongly improved in the last 20 years and reach nowadays resolution of 0.1 Å for lateral dimensions and 0.01 Å perpendicular to the surface.

4.3.2 Theory and principle

For a better understanding of the principle of a tunnelling microscope, we look at the quantum mechanical approach: electrons do not possess a defined position but a probability distribution for their positions. This probability is non-zero out of the solid but decreases exponentially with the distance. For distances of some nanometres between two materials the electron can therefore pass through the gap from one to the other by creating opposite tunnelling currents which are in equilibrium. An illustration is shown in Fig. 4.13. If a bias is applied between the tip and the sample we break the equilibrium and let the electrons pass with preference from the tip to the sample or the other way around, following the potential.

For a determination of the current, we need to know the electronic structure of the tip and the sample and the extension of the wave functions. Some simplifications have been made by Bardeen in 1961 [267]. He studied the tunnelling effect for metal-vacuum-metal junctions and introduced a disturbance factor to the electron hamiltonian of the tip and the surface. In other words, he neglected the electronic interaction between tip and surface which is a reasonable approximation for the weak superposition of electronic orbitals and the low potential difference for tip and surface. The tunnelling current can be expressed as a function of the tip wave function (ψ_μ) and of the surface (ψ_υ):
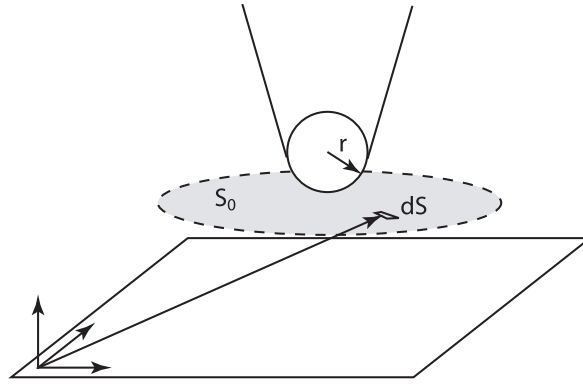
Figure 4.10: Tip geometry according to Tersoff and Hamann

$$I\left(V\right) = \frac{2\pi e}{\hbar} \sum_{\mu,\upsilon} f\left(E_\mu\right)\left(1 - f\left(E_\nu + eV\right)\right)\left|M_{\mu\upsilon}\right|^2 \delta\left(E_\mu - E_\upsilon\right) \qquad (4.12)$$

We build the sum over all nondisturbed states ψ_μ and ψ_υ. The eigenvalues E_μ and E_υ of tip and surface respectively are relative to the Fermi levels. By using the Fermi-Dirac distribution f we make sure that the transition happens between an occupied state $f\left(E_\mu\right)$ and an unoccupied one $1 - f\left(E_\upsilon + eV\right)$. The tunnelling process is an elastic phenomenon, the energy has to be conserved, therefore we introduce the Delta-Function $\delta\left(E_\mu - E_\upsilon\right)$. The transition matrix between the occupied states of the tip and the empty states of the surface or vice versa can be expressed, with respect to a characteristic surface S_0 which is defined as the concerned area between tip and surface:

$$M_{\mu\upsilon} = \frac{\hbar^2}{2m_e} \int_{S_0} \left(\psi_\mu^* \nabla \psi_\upsilon - \psi_\upsilon \nabla \psi_\mu^*\right) dS \qquad (4.13)$$

The presented approximation considers electrodes (tip and surface) with an undefined shape. We can improve the model, using the approach of Tersoff and Hamann [268, 269] who suggested a spherical shape of the tip with a small radius (see Figure 4.10). The current from equation (4.12) can thus be expressed:

$$I\left(V, x, y, z\right) \propto e^{-2z\sqrt{\frac{2m_e\left(\Phi - \frac{eV}{2}\right)}{\hbar^2}}} \int_0^{eV} \rho_{\text{sample}}\left(E, x, y\right) \rho_{\text{tip}}\left(E - eV\right) dE \qquad (4.14)$$

where x, y are the lateral positions of the tip regarding the sample, ρ_{sample} and ρ_{tip} the local density of states (LDOS) of tip and sample respectively and Φ the mean work function
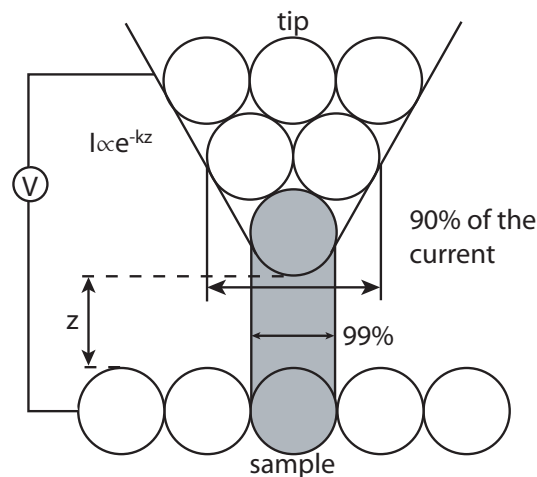
Figure 4.11: Due to the exponential decay of the current with the distance z, most of the current passes through the nearest atom(s). Values for typical tunnelling conditions: ($I_t = 0.1 - 1nA$, $V_{gap} = 1 - 2V$).

of tip and sample. Looking at Equation 4.14, one sees immediately that the current depends exponentially on the distance z between tip and surface. We can say that the majority of the current passes through the nearest atom of the tip and only minor contributions are due to further atoms. A schematic sketch representing the current distribution is shown in Figure 4.11.

The high resolution at sub-atomic scale cannot be explained by the simple model of Bardeen. In fact, there is a non-negligible interaction between the tip and the surface that has to be taken into account. It would exceed the scope of this thesis to go into details of these models, the reader is therefore referred to publications of Sacks and Noguera [270–272] and Chen *et. al.* [273, 274].

4.3.3 Working modes

A STM microscope is measuring the current between tip and surface as a function of the distance z. There are three different proceedings:

The **constant height mode** can be applied on very smooth surfaces. The vertical tip position is fixed and the resulting current measured. If the surface is too rough, there is a certain risk that the tip will crash into the sample. This will not only damage the tip, but also change the local morphology of the surface. Irreversible damage is the result.

Constant current mode avoids that risk of touching the surface. During the scan, the current is continuously controlled and the vertical position of the tip adjusted. (Section 4.3.4).
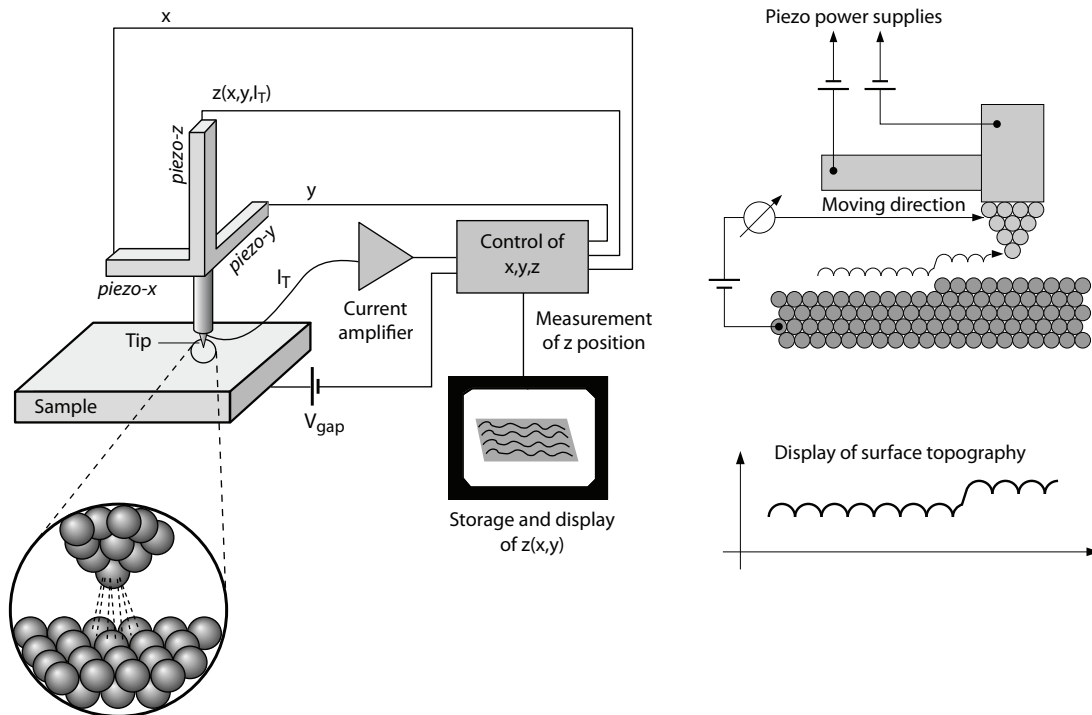
Figure 4.12: Basic principles of a scanning tunnelling microscope. A current I_T is established between the tip and the sample. An electronic device measures the current during the scan and sends a feedback signal to the z-piezo for height adjustment. The displacement in x, y, z is stored and displayed on a screen, as shown on the right side [144].

The third mode is called **Scanning Tunnelling Spectroscopy (STS)**. By changing the potential between tip and sample the electronic structure of the surface is scanned as the current depends on the local density of states (LDOS). In this mode, the tip is placed on the required position of the surface and a potential ramp applied. The information of the variation of the current as a function of the potential $\frac{dI_T}{dV}$ gives information about the LDOS of the sample under the tip. Each material and even each different atom has a specific "digital fingerprint" and it is possible to identify the exact configuration of the surface [275].

4.3.4 Image acquisition in the constant current mode

Figure 4.12 shows schematically the setup of an STM microscope. The tip approaches the surface from the top. Three piezoelectronic [1] motors move the tip vertically (Z) for approach

---

[1]Piezoelectric materials are mostly ceramics which have the property that, under an application of a potential to the ceramic, they extend or contract. The power of such devices are extremely high and the precision of movement is in the order of pm.

and distance regulation and horizontally (X,Y) for the surface scanning. The electronic system measures the actual current between tip and sample I_T and adjusts it to the reference current I_0 by varying the distance Z. The movement of the piezos are stored and displayed as a plot $Z(X, Y)$. The displayed topography of the surface is not only the image of the real surface, but also influenced by the electronic structure (LDOS) of the sample underneath the tip.

Image interpretation

The potential between tip and surface can be applied with different polarities, a representation is shown in Figure 4.13. The density of states decreases towards the Fermi energy level and the probability of transmission, called $T(E)$, increases. The electron tunnelling from the tip to the surface or vice versa originates principally from the area next to the Fermi edge. Note that generally the LDOS of the tip ρ_{tip} is considered as constant.

- $V_{\text{sample}} < V_{\text{tip}}$: the electron current flows from the sample to the tip. Considering the assumption made above that the LDOS of the tip is constant, the current is faintly sensitive to the applied potential.

- $V_{\text{sample}} > V_{\text{tip}}$: the electrons pass from the Fermi level of the tip to the unoccupied states of the sample. By varying the potential, we can study the different unoccupied states of the sample. This method is sensitive to chemical elements on the surface.

Surface convolution

The tip of the STM is the core piece of the microscope. Its quality will broadly influence the quality of the image, the easiness of handling and the time spent to acquire an image. As it has been shown in Figure 4.10, most of the current passes through the nearest atoms of the tip. It is experimentally impossible to build a tip with a single atom at the end. In most of the cases, several atoms have the same or a similar distance to the sample. Therefore, they contribute equally to the current conduction. If we pass through a pit, as shown in the example in Figure 4.14, it seems to be smaller than in reality. The rim of the graphite surface, in reality vertical (the sketch shows a rim that is not vertical but very steep), has tendency to be less abrupt, as it is shown under "displayed surface profile". We can observe an additional problem: the designed tip in the drawing shows two points, a so-called double-tip. When the
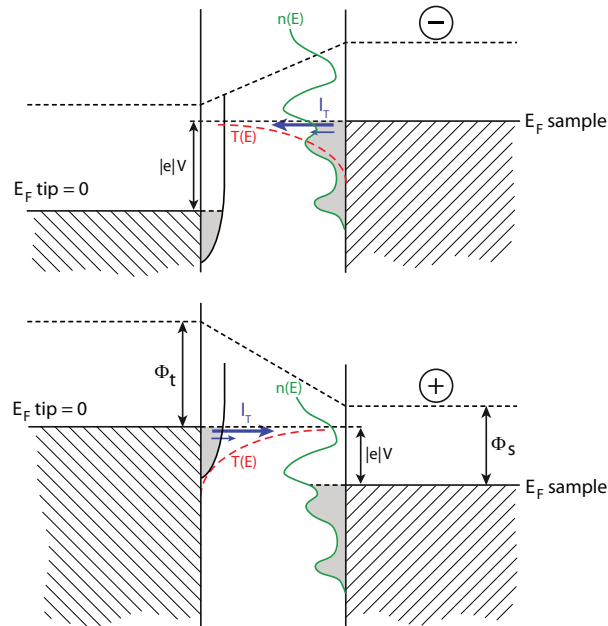
Figure 4.13: Contribution of the tunnelling current as a function of polarity and amplitude of bias voltage. The current I_T depends on the local density of states (LDOS) between the Fermi energy E_F of the tip and the sample ($E_F + eV$). The transition probability $T(E)$ is more important for high energetic electrons.
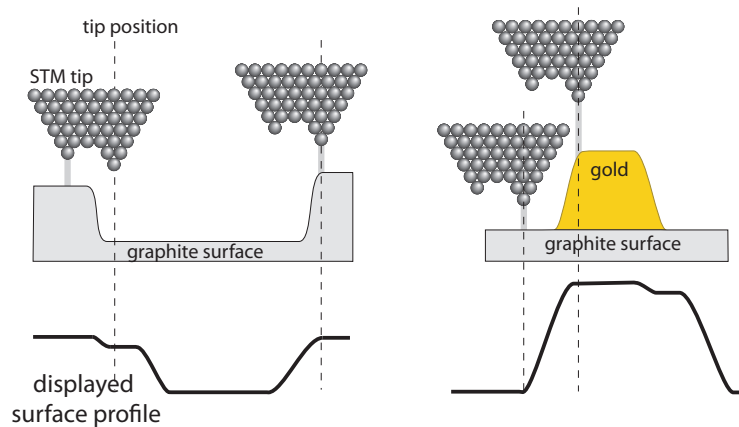
Figure 4.14: Effect of the tip size leading to surface convolution. Dotted lines indicate the recorded tip position, grey lines the point where the current passes from the tip to the sample. The profiles below show the effect for a pit (left) and a cluster protrusion (right). One sees that the pit profile shows an intermediate step at the left-handed slope as the current passes at different tip positions. The recorded pit size appears smaller than the real one. The contrary is valid for protrusions. They appear bigger than in reality. In addition, but not related to the double-tip, passing from a graphite substrate to a gold cluster, the work function changes and the distance between tip and surface is different for the same imposed current. Clusters thus appear higher (or lower) than in reality.

right tip already passes in the pit, the left one is closest to the sample and the current will pass through this one (grey band).

The effect when passing over a particle of different material (i.e. gold) is shown on the right side. This effect is not related to the double-tip. The distance between tip and graphite is not the same as between tip and gold, as the work function of gold is smaller than the one of graphite. To maintain the same current, the tip has to retract more than only the topographical height. The displayed height hence overestimates the particle size. The effect of the tip is important for small structures but loses influence for bigger ones.

### 4.3.5   Setup of the device in use

The STM device in use has been constructed in our group [80, 90]. The aim for the construction was to build a microscope able to work at variable temperatures ($4K - 300K$) and compatible with UHV conditions. During this thesis, improvements on the sensitivity as well as the reduction of vibrational noise have been achieved.

In Figure 4.1 we show an overview of the UHV chamber and Figure 4.15 gives a closer overview of the STM device. Part (a) of Fig. 4.15 shows a technical drawing and (b) a picture of the real device. The whole STM block is coated with gold in order to inhibit gas adsorption on the surfaces. The STM in the part (C) of the chamber (Fig. 4.1) is connected to a two-level cryostat. The external one consists of a cylinder in the upper part of the device and two hollow rods. Its function is to act as a thermal screen and to cool down the inner cryostat in a first step to $77K$. It is connected to the inner cryostat which is filled with liquid helium at $4K$.

The STM block is, during measurement, suspended on the roof of the chamber by three long springs. They are fixed on three vertical bars on the STM block. The purpose is to reduce the thermal contact with the hot walls and to avoid vibrations and mechanical noise. For the same reason the whole table on which the STM is positioned can be lifted up by four pneumatic feet. To maintain the cooling during measurement, some very thin gold wires ($100\mu m$ of diameter) connect the STM block to the cryostat. They are visible in Fig. 4.15 (b) between the Eddy current dampers[1].

---

[1]An eddy current damping uses electromagnetic induction, in the present setup caused by magnets, which creates resistance, and in turn stops the movements of the STM block.
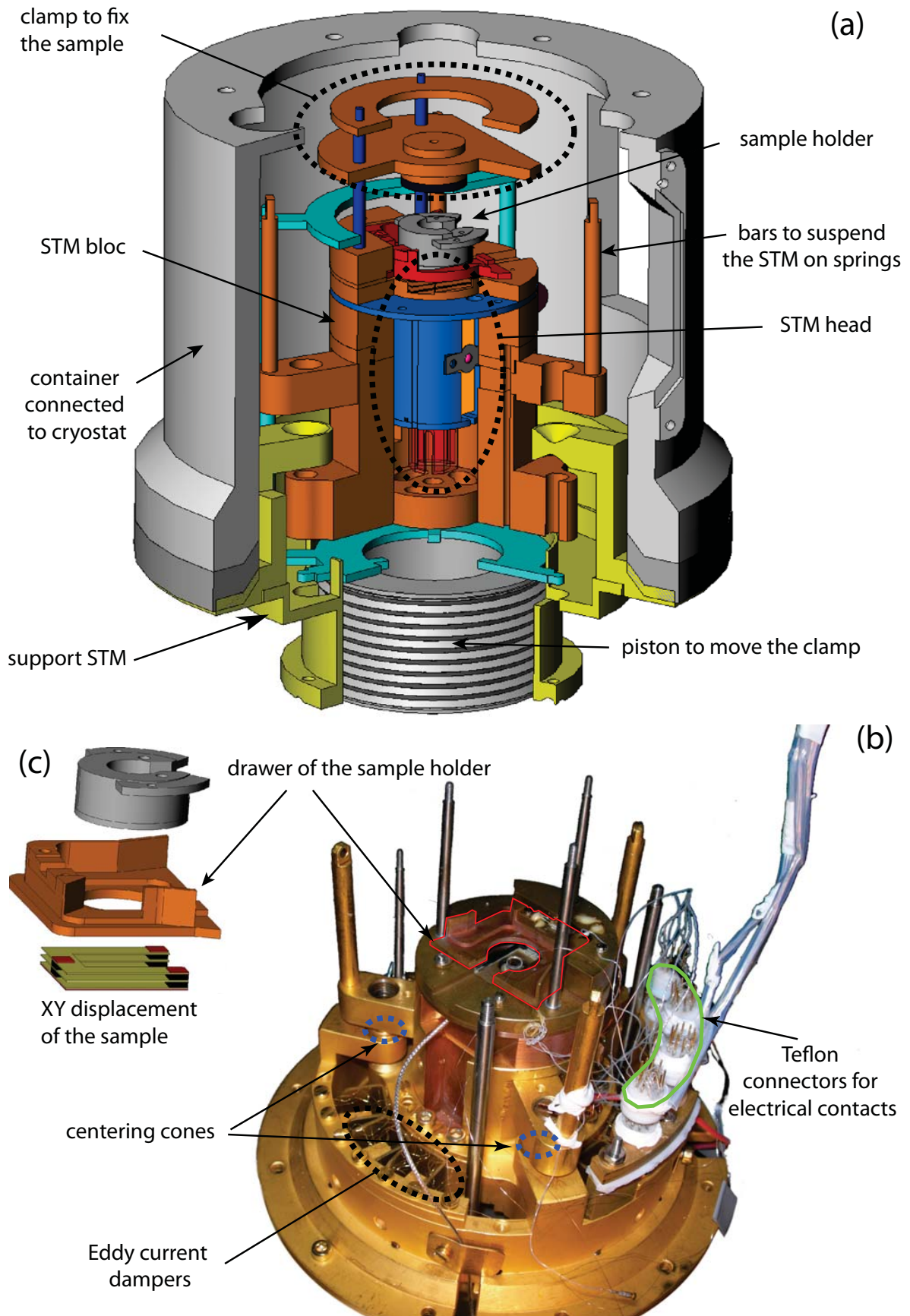
Figure 4.15: (a) partial cut through the STM block. (b) photography of the system outside of the vacuum chamber (c) detailed view of the sample-holder and the piezo stack for displacement.
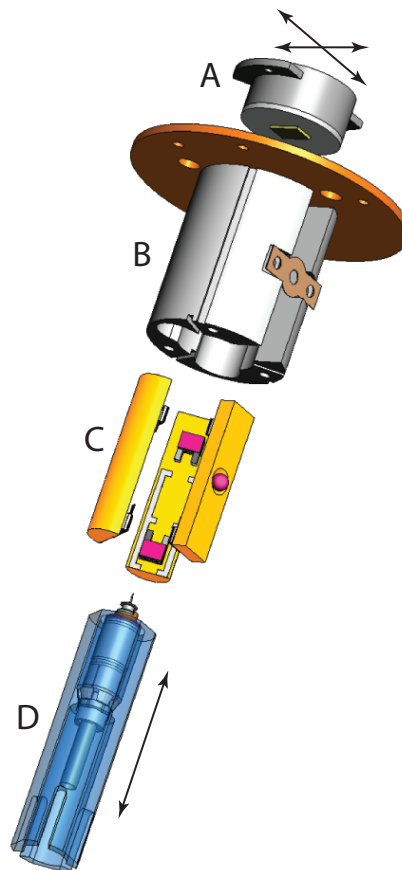
Figure 4.16: Setup of the STM head. (A) sample holder with the sample looking downward. (B) stator piece. (C) ceramic bars with piezos packed together for z coarse approach. (D) movable prism of sapphire containing the central piezoelectric motor for the scan (x-y) and the height adjustment (z) during scan. The tip is placed on top of the prism.

On top of the sample (Fig. 4.15(a)) a mechanical system clamps the sample holder to the drawer. A piston on the bottom of the device lifts the clamp up. In this position, sample transfer into the main chamber and sample displacement inside the STM is possible. As the STM tip scans only a certain area of the sample in the order of micrometers, the whole sample holder including the drawer has to be moved by means of piezoelectric motors for bigger displacements (Fig. 4.15(c)).

Eddy current dampers are placed around the STM block. These strong magnets attenuate vibrations of the STM block without mechanical contact. The only mechanical contact between the STM and the exterior are electrical Teflon coated metal wires for power supply of the STM and current measurement and the springs where the whole STM is suspended.

Figure 4.16 presents the core piece of the STM. The sample (A) is placed on the top of the STM block, looking downwards. The tip is fixed on a movable prism made out of sapphire

(D). In its interior, we find a piezoelectric actuator for the movement in Z-direction and the scan in X-Y-directions (description below). This prism is fixed in the middle of three ceramic bars (C). On the interior surface, there are two stacks of piezoelectric motors, shown in pink. They are responsible for the coarse approach of the tip. These bars are inserted into the stator piece (B) and are fixed.

When placing a sample in the STM, we have to make sure that the tip will not touch the sample. However, the retraction of some millimetres cannot be done by the simple retraction of a piezo. The piezo-stacks on (C) have the property that they execute a shear movement when a potential is applied (see Figure 4.17(a)). As the single movement of one shear-piezo is not sufficient, we put for each actuator three piezos one on top of each other. They extend simultaneously and amplify the movement. When the central prism (D) has to be retracted or approached, the actuators perform a so-called *stick and slip movement*. The potential applied has saw teeth-like shape. The slow increase of the potential makes the piezos bend and moves the prism upwards. The very fast drop of the tension makes that the surfaces of the piezo-actuators (covered with a smooth sapphire plate) slip back and the prism remains at its current position. The same process is repeated for many cycles. An electronic control system analyzes the distance between the tip and the surface after each third stick-slip movement. In this way, a well controlled approach to the surface is possible without taking the risk of a crash.

After the coarse approach another piezoelectric device will regulate the tip-surface distance. It is located inside the prism (part D in Fig. 4.16): a hollow piezo tube is separated into different parts, shown in Fig. 4.17(b). The upper part is responsible for the movement in the Z-direction. It adjusts the position of the tip according to the topography of the surface by expansion in the direction of the tube axis. The lower part is divided into four symmetric parts. The same potential with opposite polarity is applied to opposite electrodes. We thus have an elongation on one and a retraction on the other side, resulting in a bent tube. The combination and variation of the two potentials (X and Y-direction) results in the scan of the surface.

4.3.6   Tip preparation

The tip is basically a metallic wire (W or $PtIr$). There exist various well defined techniques for preparing suitable STM tips, described for example in the master thesis of Lucier [277].
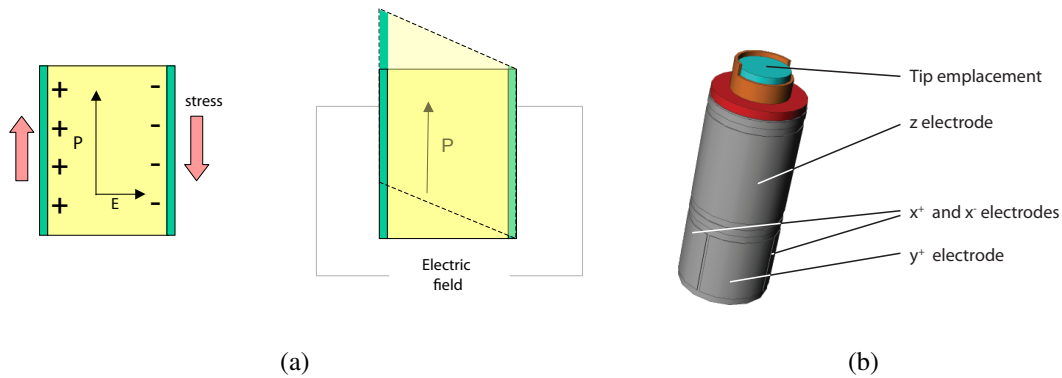
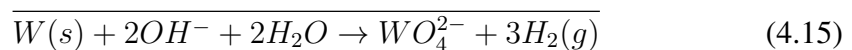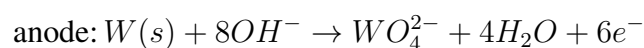**Figure 4.17:** (a) Shear effect of piezo. When a voltage is applied between the electrodes (green) the material shears vertically [276]. (b) Setup of the central piezo. The Z-electrode is in the upper part, responsible for the distance maintenance between tip and sample. On the lower part, the piezo is divided into four parts, responsible for the lateral scan by bending.
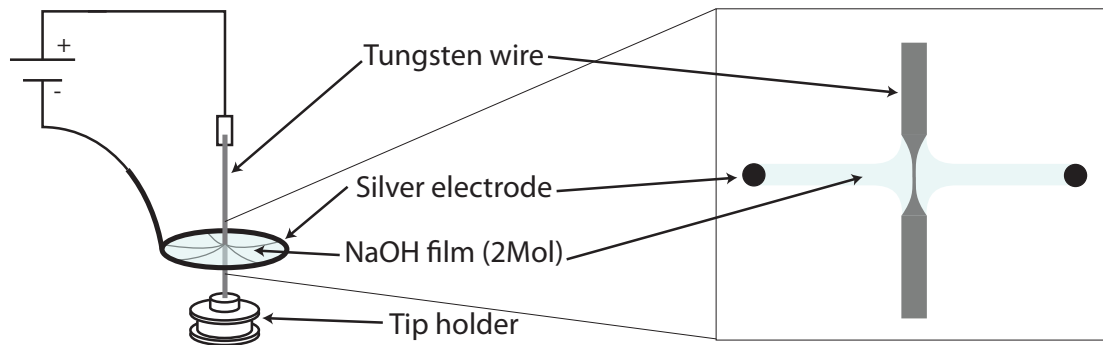
Figure 4.18: Setup of the tip preparation device. The tungsten wire is fixed in the tip holder, made out of soft iron. A metal ring surrounds the wire, therein a $NaOH$ film creates a membrane. The ring as well as the tip is connected to a power. The circulating current etches the filament at the meniscus of the film. When the wire gets too thin, it breaks under its own weight and the tip falls down.

The principle of tip preparation is an electrochemical etching process. The basic idea is to dip a small tungsten wire (we used exclusively tungsten for tip preparation) with a diameter of $0.25mm$ into an electrolyte solution. A DC potential is applied between the tip and a counter electrode and the electrons thus attack the wire, due to the presence of the basic solution [278]:

$$\text{cathode:}\, 6H_2O + 6e^- \rightarrow 3H_2(g) + 6OH^-$$

$$\text{anode:}\, W(s) + 8OH^- \rightarrow WO_4^{2-} + 4H_2O + 6e^-$$

$$\overline{W(s) + 2OH^- + 2H_2O \rightarrow WO_4^{2-} + 3H_2(g)} \tag{4.15}$$
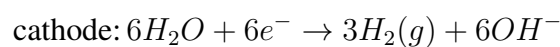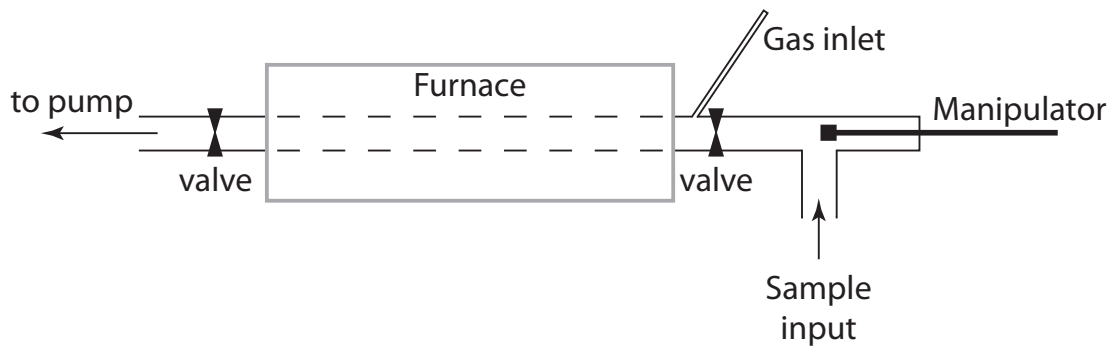
Figure 4.19: Schematic view of the vacuum furnace. The sample is inserted into the system through a load-lock chamber. A manipulator connects the load-lock chamber and the furnace. Temperature as well as gas pressure in the furnace can be controlled precisely. A pumping system maintains the vacuum at a pressure of $1 \cdot 10^{-5} mbar$.

Figure 4.18 shows the setup of the tip preparation. The tungsten wire is surrounded by a silver ring. The solution forms a film, limited by the silver ring. Due to surface tension, it ascends around the wire and forms a meniscus. The etching sharpens the tip and at a certain moment the proper weight of the tip holder becomes too heavy and the tip falls on a soft pillow made of shaving foam. The big advantage of this system is that at the moment when the tip falls down the current vanishes and the etchings stops.

4.4   Vacuum furnace

A vacuum furnace is used to prepare the HOPG samples (see Section 5.1). The main parts are shown in Figure 4.19. A load-lock chamber gives access to the manipulator where the sample is deposited. The manipulator moves the sample back- and forward from the load-lock chamber into the furnace. At a pressure of $10^{-5} mbar$, the sample is introduced into the pre-heated furnace. The temperature can be set by the operator and an internal regulation maintains the chosen value. A gas line is connected to the vacuum chamber in the furnace. During the heating process, the turbomolecular pump is disconnected and the actual pressure monitored by standard pressure gauges.
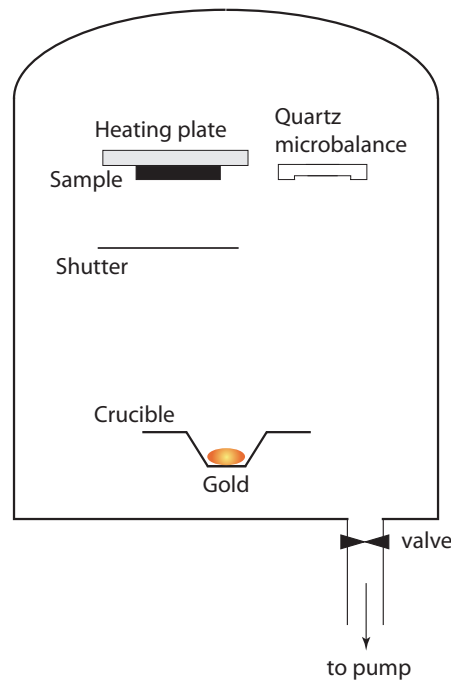
Figure 4.20: Device for physical vapour deposition PVD. A crucible, filled with the material to be evaporated (gold) is heated resistively. A shutter prevents the sample of uncontrolled deposition. The vaporized gold quantity is measured in situ with a quartz microbalance.

4.5 Gold deposition chamber

4.5.1 Physical vapour deposition (PVD)

The term physical vapour deposition (PVD) includes different vacuum-based coating processes and thin-film technologies. It was used for the first time by Michael Faraday in 1838 but appeared in 1966 for the first time in literature. The required material is deposited directly by condensation on the support, in contrast to the CVD (chemical vapour deposition) processes where a chemical reaction leads to the surface coating. The following points characterise the process:

1. Vaporization of the material.

2. Transport of the vaporized particles to the substrate.

3. Vapour condensation on the substrate and layer formation.

Different variants of PVD are known: by laser bombardment, deflected ion impact or by resistive heating the target is vaporized. All these methods have in common that the vaporized
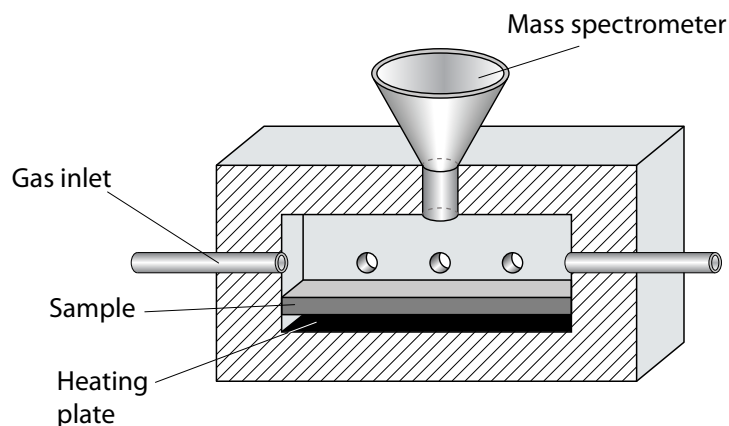
Figure 4.21: Cross section through the chemical reactor [279].

material is present in a solid form. The ejected atoms move through the chamber either by electric fields or by a simple ballistic process. In order to avoid particle loss due to collisions, one has to work at vacuum conditions. Typical working pressures are in the range of 10^{-6} to $0.1mbar$. The gold particles move in straight trajectories from their origin towards the sample. For a target heated by resistance, the spatial abundance of ejected particles follows a $\cos^2\theta$ distribution, where θ is the angle of the trajectory with respect to the surface.

4.5.2   Device in use

Gold atoms are deposited on the HOPG samples in a separate vacuum chamber (Fig. 4.20). The gold target is placed in a crucible on the bottom of the chamber. Electrical connectors ensure the resistive heating of the crucible and the vaporization of gold atoms. The sample is placed on a sample holder in the upper part of the chamber. At the same level and in a symmetric position with the sample, a quartz microbalance measures in situ the evaporated gold quantity by analyzing the frequency change of a quartz crystal resonator (in $\frac{\text{Å}}{s}$). The resonance is disturbed by the addition of evaporated material on the surface of the acoustic resonator. A shutter is placed in front of the sample that is mounted on a heating plate. During deposition, the sample temperature is kept constant and carefully monitored with a connected thermocouple, the shutter is opened and the quartz microbalance set to zero. The pressure during deposition is of the order of $10^{-5}mbar$.

4.6 Chemical reactor for catalysis

A chemical reactor as shown in Fig. 4.21 has been used for the catalytic measurements on HOPG. The sample is fixed in a container, called chemical reactor. The reactor is introduced in a high vacuum chamber with a pressure of $10^{-7}mbar$. The walls on the back and the front side of the reactor present holes through which a free gas exchange is possible and which helps to increase the pumping speed. Gas lines are laterally connected to bring the reactants (gases) onto the surface. A central hole (top) gives access to the mass spectrometer for residual gas analysis (RGA). The temperature control is assured by a thermocouple mounted on the sample (not shown). A heating plate, in tight contact with the sample, supplies the necessary power for heating. The detailed setup of the reactor has been published by our coworkers [279].

Chapter 5

Results: Gold on HOPG

Contents

This Chapter is dedicated to results of gold particles deposited on pre-structured HOPG surfaces. The purpose of this investigation was to study catalytic activity of gold clusters. Therefore, we have to stabilize them on the graphite surface. In the first Section (5.1) we give information about the sample preparation that precedes the gold deposition. In the follow-

ing, (Section 5.2), electrochemical measurements have been performed to see under which conditions the clusters remain stable on the surface.

For increasing surface coverage of gold, the cluster auto-organize themselves on the surface and form uniformly sized corrals along the rim of the pits. We show these results in Section 5.3. These corrals have been studied for their thermal evolution and stability in Section 5.4. When the sample are annealed at temperatures above $700 K$, gold clusters start to show particle-enhanced local etching of graphite that leads to the formation of channels in the HOPG layers (5.5). Finally, a detailed analysis of the desorbing products during annealing in an oxygen atmosphere has shown that gold particles dissociate oxygen molecules already at low temperatures (5.6).

5.1 Sample preparation

Grade-1, highly oriented pyrolytic graphite (HOPG) was purchased from *SPI supplies*®. They exhibit great crystalline perfection ($0.4° \pm 0.1°$). The crystal is cleaned before each new sample preparation with an adhesive tape resulting in atomically clean terraces containing typically $1\% - 3\%$ step edges. The samples are immediately transferred into the UHV chamber for surface preparation.
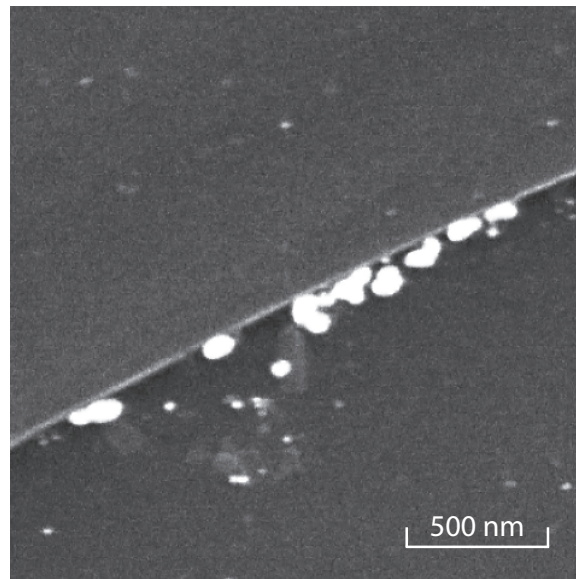
Figure 5.1: SEM image of HOPG after Au deposition by magnetron sputtering at room temperature in high vacuum conditions (p=$10^{-4}Pa$) followed by a subsequent heat treatment at $700K$. Acc.V= $10\,kV$, Magn: $2 \cdot 10^4$. Image size: $2\mu m \times 2\mu m$.

Nanoparticles on clean HOPG surfaces are not stable. As it is shown in Fig. 5.1 most of the particles nucleate at step edges that provide the strongest nucleation sites. This picture has been taken by SEM (scanning electron microscopy). Gold clusters have been deposited by magnetron sputtering at room temperature in high vacuum conditions. Sputtered clusters create themselves defects, but clusters pinned to these self-produced defects on terraces are less stable than clusters at step edges. Subsequent heating of the sample under vacuum to $700K$ confirms this statement: clusters are exclusively found on step edges, as shown in Figure 5.1.

The presence of unstable clusters is not useful for the intended measurements. The purpose is to find a system where gold particles are stabilized even at elevated temperatures. As

(a) (b)
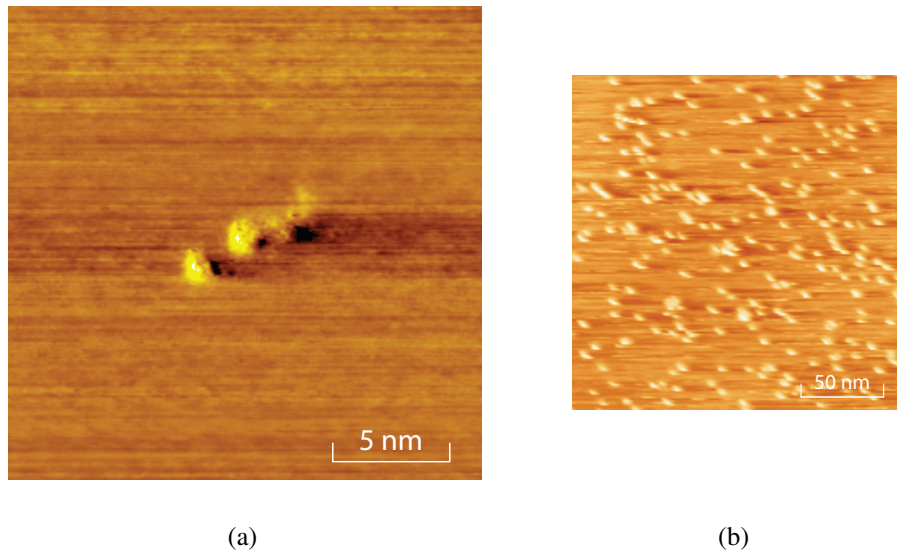
Figure 5.2: STM images of two different magnifications of Au_5 clusters implanted in HOPG. Incident kinetic energy: $E_{kin} = 3keV$; impact density: 1000 μm^{-2}. STM measurements performed at room temperature in air, $V_{gap} = 0.5\,V$, $I_T = 0.5\,nA$. Image size in a: $20nm \times 20nm$, b: $120nm \times 120nm$.

discussed in Section 3.1.3, nanopits in the HOPG surface show such stabilizing properties.

The samples are exposed to a high energetic cluster beam from a cluster source, identical with the device described in Section 4.1.3. The clusters are mass-selected and deposited on the surface with a well-defined energy. Au_5^+ have been implanted at $3kV$ under high vacuum conditions at room temperature. The choice of the cluster size is a compromise between cluster flux (small particles) on one side and the creation of deeper defects (larger particles) on the other. The impacts on the surface are visible in Figure 5.2 even without etching. This STM images show the surface directly after cluster bombardment. Cluster-induced defects are visible as hillocks (Fig. 5.2(a)) which are randomly distributed over the whole surface (Fig. 5.2(b)). These hillocks have been observed for the first time by Yan and co-workers [280] and were reproduced by many groups. Furthermore, Palmer *et. al.* measured the size of hillocks after silver cluster implantation and found values of $0.03 - 0.04nm$ in height and $0.2 - 0.3nm$ in diameter [281]. Protrusions of similar size are also observed for other ion impacts on graphite [282, 283]. Each of these surface defects present a starting point for graphite etching process, described in detail in Section 3.1. According to the work of Seminara [143, 144], the depth of such defects is principally defined by two parameters: the cluster size and the impact energy. As it will be shown below, the depths are well defined.

The etching stage is performed in a vacuum furnace $(p < 1 \cdot 10^{-4} \text{mbar})$ at 950 K (see
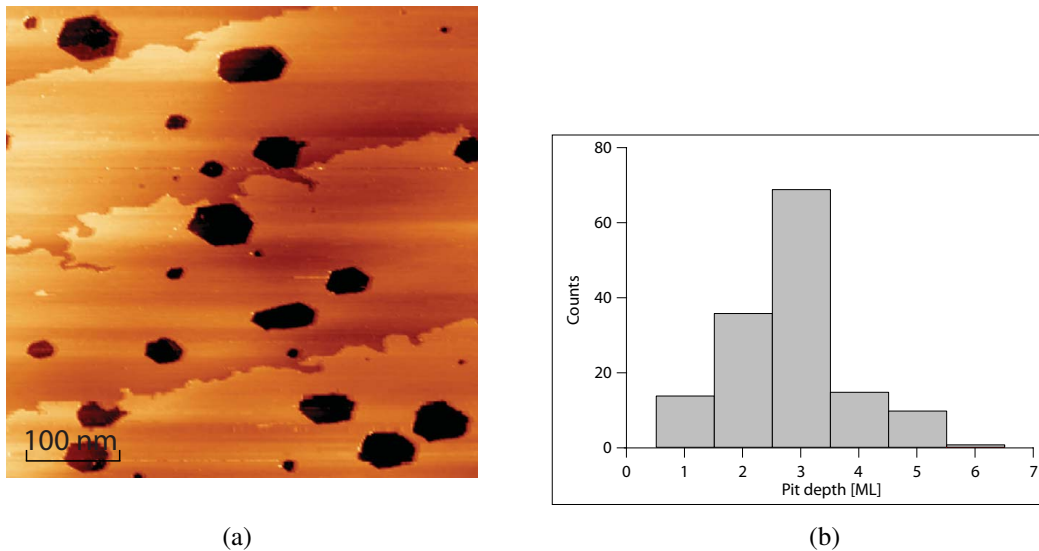
Figure 5.3: (a) STM image of pits after etching, $V_{gap} = 0.5\,V$, $I_T = 0.5\,nA$. Image size: $500nm \times 500nm$. (b) Histogram presenting the pit depth for Au_5^+ clusters at impact energy of $3kV$. Mean pit depth is $2.84ML$.

Section 4.4). During etching, the temperature varies by $\pm$ 20K. Typical etching durations are of the order of 10 minutes at an oxygen pressure of 80 $\pm 3mbar$. Once the sample attained room temperature, it is examined by scanning tunneling microscopy (STM) in air to control the quantity and the size of the pits. Figure 5.3(a) shows an example of the etch pits (estimated pit diameter between 10 to $50nm$) and Fig. 5.3(b) the depth distribution which yields a mean value of 2.84 monolayers (ML).

5.1.1 Pit quantity optimization

It is of great importance to optimize the surface, i.e. to produce as many nanopits as possible for a given pit size. The more pits are present on the surface, the larger the number of particles for statistics and the stronger the signal for catalytic measurements. But since the nanoparticles are located on the rim of the pits, one should avoid a big overlap between the pits. The larger the total perimeter, the larger the number of gold nanoparticles we can create on the surface.

A numerical model has been developed to simulate the total rim length. The starting point is a clean HOPG surface. Defects with a predefined diameter are created one by one at random positions. After each defect creation, the total rim perimeter is calculated and plotted as a
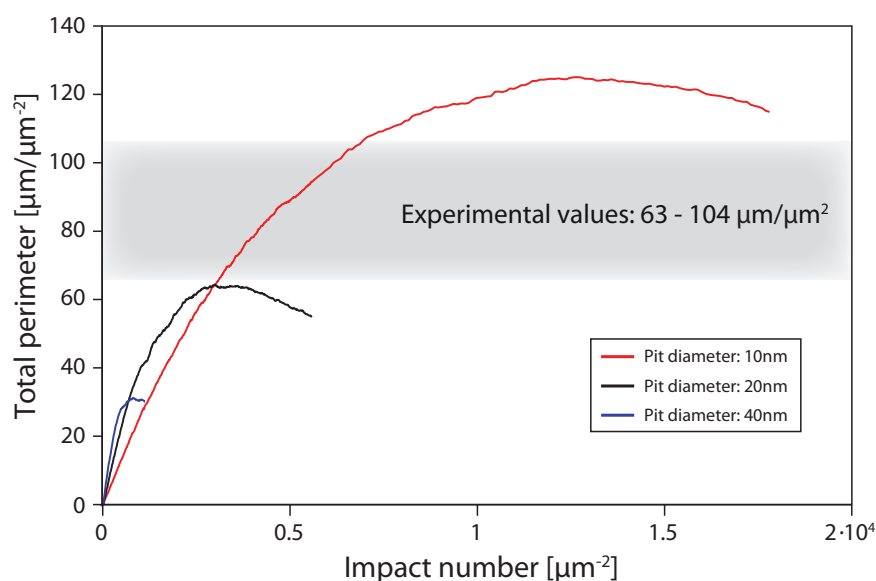
Figure 5.4: Simulation of the total pit perimeter vs. impact number and pit dimensions. A maximum of $120 \frac{\mu m}{\mu m^2}$ has been found for pit diameters of $10nm$. Experimental values (grey highlight) for pit diameters of approx. $15nm$ fit perfectly with the simulation.

function of the number of defects (see Fig. 5.4). At the beginning (low quantity of pits), the increase of the total perimeter is linear, since there is no overlap between the pits. Little by little, the surface is filled up with pits and this makes it difficult for new defects to contribute to the increase of the total perimeter. At a certain point, additional defects do not contribute anymore to the total length and finally have the opposite effect: the total perimeter decreases.

The number of primary impacts has been chosen to optimize the total pit rim length which itself depends on the mean diameter. Different pit diameters have been simulated and are reported in Fig. 5.4 for diameters between 10 and $40nm$. Smaller pits have not been simulated as their experimental production is very difficult. One sees that with increasing diameter, the total available perimeter length decreases. The comparison of the simulation results with the experimental values shows a good match: the total perimeter (simulation) for pits of 10 to $20nm$ is situated between 64 and $125 \frac{\mu m}{\mu m^2}$ as shown in Fig. 5.4 whereas the experimental values measured on different samples vary between 63 and $104 \frac{\mu m}{\mu m^2}$ for the mentioned pit diameters (grey zone). The number of impacts (experimental values) per unit surface are contained between 3500 and 11000 impacts per μm^2. The reproducibility of precise pit diameters is not evident as it varies with the etching temperature, oxygen pressure and exposure time. Slight changes can have strong effects.

5.1.2 Gold atom deposition

Gold is deposited on the nanostructured surface by physical vapour deposition (PVD). The samples are heated to $673K$ under vacuum at a pressure of $5 \cdot 10^{-6} mbar$. A molybdenum crucible with pure gold (99.9%) is resistively heated and gold atoms and clusters are evaporated onto the HOPG sample. The thermal energy of the gold atoms ensures soft landing conditions without any defect creation on the HOPG surface. Elevated temperatures of the sample during the deposition process enhance the mobility of gold on the graphite surface. Gold particles move in random walk motion on the surface and nucleate at strong binding sites. These sites are present at step edges and at the rim of the pits. Terraces do not contain carbon atoms with free sp^2 binding sites, and thus gold atoms cannot be fixed on terraces. Deposition at room temperatures does not supply sufficient energy to the gold particles to enhance their mobility. In this case, particles remain at the deposited position. The total amount of gold is monitored with a quartz-crystal microbalance. After deposition, the sample is cooled down in a nitrogen atmosphere. The Figure 5.10(a) shows an STM image of a graphite sample after gold deposition. One can see gold particles all over the step edges and the rim of the pits. The mean height of the particles is $h = 1.8 \pm 0.2nm$ and their density is $\delta = 3800\mu m^{-2}$.

5.2 Electrochemical stability of gold clusters

The stability of gold nanoparticles has been analyzed by cyclic voltammetry (CV). To perform such measurements, we use an electrochemical cell, described in the thesis of Limat [68]. A potential is applied between the sample and a counter electrode that varies with time. The established current between the two electrodes is measured. The measurement cycle is entirely controlled by an electronic device, so-called potentiostat. Supplied software analyzes the data and converts it directly into a voltammogram. A typical measurement contains a series of ten to several hundred potential cycles. We therefore call the method cyclic voltammetry (CV).

We compare samples with gold deposited on a clean and unstructured surface to samples with nanopits, as described above. The group of Comninellis [284] has already studied the stability of gold on boron-doped diamond. They revealed that the gold nanoparticles are not
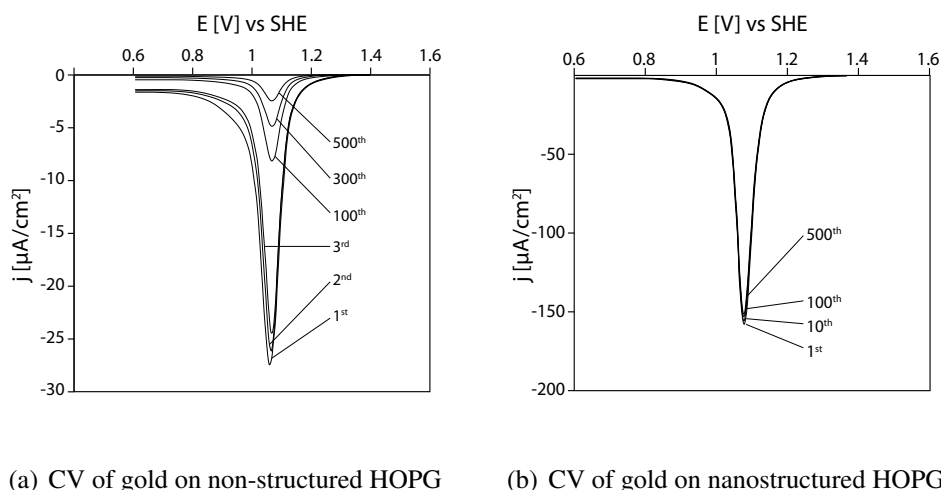
(a) CV of gold on non-structured HOPG   (b) CV of gold on nanostructured HOPG

Figure 5.5: Evolution of cyclic voltammograms of (a) sputter-deposited gold on a non-structured HOPG substrate and (b) gold deposited by PVD on a nanostructured HOPG surface as a function of the number of cycles. Cyclic voltammetry in $0.5M\ H_2SO_4$ at $T = 300K$. Scan rate of $S = 100\frac{mV}{s}$, potential limits: $0.6 - 1.4V$.

stable and are washed away during the potential cycles. The same method is used in this study.

Gold particles are evaporated on HOPG samples with the process mentioned in the previous Section. Clean HOPG and pre-structured samples are used as cluster support. The sample undergoes a heat treatment at $673K$ under vacuum (10^{-5} to $10^{-6} mbar$) subsequent to sputter deposition at room temperature. The evolution of cylic voltammograms is shown in Fig. 5.5. We plot the applied potential V versus the current density j. The current density has been normalized by the active surface covered by the gold particles. Figure 5.5(a) presents the evolution for gold nanoparticles on a non-structured graphite sample. The reduction peak of gold oxide decreases with each cycle and reaches a final loss 91% after 500 cycles. The loss can be explained by the sintering of the particles and thus a reduction of the active surface area. We observed a decreased density and the aggregation of gold on the surface. This shows clearly that gold deposited on non-structured HOPG cannot be considered as stable during the potential cycling. The same cycles of voltammetry have been made on pre-structured graphite (Fig. 5.5(b)). No significant loss in the current density can be observed after 500 cycles, gold nanoparticles are well fixed and remain in the pits during many voltammetry cycles.

The properties of stable deposits depend on several parameters; two of them have been studied in this work : (i) the amount of deposited gold and (ii) the dispersion of such a catalyst. For these investigations, a standard procedure has been applied taking the third voltam-
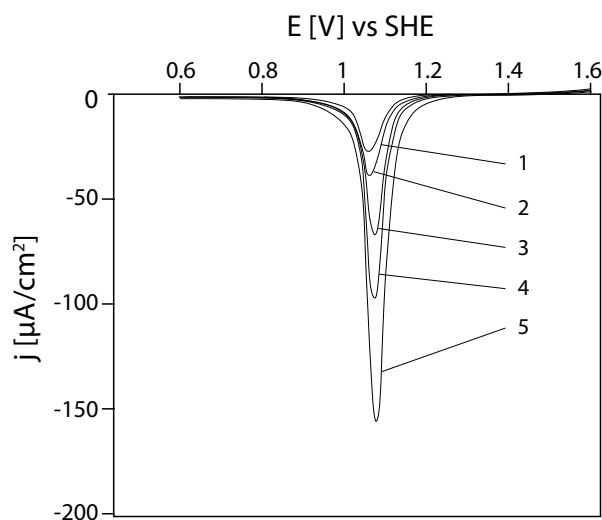
Figure 5.6: Cyclic voltammograms as a function of gold loading on a structured HOPG surface. (1) $3 \cdot 10^{14}$, (2) $5.9 \cdot 10^{14}$, (3) $1.2 \cdot 10^{15}$, (4) $1.8 \cdot 10^{15}$ and (5) $3 \cdot 10^{15} \frac{\text{atoms}}{cm^{-2}}$. Cyclic voltammetry in $0.5M \ H_2SO_4$ at $T = 300K$; scan rate $S = 100\frac{mV}{s}$; potential limits : $0.05 - 1.8V$.

metric scan in order to ensure electrochemical steady-state conditions. Gold nanoparticles of different metal loading have been studied and the voltammograms are shown in Fig. 5.6. The peak current response j increases with metal loading, while the peak potential of gold oxide reduction is rather stable at $E_{red} = 1.08\,V$, with the exception of gold loadings below $10^{15} \frac{\text{atoms}}{cm^2}$. The slight negative shift in reduction peak potential noticed at such low loadings is probably related to the instability discussed above. On the other hand, increasing the load leads only to an increase of the particle size but not to that of the particle density which is evidenced by looking at the dispersion (N_s/N_d) as a function of metal loading, shown in Fig. 5.7. N_s denotes the number of gold atoms on the surface of the nanoparticles accessible to the electrolyte, was calculated from the voltammetric charge of the reduction peak of gold oxide and N_d the total number of deposited atoms. This fraction (N_s/N_d) decreases as the particle size increases. According to the fraction N_s/N_d, it can be suggested that during the gold deposition process, an arriving atom links preferentially to an existing nucleus within a nanopit than to create a new nucleus. In fact, the deposition of gold by evaporation on the tailored surface takes place via formation and growth of separate three-dimensional islands and not via completion of successive monolayer.

The computed fitting line in Figure 5.7 follows the theoretical surface to volume ratio

N_s/N_d; for small clusters we can approximate the shape of the cluster with a sphere. The size of each atom can be approximated with the Wigner–Seitz radius r_s, where r_s is simply the radius for a sphere whose volume is equal to the volume of one atom in the solid. Considering a cluster with N atoms the total volume of the cluster is given by

$$V = \frac{4}{3}\pi R^3 \simeq \frac{4}{3}\pi r_s^3 N. \tag{5.1}$$

We use the approximation that the surface contribution of each atom is πr_s^2 (for $R \gg r_s$) and thus find a total number of surface atoms of

$$n_{surface} \simeq 4\left(\frac{R}{r_s}\right)^2 \simeq 4N^{2/3}. \tag{5.2}$$

The surface to volume ratio $F_{surface}$ is then:

$$F_{surface} = \frac{n_s}{N} \simeq 4N^{-\frac{1}{3}}. \tag{5.3}$$

The indicated fitting curve with the exponential $-\frac{1}{3}$ approximates the data point in a very precise way. Furthermore, using this relation, we can estimate the size of the gold nanoparticles for the corresponding surface to volume ratio. The number of atoms per cluster N can be expressed, using Equation 5.1:

$$N^{-\frac{1}{3}} = \frac{r_s}{R} \tag{5.4}$$

and thus:

$$F = 4 \cdot N^{-1/3} = 4\frac{r_s}{R} \Leftrightarrow R = \frac{4r_s}{F} \tag{5.5}$$

The highest surface to volume ratio in Figure 5.7 of $F = 0.55$ gives a cluster radius, assuming the Wigner-Seitz radius of gold $r_s = 0.159nm$ of $R = 1.15nm$. The particle radius for the lowest ratio of $F = 0.15$ is then $R = 4.23nm$. As it will be shown below, this estimated cluster size matches very well with the measured cluster dimensions (see Section 5.3.1). This method is a very interesting way to analyze the cluster size on surfaces without using STM microscopy. We have shown that the estimation of the cluster size by means of the dispersion curve is in very good agreement with the measured cluster values mentioned below.
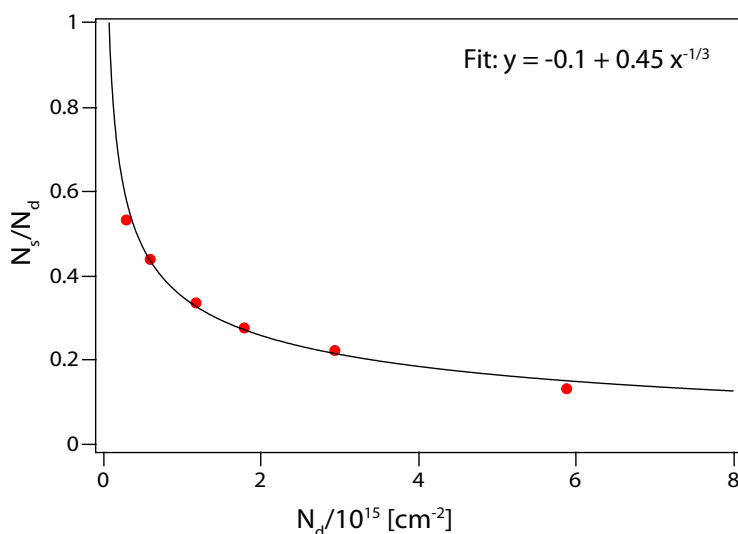
Figure 5.7: Dispersion (N_s/N_d) of Au nanoclusters on structured HOPG substrates as a function of the deposited amount (N_d). The density of surface gold atoms (N_s) was calculated from the voltammetric charge of the reduction peak of gold oxide.

5.3 Corral formation

Gold deposited on nanostructured graphite has been found to nucleate in form of small nanoparticles at the step edges and at the rim of pits [148, 149, 152]. Existing studies focus on monolayer high step edges or rims by etched natural defects [152], low coverage of multilayer deep pits [148, 149] and large cluster with completely saturated small pits with gold [149]. In this study, the number of particles, their size and shape has been investigated in detail. The height is systematically measured from the lower step (or rim) to the highest point of the particle, see Fig. 5.8.

At low gold loadings, the particles do not fill up the complete available rim space but form individual clusters independent from each other. Their preferred position situates in the corner of the pits where the interaction between graphite and gold cluster is the strongest. Figure 5.9 shows an STM image with a very small gold load ($1.4 \cdot 10^{14} \frac{\text{atoms}}{cm^2}$). No continuous decoration of the steps with gold particles can be found, in contrast to Fig. 5.10(a), where the gold load is $5 \cdot 10^{14} \frac{\text{atoms}}{cm^2}$. The particles on this picture show closed beads with identical dimensions. Even in the case of completely filled pits, differences between corner clusters and particles connected to straight steps can be found. This result is in agreement with studies from Hövel on monolayer deep pits [149].
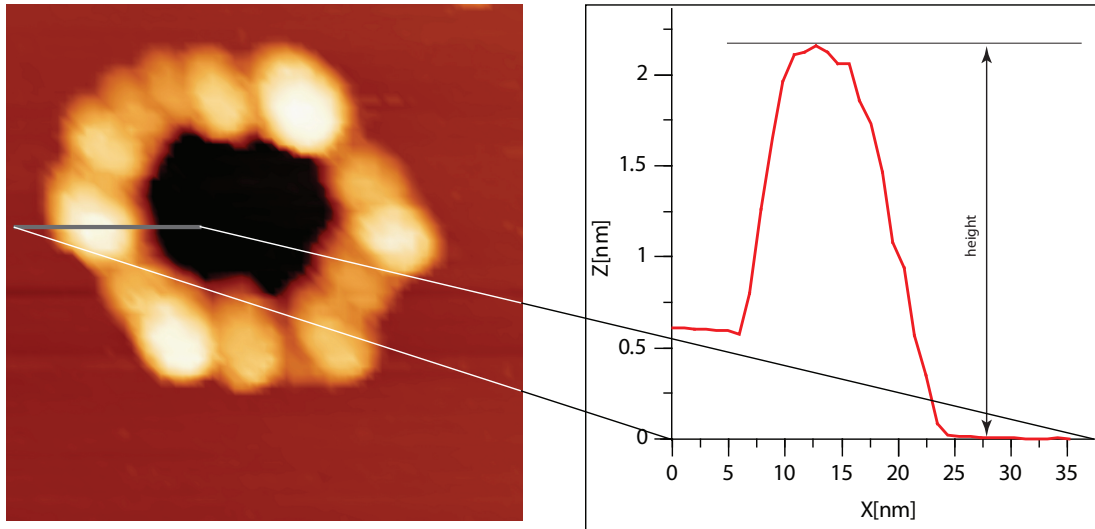
Figure 5.8: Schematic cross-section through a gold cluster. The measured height is indicated.
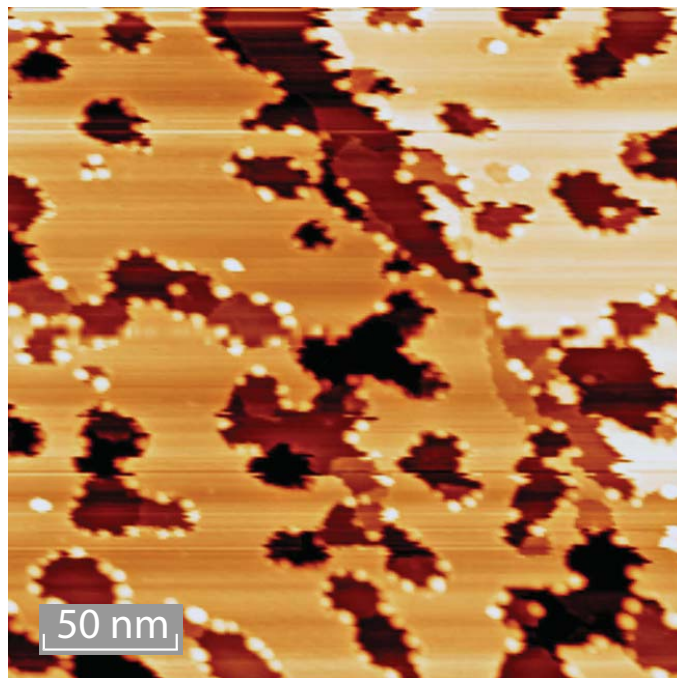
Figure 5.9: STM image after deposition of a small gold quantity. The clusters are located on the rim with preference in the corners but do not form continuous corrals. $V_{gap} = 0.7\,V$, $I_T = 50\,pA$. Image size: $250nm \times 250nm$.
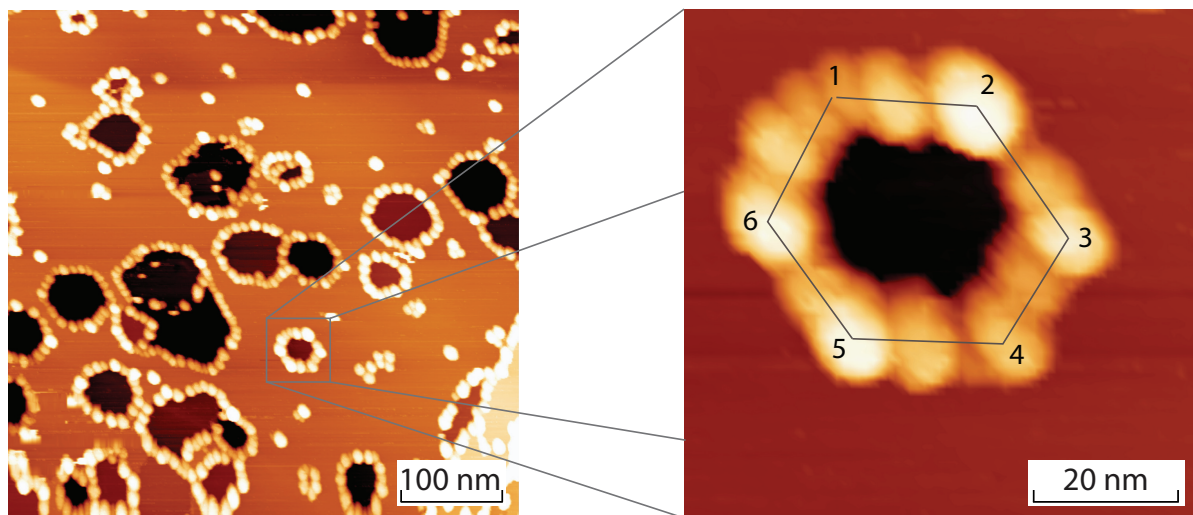
(a)
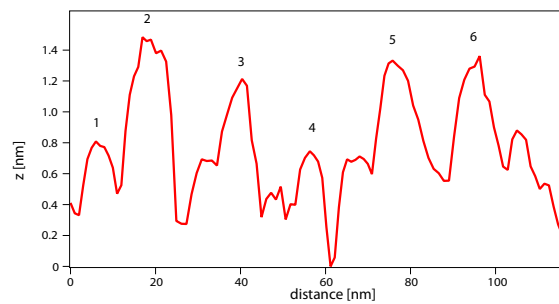
(b)

Figure 5.10: a: STM image of gold deposited on structured HOPG. $V_{gap} = 1.4\,V$, $I_T = 100\,pA$. Image size: $500\,nm \times 500\,nm$. Inset shows a single pit decorated with gold nanoparticles. In the line profile (b) the edge particles are higher than particles at straight rims.

5.3.1   Cluster size of corral particles

A profile along the pit rim shows the topography of these particles. Clusters sitting in the corners are significantly higher than clusters on straight steps. The higher interacting forces in these positions promote gold accumulation and thus bigger clusters. The detailed view of Fig. 5.10(a) and the corresponding line profile show that corner particles are brighter, which represents a larger apparent height. The hexagonal structure of small pits can also be observed on the picture. The etching of small pits goes along crystallographic directions of graphite, as it is discussed in Section 3.1.2. For larger pits, this hexagonal structure vanishes. The particle size in these pits is uniform, as shown in Figure 5.11.
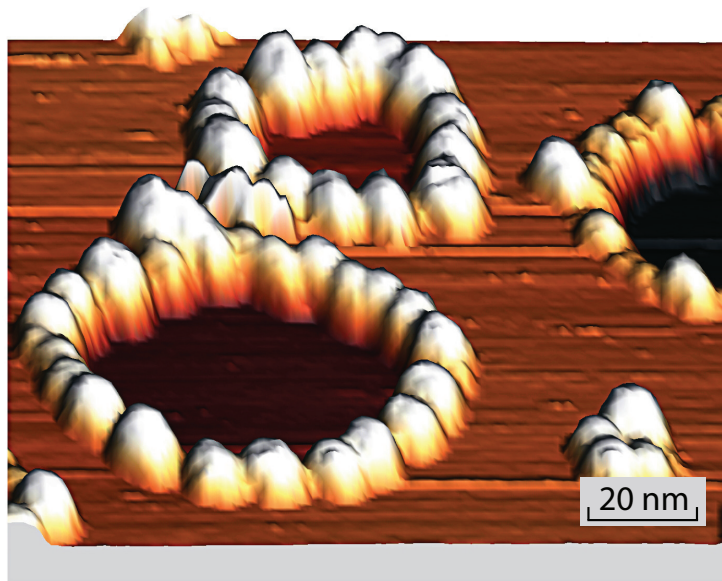
Figure 5.11: Three-dimensional representation of gold clusters on big pits. The cluster size is uniform as the pit do not show hexagonal structures. $V_{gap} = 1.4\,V$, $I_T = 100\,pA$. Image size: $130nm \times 130nm$.

The measured cluster diameter is of very low reliability because of the surface-tip convolution. The measured dimensions of gold clusters are close to the detection limits and as many different tips have been used and the shape of the tip changed sometimes several times during one image scan, the convolution can hardly be evaluated. Hövel and Barke presented in their study data that propose a diameter to height ratio of 1.4 in a truncated sphere model [148]. This value has been used in this work whenever a cluster diameter is mentioned.

Starting from small particles for deposition of low gold quantities, the cluster size increases with increasing gold quantity (see Fig. 5.13). There is a linear increase in cluster height. For the smallest gold load ($1.4 \cdot 10^{14} \frac{\text{atoms}}{cm^2}$), a mean height of $h = 1.93 \pm 0.3 nm$ was measured, averaged over 60 particles. At the highest measured gold loads of $2.6 \cdot 10^{15} \frac{\text{atoms}}{cm^2}$, the statistics of three different samples show a mean height of $3.98 \pm 0.79 nm$ to $4.35 \pm 0.62 nm$, averaged over more than 200 particles for each sample. Assuming the mentioned ratio of 1.4, we can estimate the total number of atoms per cluster. The volume V goes with $V(h) \approx 1.15 h^3$, which gives for the actual deposited quantities clusters with 490 to 5600 atoms per cluster. The height of clusters has been measured, as it was mentioned before, from the bottom of the pit (or step) to the top of the particle.

A very interesting fact has been found when the height of particles on pits with different

depth were compared: independent of the pit depth, the clusters always present the same height. The plot in Fig. 5.12 shows the cluster height distribution for different pit depths. The mean height of gold clusters is situated between 1.72 and $1.81nm$ (Notice that the gold load on the sample was very low ($5 \cdot 10^{14}\frac{\text{atoms}}{cm^2}$), which explains the low mean cluster height). This result is surprising, since we would expect the increased number of dangling bonds on the rim of the pits to have an influence on the particle morphology.
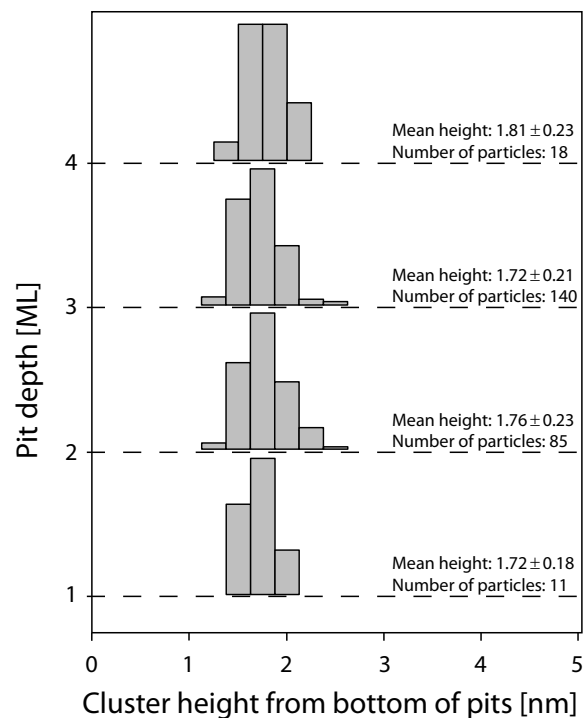
Figure 5.12: Cluster height for different pit depths. The size distribution remains constant with increasing pit depth. The measurement was taken on a sample with very low gold loading ($5 \cdot 10^{14}\frac{\text{atoms}}{cm^2}$).

We presented in Section 3.1.3 the results of Hövel and Barke [148]: the total number of gold particles on samples with different gold loadings remains essentially constant, even if pits are large enough to allow formation of additional clusters at their edges. In fact, it is difficult to compare the results of different samples, as the quantity and size of pits vary sometimes quite strongly. In order to compare them, the criterion has been chosen to be the number of clusters per unit rim length (i.e. per micrometer of rim length). Based on several STM images for each calibration, we measured the total rim length and counted the number of clusters on
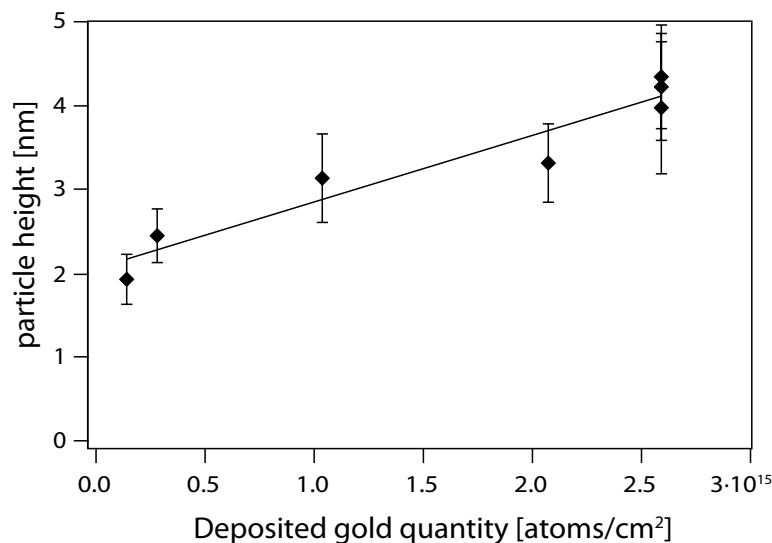
Figure 5.13: Particle height vs. deposited gold quantity. The cluster size is linearly proportional to the gold quantity.

the pits per image. The division of rim length by cluster number gave a number indicating how many clusters are situated on one micrometer of rim length.

Figure 5.14 shows the particle number per μm versus deposited gold quantity. The number of particles remains approximately constant for all studied gold quantities. When gold is evaporated on HOPG at elevated temperature ($673K$), atoms individually occupy all available dangling bonds. Additional atoms prefer to attach to existing nanoparticles than to create additional nucleation sites. Clusters thus grow uniformly in size. At very big gold loads, the clusters change shape from circular to slightly elliptic (see Fig. 5.10(a)). However, their growth is laterally limited by the presence of neighbouring clusters. The particles increase toward the centre of the pits. We did not observe merging of particles, as it has been observed by Beebe [152]. We suppose that the deposited gold loads were not sufficiently high to observe this behaviour.

An open question is whether the clusters on a rim touch each other or if there is some open space between. Measurements have been performed on two samples with different gold loadings ($1 \cdot 10^{15}$ and $2.6 \cdot 10^{15} \frac{atoms}{cm^2}$). Clusters on the sample with lower gold loading are separated by $8.8nm$ for an estimated cluster diameter of $d = 4.4nm$. The second sample show
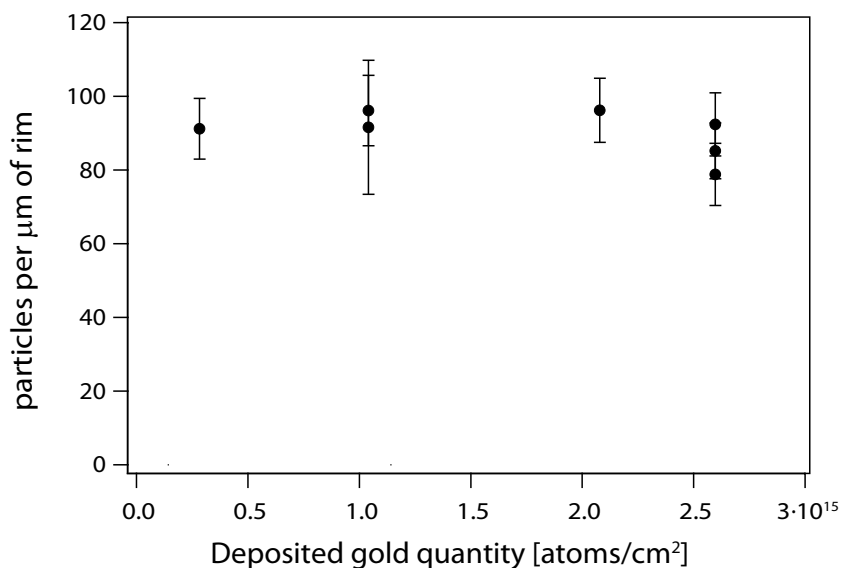
Figure 5.14: Gold quantity deposited on HOPG vs. the number of particles on 1 micrometer of rim. The constant value of approx. 100 particles per unit length indicates that the gold quantity is not the primary limiting factor for the particle number.

a distance of $10.6nm$ for particles with $6.1nm$ of diameter [1]. This means that, even though the STM image shows a closed chain of cluster, the particles are clearly separated each from the other. This is an important fact that has to be considered when the catalytic activity of gold clusters will be discussed. While the STM shows touching nanoparticles because of tip convolution effects, this problem is avoided in electron microscope images where the distance is well visualized.

5.4 Thermal evolution of gold nanoparticles

The thermal evolution of gold clusters stabilized in nanopits has been studied for several annealing temperatures. The sample has been introduced into a furnace at atmospheric pressure and was heated during 15 minutes. Heating cycles enhance the mobility of gold and in consequence decrease the number of particles with increasing temperature. Bear in mind however that particles have been created at $673K$. From this point of view, we do not expect thermal activated morphology change up to this temperature. However the exposure to environmental gases, especially oxygen might result in a morphology change.

---

[1]The diameter is estimated with the ratio $\frac{d}{h} \approx 1.4$ from the measured cluster height [148].

5.4.1   Cluster location on the surface
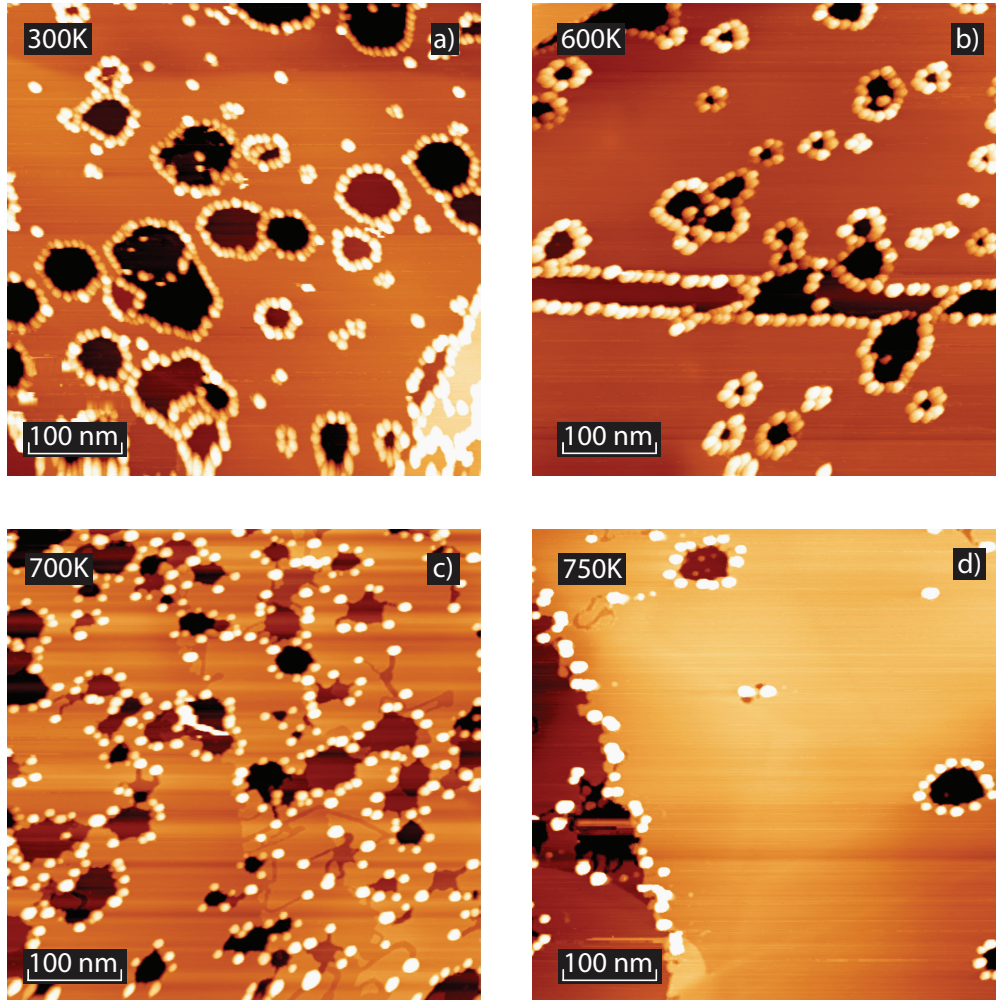
Figure 5.15: Evolution of gold particles on structured HOPG surface. The deposited gold quantity is $5 \cdot 10^{14} \frac{atoms}{cm^2}$. At $300K$ (a) particles occupy the rim of pits, steps, as well as point defects on terraces. At higher temperatures particles on point defects vanish (b) and local, particle-enhanced etching occurs (starting at $700K$ on (c)). $V_{gap} = 0.7\,V$, $I_T = 50\,pA$. Image size: $500nm \times 500nm$.

Figure 5.15 illustrates the evolution of gold clusters for different annealing temperatures. At $300K$, clusters are located on steps, pit rims and also on point defects on terraces. Local defects in the HOPG structure can offer nucleation sites for migrating gold particles to anchor them to the surface. No underlying defect is visible in the STM image. The annealed sample at $600K$ does not show clusters on point defects. Apparently, the supplied energy has been sufficient to enable the mobility of such particles. They migrate on the terraces until they join particles on rim or steps. Particles on the rim did not move neither agglomerate with

each other. This behaviour changes for annealing at higher temperatures ($700K$). Clusters still stay on rim sites, but a catalytically driven process starts which etches channels into the graphite surface (see Section 5.5). The image for annealing at $750K$ has been taken on the same sample as the ones before but at the edge of the prepared surface. Therefore the pit density is strongly reduced. The movement of the gold particles can still be observed. The catalytic channel formation continues and an agglomeration of particles can be detected. The density of clusters on the rim decreases, compared to the image at lower annealing temperature (see also discussion in the next Section 5.4.2).

5.4.2 Particle size distribution
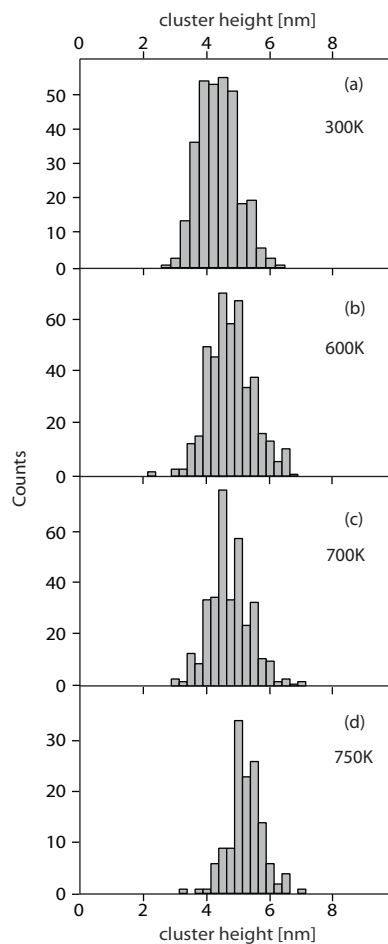
Figure 5.16: Histogram of cluster height for different annealing temperatures. Deposited gold quantity: $2.6 \cdot 10^{15} \frac{atoms}{cm^2}$. The corresponding data in Fig. 5.17 are the black squares (■).

The heights of particles have been measured for different annealing temperatures and are plotted in Fig. 5.17. The mean value between room temperature and $700K$ varies between $4.35nm$ and $4.76nm$. Regarding the standard deviation of $\sigma = 0.65$ (Statistics are made over more than 100 particles for each temperature), the height can be considered as constant. This is not surprising as the gold has been evaporated on the HOPG sample at $673K$. Above $700K$, a slight increase in cluster height can be observed, even if the change is in between the error estimation. This would suggest that there is no morphology change due to reactions until this temperature. Figure 5.16 illustrates the histograms of the cluster height. The size distribution remains almost unchanged until $700K$, which confirms the statement that clusters do not agglomerate. At $750K$, the distribution is significantly narrower and shifted towards bigger clusters sizes. It can be interpreted as a diffusion of small particles and a growth of clusters to a particular size where they are most stable. Heating to even higher temperatures ($800K$) leads to the evaporation of the particles from the surface.
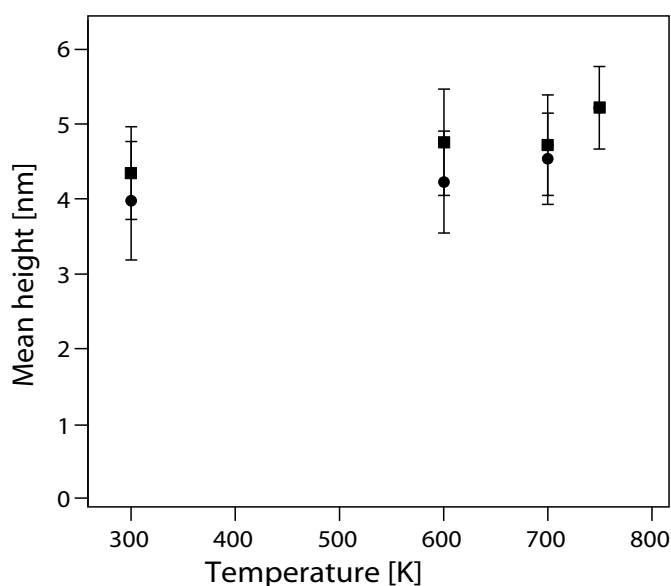
Figure 5.17: Mean particle height vs. annealing temperature. Measurement have been done on two different samples (● and ■).

Similar to the analysis in Fig. 5.14, the number of particles per rim length has been studied after annealing. A visual guideline was presented in Fig. 5.15 and a quantitative analysis is given in Fig. 5.18. Until a temperature of $600K$, the particle number remains constant. Particles on the rim stay immobile. This is consistent with the stable cluster size for the mentioned annealing temperatures. Above $600K$ the density of particles on the rim decreases. As the
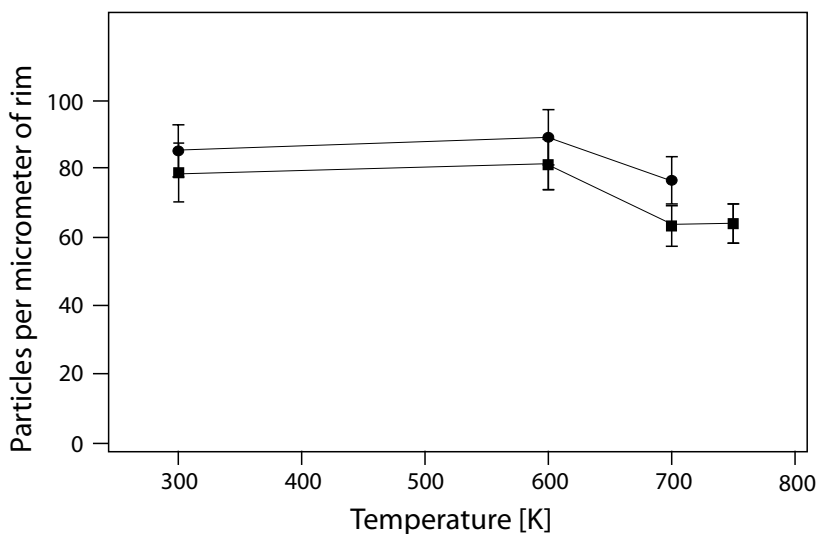
Figure 5.18: Particle number on the rim vs. annealing temperature. Data of two different samples (●, ■) with similar initial gold loading ($2.6 \cdot 10^{15} \frac{\text{atoms}}{cm^2}$).

mean height does not increase significantly, the cluster probably changes slightly its shape (ratio of diameter to height). This suggestion cannot be proven in detail by lack of additional measurements. The drop of cluster density above $700K$ is again consistent with the cluster morphology in Figs. 5.16 and 5.17.

5.5 Channel etching

5.5.1 Etching process

HOPG is inert to oxygen etching up to a temperature of $920K$, as discussed in Section 3.1.2. However, the presence of gold clusters enables the catalytic etching of dangling bonds at lower temperatures. The graphite crystal is attacked whenever a gold particle is present. As mentioned in the preceding Section and illustrated in Fig. 5.19, the annealing at high temperatures leads to a decrease in the particle number and reveals again the preferred position of gold nanoparticles in the corners of the pits. The catalytic oxidation by gold nanoparticles has been discussed in Section 3.1.4 according to the study of Severin *et. al.* [168]. The model shown in Fig. 5.20 (c) and (d) suggests the following process: oxygen molecules (blue spheres) chemisorb and dissociate on the Au catalysts and diffuse to the interface between gold and
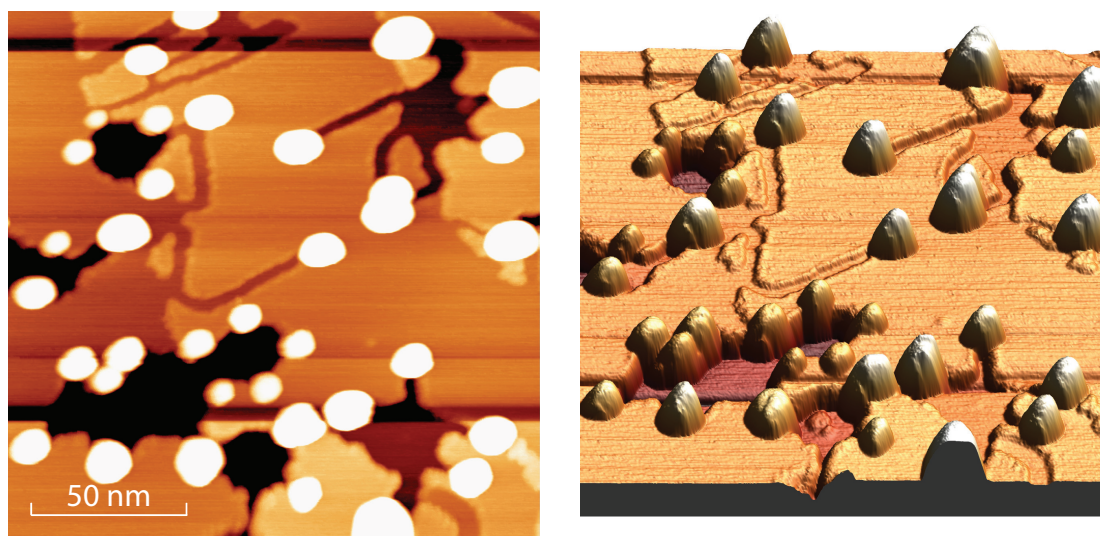
Figure 5.19: STM image of gold nanoparticles on structured HOPG after annealing at $700\,K$. Gold particles enhance catalytic etching of graphite and thus create channels in the graphene sheets. $V_{gap} = 0.7\,V$, $I_T = 50\,pA$. Image size: $170nm \times 170nm$.

graphite. At the interface between the gold particle and the graphite surface, oxygen atoms break the strong intralayer-bonds of graphite. The free carbon atom combines with an oxygen atom to form CO or CO_2. Once the gaseous complex has been formed, it leaves the surface. The desorption temperatures of CO and CO_2 from Au clusters will be discussed further below. During etching, the whole gold particles move ahead and always stay in contact with the graphite edge. Figure 5.20 (a) shows the gold particles after deposition, (b) during the catalytic etching. Step by step a channel grows in length but neither in width nor in depth. Furthermore, the contact area of the gold particle with the dangling bonds of graphite defines the width and the depth of the channel. The larger the particles, the larger the surface in contact with the graphite edge and thus the wider the channel. This correlation is shown in Fig. 5.21, the dashed line indicates a linear fit. The slope of 1 indicates the direct dependence of the channel width on particle size. As the channel etching is obviously related to the presence of gold particles, the particle cannot be bigger than the channel it formed.

5.5.2   Correlation between channel length and depth

A further correlation between the depth and length of channels can be observed, see Fig. 5.22. The deeper the channels the shorter they are. The number of carbon atoms to etch away
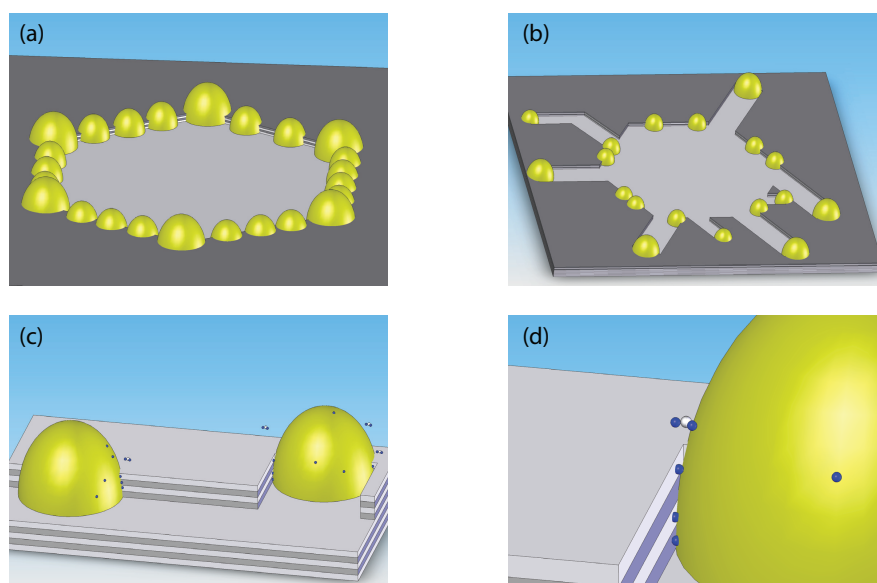
Figure 5.20: Model of gold nanoparticles on structured graphite. a) Nanoparticles decorate the hexagonal pits. b) During the etching process, clusters first assemble with preference in the corners and create lateral channels. c) Details of the etching process: (1) Oxygen molecules (blue) adsorb on the gold cluster (yellow) and dissociate (2). They migrate to the cluster-carbon interface (3), break the carbon bonds (grey) and recombine to form either CO or CO_2.
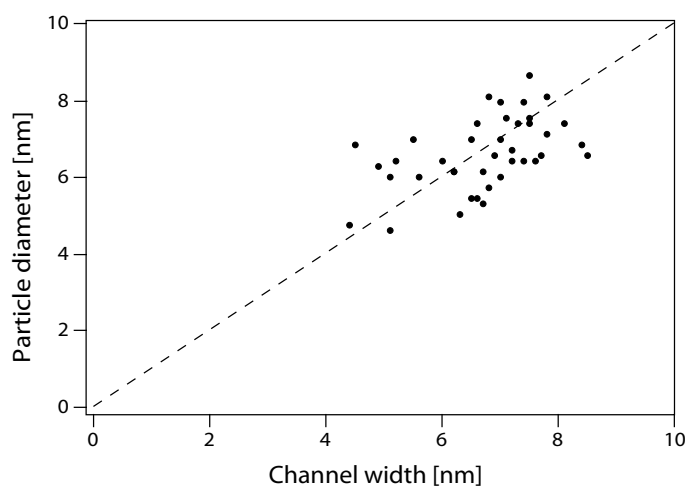
Figure 5.21: Diagram showing the particle diameter versus channel width. A linear fit with a slope of 1 is drawn to show the direct dependence of particle size and channel width.
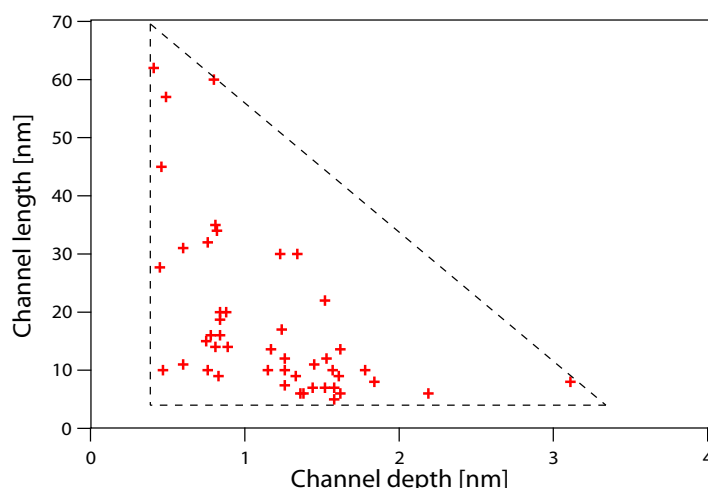
Figure 5.22: Channel length versus depth. The deeper the channels the slower they grow in length. Note that the opposite in not necessarily true; a shallow channel can also be short.

increases with each additional graphite layer. As the oxygen supply is constant for all channels and limited by the adsorption rate on the particle, deep channels inevitably grow slower than shallow ones. No correlation can be found between the remaining combinations of channel width, depth, length and particle size.

5.5.3   Channel orientation

Channels always start at the particle position and thus mostly in the corner of pits. They grow straight in one of the three crystallographic directions, as shown in Fig. 5.23. Their direction is parallel to the crystallographic orientation of graphite. The fitted curve shows peaks at orientations of $-0.4°, 60.7°$ and $112.6°$. The rather broad distribution is due to measurement errors as the orientation of very short channels is difficult to determine with precision. During the etching process, channels usually bend at well defined angles of $120°$, as shown in the inset in Fig. 5.23 and in Figure 5.19. Nevertheless, bending at $60°$ is also possible but less frequent, in agreement with the results in literature [169, 170, 173].

5.6   Catalysis of gold nanoparticles on HOPG

Catalysis measurements are performed on similar samples to the one presented in Fig. 5.10(a). In the chemical reactor (described in Section 4.6) the sample is exposed to a constant oxygen pressure. In the present experiment, isotopic labelled oxygen $^{18}O_2$ is used. It is useful
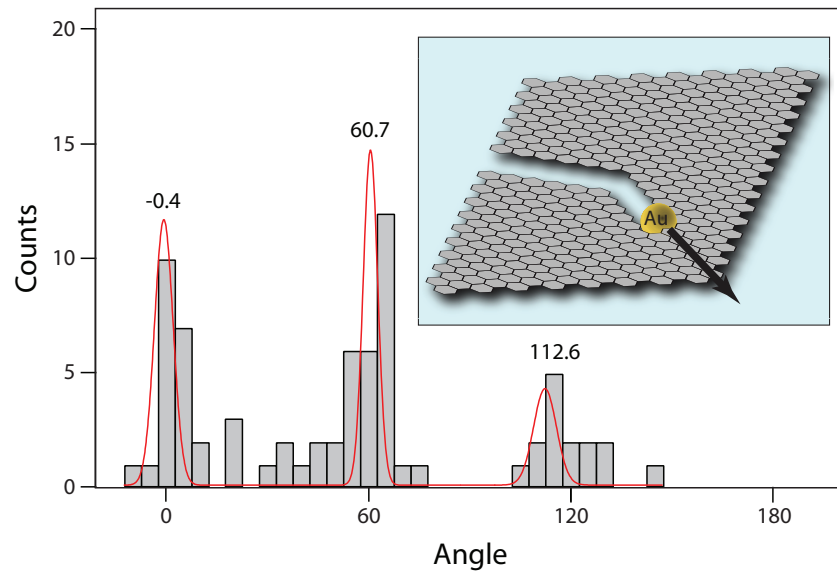
Figure 5.23: Histogram of the channel orientation created by gold-particle enhanced etching. The main peaks are at $-0.4°, 60.7°$ and $112.6°$ with respect to a pre-defined zero-direction. The red curve is a three-peak Gaussian fit with the maximum values indicated above. The inset shows a schematic view of the graphite etching process and the channel orientation. Bending mostly occurs at angles of $120°$.

to distinguish between different products of the catalytic reaction:

$$
\begin{aligned}
{}^{12}C + \tfrac{1}{2}\,{}^{16}O_2 &\rightarrow {}^{12}C^{16}O \\
{}^{12}C + \tfrac{1}{2}\,{}^{18}O_2 &\rightarrow {}^{12}C^{18}O \\
{}^{12}C + {}^{16}O_2 &\rightarrow {}^{12}C^{16}O_2 \\
{}^{12}C + \tfrac{1}{2}\,{}^{16}O_2 + \tfrac{1}{2}\,{}^{18}O_2 &\rightarrow {}^{12}C^{16}O^{18}O \\
{}^{12}C + {}^{18}O_2 &\rightarrow {}^{12}C^{18}O_2
\end{aligned}
\tag{5.6}
$$
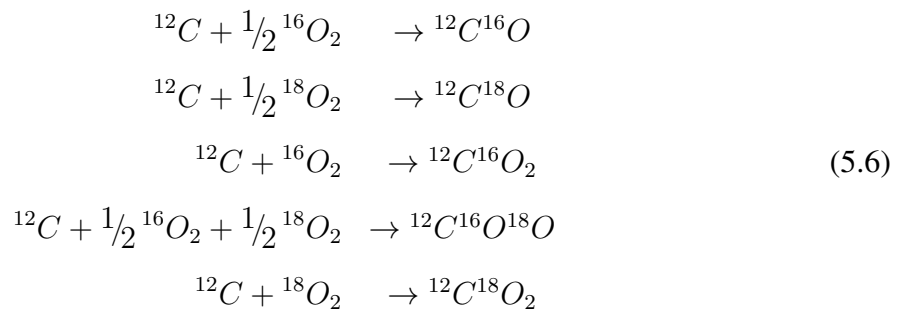
The different products mentioned above are recorded in a mass spectrometer while the sample is heated with a constant temperature ramp of $2\frac{K}{s}$. Figure 5.24 represents the resulting partial gas pressures as a function of temperature. The linear decrease of oxygen during the measurements is related to the decreasing pressure in the gas line. At $670K$, the CO_2 production starts. The signals of $C^{16}O_2$ as well as isotopic labelled $C^{16}O^{18}O$ and $C^{18}O_2$ increase strongly. We see simultaneously a bend of $^{18}O_2$ (circle) which is related to the combustion of oxygen. These results show that oxygen is adsorbed on gold clusters and

combine with carbon atoms. We observe a dissociation of oxygen and an increase of isotopic labelled carbon monoxide. Normal $C^{16}O$ does not show a similar behaviour and decreases with temperature.

| Reaction Steps			Reaction Numbering
$H_2{}^{16}O\,(g) + \; *$	$\rightleftarrows$	$H_2{}^{16}O^*$	1
$^{18}O_2\,(g) + \; 2*$	$\rightleftarrows$	$2^{18}O^*$	2
$H_2{}^{16}O^* + \; *$	$\rightleftarrows$	$^{16}OH^* + H^*$	3
$2^{18}O^* + \; *$	$\rightleftarrows$	$^{18}O^* + {}^{18}O^*$	4
$^{16}OH^* + \; *$	$\rightleftarrows$	$^{16}O^* + H^*$	5
$H^* + H^*$	$\rightleftarrows$	$H_2\,(g) + 2\;*$	6
$^{18}O^* + H^*$	$\rightleftarrows$	$^{18}OH^* + \; *$	7
$^{16}O^* + H^*$	$\rightleftarrows$	$^{16}OH^* + \; *$	8
$^{18}O^* + C\,(s)$	$\rightleftarrows$	$C^{18}O^*$	9
$^{16}O^* + C\,(s)$	$\rightleftarrows$	$C^{16}O^*$	10
$H^* + {}^{18}OH^*$	$\rightleftarrows$	$H_2{}^{18}O^* + \; *$	11
$H^* + {}^{16}OH^*$	$\rightleftarrows$	$H_2{}^{16}O^* + \; *$	12
$C^{18}O^* + {}^{18}O^*$	$\rightleftarrows$	$C^{18}O_2^* + \; *$	13
$C^{18}O^* + {}^{16}O^*$	$\rightleftarrows$	$C^{18}O^{16}O^* + \; *$	14
$C^{16}O^* + {}^{18}O^*$	$\rightleftarrows$	$C^{18}O^{16}O^* + \; *$	15
$C^{16}O^* + {}^{16}O^*$	$\rightleftarrows$	$C^{16}O_2^* + \; *$	16
H_2O^*	$\rightleftarrows$	$H_2O\,(g) + \; *$	17
CO_2^*	$\rightleftarrows$	$CO_2\,(g) + \; *$	18
CO^*	$\rightleftarrows$	$CO\,(g) + \; *$	19

Table 5.1: Reaction steps for the water-gas shift reaction. The number of possible reactions increases due to the supply of isotopically labelled oxygen and CO (compare with Table 2.2).

In order to collect more detailed results, we record mass spectra at different temperatures, ranging from $473K$ to $823K$. The peaks of interest are integrated and plotted in Fig. 5.25. Part (a) shows the signals of H, CO and CO_2. Above $673K$, the isotopically different peaks of CO_2 and CO increase. Both production (CO and CO_2) are in agreement with the catalytic etching of graphite, described in the preceding Section 5.5.

Gold particles on HOPG do not only enhance the graphite etching but do also enhance catalytic reactions such as the water-gas shift reaction (Section 2.2.6). As we have to take into account isotopic labelled oxygen, the variety of reactions is broad. Table 5.1 summarizes all possible reactions. Water, present as residual gas in the vacuum chamber, adsorbs on the gold
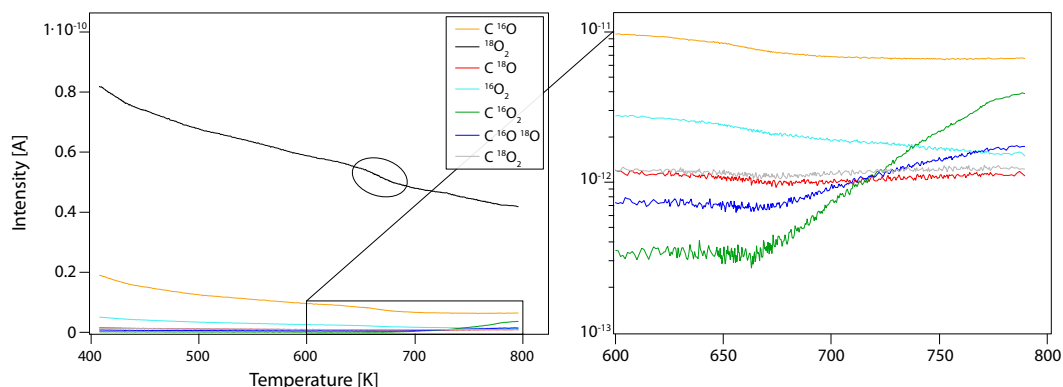
Figure 5.24: Signal intensities as a function of annealing temperature. The decrease in oxygen $^{18}O_2$ is due to the pressure decrease in the supply device. The fast drop at $673K$ (circle) is due to catalytic etching of graphite. A strong increase of carbon dioxide as well as isotopically labelled carbon monoxide can be observed at the same temperature as the oxygen consumption.
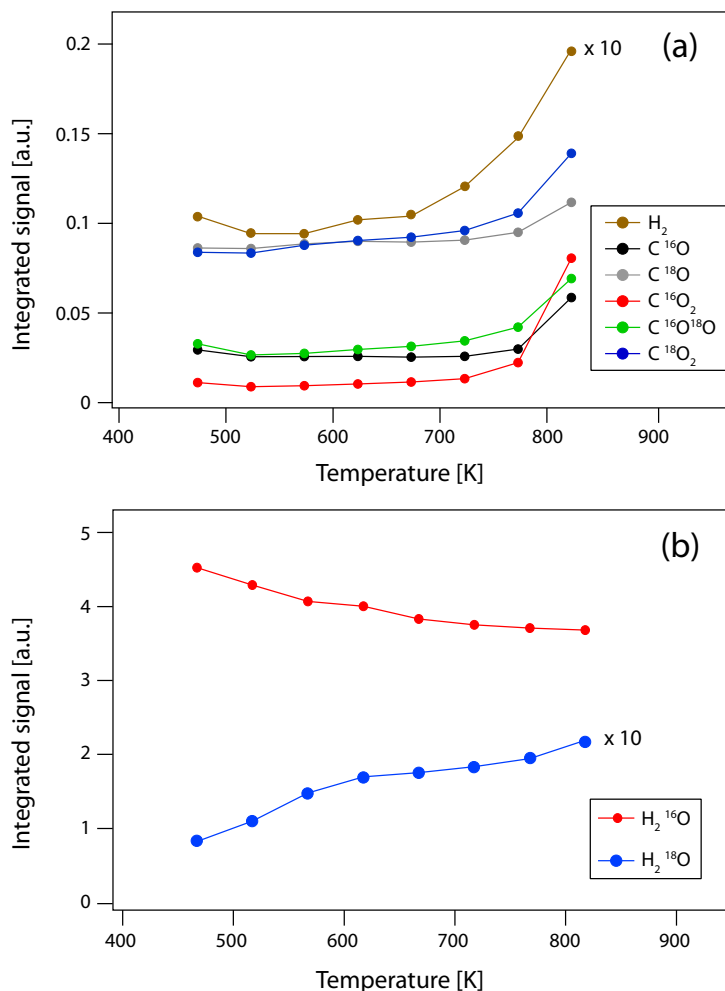
Figure 5.25: Integrated signals from the mass spectra recorded at different temperatures. An increase of all CO and CO_2 isotopes can be observed in (a) for temperatures above $700K$. The hydrogen increase (signal multiplied by 10) is related to the water-gas shift reaction and thus the formation of isotopically labelled water $H_2{}^{18}O$ (also multiplied by 10) in (b).

particles on HOPG, dissociates and forms different isotopically labelled complexes with oxygen atoms. Figure 5.25 (b) shows the signal of normal and isotopically labelled water. Normal water $H_2{}^{16}O$ decreases with increasing temperature. The total loss is of 19%. On the other hand, isotopically labelled water $H_2{}^{18}O$ increases simultaneously by a factor of two. Hydrogen as a byproduct of the water-gas shift reaction increases by 90% with temperature (Figure 5.25 (a)). The increase of this signal confirms the strong catalytic power of gold particles. We can conclude that gold particles on HOPG exhibit similar catalytic properties as gold on metal oxide surfaces [117, 118].

5.7   Conclusion: Gold on HOPG

The stability of gold clusters on structured HOPG surfaces has been investigated, using different experimental methods. The preparation consists in three consecutive steps. In the first step, gold clusters (Au_5^+) are implanted into the graphite surface in order to create defects of specific depth. In the second step the defects are etched to a mean pit diameter, varying between 10 and $50nm$. Subsequent gold evaporation by PVD under vacuum at elevated temperatures ($673K$) leads to the formation of gold beads along the rim of the pits.

The Au clusters confined in the pits show to be very stable against electrochemical processes, in contrast to gold clusters deposited on clean HOPG. Continuous potential cycling, under usual electroanalytical conditions does not alter the gold morphology. We clearly show that the HOPG surface can be nanostructured to stabilize Au clusters, which means that these particles are applicable for electroanalysis studies which are underway. Furthermore, we were able to estimate the mean cluster size by means of the dispersion curve, i.e. the number of surface to volume atoms in the cluster. This way of size estimation is interesting, because there is no need to use electron microscopy techniques.

Furthermore we have investigated the morphology of Au clusters grown in these multi-layer deep HOPG nanopits. The actual cluster size after deposition is comprised between 4 and $6nm$. At intermediate coverage these clusters arrange to form beads with a constant density and a very narrow size distribution. The spacing between these beads varies between 3.9 and $5.6nm$ depending on the gold load. The height is essentially independent on the pit depth i.e. the number of fixing dangling bonds. The Au clusters are stable against thermal annealing

under ambient conditions up to $700K$ and do not alter significantly their mean size with increasing annealing temperature. The size distribution sharpens at higher temperatures $(750K)$ indicating a particular stability for a given size.

Gold clusters in this specific size range are catalytically active. Their presence on the rims enables the catalytical etching of carbon atoms and leads to formation of channels in the graphene layers. The channels grow in the directions of the crystallographic orientation of HOPG and their width depends of the cluster size. Not only do gold clusters enhance the etching of graphite, they are able to dissociate water, known as the water-gas shift reaction. This is the first time that the catalytic etching of graphite has been related to the chemical reaction products. Comparable measurements have been performed for other catalytic active metals such as nickel [170, 171] or platinum [162] but not for gold.

Chapter 6

Results: Platinum on YSZ

Contents

Platinum films deposited on YSZ is a well known system for catalytic reactions, as mentioned before in Section 3.3.2. We use the same system to investigate the oxidation of carbon monoxide as one of the numerous reactions that take place on this surface. It has been studied by different groups [231, 232, 234–236, 285] and the characterizations of the reaction are well known.

Our motivation to do measurements on Pt/YSZ was to study the performance of the gas analysis system. The old setup has been used for the catalysis measurements on Au/TiO_2 (see Section 7.5.1), but the obtained results were somehow doubtful and the decision was taken to test the performance of the sniffer with a well known system. Hence, platinum on YSZ was predestinated to be studied.

Section 6.1 shows thermal desorption spectra (TDS) of O_2 and CO adsorbed on Pt/YSZ. Heterogeneous catalysis, i.e. the catalytic CO oxidation, has also been studied and the results are presented in Section 6.2. The results obtained with the old sniffer setup confirmed the results of Pt/YSZ in literature. However, the performance, especially the sensitivity for gas

detection was not satisfying and we took the decision to completely modify the sniffer system.

It was almost at the end of this thesis that the new sniffer setup was operational. We compare the results of the two sniffer systems in Section 6.3. The same system (catalytic CO oxidation on Pt/YSZ) is investigated. In addition to the improvement of the gas analysis system we also modified the sample holder in order to get a more precise temperature measurement of the sample. Thus, the reader has to be aware that the temperatures for measurements with the new system can differ from the ones measured with the old one.

6.1 TDS of O_2 and CO adsorption on Pt/YSZ

Measurement procedure: The sample preparation has been described in Section 3.3.2. Thermal desorption measurements on Pt/YSZ samples have been performed in order to reproduce the results of Vayenas and Craig, presented in Figure 3.16. The sample is cleaned from residual gas particles on the surface by annealing at $825K$ for 5 minutes. Isotopically labelled carbon monoxide ^{13}CO is supplied to the sample during the cooling of the sample ($600K - 120K$) at a pressure of $1 \cdot 10^{-6}mbar$ during 20 minutes, corresponding to $0.9kL$. The sample temperature is kept at $120K$ until the pressure in the chamber reaches a value low enough for precise measurement ($p < 1 \cdot 10^{-9}mbar$). The temperature is increased with a constant rate of $0.2\frac{K}{s}$ and O_2, CO and CO_2 signals are recorded in the QMS. The same procedure is applied for oxygen adsorption (exposure to $^{18}O_2$ from $600K$ to $120K$ during 30 minutes at $p = 1 \cdot 10^{-6}mbar$ corresponding to $1.4kL$).

(a) CO desorption spectrum

(b) O_2 desorption spectrum
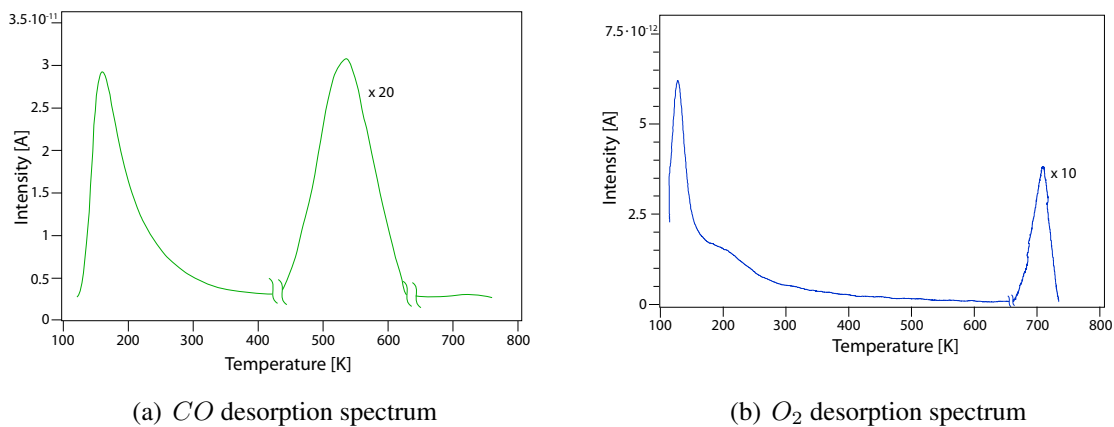
Figure 6.1: TDS spectra for ^{13}CO (a) and $^{18}O_2$ (b) respectively after dosing of $1kL$ at $T = 600K - 120K$ during the cooling of the sample. Heating rate during TDS measurements: $0.2\frac{K}{s}$. The big feature visible in both spectra at low temperature $T < 200K$ corresponds to desorption from the manipulator and is of no physical relevance for the experiment. The desorption peak of ^{13}CO (a) is located at $535K$, the peak of oxygen $^{18}O_2$ (b) at $705K$.

CO_2 is produced at high temperatures when both gases, oxygen and carbon monoxide, are present on the surface (see Section 6.2). In the present experiment, no traces of CO_2 are observed in the spectrum for both oxygen and carbon monoxide exposures. This is the expected result, as we only adsorb one of the two necessary species on the surface. Furthermore we do not detect signals for the relative missing gas (^{13}CO for $^{18}O_2$ measurements and vice versa).

Figure 6.1(a) shows the TDS spectra of adsorbed ^{13}CO on Pt/YSZ. Two mass spectrometers record the desorption evolution in the Sniffer (see Fig. 4.7) and in the vacuum chamber next to the manipulator. The spectrum in the chamber serves as reference spectrum in order to identify the background signal and is not shown here. The low temperature peak at $T = 160K$ corresponds to the desorption of carbon monoxide from the manipulator made out of molybdenum and other cold surfaces. Note that the background signal recorded in the chamber for this peak is a factor of two higher than the signal in the sniffer. This is a strong indication that this peak has its origins in cold surfaces present in the chamber. At $T = 535K$, we observe a peak that does not appear in the background spectrum. It can be associated with the desorption temperature of ^{13}CO on Pt/YSZ. The origin of this peak in Fig. 6.1(a) can clearly be identified. It has the same origin as the CO desorption from steps on $Pt(111)$ [244] and Pt/TiO_2 [286]. This result confirms that a structured Pt surface presents stronger binding properties for CO than clean (unstructured) single-crystal surfaces (i.e. terraces on $Pt(111)$).

The desorption peak of oxygen (Fig. 6.1(b)) corresponds to the reported values in literature [239, 240]. We observe a peak at $705 \pm 15K$. This value is in good agreement with Vayenas' measurements.

6.2 Catalysis measurements on Pt/YSZ

We studied the catalytic oxidation of carbon monoxide on a platinum coated YSZ surface. Different experimental procedures have been used and the results are presented in this Section.

Oxygen $^{16}O_2$ is introduced into the chamber with a local pressure of $1 \cdot 10^{-7}mbar$. The sample is slowly heated with a typical heating rate of $1\frac{K}{s}$ starting at $T = 200K$. During the heating process, ^{13}CO is pulsed onto the sample and the different products are recorded with the mass spectrometer. Of special interest is the signal of $^{13}C^{16}O_2$, displayed in Figure 6.2. The catalytic reaction follows a Langmuir-Hinshelwood mechanism, explained in Section 2.2.2. Oxygen as well as CO has to adsorb on the surface to enable the catalytic process. Furthermore, oxygen dissociates after adsorption on the surface. Below $350K$, no CO_2 signal and thus no catalysis can be detected. This is due to the CO saturation of the Pt surface
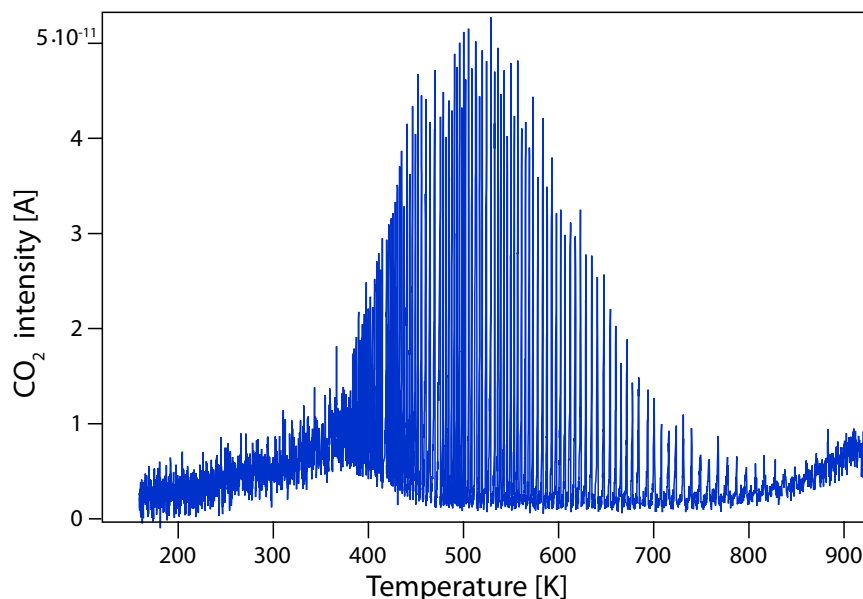
Figure 6.2: Intensity of CO_2 production as a function of temperature. A constant pressure of $^{16}O_2$ is introduced into the chamber during heating of the sample ($1\frac{K}{s}$). ^{13}CO is pulsed on the surface with a frequency of $0.2Hz$ during the heating process.

at low temperatures. Therefore no adsorption and dissociation of O_2 can take place. This phenomenon is known as CO poisoning of the catalyst [287, 288]. Above $400K$, the catalytic reaction starts. When the surface reaches a temperature at which CO starts to desorb, the empty sites can be occupied by oxygen molecules. The catalytic process is now possible and with increasing temperature, more and more CO desorbs from the surface. The maximum in CO_2 production is reached at $520K$, the same temperature as the peak of CO desorption on Figure 6.1(a). For each arriving pulse, there is a maximum number of sites available; hence the highest conversion rate to CO_2. Above $520K$, the catalysis decreases rapidly. The CO molecules do not adsorb any more on the surface because the temperature is too high.

The same behaviour can be observed in another experiment, shown in Fig. 6.3. ^{13}CO and $^{18}O_2$ gas is simultaneously pulsed onto the surface with identical intensities during annealing. The oxygen pulses are not displayed on the plot as they do not show any interesting features. The black curve shows the CO pulses as a function of temperature, the red curve the CO_2 signal. Below $400K$ the surface is completely covered with CO molecules (CO poisoning). At temperatures close to the CO desorption temperature, the lifetime of adsorbed CO molecules on the surface becomes comparable to the time delay between pulses. The increase of the background signal of CO between $400K$ and $620K$ is due to the desorption of CO from the
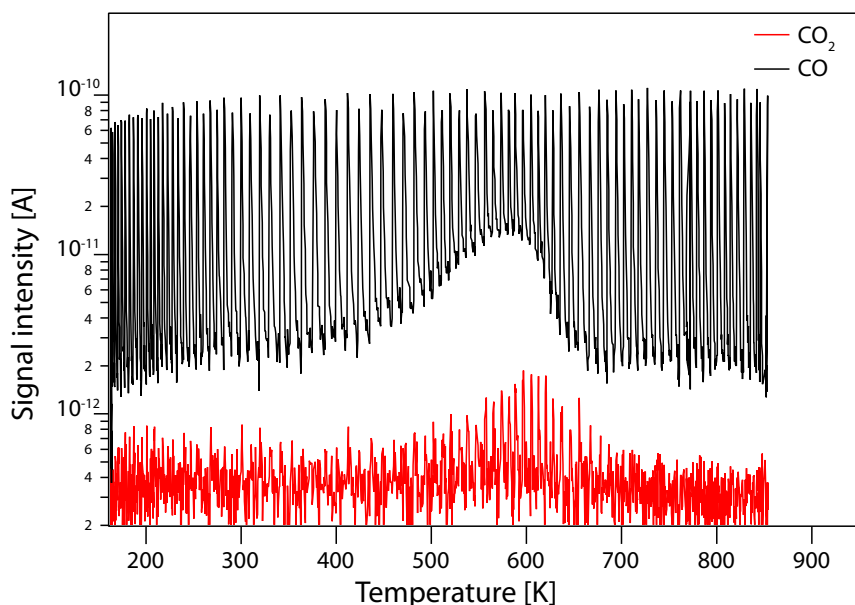
Figure 6.3: Signal intensities of CO and CO_2 as a function of temperature. $^{18}O_2$ and ^{13}CO are pulsed simultaneously onto the sample with a frequency of $0.2Hz$ during the heating phase ($1\frac{K}{s}$). The $^{18}O_2$ pulses do not show any special feature and are thus not presented on the graph.

surface. This desorption temperature matches the TDS spectrum, shown in Figure 6.1(a).

The production of CO_2 starts at $500K$. The desorption of CO makes it possible for O_2 molecules to adsorb and dissociate. The peak maximum of CO_2 production is reached at $600K$. Above this temperature, only dissociated oxygen remains adsorbed on the surface and therefore the CO_2 production decreases. CO cannot adsorb any more and the reaction stops. The presented results show that we are able to see the dynamics of the catalytic CO oxidation on Pt/YSZ.

6.3   Heterogeneous catalysis on Pt/YSZ

The insets in Fig. 6.4 show the CO_2 ($^{13}C^{16}O^{18}O$ blue) signal obtained on Pt/YSZ when isotopic ^{13}CO (red) and $^{18}O_2$ (black) reactants are pulsed alternatingly with a delay of 5 seconds between the pulses. With the heating rate of $0.1\frac{K}{s}$ one period of dose pulsed corresponds to a temperature increase of $1K$. The CO_2 signal, synchronized with the CO and O_2 pulses, has been integrated at each peak. Fig. 6.4 shows the CO_2 production as a function of temperature. Both curves have been smoothed in order to compensate the aliasing effect due to the limited QMS time resolution. Two temperature regimes of CO_2 production are seen in Fig.
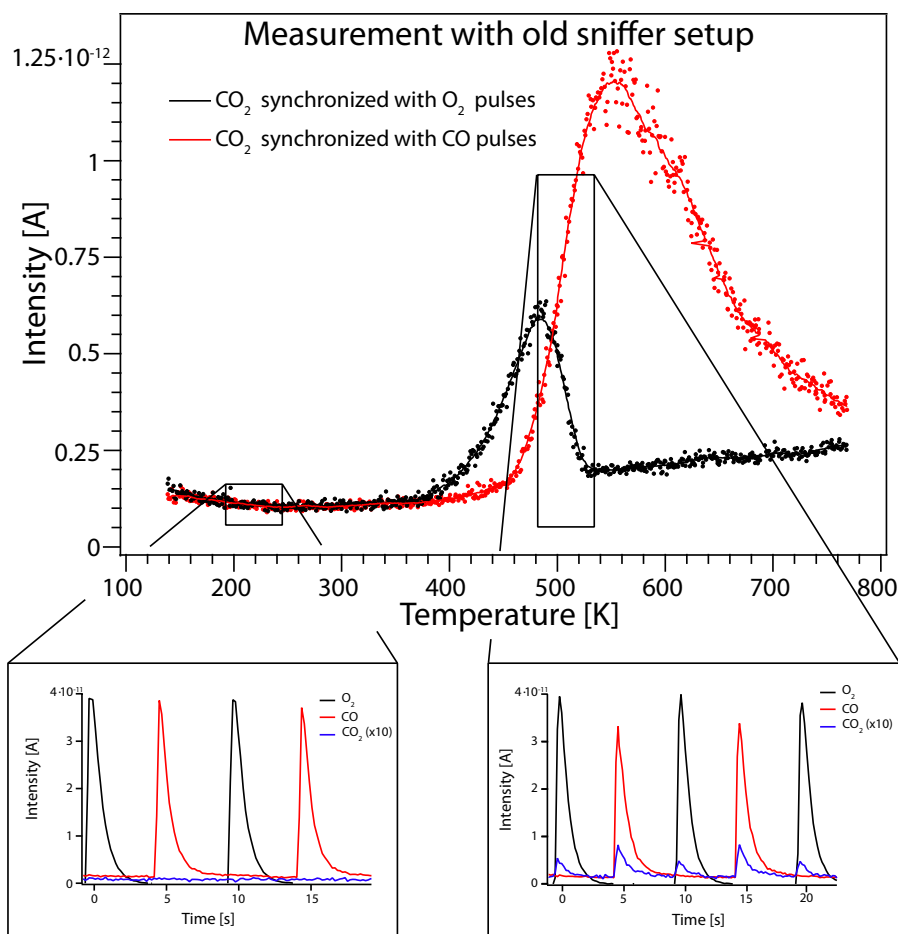
Figure 6.4: CO_2 production vs. temperature. Each dot corresponds to the integration over a pulse. The measured CO_2 peaks are synchronized with oxygen (black) and CO pulses (red). Maxima are located at $450 \pm 30K$ (black) and at $530 \pm 20K$ (red). The insets below show details of the gas pulses.

6.4. Between 400 and $500K$, the CO_2 production is mainly synchronized with the O_2 pulses, while above $500K$, the CO_2 production is mainly synchronized with the CO pulses.

At temperatures below $500K$, we observe the same behaviour as it has been mentioned above (Section 6.2): the adsorbed CO poisons the surface and oxygen cannot adsorb and dissociate. Thus, the low temperature regime is characterized by a CO rich surface. Above $500K$ the CO_2 production synchronized with the CO pulses takes over. This shows that the surface becomes oxygen rich and from $560K$ on, where the maximum CO_2 production is observed only dissociated oxygen remains adsorbed on the surface, and therefore the CO_2 production is synchronized with the CO pulses.

6.4   Performance tests with the new sniffer system

In order to compare the sensitivity of the two sniffer systems, the conversion ratio $\frac{CO_2}{CO}$ has been calculated. The measurements obtained with the new sniffer setup are shown in Figure 6.5. Note that the displayed temperatures do not match with the preceding results and the interpretation of the results. Here, we only focus on the peak intensities, shown in the insets of Figures 6.4 and 6.5.
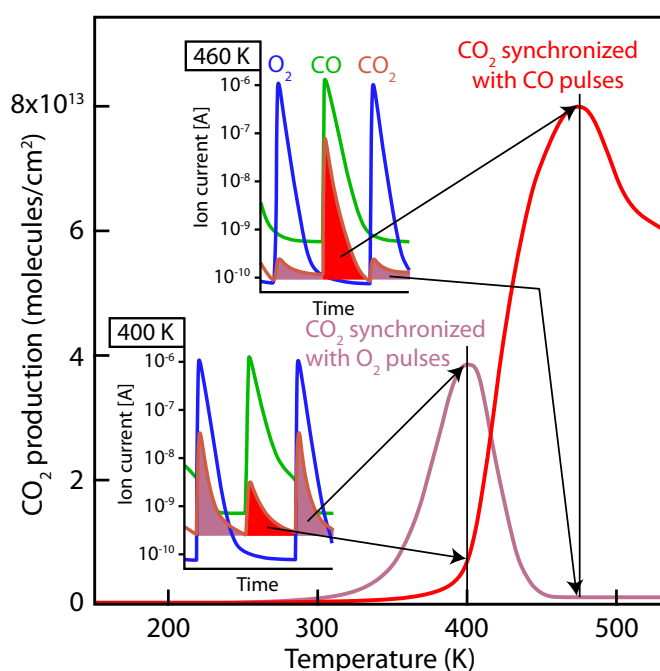
Figure 6.5: CO_2 production versus temperature on Pt/YSZ. The heating rate is $0.1\frac{K}{s}$. As shown in the insets around two different temperatures, isotopic ^{13}CO (green) and $^{18}O_2$ (blue) gases have been pulses alternatively, with a delay of 5 seconds in-between, and CO_2 ($^{13}C^{16}O^{18}O$, orange) has been measured. The CO_2 production, integrals of the CO_2 peaks, is reported versus temperature in pink if the CO_2 peaks are synchronized with O_2 pulses and in red if the CO_2 peaks are synchronized with CO pulses.

The measured ion currents for the CO_2 peaks (red colours in Figure 6.5) reach $10^{-7}A$, corresponding to 5% of the intensity for the CO and O_2 pulses. Measurements with the old sniffer system gave a conversion ratio of 3% for a maximum intensity of $\approx 10^{-11}A$ (see insets in Figure 6.4). The two ratios of 5% and 3% respectively are comparable, the big difference and thus the improvement of the system is based on the measured current intensity. This means that much smaller gas quantities can be detected and that the sensitivity is strongly enhanced.

6.5 Conclusion: Platinum on YSZ

The mean purpose of the measurements presented in this Chapter was to obtain information about the sensitivity of the two sniffer systems. This goal has been achieved and the results obtained with the new setup are very promising. We have shown that the sensitivity of the system has been enhanced by several magnitudes and that we are thus able to detect much lower gas quantities [286].

In addition to the performance confirmation of the sniffer, the presented results are coherent with the literature and show even interesting new properties of Pt/YSZ, such as the desorption spectrum of CO or the catalysis measurement where the produced CO_2 peak can clearly be attributed either to oxygen or the CO pulses. These promising results will be continued, especially the influence of a potential applied to the platinum particles and the increase in catalytic activity [289, 290].

Chapter 7

Results: Gold on TiO_2

Contents

In this Chapter, we present the results obtained for gold clusters deposited on TiO_2 . The experimental methods are mentioned in Section 7.1. Different surface reconstructions have been investigated and the results are presented individually. Section 7.2 shows the thermal stability, cluster size evolution and the migration of clusters to steps for the $TiO_2(110)-(1\times2)$

surface, Section 7.3 the results on the $TiO_2(110) - (1 \times 1)$ reconstruction. These results are compared in Section 7.4. In the last part (7.5) of this Chapter the catalytic activity of Au clusters on TiO_2 is presented.

7.1 Experimental methods

The experiments are conducted in an ultrahigh vacuum chamber, described in Section 4.1. The TiO_2 single crystals are cleaned by sputtering cycles, followed by annealing at $1000K$ and $950K$ for the $TiO_2(110) - (1 \times 2)$ and $TiO_2(110) - (1 \times 1)$ surface reconstruction respectively. The surface quality is systematically checked by means of STM measurements to make sure that the desired surface reconstruction has been obtained.

The cluster source, based on sputtering of the metal target, has been described in Section 4.1.3. The ionized gold particles from the target are accelerated towards the surface by an electrostatic potential difference between target and TiO_2 sample. This potential defines the deposition energy of the cluster ($E_{dep} = 7.1\frac{eV}{\text{atom}}$). The deposited gold quantity is measured periodically by replacing the sample with a Faraday cup, taking into account the beam profile for the determination of the current. Typical cluster fluxes are of the order of $0.06\frac{ML}{h}$ where one monolayer (ML) is defined as the packing density of a $Au(111)$ plane, corresponding to $1.39 \cdot 10^{15}\frac{\text{atoms}}{cm^2}$. The quantity of deposited gold varies between 0.005 and $0.04ML$, depending on the sample. During deposition, the sample is kept at room temperature. The residual gas during the deposition process consists mainly of the ionized rare gas (Xe) and hydrogen (H_2).

After each cluster deposition process and between the annealing cycles, the sample is transferred into the STM vacuum chamber to perform *in situ* measurements of the surface morphology. In the STM image, the gold particles can clearly be identified as protrusions (see Figure 7.1). The apparent height, diameter and anchoring position (substrate step or terrace) for each Au particle are determined by an automated and thoroughly tested analysis procedure using the image recognition procedure of the used STM image analysis softwares (SPIP from Image Metrology and the open-source program WSxM [291]). Almost no gold particles are smaller than 1 Å in height which indicates that we have only few cluster fragmentation. Hence, only particles with an apparent height of more than 1 Å above the surface terrace are considered for the statistics. By doing so, we avoid counting also surface defects such as oxygen vacancy sites (they appear as well as protrusions) but do not miss any gold particles in the statistics.

7.2 Thermal stability of size-selected Au_n^+ clusters on $TiO_2(110) - (1 \times 2)$

STM observation of the clean surface, shown in Fig. 7.1(a) displays a typical (1×2) surface reconstruction of a $TiO_2(110)$ single crystal. As described in Section 3.2.3, the (1×2) reconstruction appears in STM as series of bright stripes. We can also see on all four images in Fig. 7.1 that the crystal is strongly reduced and shows a large number of oxygen vacancy sites.
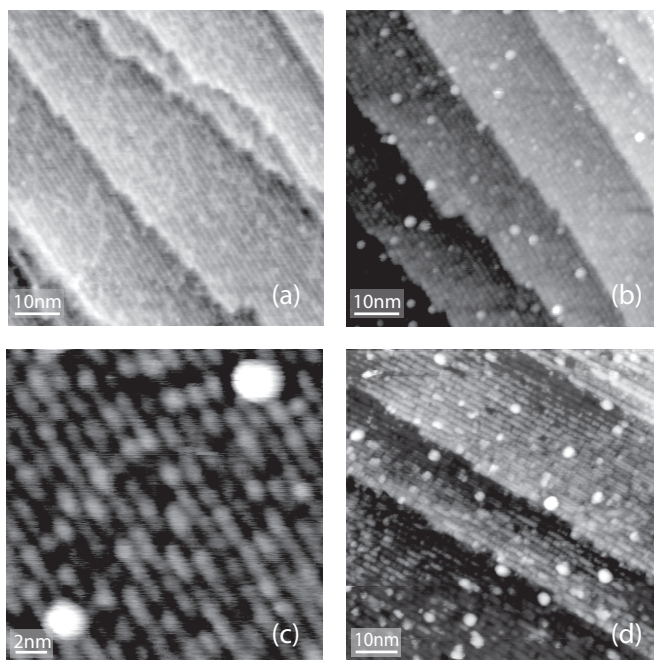
Figure 7.1: STM images of (a) a clean $TiO_2(110) - (1 \times 2)$ surface. (b) The same surface after deposition at $300K$ of $0.03ML$ Au_7^+ at $E_d = 7.1\frac{eV}{atom}$. Image size: $70nm \times 70nm$. (c) Detail of (b) showing both surface reconstruction and Au_7^+ clusters. (d) Same surface after annealing at $600K$. $V_{gap} = 1.2\,V$, $I_T = 150\,pA$. $T = 300K$

Au_n^+ clusters are deposited on a well-prepared and clean surface (Fig. 7.1a) at the mentioned energy. Two cluster sizes ($n = 5$ and $n = 7$) have been measured. For each cluster size an annealing cycle is followed by STM measurements. This procedure is repeated for different annealing temperatures between $300K$ and $800K$. The results obtained for the two cluster sizes are similar and we concentrate for the first part of results on Au_7^+ clusters. Quan-

titative differences will be discussed afterwards. The STM image in Fig. 7.1(b) shows that the distribution of the clusters on the surface is homogeneous and that gold clusters did not migrate to steps. The coverage observed by STM is in very good agreement with the calculated deposition quantity. We obtained a cluster density of $0.025\frac{\text{clusters}}{nm^2}$, a value which corresponds precisely to the density of clusters deposited from the gas phase, which indicates that the clusters preserve their size during and after deposition i.e. the mean number n of atoms per deposited clusters is not altered. This is an important result because it shows that there is no or only very little fragmentation of the clusters during impact and sintering can be neglected at room temperature. We mentioned in Section 2.1.5 the instability of clusters on vacancy-poor surfaces. Hence we can expect that the presence of such vacancies serves as pinning sites for clusters. The density of oxygen vacancies on the $TiO_2(110) - (1 \times 2)$ surface is very high. Figure 7.1(c) is a detailed view of Fig. 7.1(b) and one can suppose that the clusters are in contact with these vacancies.
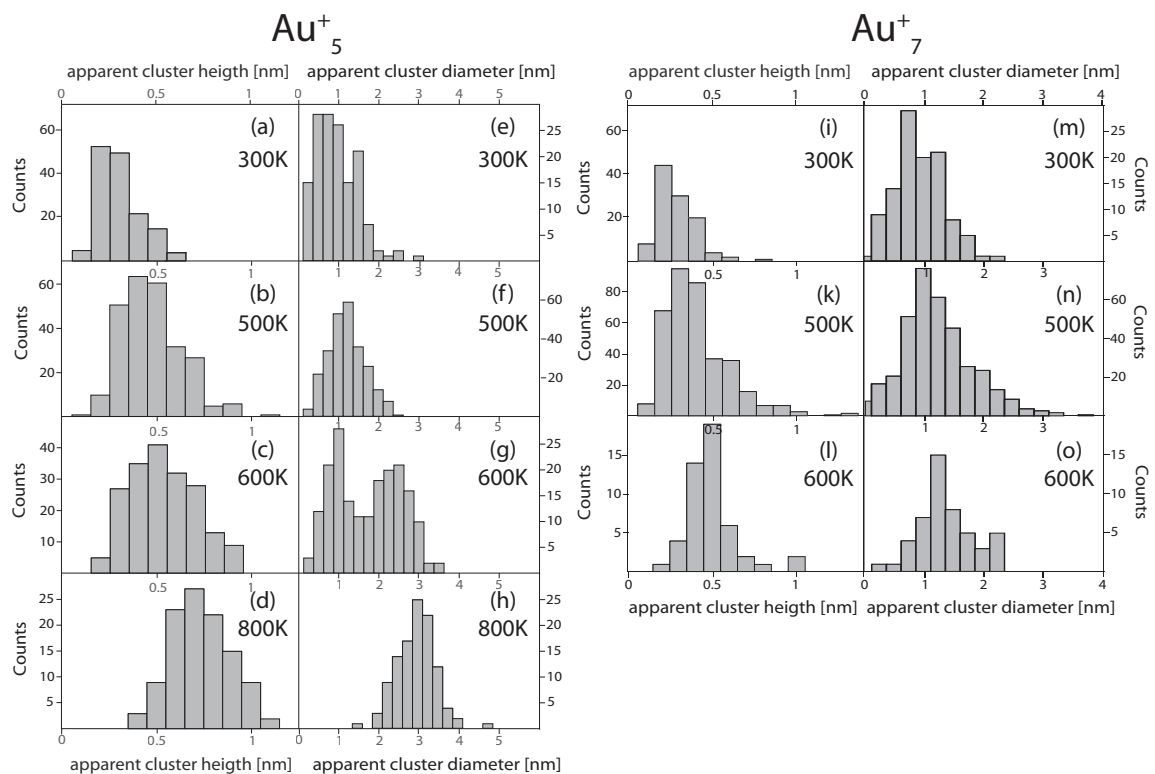
Figure 7.2: Histograms of heights and diameters as measured by means of STM on a $TiO_2(110) - (1 \times 2)$ surface covered with $0.03ML$ of Au_5^+ (left) and Au_7^+ (right) clusters. The sample is annealed at the indicated temperature and cooled down to room temperature for STM measurements.

One should keep in mind that, in scanning tunnelling microscopy, height and diameter are influenced by electronic and tip effects, as discussed in Section 4.3.4. We therefore corrected all STM images for surface convolution. The convolution of the tip has been estimated by the difference of the measured cluster diameter and the theoretical value by Gilb *et. al.* [7]. For Au_5^+, the measured diameter is of $1.89nm$, the theoretical value $0.86nm$ that gives a convolution of $1.03nm$. This value has been subtracted from all measurements for Au_5^+. The convolution for Au_7^+ is $1.51nm$, estimated in a similar way. As different STM tips has been used for Au_5^+ and Au_7^+, the convolution shows different values.

7.2.1   Cluster size evolution

The first point to discuss is the height evolution of the clusters. The results in the literature have been presented in Section 2.1.5. The distribution of apparent height and cluster diameter for Au_5^+ and Au_7^+ deposition at $300K$ is shown in Fig. 7.2(a), (e), (i) and (m). We estimate a mean value for the apparent height of $0.28nm$ and $0.3nm$ for Au_5^+ and Au_7^+ clusters respectively.
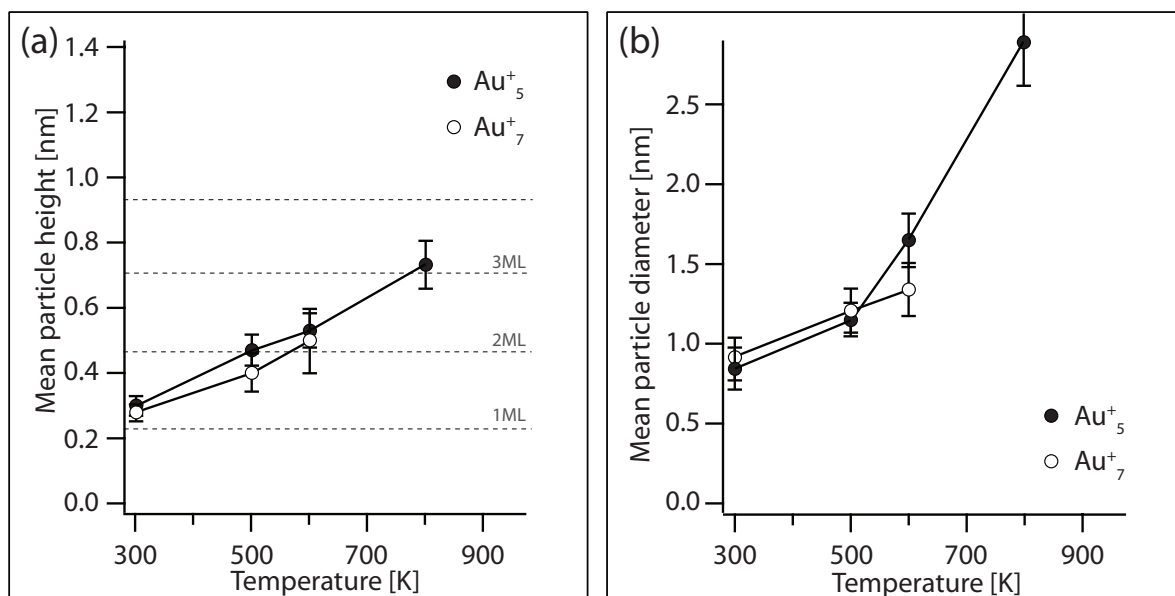
Figure 7.3: Apparent heights (a) and apparent diameters (b) of Au clusters as a function of annealing temperature for both Au_5^+ (●) and Au_7^+ (○) deposition.

The stability of the clusters can be probed by increasing the surface temperature. STM investigations have been conducted for different annealing temperatures up to $800K$. From
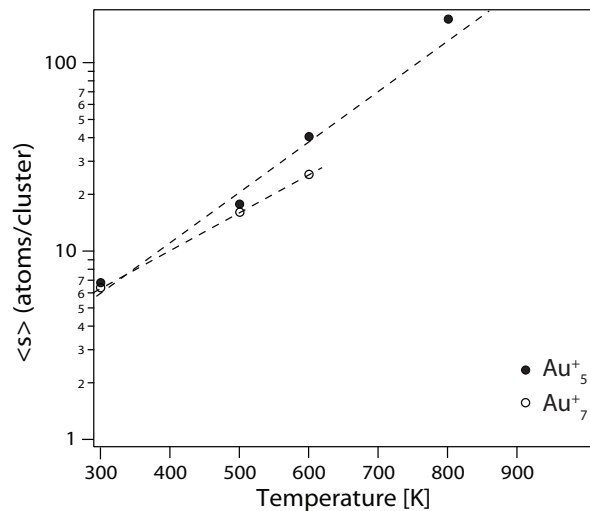
Figure 7.4: Mean size $<s>$ (number of atoms per cluster) plotted as a function of annealing temperature for both Au_5^+ (●) and Au_7^+ (○) deposition.

Fig. 7.1(d) it becomes evident that the average size of the clusters increases upon annealing. This is quantitatively represented in Fig. 7.2(b-o). Between $300K$ and $500K$ growth starts to be three-dimensional and the planar clusters are no longer observed for annealing above $500K$. In addition, the width of the height distribution becomes slightly larger. We identify the growth with the described Volmer-Weber type growth (see Section 2.1.3). The evolution of the average height and diameter of the clusters for both Au_5^+ and Au_7^+ as a function of annealing temperature is summarized in Fig. 7.3. We observe a linear increase in height for both deposited cluster sizes Au_5^+ and Au_7^+. The startings points at $0.3nm$ and $0.28nm$ respectively are in good agreement with the results in the literature, mentioned before. At temperatures of $500K$ to $600K$ the mean height is around $2ML$ and the cluster hence grows in three dimensions. Finally, at very high annealing temperatures ($800K$), we observe cluster heights of 3 to $4ML$. We conclude that both Au clusters have a similar behaviour, characterized by a monotonous tendency to grow three-dimensionally. By lack of measurements, no results of Au_7^+ annealed at $800K$ are shown.

The evolution of the cluster diameter is illustrated in Fig. 7.3(b). Again, both samples show similar, monotonous, evolution. The particle shape on each of the sample follows the relation given by Mitchell and co-workers [81]. Particle height (h) and diameter (d) are effectively related by the expression $h(d) = \alpha(d - d_0)$ with $\alpha = 0.65$ and $d_0 = 0.91nm$. Theoretical values are $\alpha = 0.48$ and $d_0 = 1.67nm$.

To further elucidate the growth process of the clusters during annealing, we plot the mean

number of atoms per cluster $<s>$ as a function of annealing temperature. The result is shown in Fig. 7.4. The mean size exhibits an exponential evolution for both Au_5^+ and Au_7^+ deposition. This is characteristic for Ostwald ripening (Section 2.1.2). The prediction for Ostwald ripening, namely the narrow size distribution (see histograms in Figure 7.2), is coherent with our measurements. The full width at half maximum (FWHM) has been computed for both cluster sizes, based on the histograms in Fig. 7.2. The FWHM at different annealing temperatures remains constant for both cluster sizes ($\approx 1nm$). This indicates a simultaneous growth of particles and supports the assumption of Ostwald ripening.
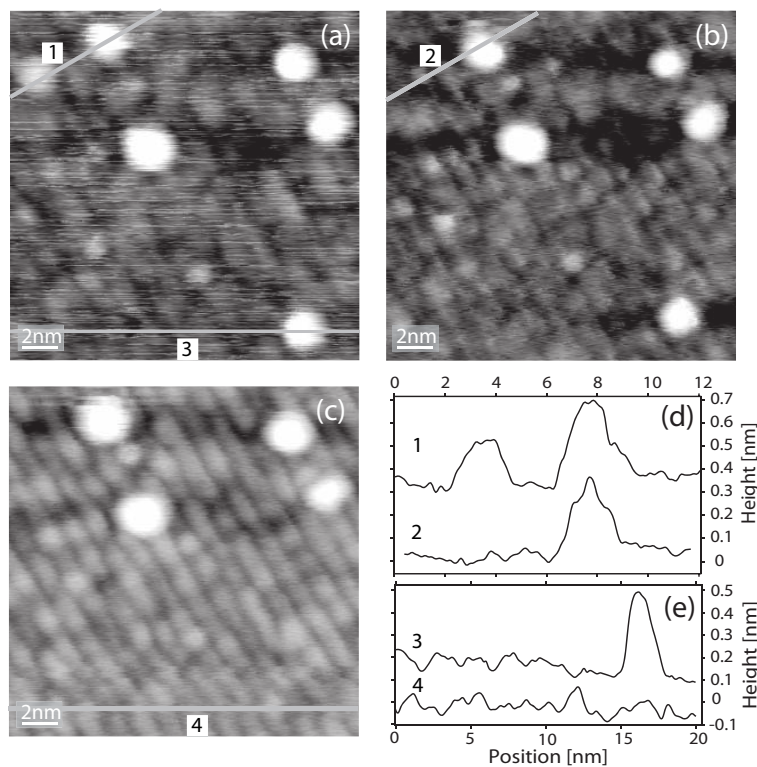
Figure 7.5: Three successive STM images of the same surface area of $Au_7^+/TiO_2(110) - (2 \times 1)$ deposited at $T = 300K$. The cluster on the upper left corner disappeared during imaging between Fig.(a) and (b), and the one on the lower right corner between (b) and (c) respectively. Fig. (d) and (e) show line profiles as labelled. $V_{gap} = 1.25\,V$, $I_T = 150\,pA$, $T = 300K$. Image sizes: $20nm \times 20nm$.

7.2.2   Step migration and cluster removal

Information on the stability of the clusters can be extracted from their tendency to migrate to steps. The fraction P_{step} of particles at step edges versus the total number of particles is in the range of 20% for both cluster sizes. This value depends on the step density of the substrate. More important, no significant evolution of this fraction as a function of annealing

temperature can be noticed. Single atoms quit the gold particles and migrate individually on the surface until they find a new particle to adhere. The big concentration of surface defects on the $TiO_2(110) - (1 \times 2)$ reconstructed surface could be an explication; they increase on one side the binding energy between cluster and surface and on the other side, they significantly increase the surface rugosity. As the mean free path of atoms is strongly reduced, weaker bound particles on terraces still move but are fixed on surface defects before they reach a step. This is an explanation for the constant step fraction on one and the sharp size distribution at high temperatures on the other side for both Au_5^+ and Au_7^+ clusters.

A closer look at the pinning mechanism is possible by performing local tests with the STM tip on a single cluster. This method consists in performing STM images of the clusters at different tunnelling currents and determining the condition in which a cluster can be removed by the tip. Fig. 7.5 shows three successive STM images of a $TiO_2(110) - (1 \times 2)$ surface after a deposition of Au_7^+ at $300K$. The bias voltage and tunnelling current are respectively $U = 1.25V$ and $I_T = 150pA$. The two clusters located in the top left and bottom right corner disappeared during imaging between Fig. 7.5(a) and 7.5(b), and between Fig. 7.5(b) and 7.5(c) respectively. Fig. 7.5(d) and (e) show the different line profiles indicated on each figure by a grey line. Under these tunnelling conditions, white dots on the TiO_2 lines can be identified as oxygen vacancies or more probably oxygen vacancies filled with OH groups [79, 292] due to a residual gas pressure ($P \cong 10^{-10}mbar$) not low enough to prevent water adsorption and subsequent dissociation. Looking at the cluster site, neither specific traces of the removed cluster nor irregularities of the surface underneath can be detected. Note that oxygen vacancies or OH groups appear everywhere on the surface and are not related to cluster presence. The absence of surface defects under the removed cluster suggests that this cluster was rather stabilized by its size. This model is coherent with our observation that only particles that are not stabilized on surface defects can be removed with the STM tip whereas clusters stabilized on defects with a similar size do not react to the tip.

7.3   Thermal stability of size-selected Au_7^+ clusters on $TiO_2(110) - (1 \times 1)$

7.3.1   General remarks

Gold clusters are deposited on a $TiO_2(110) - (1 \times 1)$ surface reconstruction. STM control scans are made before deposition and after each annealing cycle. These control images are also used for cluster statistics of height, diameter, abundance and surface positioning. Three samples are prepared and analyzed with the same deposition parameters as the gold clusters on $TiO_2(110) - (1 \times 2)$ (7.1$\frac{eV}{\text{atom}}$, deposition temperature $T = 300K$, $3\% ML$ surface coverage). The results of all three samples are comparable and show the same growth mechanism.

On one of our samples, catalysis measurements are performed between each annealing cycle. Isotopically labelled carbon monoxide ^{13}CO and oxygen $^{18}O_2$ are pulsed on the surface at temperatures below the annealing temperature. Gas pressures do not exceed $p < 5 \cdot 10^{-5} mbar$. However, the evolution of this sample is identical to the UHV annealed samples without catalysis measurements and no influence of the gas to the cluster growth can be detected. Goodman *et. al.* have shown that for exposure to high gas pressures in the order of $p = 0.1 mbar$, the cluster growth is influenced [293]. They observed much bigger clusters at elevated pressures than for annealing in UHV. Our results are not surprising when we take into account the big difference in gas pressure between Goodman and the present study. Hence we use these measurements also for the statistics of the cluster size evolution for different annealing temperatures. All statistics refer to this specific sample, if not mentioned differently. The drawback of the catalysis measurements between the annealing cycles is that gas adsorbs on the surface at intermediate temperatures. We observe, for annealing temperatures between $500K$ and $815K$, a gas layer that partially masks the surface. It is therefore difficult to make conclusions about, e.g. the fraction of clusters on the surface steps. This point is mentioned in the following discussion whenever it has to be taken into account.

STM images have been corrected for surface convolution in the same way as in the preceding Section. A surface-tip convolution of $d = 0.64 nm$ was determined and subtracted from the experimentally measured values.

(a)   (b)
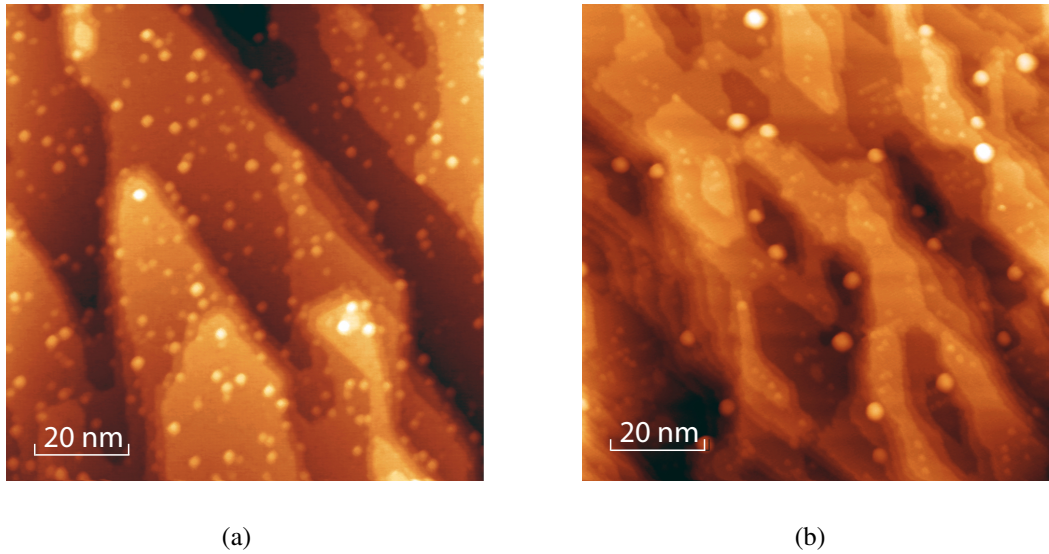
Figure 7.6: STM image of $TiO_2(110)-(1\times1)$, covered by $3\%ML$ of Au_7^+. (a) Image after deposition at $300K$. (b) After annealing of the sample at $945K$. $V_{gap} = 1.25\,V$, $I_T = 100\,pA$, $T = 300K$. Image sizes: $100nm \times 100nm$.

7.3.2   Cluster size

Figure 7.6 shows STM images of the $TiO_2(110) - (1 \times 1)$ surface after annealing at different temperatures. Fig. 7.6(a) is a survey of the surface after deposition at $300K$. The clusters are distributed homogeneously on the surface and are similar in size. The density of deposited clusters is estimated to be $3\%ML$, whereas the analysis of STM data resulted in $2.52\%ML$. The agreement between estimation and measurement is fair and comparable with the value obtained for the $TiO_2(110) - (1 \times 2)$ reconstruction[1]. It indicates that, as in the results on $TiO_2(110) - (1 \times 2)$ before, no or only very little fragmentation occurs. Fig. 7.6(b) is taken after annealing at $945K$. One can observe the reduced number of clusters and their increase in size.

The mean height of the clusters at deposition temperature is $h = 0.41nm$. The obtained value has to be regarded in the context (i.e. compared to higher temperatures. The strong tip-gold cluster interaction influences the apparent height). Figure 7.7 shows the evolution of apparent cluster height (a) and diameter (b) as a function of annealing temperature. The cluster height varies only slightly up to a temperature of $700K$. In the same range, the cluster

---

[1]One has to take into account that the measurement of deposition current is not *in situ* but only punctual during the deposition process. Fluctuation in cluster current (up to 20%) can thus not be taken into account and creates an uncertainty.
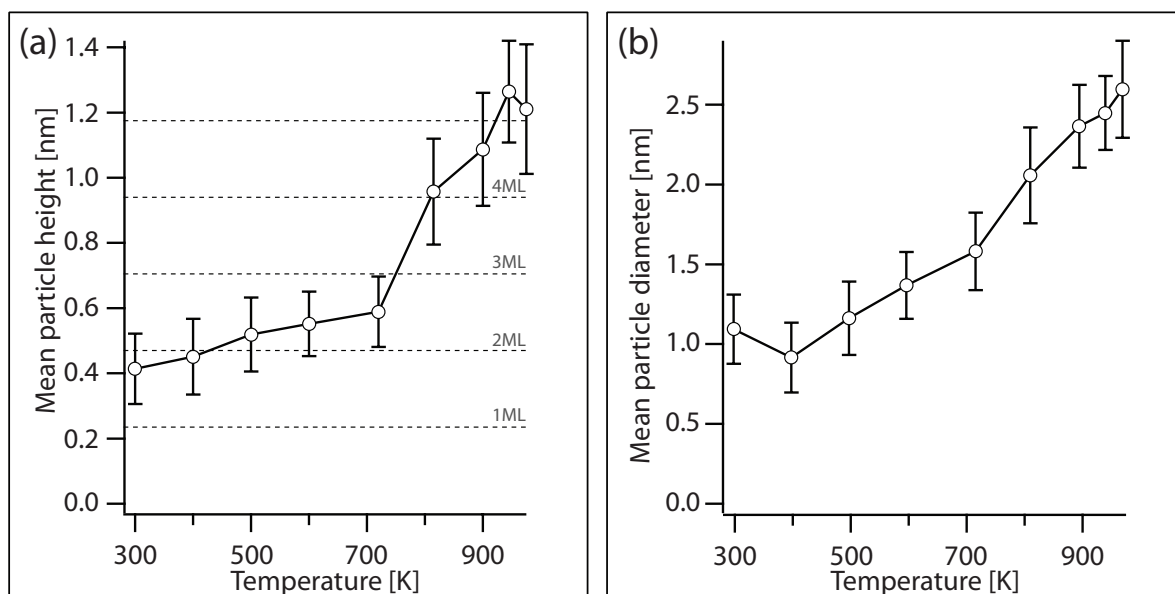
Figure 7.7: Mean particle height (a) and diameters (b) of Au_7^+ clusters as a function of annealing temperature.

diameter increases linearly. So, the cluster grows principally in two dimensions. A dramatic change in the growth mechanism occurs above $720K$. Where the cluster grew in the plane before, it now also increases its height. An obvious change from 2-d to 3-d growth can be observed. The lateral size of the clusters does not present a change in behaviour and increases linearly until $975K$, the highest annealing temperature. This behaviour was detected for several samples. The change in cluster growth between a 2-d and a 3-d growth mechanism occurs between $600K$ and $700K$ where the cluster reach a critical size. The computation of atoms per cluster, presented in Fig. 7.10, indicates that the cluster size is between 20 and 30 atoms per cluster. The cluster configuration is apparently such that it is preferable for the cluster to stack additional layers on top of the ground layer in order to minimize its total energy.

Looking at the relation between cluster height and diameter, we calculate a linear fit for the particles height vs. diameter (in $[nm]$). The obtained equation

$$h(d) = 0.48\,(d - 0.172) \tag{7.1}$$

is coherent with the Mitchell relation that says: $h(d) = 0.48\,(d - d_0)$ with $d_0 = 1.67nm$ [81]. We find a similar slope for the relation which confirms the growth mechanism (Volmer-Weber) presented in Section 2.1.3. The difference in the offset is caused by the tip convolution

and the influence of the substrate to the measured height. Different corrections have been made in this study compared to Mitchells study [81]. The clusters in the present study follow a Volmer-Weber growth mechanism where clusters grow individually in three dimensions.

7.3.3 Cluster location

As shown in the previous Figure 7.6(a) and mentioned in the text, the cluster distribution on the surface at low temperature is almost homogeneous. However, Figure 7.6(b) does not show the same distribution. A huge quantity of particles is located on step edges. The evolution of clusters pinning on step edges with increasing annealing temperature is represented in Figure 7.8. The initial percentage of clusters on steps is at 40%. This value is slightly higher than the value obtained by Convers [80], but one has to take into account the surface step density. The studied sample presents many steps, the measured step length is of the order of $\frac{200\mu m}{\mu m^2}$. The sample of Convers contained only half the step length per unit surface ($\frac{100\mu m}{\mu m^2}$). This difference is also present in the step fraction of gold clusters. Convers counted 20%, the present sample has, as mentioned, 40% of gold clusters on step edges. Similar step fractions have been found on different samples and for different annealing temperatures. At $650K$, the ratio increases to 55%. This value has to be interpreted with care. As we explained before, the sample is at this temperature covered with adsorbed gas and the steps are not clearly visible. However, the increase of the cluster proportion on steps at $900K$ to more than 90% cannot be caused by the poor image quality. Gas molecules did already desorb from the surface at these temperatures and the surface is clean again.

The surface changes the reconstruction when it is annealed at very high temperatures (above $950K$). Already below this temperature, parts of the surface change their structure. The formation of Ti_2O_3 bands on terraces can be observed. This structural change, displayed in Fig. 7.9, could have an influence to cluster mobility. We guess that the formation of $TiO_2(110) - (1 \times 2)$ structures pins the clusters to newly created steps where they stay attached. Convers did not anneal his sample to such high temperatures and thus did not observe an increase in clusters connected to steps.
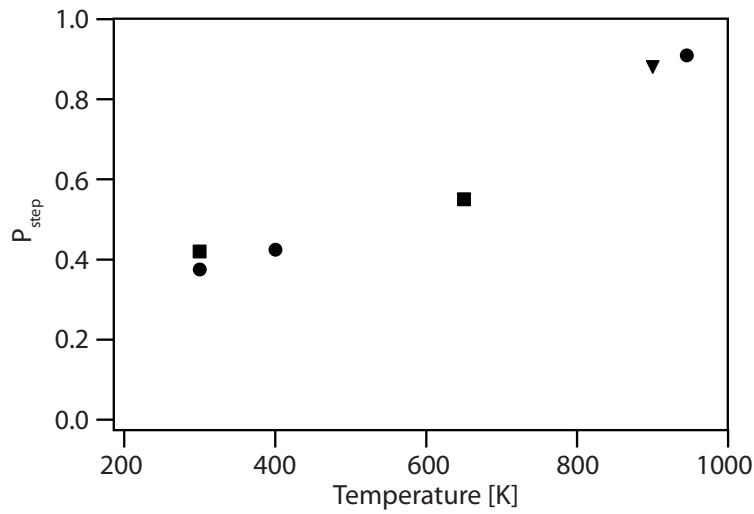
Figure 7.8: Fraction of clusters on steps for the deposition of Au_7^+. Different symbols ($\bullet$, $\blacksquare$, $\blacktriangledown$) represent different samples. Uncertainty is in the range of 4%.
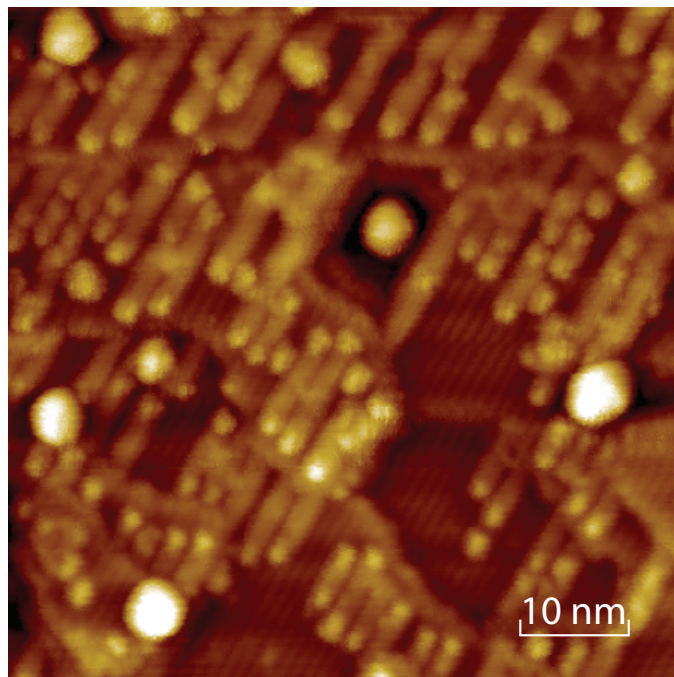
Figure 7.9: STM image of a $TiO_2(110) - (1 \times 1)$ surface shows the appearance of (1×2) surface reconstruction after annealing at $850K$. The bright stripes are Ti_2O_3 bands which initiate the $TiO_2(110) - (1 \times 2)$ reconstruction. $V_{gap} = 1.5\,V$, $I_T = 100\,pA$, $T = 82K$. Image size: $60nm \times 60nm$.
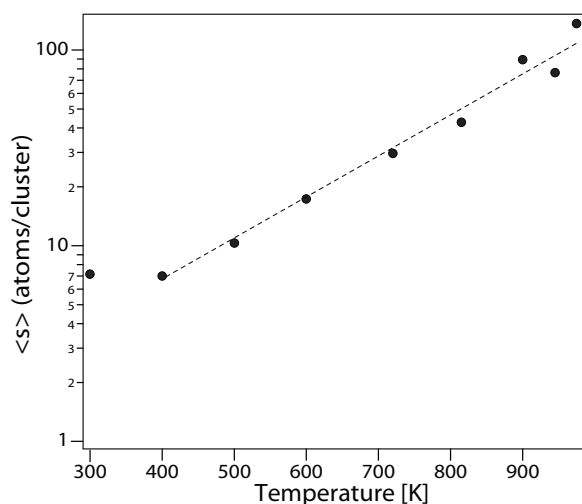
Figure 7.10: Mean size <s> (number of atoms per cluster) plotted as a function of annealing temperature for deposition of Au_7^+ clusters. Clusters do not increase in size until a temperature of $400K$. A linear fit for the cluster growth above $400K$ is shown by the dashed line.

7.3.4 Growth mechanism - Ostwald ripening

The characteristic behaviour for Ostwald ripening are observed for gold clusters on $TiO_2(110) - (1 \times 1)$ surface reconstructions. The mean particle number per cluster versus the annealing temperature is displayed in Fig. 7.10. The plot is similar to the one for gold on $TiO_2(110) - (1 \times 2)$. Until an annealing temperature of $400K$, the clusters do not increase in size. Above this temperature, the typical growth mechanism for Ostwald ripening, characterized by the exponential increase of the number of atoms per cluster as a function of annealing temperature is clearly visible.

One notices that the migration of the clusters to the steps at elevated temperatures does not influence the behaviour of the cluster growth. In a first step, simultaneously to single atom diffusion, small and weakly attached clusters migrate as a whole on the surface and attach to a step site where they find much stronger bonds. Subsequently, the normal Ostwald diffusion process, where single atoms quit the clusters and migrate on the surface, takes place. Only few clusters remain on the terraces at very high temperatures. These clusters are bound to the appearing Ti_2O_3 islands, where interstitial Ti atoms migrate to the surface and create these islands. They present strong binding sites for gold clusters, as do the steps.

7.4 Comparison of Gold deposited on $TiO_2(110) - (1 \times 1)$ and $TiO_2(110) - (1 \times 2)$

7.4.1 Size evolution

We have shown the evolution of Au_n^+ clusters on two different surface reconstructions of TiO_2 for different annealing temperatures in the preceding Sections. The deposited quantity of Au_5^+ and Au_7^+ clusters respectively has been identical. The estimated and experimentally measured deposition quantities are in excellent agreement for both surfaces. There is only very little fragmentation of clusters during the impact process and a narrow size distribution is observed for both samples. Cluster growth follows the Ostwald ripening mechanism for both surfaces. This has also been observed in previous studies by Convers *et. al.* [80]. The cluster growth seems thus to be independent of surface reconstruction.

The mean particle diameter for both (1×1) and (1×2) surface reconstructions show similar evolution. The graphics from Fig. 7.3 and 7.7 are summarized in Fig. 7.11.
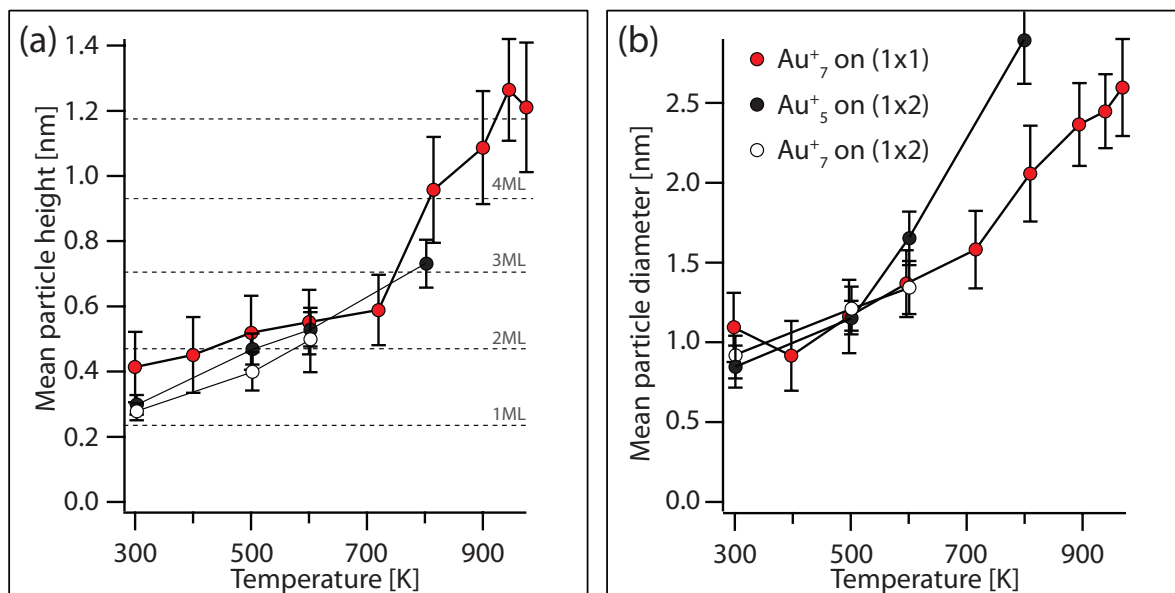
Figure 7.11: Summary of Figures 7.3 and 7.7. The cluster evolution on both surface reconstructions is similar.

Due to the lack of experimental values at very high temperature for the $TiO_2(110)-(1\times2)$ sample, no bending in the cluster height evolution is visible for this sample. However, we ob-
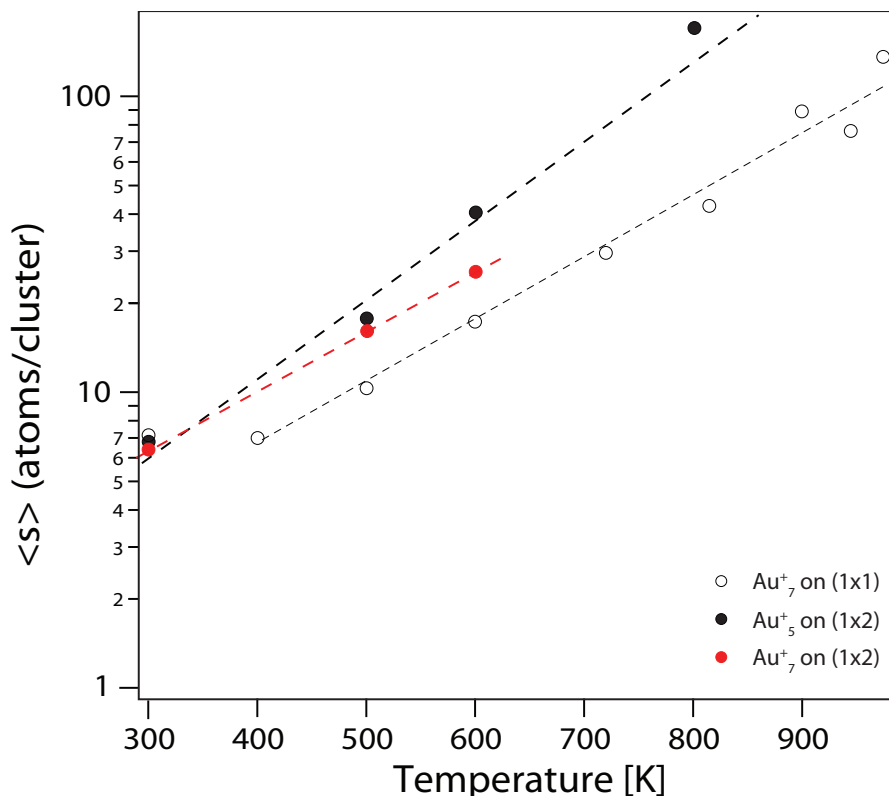
Figure 7.12: Mean size <s> plotted as a function of annealing temperature for $TiO_2(110) - (1 \times 1)$ and $TiO_2(110) - (1 \times 2)$ surface reconstruction.

serve the mentioned behaviour on the $TiO_2(110) - (1 \times 1)$ between $600K$ and $750K$. The growth mode changes from 2-d to 3-d structures, supported by theoretical predictions that small gold clusters as Au_7^+ lie flat on the surface of TiO_2 . We infer that the influence of the substrate leads to an initial planar growth until a cluster size of approximately 20 atoms (see the compilation in Fig. 7.12). Above this size, the energetic configuration is no more favourable for planar structures and clusters grow according to a Volmer-Weber growth process in three dimensions. We conclude that the surface reconstruction does not play a crucial role for the evolution of the cluster size and their internal structure as a function of different annealing temperatures.

7.4.2 Cluster migration

An obvious difference has been detected for the step migration of the clusters at high temperatures. After deposition at room temperature, the samples show a big difference in the number of steps, the (1×2) reconstruction has a total step length of $\frac{5\mu m}{\mu m^2}$, whereas the (1×1)

reconstruction has four times more steps $\left(\frac{20\mu m}{\mu m^2}\right)$. Consequently, the fraction of clusters on steps is also different: 20% of clusters stay on steps on one and 40% on the other surface reconstruction. This explains the different starting points for the step fraction evolution.

During annealing, the two surfaces do not behave in a similar way: on the (1×2) surface, almost no step fraction increase can be observed. Clusters agglomerate randomly without preference to attach to steps. The poor migration to steps for the $TiO_2(110) - (1 \times 2)$ surface is due to the presence of many local defects such as oxygen vacancy sites or protruding OH-groups. They present the necessary anchor points for clusters on terraces. As the anchoring is strong enough to avoid migration, the ratio of step-anchored clusters remain constant for annealing up to $800K$.

On the other hand, $TiO_2(110) - (1 \times 1)$ favours strongly the agglomeration on steps, 9 out of 10 clusters are attached to steps for annealing temperatures above $900K$. This migration is due to the limited terrace size on the one hand and to the surface reconstruction change (Ti_2O_3 islands) at high temperatures on the other. The small amount of surface defects (oxygen vacancies) for low annealing temperatures on the (1×1) surface enhances the mobility of clusters. Annealing at elevated temperatures leads to a partial surface reconstruction change (Ti_2O_3 islands, as presented in Fig. 7.9). These islands act as local anchor points situated on terraces and bind the clusters strongly.

7.4.3   Cluster manipulation

Cluster manipulation has been investigated on the $TiO_2(110) - (1 \times 2)$ surface. We have been able to remove clusters at tunnelling currents in the range of $0.2nA$. Compared to the $TiO_2(110) - (1 \times 1)$ surface, where the minimum tunnelling current necessary to remove a cluster is of the order of $10nA$ [80], the observed current is very low. This is an apparent contradiction with the above mentioned properties. Clusters are apparently stronger bound on $TiO_2(110) - (1 \times 2)$ where they do not move to steps, but can be manipulated easier.

7.5   Catalysis measurements of Au clusters on TiO_2

Catalytic measurements are performed on the $TiO_2(110) - (1 \times 1)$ sample. On the clean surface, $3\%ML$ of Au_7^+ clusters are deposited at room temperature with an impact energy of

7.1 $\frac{eV}{\text{atom}}$. An STM control scan is necessary to control the morphology before each catalysis measurement. The sample is transferred into the sniffer gas analysis system where catalysis measurements are performed.

Isotopically labelled gases: during all catalysis measurements, isotopically labelled gases are used, unless otherwise noted. They can be distinguished from ordinary gases in the vacuum chamber by their different atomic masses. Equation 7.2 shows the different possible combinations between CO and O_2. The number (superscript) indicates the respective atomic masses.

$$
\begin{aligned}
{}^{12}C^{16}O + \tfrac{1}{2}\,{}^{16}O_2 &\;\rightarrow\; {}^{12}C^{16}O_2 \\
{}^{13}C^{16}O + \tfrac{1}{2}\,{}^{16}O_2 &\;\rightarrow\; {}^{13}C^{16}O_2 \\
{}^{12}C^{16}O + \tfrac{1}{2}\,{}^{18}O_2 &\;\rightarrow\; {}^{12}C^{16}O^{18}O \\
{}^{13}C^{16}O + \tfrac{1}{2}\,{}^{18}O_2 &\;\rightarrow\; {}^{13}C^{16}O^{18}O
\end{aligned}
\tag{7.2}
$$
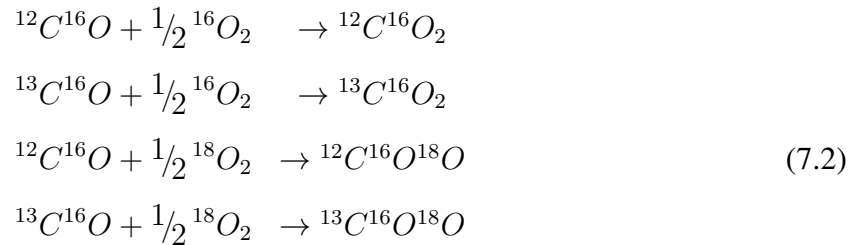
Measurement procedure: during catalysis measurements the sample is kept at room temperature. A constant oxygen pressure is supplied, in the present case non-isotopic oxygen ($^{16}O_2$). $^{13}C^{16}O$ gas is continuously pulsed onto the surface and the gas signals of the above mentioned products are recorded. The oxygen pressure is stepwise increased until a pressure of $5 \cdot 10^{-6} mbar$. After a catalysis cycle, the gases pulses are stopped and the sample is annealed. The annealing temperature for each cycle is increased from $100K$ up to a maximum temperature of $900K$.

7.5.1 Catalytic activity of gold nanoparticles on $TiO_2(110) - (1 \times 1)$

Figure 7.13 presents the catalytic activity for different annealing temperatures ($400K$ in (a) and $720K$ in (b)). One can see the oxygen pressure increases by steps (green curve) as a function of time. Blue peaks represent the carbon monoxide gas pulses (note that the even-odd difference in signal is an electronic problem of the valve power supply). The red signal is the production of $^{13}C^{16}O_2$. An increase in carbon dioxide for very high oxygen pressures is observed in (a), but this signal is related to the increase in background pressure in the
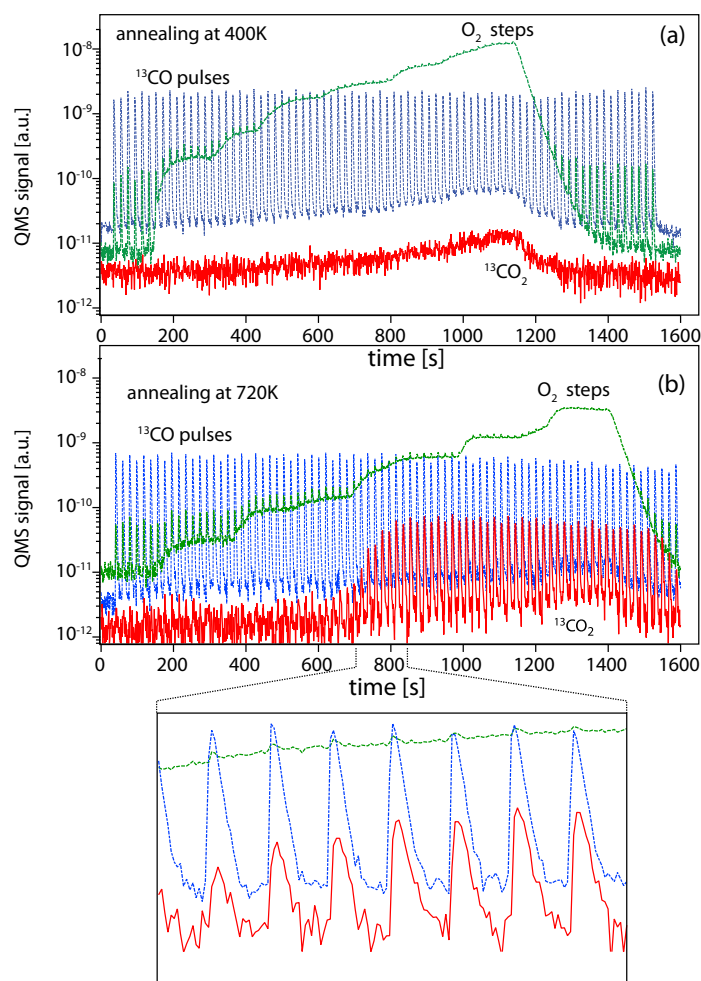
Figure 7.13: Catalytic activity of Au_7^+ on $TiO_2(110) - (1 \times 1)$, annealed at different temperatures. The chamber is exposed to a constant oxygen gas flow (green) and gas pulses of CO (blue) are supplied to the sample. (a) Annealing at $400K$. No catalytic activity can be observed. (b) Annealing at $720K$. The response of the CO_2 signal (red) is in phase with the CO gas pulses (see inset below).

chamber. No significant synchronized signal can be detected. In Figure 7.13(b), we observe a different behaviour. At a certain oxygen pressure ($2 \cdot 10^{-7} mbar$) the signal of CO_2 increases simultaneously with the CO pulses. CO_2 pulses do not increase with the oxygen pressure but are limited by the supplied CO pressure. The maximal conversion from CO to CO_2 is 10%.

The maximal conversion factor of CO combustion is measured at different oxygen pressures (Fig. 7.14). The results show that annealing at $400K$ as well as $500K$ does not show any catalytic activity, i.e. the conversion rate remains below 0.5%. After annealing at $720K$, the conversion curve increases at an oxygen pressure threshold of $2 \cdot 10^{-7} mbar$ and reaches a maximum above $5 \cdot 10^{-7} mbar$, a clear sign that the conversion is limited by the supplied CO gas pressure.
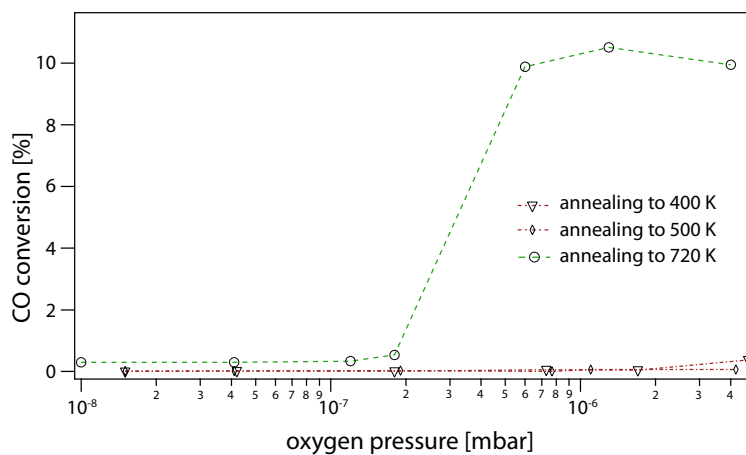
Figure 7.14: CO conversion as a function of oxygen pressure. The curves show the results at different annealing temperatures. Above $600K$, the catalytic activity takes off and reaches a conversion maximum at $720K$.
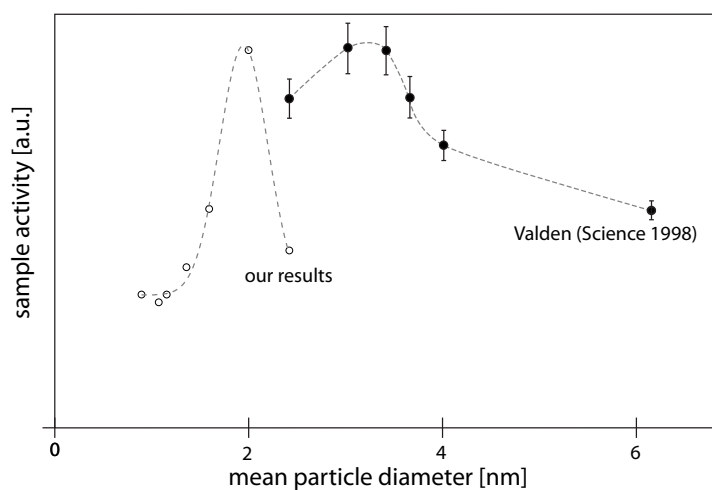
Figure 7.15: Activity of gold nanoparticles on $TiO_2(110) - (1 \times 1)$ as a function of particle size. The obtained results are compared with data of Valden *et. al.* [24]. Their maximal activity is situated at particle with a diameter of $3.5nm$, compared to $2nm$ in diameter for the present measurements.

The change in catalytic activity is related to the size of gold particles on $TiO_2(110) - (1 \times 1)$. As shown before, the clusters change shape between $600K$ and $750K$ where their growth becomes three-dimensional. The measured sample exhibits a maximal catalytic activity for particles with a diameter slightly inferior to $2nm$. This result is coherent with the morphologic measurements presented in Section 7.3.2. The present results are compared to the values obtained by Valden and Goodman [24, 122], displayed in Figure 7.15. There is a difference of $1nm$ in diameter of gold particles showing a maximal activity in CO combustion. It was not possible to identify whether the measurements of Valden have been corrected for tip-induced convolution, which would explain this particle size difference.

Towards confirmation of catalytic activity of gold nanoparticles Encouraged by these results new samples have been prepared in the same way in order to confirm the catalysis obtained before. Several attempts have been made to reproduce the results. Prepared in the same way and exposed to the same gas quantities, all these samples have shown a similar behaviour, namely no CO conversion. Many tests and checks have been performed in order to find the origin of the absence of catalytic activity, but the reason has not yet been identified.

Chapter 8

Conclusion

This thesis consists of different studies on morphology, stability and reactivity of metal clusters deposited on surfaces. In addition to experimental results, important improvements on the experimental setup have been achieved: the existing UHV scanning tunnelling microscope has been modified in order to enhance the sensitivity and to reduce the vibration noise. A new setup for the gas analysis system (sniffer) has been developed in our group and integrated in the UHV system equipped with a STM microscope and a mass-selected cluster source. This unique combination enables the study of correlation between morphology, mobility and catalytic reactivity.

Three different systems have been investigated, all with the goal to show catalytic activity of metal clusters. Pt/YSZ is a well known catalytic active system. TDS studies have been performed with CO and O_2 adsorbed on YSZ. A total amount of $0.9kL$ has been deposited at low temperature ($120K$). With a rate of $0.2\frac{K}{s}$ the sample is heated and the desorbing gas measured. Oxygen desorbs at a temperature of $T = 705K$, according to the values given in literature. The desorption temperature of CO has been found to be centred on $535K$. Compared with the desorption of CO on a $Pt(111)$ surface, the observed peak can be identified with the high-temperature shoulder on Pt/YSZ which corresponds to adsorption of CO on surface steps. Heterogeneous catalysis measurements confirmed the observed values: by pulsing oxygen and CO alternatively to the surface while heating, CO_2 is produced above a temperature of $400K$. The new design using pulsed molecular beams give insight into the kinetics of the system. CO poisoning inhibits the reaction at lower temperature but with the desorption of

CO, binding sites are now available of incoming O_2 molecules which dissociate on the gold particles. At higher temperatures, all CO molecules are desorbed and only molecular oxygen remains on the surface, hence pulses are now synchronized with CO pulses.

These measurements served, beside the confirmation of desorption temperatures, for tests and calibration of a new sniffer setup. The sensitivity of the device is, compared to the predecessor, several magnitudes higher. The main improvement has been achieved by tightening the aperture between sample and the collector volume.

Gold particles Au_5^+ and Au_7^+ have been deposited on a TiO_2 surfaces with different surface reconstructions ($TiO_2(110) - (1 \times 1)$ and $TiO_2(110) - (1 \times 2)$). Several sputtering cycles and subsequent STM imaging to control the surface reconstruction preceded the cluster deposition at low energy ($E_{dep} = 7.1 \frac{eV}{\text{atom}}$) and room temperature. Morphologic studies by STM analysis have shown that the clusters did not fragment after deposition. Their evolution with temperature shows a behaviour following the Ostwald ripening mechanism. Cluster sizes are identical on both surface reconstructions and the transition from 2-d to 3-d structures has been observed around $700K$. A difference is found for clusters connected to surface steps: a majority of gold particles on $TiO_2(110) - (1 \times 1)$ migrate to steps for annealing at elevated temperatures. Clusters on $TiO_2(110) - (1 \times 2)$ surfaces do not show the same behaviour: the presence of many surface defects such as oxygen vacancies anchors the particles to their position and only single atoms or very small molecules migrate on the surface.

Catalysis measurements have been performed for Au_7^+ clusters on $TiO_2(110) - (1 \times 1)$ surface. For a given temperature ($700K$), the sample is exposed to a constant oxygen pressure and periodical CO gas pulses. When the oxygen pressure exceed a threshold level, the CO_2 signal shows peaks synchronized with the CO pulses. The synchronized production indicates that a catalytic conversion of CO takes place on Au/TiO_2. These measurements have not been confirmed so far.

Interesting results have been found for the last and most applied of the three systems: gold particles deposited on pre-structured HOPG. Clean HOPG samples have been prepared by sputtering in order to produce pits with a well-defined depth and diameter. The number of pits has been calculated to maximize the total rim length of the sample. When gold is deposited

on such HOPG surfaces (by PVD deposition at $673K$), they organize themselves and form nanoparticles along the steps and rims of pits. Electrochemical analysis has been performed to investigate the stability of such gold clusters on structured HOPG surfaces. Cyclic voltammetry (CV) measurements have shown that gold particles remain stable during many potential cycles, in contrast to gold particles deposited on non-structured HOPG. The dispersion curve, i.e. the number of surface to bulk atoms gives an interesting alternative way to determine the mean cluster size without referring to microscope techniques.

For very small, hexagonal pits, a size dependence can be found for different attach points. Clusters in the edges of the pits are significantly higher than gold particles on straight rims, indicating that the binding forces in edges are stronger, which leads to larger particles. On very large, circular pits (diameter of $50nm$), all gold particles show the same apparent height and form very regular beads of gold clusters. The cluster size depends on the deposited gold quantity but the number of particles per rim unit length remains constant. For the highest gold loadings of $2.6 \cdot 10^{15} \frac{\text{atoms}}{cm^2}$, the mean particle height is between $3.98 \pm 0.79nm$ and $4.35 \pm 0.62nm$ for different samples. Gold particles attach to dangling bonds on the graphene layers and additional atoms adhere to existing particles. Even for high gold depositions, the particle density is such that they are well separated. The cluster diameter can be estimated, assuming a truncated sphere model, by the ratio of $\frac{d}{h} \approx 1.4$. A very interesting fact has been found when clusters in pits with different depths have been investigated. Independent of the pit depth, clusters always exhibit the same total height. Hence, the cluster height does not depend on the number of dangling bonds on which it attach but only on the total height of the particle.

Heating under atmospheric pressure of the sample does not lead to agglomeration of particles but to catalytic etching of graphene multilayer due to the presence of gold nanoparticles. Oxygen atoms from the gas phase adsorb on the gold nanoparticles and dissociate. They migrate to the cluster-graphite interface and combine with carbon atoms. This leads to formation of CO and CO_2 which itself desorbs and departs into the gas phase. This catalytic etching of graphite leads to a channel formation. Channels grow in the crystallographic directions of HOPG parallel to the surface but do not dig holes in the graphite. The channel depth is identical to the pit depth, the bottom of the clusters is thus at the same level as the bottom of the pits. This fact confirms the suggestion that gold nanoparticles grow from the

bottom of the pits. In addition to the catalytic etching, we showed the hydrogen dissociation on gold clusters and the formation of isotopically labelled water. At temperatures above $700K$ we detect an increase of CO and CO_2 gas pressures in addition to the water desorption. This is the first time that catalytic etching of HOPG (STM images) and chemical analysis of the products has been combined. Additionally, the catalytic power of gold has been demonstrated, a very promising result for further investigations.

Perspectives: the new sniffer system revealed high sensitivity for the gas analysis and can be definitely implemented and used for further measurements. Recently, we started to investigate platinum nanoparticles deposited on TiO_2 . These small Pt clusters show a high catalytic activity for the CO oxidation and are promising candidates for interesting results. As we have mentioned in the text, the gold catalysis measurements on TiO_2 need confirmation. It is suggested to resume this work with the new sniffer setup in order to obtain an experimental proof.

Investigations on gold clusters deposited on pre-structured HOPG have to be continued. One can imagine studying the behaviour of clusters in very deep pits. What happens when the cluster does not exceed the rim? Is it possible to etch tunnels in the graphite? How do other materials behave, such as palladium, rhodium or platinum? Are there even potential applications? It would be interesting to have answers to such questions.

Bibliography

[1] G. Mie, Ann. Phys. **330**, 377 (1908).

[2] M. Reibold, P. Paufler, A. A. Levin, W. Kochmann, N. Patzke, and D. C. Meyer, Nature **444**, 286 (2006).

[3] R. L. Johnston, *Atomic and Molecular Clusters* (Taylor & Francis, London (UK), 2002).

[4] W. D. Knight, K. Clemenger, W. A. de Heer, W. A. Saunders, M. Y. Chou, and M. L. Cohen, Phys. Rev. Lett. **52**, 2141 (1984).

[5] W. A. d. Heer, Rev Mod Phys **65**, 611 (1993).

[6] J. Li, H.-J. Zhai, and L.-S. Wang, Science **299**, 864 (2003).

[7] S. Gilb, P. Weis, F. Furche, R. Ahlrichs, and M. M. Kappes, J Chem Phys **116**, 4094 (2002).

[8] F. Furche, R. Ahlrichs, P. Weis, C. Jacob, S. Gilb, T. Bierweiler, and M. M. Kappes, J Chem Phys **117**, 6982 (2002).

[9] R. H. Hudgins, M. Imai, M. F. Jarrold, and P. Dugourd, J Chem Phys **111**, 7865 (1999).

[10] A. A. Shvartsburg, B. Liu, Z.-Y. Lu, C.-Z. Wang, M. F. Jarrold, and K.-M. Ho, Phys Rev Lett **83**, 2167 (1999).

[11] X. Xing, B. Yoon, U. Landman, and J. H. Parks, Phys Rev B **74**, 165423 (2006).

[12] M. Maier-Borst, D. B. Cameron, M. Rokni, and J. H. Parks, Phys Rev A **59**, 3162 (1999).

[13] M. P. Johansson, A. Lechtken, D. Schooss, M. M. Kappes, and F. Furche, Phys Rev A **77**, 053202 (2008).

[14] A. Lechtken, D. Schooss, J. R. Stairs, M. N. Blom, F. Furche, N. Morgner, O. Kostko, B. V. Issendorff, and M. M. Kappes, Angew Chem , Int Ed **46**, 2944 (2007).

[15] M. N. Blom, D. Schooss, J. Stairs, and M. M. Kappes, J Chem Phys **124**, 244308 (2006).

[16] D. Schooss, M. N. Blom, J. H. Parks, B. V. Issendorff, H. Haberland, and M. M. Kappes, Nano Lett. **5**, 1972 (2005).

[17] A. Fielicke, A. Kirilyuk, C. Ratsch, J. Behler, M. Scheffler, G. V. Helden, and G. Meijer, Phys Rev Lett **93**, 023401 (2004).

[18] A. Fielicke, I. Rabin, and G. Meijer, J Phys Chem A **110**, 8060 (2006).

[19] M. Haruta, Catal Today **36**, 153 (1997).

[20] M. Haruta, Catalysis Surveys of Japan **1**, 61 (1997).

[21] M. Haruta, S. Tsubota, T. Kobayashi, H. Kageyama, M. J. Genet, and B. Delmon, J Catal **144**, 175 (1993).

[22] M. Haruta, N. Yamada, T. Kobayashi, and S. Iijima, J Catal **115**, 301 (1989).

[23] G. Bond, C. Louis, and D. Thompson, *Catalysis by Gold* (Imperial College Press, ADDRESS, 2006).

[24] M. Valden, X. Lai, and D. W. Goodman, Science **281**, 1647 (1998).

[25] U. Heiz and E. Bullock, J Mater Chem **14**, 564 (2004).

[26] U. Heiz, A. Sanchez, S. Abbet, and W. Schneider, J Am Chem Soc **121**, 3214 (1999).

[27] S. Lee, C. Fan, T. Wu, and S. Anderson, J Am Chem Soc **126**, 5682 (2004).

[28] S. Lee, C. Fan, T. Wu, and S. L. Anderson, J Chem Phys **123**, 124710 (2005).

[29] S. Lee, C. Fan, T. Wu, and S. L. Anderson, Surf Sci **578**, 5 (2005).

[30] P. Fayet, F. Granzer, G. Hegenbart, E. Moisar, B. Pischel, and L. Woste, Phys Rev Lett **55**, 3002 (1985).

[31] M. Broyer, G. Delacretaz, P. Labastie, J. P. Wolf, and L. Wöste, Phys Rev Lett **57**, 1851 (1986).

[32] M. Turner, V. B. Golovko, O. P. H. Vaughan, P. Abdulkin, A. Berenguer-Murcia, M. S. Tikhov, B. F. G. Johnson, and R. M. Lambert, Nature **454**, 981 (2008).

[33] S. Vajda *et al.*, Nat Mater **8**, 213 (2009).

[34] S. Vajda, R. Winans, J. Elam, B. Lee, M. Pellin, S. Seifert, G. Tikhonov, and N. Tomczyk, Top Catal **39**, 161 (2006).

[35] J. A. Alonso, L. C. Balbás, A. Aguado, L. M. Molina, A. Mañanes, and M. B. Torres, The European Physical Journal D - Atomic, Molecular, Optical and Plasma Physics **52**, 1 (2009).

[36] U. Heiz and U. Landman, *Nanocatalysis* (Springer, Berlin, 2006).

[37] U. Kreibig and M. Vollmer, in *Optical properties of Metal clusters*, edited by S. S. in Material Science (Springer, Berlin, ADDRESS, 1995).

[38] H. Häkkinen, M. Moseler, and U. Landman, Phys. Rev. Lett. **89**, (2002).

[39] R. Moro, X. Xiaoshan, and Y. Shuangye, Science **300**, 1265 (2003).

[40] K.-H. Meiwes-Broer, *Clusters at Surfaces: Electronic Properties and Magnetism* (Springer, Berlin, ADDRESS, 2006).

[41] D. M. Popolan and T. M. Bernhardt, Chem Phys Lett **470**, 44 (2009).

[42] S. M. Lang and T. M. Bernhardt, Int J Mass Spectrom **286**, 39 (2009).

[43] S. M. Lang and T. M. Bernhardt, J. Chem. Phys. **131**, 024310 (2009).

[44] T. M. Bernhardt, J. Hagen, S. M. Lang, D. M. Popolan, L. D. Socaciu-Siebert, and L. Wöste, The Journal of Physical Chemistry A **113**, 2724 (2009).

[45] C. Harding, V. Habibpour, S. Kunz, A. N.-S. Farnbacher, U. Heiz, B. Yoon, and U. Landman, J Am Chem Soc **131**, 538 (2009).

[46] J. Fujita, H. Watanabe, Y. Ochiai, S. Manako, J. S. Tsai, and S. Matsui, Appl Phys Lett **66**, 3064 (1995).

[47] S.-W. Hla, K.-F. Braun, and K.-H. Rieder, Phys Rev B **67**, 201402 (2003).

[48] D. M. Eigler and E. K. Schweizer, Nature **344**, 524 (1990).

[49] H. Brune, M. Giovannini, K. Bromann, and K. Kern, Nature **394**, 451 (1998).

[50] H. Hsieh, R. S. Averback, H. Sellers, and C. P. Flynn, Phys Rev B **45**, 4417 (1992).

[51] C. Cleveland and U. Landman, Science **257**, 355 (1992).

[52] W. Harbich, *Physique des agrégats* (Lecture Notes EPFL, ADDRESS, 2005).

[53] S. Lecoultre, A. Rydlo, and C. Felix, J. Chem. Phys. **126**, 204507 (2007).

[54] S. Lecoultre, A. Rydlo, C. Félix, and W. Harbich, The European Physical Journal D - Atomic, Molecular, Optical and Plasma Physics **52**, 187 (2009-04-01).

[55] W. Ostwald, Z Phys Chem **34**, 495 (1900).

[56] I. Lifshitz and V. Slyozov, J Phys Chem Solids **19**, 35 (1961).

[57] P. W. Voorhees, J Stat Phys **38**, 231 (1985).

[58] S. Longwitz, Ph.D. thesis, Ecole Polytechnique Fédérale de Lausanne, 2004.

[59] H. Brune, G. S. Bales, J. Jacobsen, C. Boragno, and K. Kern, Phys. Rev. B **60**, 5991 (1999).

[60] H. Brune, in *Handbook of Surface Science*, edited by E. Hasselbrink (Elsevier, Amsterdam, 2008), Vol. 3 Dynamics, Chap. 15 Creating Metal Nanostructures at Metal Surfaces Using Growth Kinetics, pp. 761–786.

[61] C. Clarke, in *The Science of Ice Cream*, edited by (Royal Society of Chemistry, ADDRESS, 2004).

[62] N. L. Sitnikova, R. Sprik, G. Wegdam, and E. Eiser, Langmuir **21**, 7083 (2005).

[63] E. Bauer, Thin Solid Films **12**, 167 (1972).

[64] E. Bauer, Z Kristallogr **110**, 395 (1958).

[65] F. Cosandey, L. Zhang, and T. Maey, Surf Sci **474**, 1 (2001).

[66] L. Zhang, R. Persaud, and T. E. Madey, Phys Rev B **56**, 10549 (1997).

[67] S. Parker, A. Grant, V. Bondzie, and C. Campbell, Surf Sci **441**, 10 (1999).

[68] M. Limat, Ph.D. thesis, Ecole Polytechnique Fédérale de Lausanne, 2009.

[69] C. Solliard and M. Flueli, Surface Science **156**, 487 (1985).

[70] C. Mays, J. Vermaak, and D. Kuhlmann-Wilsdorf, Surface Science **12**, 134 (1968).

[71] J. Lee, M. Nakamoto, and T. Tanaka, Journal of Materials Science **40**, 2167 (2005).

[72] H. Häkkinen, S. Abbet, A. Sanchez, U. Heiz, and U. Landman, Ang Chem Int Ed **42**, 1297 (2003).

[73] H. Häkkinen and U. Landman, Phys Rev B **62**, R2287 (2000).

[74] E. M. Fernandez, J. M. Soler, I. L. Garzon, and L. C. Balbas, Phys. Rev. B **70**, 165403 (2004).

[75] I. Katakuse, T. Ichihara, Y. Fujita, T. Matsuo, T. Sakurai, and H. Matsuda, Int J Mass Spectrom Ion Process **67**, 229 (1985).

[76] H. M. Lee, M. Ge, B. R. Sahu, P. Tarakeshwar, and K. S. Kim, Journal of Physical Chemistry B **107**, 9994 (2003).

[77] N. Spiridis, J. Haber, and J. Korecki, Vacuum **63**, 99 (2001).

[78] X. Tong, L. Benz, P. Kemper, H. Metiu, M. T. Bowers, and S. K. Buratto, J Am Chem Soc **127**, 13516 (2005).

[79] D. Matthey, J. G. Wang, S. Wendt, J. Matthiesen, R. Schaub, E. Laegsgaard, B. Hammer, and F. Besenbacher, Science **315**, 1692 (2007).

[80] P. Convers, Ph.D. thesis, Ecole Polytechnique Fédérale de Lausanne, 2005.

[81] C. E. J. Mitchell, A. Howard, M. Carney, and R. G. Egdell, Surface Science **490**, 196 (2001).

[82] E. Wahlstroem, N. Lopez, R. Schaub, P. Thostrup, A. Ronnau, C. Africh, E. Laegsgaard, J. Norskov, and F. Besenbacher, Phys Rev Lett **90**, 026101 (2003).

[83] Y. Maeda, T. Fujitani, S. Tsubota, and M. Haruta, Surf Sci **562**, 1 (2004).

[84] T. Minato, T. Susaki, S. Shiraki, H. S. Kato, M. Kawai, and K. I. Aika, Surf Sci **566**, 1012 (2004).

[85] N. Lopez and J. K. Nørskov, Surface Science **515**, 175 (2002).

[86] N. Lopez, J. Nørskov, T. Janssens, A. Calsson, A. Puig-Molina, B. Clausen, and J.-D. Grunwaldt, J Catal **225**, 86 (2004).

[87] R. Schaub, E. Wahlstroem, A. Ronnau, E. Laegsgaard, I. Stensgaard, and F. Besenbacher, Science **299**, 377 (2003).

[88] I. A. Kuyanov, D. J. Lacks, and U. Diebold, Phys Rev B **68**, 233404 (2003).

[89] M. Roberts, Catalysis Letters **67**, 1 (2000).

[90] R. Vallotton, Ph.D. thesis, Ecole Polytechnique Fédérale de Lausanne, 2009.

[91] H. Schindelin, C. Kisker, J. L. Schlessman, J. B. Howard, and D. C. Rees, Nature **387**, 370 (1997).

[92] J. W. Peters and R. K. Szilagyi, Curr Opin Chem Biol **10**, 101 (2006).

[93] A. Bongiorno and U. Landman, Phys Rev Lett **95**, 106102 (2005).

[94] A. Sanchez, S. Abbet, U. Heiz, W.-D. Schneider, H. Haekkinen, R. Barnett, and U. Landman, J Phys Chem A **103**, 9573 (1999).

[95] J. Libuda, S. Schauermann, M. Laurin, T. Schalow, and H.-J. Freund, Monatshefte fuer Chemie / Chemical Monthly **136**, 59 (2005).

[96] J. Libuda and H.-J. Freund, Surf Sci Rep **57**, 157 (2005).

[97] G. Schwab and E. Pietsch, Z Phys Chem **1**, 385 (1929).

[98] H. Schmidbaur, Naturwiss Rundsch **48**, 443 (1995).

[99] C. Bond, P. Sermon, G. Webb, D. Buchanan, and P. Wells, J Chem Soc Chem Comm **13**, 444 (1973).

[100] A. S. K. Hashmi and G. J. Hutchings, Angewandte Chemie International Edition **45**, 7896 (2006).

[101] G. C. Bond and D. T. Thompson, Catal Rev Sci Eng **41**, 319 (1999).

[102] M. Haruta, CatTech **6**, 102 (2003).

[103] M. Cortie and E. van der Lingen, Materials Forum **26**, 1 (2002).

[104] M.-C. Daniel and D. Astruc, Chem Rev **104**, 293 (2004).

[105] R. Meyer, C. Menire, S. Shaikhutdinov, and H.-J. Freund, Gold Bull **37**, 72 (2004).

[106] D. Thompson, Topics in Catalysis **38**, 231 (2006).

[107] S. Galvagno and G. Parravano, Journal of Catalysis **55**, 178 (1978).

[108] G. Bond and D. Thompson, Gold Bull **33**, 41 (2000).

[109] M. Haruta, T. Kobayashi, H. Sano, and N. Yamada, Chem Lett (Jpn) **2**, 405 (1987).

[110] H. Huber, D. McIntosh, and G. A. Ozin, Inorganic Chemistry **16**, 975 (1977).

[111] G. J. Hutchings, Gold Bull **37/1**, 2 (2004).

[112] F. Boccuzzi, A. Chiorino, and M. Manzoli, Mater Sci Eng , C **15**, 215 (2001).

[113] A. Ueda, T. Oshima, and M. Haruta, Applied Catalysis B: Environmental **12**, 81 (1997).

[114] H. Sakurai, S. Tsubota, and M. Haruta, Applied Catalysis A: General **102**, 125 (1993).

[115] H. Sakurai and M. Haruta, Catalysis Today **29**, 361 (1996).

[116] D. Andreeva, T. Tabakova, V. Idakiev, P. Christov, and R. Giovanoli, Applied Catalysis A: General **169**, 9 (1998).

[117] D. Andreeva, V. Idakiev, T. Tabakova, A. Andreev, and R. Giovanoli, Applied Catalysis A: General **134**, 275 (1996).

[118] D. Andreeva, V. Idakiev, T. Tabakova, L. Ilieva, P. Falaras, A. Bourlinos, and A. Travlos, Catalysis Today **72**, 51 (2002).

[119] D. Andreeva, Gold Bull **35**, 82 (2002).

[120] F. Boccuzzi, A. Chiorino, M. Manzoli, D. Andreeva, and T. Tabakova, Journal of Catalysis **188**, 176 (1999).

[121] M. Valden, S. Pak, X. Lai, and D. Goodman, Catal Lett **56**, 7 (1998).

[122] D. W. Goodman, Catal Lett **V99**, 1 (2005).

[123] M. Haruta, The Chemical Record **3**, 75 (2003).

[124] D. C. Grenoble, M. M. Estadt, and D. F. Ollis, Journal of Catalysis **67**, 90 (1981).

[125] C. Ovesen, P. Stoltze, J. Nørskov, and C. Campbell, Journal of Catalysis **134**, 445 (1992).

[126] N. Schumacher, A. Boisen, S. Dahl, A. Gokhale, S. Kandoi, L. Grabow, J. Dumesic, M. Mavrikakis, and I. Chorkendorff, Journal of Catalysis **229**, 265 (2005).

[127] R. C. Tatar and S. Rabii, Phys. Rev. B **25**, 4126 (1982).

[128] S. Lee, Y. Lee, Y. Hwang, J. Hahn, and H. Hang, Phys Rev Lett **82**, 217 (1999).

[129] A. Tracz, G. Wegner, and J. P. Rabe, Langmuir **9**, 3033 (1993).

[130] H. Chang and A. J. Bard, J Am Chem Soc **112**, 4598 (1990).

[131] J. Hahn, Carbon **43**, 1506 (2005).

[132] G. Hennig, in *Chemistry and Physics of Carbon*, edited by J. Walker (Marcel Dekker, New York, -, 1966).

[133] E. L. Evans, R. J. M. Griffiths, and J. M. Thomas, Science **171**, 174 (1971).

[134] R. Yang and C. Wong, J Chem Phys **75**, 4471 (1981).

[135] F. Stevens, L. A. Kolodny, and T. P. Beebe, The Journal of Physical Chemistry B **102**, 10799 (1998).

[136] Y.-J. Zhu, T. A. Hansen, S. Ammermann, J. D. McBride, and T. P. Beebe, The Journal of Physical Chemistry B **105**, 7632 (2001).

[137] J. R. Hahn, H. Kang, S. M. Lee, and Y. H. Lee, The Journal of Physical Chemistry B **103**, 9944 (1999).

[138] G. Braeuchle, S. Richard-Schneider, D. Illig, J. Rockenberger, R. Beck, and M. Kappes, Appl Phys Lett **67**, 52 (1995).

[139] G. Braeuchle, S. Richard-Schneider, D. Illig, R. Beck, H. Schreiber, and M. Kappes, Nucl Instrum Methods Phys Res , Sect B **112**, 105 (1996).

[140] S. Carroll, S. Hall, R. Palmer, and R. Smith, Phys Rev Lett **81**, 3715 (1998).

[141] S. Carroll, P. Nellist, R. Palmer, S. Hobbday, and R. Smith, Phys Rev Lett **84**, 2654 (2000).

[142] S. Pratontep, P. Preece, C. Xirouchaki, R. E. Palmer, C. F. Sanz-Navarro, S. D. Kenny, and R. Smith, Phys Rev Lett **90**, 055503 (2003).

[143] L. Seminara, P. Convers, R. Monot, and W. Harbich, Eur Phys J D **29**, 49 (2004).

[144] L. Seminara, Ph.D. thesis, Ecole Polytechnique Fédérale de Lausanne, 2004.

[145] M. Hugentobler, Master's thesis, Ecole polytechnique fédérale de Lausanne, 2006.

[146] F. Ghaleh, R. Koster, H. Hovel, L. Bruchhaus, S. Bauerdick, J. Thiel, and R. Jede, J. Appl. Phys. **101**, 044301 (2007).

[147] A. Böttcher, M. Heil, N. Stürzl, S. Jester, S. Malik, F. Pérez-Willard, P. Brenner, D. Gerthsen, and M. Kappes, Nanotechnology **17**, 5889 (2006).

[148] H. Hövel and I. Barke, Prog Surf Sci **81**, 53 (2006).

[149] T. Irawan, I. Barke, and H. Hövel, Applied Physics A: Materials Science & Processing **80**, 929 (2005).

[150] H. Hövel, T. Becker, A. Bettac, B. Reihl, M. Tschudy, and E. J. Williams, Journal of Applied Physics **81**, 154 (1997).

[151] H. Hövel, T. Becker, A. Bettac, B. Reihl, M. Tschudy, and E. J. Williams, Appl Surf Sci **115**, 124 (1997).

[152] J. D. McBride, B. Van Tassell, R. C. Jachmann, and T. P. Beebe, The Journal of Physical Chemistry B **105**, 3972 (2001).

[153] J. Akola and H. Häkkinen, Phys. Rev. B **74**, 165404 (2006).

[154] R. Anton and I. Schneidereit, Phys. Rev. B **58**, 13874 (1998).

[155] R. Anton and P. Kreutzer, Phys. Rev. B **61**, 16077 (2000).

[156] G. Hennig, Journal of Inorganic and Nuclear Chemistry **24**, 1129 (1962).

[157] A. Tomita, N. Sato, and Y. Tamai, Carbon **12**, 143 (1974).

[158] A. Tomita and Y. Tamai, Journal of Catalysis **27**, 293 (1972).

[159] R. T. K. Baker, J. A. France, L. Rouse, and R. J. Waite, Journal of Catalysis **41**, 22 (1976).

[160] R. T. K. Baker and R. D. Sherwood, Journal of Catalysis **61**, 378 (1980).

[161] R. T. K. Baker and R. D. Sherwood, Journal of Catalysis **70**, 198 (1981).

[162] P. J. Goethel and R. T. Yang, Journal of Catalysis **119**, 201 (1989).

[163] H. Y. Huang and R. T. Yang, Journal of Catalysis **185**, 286 (1999).

[164] S. Konishi, W. Sugimoto, Y. Murakami, and Y. Takasu, Carbon **44**, 2338 (2006).

[165] H. Watanabe, Japanese Journal of Applied Physics **32**, 2809 (1993).

[166] F. Schäffel, J. H. Warner, A. Bachmatiuk, B. Rellinghaus, B. Büchner, L. Schultz, and M. H. Rümmeli, physica status solidi (b) **246**, 2540 (2009).

[167] Y. Takasu, S. Konishi, R. Miyoshi, K. Nukii, T. Matsuse, W. Sugimoto, and Y. Murakami, Chem Lett (Jpn) **34**, 1008 (2005).

[168] N. Severin, S. Kirstein, I. M. Sokolov, and J. P. Rabe, Nano Letters **9**, 457 (2009).

[169] S. S. Datta, D. R. Strachan, S. M. Khamis, and A. T. C. Johnson, Nano Letters **8**, 1912 (2008).

[170] L. C. Campos, V. R. Manfrinato, J. D. Sanchez-Yamagishi, J. Kong, and P. Jarillo-Herrero, Nano Letters **9**, 2600 (2009).

[171] L. Ci, Z. Xu, L. Wang, W. Gao, F. Ding, K. Kelly, B. Yakobson, and P. Ajayan, Nano Research **1**, 116 (2008).

[172] F. Ding, P. Larsson, J. A. Larsson, R. Ahuja, H. Duan, A. Rosen, and K. Bolton, Nano Letters **8**, 463 (2008).

[173] A. Tomita and Y. Tamai, J Phys Chem **78**, 2254 (1974).

[174] C. J. Boxley, H. S. White, T. E. Lister, and P. J. Pinhero, The Journal of Physical Chemistry B **107**, 451 (2003).

[175] Y.-J. Zhu, A. Schnieders, J. D. Alexander, and T. P. Beebe, Langmuir **18**, 5728 (2002).

[176] B. O'Regan and M. Gratzel, Nature **353**, 737 (1991).

[177] M. Gratzel, Nature **414**, 338 (2001).

[178] U. Diebold, Surface Science Reports **48**, 53 (2003).

[179] R. A. Bennett, S. Poulston, P. Stone, and M. Bowker, Phys Rev B **59**, 10341 (1999).

[180] M. Ramamoorthy, R. D. King-Smith, and D. Vanderbilt, Phys Rev B **49**, 7709 (1994).

[181] U. Diebold, M. Li, O. Dulub, E. L. D. Hebenstreit, and W. Hebenstreit, Surf. Rev. Lett. **7**, 613 (2000).

[182] J. Sasaki, N. L. Peterson, and K. Hoshino, J Phys Chem Solids **46**, 1267 (1985).

[183] M. A. Henderson, Surf Sci **343**, L1156 (1995).

[184] M. Henderson, Surf Sci **419**, 174 (1999).

[185] L. S. Dubrovinsky, N. A. Dubrovinskaia, V. Swamy, J. Muscat, N. M. Harrison, R. Ahuja, B. Holm, and B. Johansson, Nature **410**, 653 (2001).

[186] M. Haruta, private communication, 2006.

[187] B. Grossmann and P. Piercy, Phys Rev Lett **74**, 4487 (1995).

[188] S. Fischer, A. W. Munz, K.-D. Schierbaum, and W. Göpel, Surf Sci **337**, 17 (1995).

[189] P. J. Møller and M.-C. Wu, Surf Sci **224**, 265 (1989).

[190] M. Sander and T. Engel, Surf Sci **302**, L263 (1994).

[191] H. Onishi and Y. Iwasawa, Surf Sci **313**, L783 (1994).

[192] H. Onishi, Bull Chem Soc Jpn **68**, 2447 (1995).

[193] C. L. Pang, S. A. Haycock, H. Raza, P. W. Murray, G. Thornton, O. Gülseren, R. James, and D. W. Bullett, Phys. Rev. B **58**, 1586 (1998).

[194] R. E. Tanner, M. R. Castell, and G. A. D. Briggs, Surface Science **412-413**, 672 (1998).

[195] H. Onishi and Y. Iwasawa, Phys Rev Lett **76**, 791 (1996).

[196] S. Takakusagi, K.-i. Fukui, F. Nariyuki, and Y. Iwasawa, Surf Sci **523**, L41 (2003).

[197] K. F. McCarty, Surf Sci **543**, 185 (2003).

[198] K. F. McCarty and N. C. Bartelt, Surf Sci **527**, L203 (2003).

[199] P. Stone, R. A. Bennett, and M. Bowker, New J Phys **1**, 8 (1999).

[200] J. Pascual, J. Camassel, and H. Mathieu, Phys Rev Lett **39**, 1490 (1977).

[201] T. Umebayashi, T. Yamaki, H. Itoh, and K. Asai, J Phys Chem Solids **63**, 1909 (2002).

[202] H. Wang and J. P. Lewis, Journal of Physics Condensed Matter **18**, 421 (2006).

[203] U. Diebold, J. F. Anderson, K.-O. Ng, and D. Vanderbilt, Phys Rev Lett **77**, 1322 (1996).

[204] U. Diebold, J. Lehman, T. Mahmoud, M. Kuhn, G. Leonardelli, W. Hebenstreit, M. Schmid, and P. Varga, Surf Sci **411**, 137 (1998).

[205] W. S. Epling, C. H. F. Peden, M. A. Henderson, and U. Diebold, Surf Sci **412-413**, 333 (1998).

[206] M. Casarin, C. Maccatoo, and A. Vittadini, J Phys Chem B **102**, 10745 (1998).

[207] Z. Yang, R. Wu, Q. Zhang, and D. W. Goodman, Phys Rev B **63**, 045419 (2001).

[208] H. Kobayashi and M. Yamaguchi, Surf Sci **214**, 466 (1989).

[209] A. Linsebigler, G. Lu, and J. John T. Yates, J Chem Phys **103**, 9438 (1995).

[210] G. Rocker and W. Göpel, Surf Sci **175**, L675 (1986).

[211] W. Goepel, G. Rocker, and R. Feierabend, Phys Rev B **28**, 3427 (1983).

[212] M. A. Henderson, Surf Sci Rep **46**, 1 (2002).

[213] M. B. Hugenschmidt, L. Gamble, and C. T. Campbell, Surface Science **302**, 329 (1994).

[214] D. Brinkley, M. Dietrich, T. Engel, P. Farrall, G. Gantner, A. Schafer, and A. Szuchmacher, Surf Sci **395**, 292 (1998).

[215] V. Henrich and P. Cox, in *The Surface Science of metal oxides*, edited by Cambridge (Cambridge University Press, ADDRESS, 1994).

[216] G. Lu, A. Linsebigler, and J. T. Yates, J Phys Chem **98**, 11733 (1994).

[217] R. L. Kurtz, R. Stock-Bauer, T. E. Msdey, E. Román, and J. De Segovia, Surface Science **218**, 178 (1989).

[218] E. L. Bullock, L. Patthey, and S. G. Steinemann, Surface Science **352-354**, 504 (1996).

[219] J.-M. Pan, B. L. Maschhoff, U. Diebold, and T. E. Madey, Journal of Vacuum Science & Technology A: Vacuum, Surfaces, and Films **10**, 2470 (1992).

[220] L.-Q. Wang, A. N. Shultz, D. R. Baer, and M. H. Engelhard, Journal of Vacuum Science & Technology A **14**, 1532 (1996).

[221] L.-Q. Wang, D. R. Baer, M. H. Engelhard, and A. N. Shultz, Surface Science **344**, 237 (1995).

[222] M. A. Henderson, Langmuir **12**, 5093 (1996).

[223] M. A. Henderson, Surf Sci **400**, 203 (1998).

[224] M. A. Henderson, Surf Sci **355**, 151 (1996).

[225] I. M. Brookes, C. A. Muryn, and G. Thornton, Phys. Rev. Lett. **87**, 266103 (2001).

[226] r. Schaub, P. Thostrup, N. Lopez, E. Laegsgaard, I. Stensgaard, J. Norskov, and F. Besenbacher, Phys Rev Lett **87**, 266104 (2001).

[227] P. J. Gellings and H. J. M. Bouwmeester, Catalysis Today **12**, 1 (1992).

[228] O. Baranova, Ph.D. thesis, Ecole Polytechnique Fédérale Lausanne, 2005.

[229] J.-H. Park and R. N. Blumenthal, J Electrochem Soc **136**, 2867 (1989).

[230] A. Jaccoud, C. Falgairette, G. Fóti, and C. Comninellis, Electrochim Acta **52**, 7927 (2007).

[231] A. Jaccoud, Ph.D. thesis, Ecole Polytechnique Fédérale de Lausanne, Lausanne, 2007.

[232] B. LuerSSen, J. Janek, and R. Imbihl, Solid State Ionics **141-142**, 701 (2001).

[233] C. Vayenas, S. Bebelis, I. Yentekakis, and H.-G. Lintz, Catal Today **11**, 303 (1992).

[234] J. Poppe, S. Völkering, A. Schaak, E. Schütz, J. Janek, and R. Imbihl, Phys. Chem. Chem. Phys. **1**, 5241 (1999).

[235] A. Katsaounis, Z. Nikopoulou, X. E. Verykios, and C. G. Vayenas, Journal of Catalysis **226**, 197 (2004).

[236] L. Bultel, P. Vernoux, F. Gaillard, C. Roux, and E. Siebert, Solid State Ionics **176**, 793 (2005).

[237] S. Souentie, C. Xia, C. Falgairette, Y. Li, and C. Comninellis, Electrochem Commun **12**, 323 (2010).

[238] C. Vayenas, S. Bebelis, C. Pliangos, S. Brosda, and D. Tsiplakides, *Electrochemical activation of catalysis: promotion, electrochemical promotion, and metal-support interaction* (Kluwer Academic/Plenum Publishers, ADDRESS, 2001).

[239] D. Tsiplakides, S. Neophytides, and C. Vayenas, Ionics **3**, 201 (1997).

[240] S. G. Neophytides, D. Tsiplakides, and C. G. Vayenas, Journal of Catalysis **178**, 414 (1998).

[241] J. Craig Jr., Appl Surf Sci **25**, 333 (1986).

[242] P. Norton, J. Goodale, and E. Selkirk, Surface Science **83**, 189 (1979).

[243] G. Ertl, M. Neumann, and K. M. Streit, Surf Sci **64**, 393 (1977).

[244] D. M. Collins, J. B. Lee, and W. Spicer, Surf Sci **55**, 389 (1976).

[245] R. Behrisch, *Sputtering by Particle bombardment* (Springer, ADDRESS, 1981).

[246] A. Oliva-Florio, R. A. Baragiola, M. M. Jakas, E. V. Alonso, and J. Ferrón, Phys. Rev. B **35**, 2198 (1987).

[247] M. Schaffner, J. Jeanneret, F. Patthey, and W.-D. Schneider, J. Phys. D Appl. Phys. **31**, 3177 (1998).

[248] J. Samela, J. Kotakoski, K. Nordlund, and J. Keinonen, Nuclear Instruments and Methods in Physics Research Section B: Beam Interactions with Materials and Atoms **239**, 331 (2005).

[249] P. H. Dawson, *Quadrupole mass spectrometry and its applications* (Elsevier-Science, New York, 1976).

[250] K. L. Brown and G. W. Tautfest, Rev Sci Instrum **27**, 696 (1956).

[251] A. M. de Jong and J. W. Niemantsverdriet, Surf Sci **233**, 355 (1990).

[252] D. A. King, Surf Sci **47**, 384 (1975).

[253] E. Habenschaden and J. Küppers, Surf Sci **138**, L147 (1984).

[254] P. A. Redhead, Vacuum **12**, 203 (1962).

[255] C. Chan, Appl Surf Sci **1**, 360 (1978).

[256] J. Taylor and W. Weinberg, Surf Sci **78**, 259 (1978).

[257] J. A. Konvalinka, J. J. F. Scholten, and J. C. Rasser, J Catal **48**, 365 (1977).

[258] S. Bonanni, K. Ait-Mansour, M. Hugentobler, H. Brune, and W. Harbich, In preparation (2010).

[259] M. F. Crommie, C. P. Lutz, and D. M. Eigler, Science **262**, 218 (1993).

[260] E. Schrödinger, Phys. Rev. **28**, 1049 (1926).

[261] R. Young, J. Ward, and F. Scire, Phys Rev Lett **27**, 922 (1971).

[262] G. Binnig, H. Rohrer, C. Gerber, and E. Weibel, Physica BC **109-110**, 2075 (1982), 16th International Conference on Low Temperature Physics.

[263] G. Binnig and H. Rohrer, Surf Sci **126**, 236 (1983).

[264] G. Binnig and H. Rohrer, Ultramicroscopy **11**, 157 (1983).

[265] G. Binnig, H. Rohrer, F. Salvan, C. Gerber, and A. Baro, Surf Sci **157**, L373 (1985).

[266] G. Binnig, H. Rohrer, C. Gerber, and E. Weibel, Phys. Rev. Lett. **50**, 120 (1983).

[267] J. Bardeen, Phys. Rev. Lett. **6**, 57 (1961).

[268] J. Tersoff and D. R. Hamann, Phys Rev B **31**, 805 (1985).

[269] J. Tersoff and D. R. Hamann, Phys Rev Lett **50**, 1998 (1983).

[270] W. Sacks and C. Noguera, J Vac Sci Technol B **9**, 488 (1991).

[271] W. Sacks and C. Noguera, Phys Rev B **43**, 11612 (1991).

[272] W. Sacks and C. Noguera, Ultramicroscopy **42-44**, 140 (1992).

[273] C. J. Chen, Phys Rev Lett **65**, 448 (1990).

[274] C. Chen, *Introduction to Scanning Tunneling Microscopy* (Oxford University Press, Oxford, 1993).

[275] R. J. Hamers and D. F. Padowitz, in *Scanning Probe Microscopy and Spectroscopy: Theory, Techniques, and Applications*, edited by D. A. Bonnell (New York: Wiley-VCH, Inc, -, 2001).

[276] D. Damjanovic, Piezoelectric materials, properties and devices, Master Degree Lecture, EPFL (2006).

[277] A. Lucier, Master's thesis, McGill University, 2004.

[278] J. P. Ibe, P. P. Bey, Jr., S. L. Brandow, R. A. Brizzolara, N. A. Burnham, D. P. DiLella, K. P. Lee, C. R. K. Marrian, and R. J. Colton, J. Vac. Sci. Technol. A **8**, 3570 (1990).

[279] A. Jaccoud, G. Fóti, and C. Comninellis, Electrochim Acta **51**, 1264 (2006).

[280] J. Yan, Z. Li, C. Bai, W. S. Yang, Y. Wang, W. Zhao, Y. Kang, F. C. Yu, P. Zhai, and X. Tang, J. Appl. Phys. **75**, 1390 (1994).

[281] S. Hall, M. Nielsen, and R. Palmer, J Appl Phys **83**, 733 (1998).

[282] R. Coratger, A. Claverie, A. Chahboun, V. Landry, F. Ajustron, and J. Beauvillain, Surface Science **262**, 208 (1992).

[283] T. Li, B. King, R. MacDonald, G. Cotterill, D. O'Connor, and Q. Yang, Surface Science **312**, 399 (1994).

[284] B. E. Roustom, G. Fóti, and C. Comninellis, Electrochemistry Communications **7**, 398 (2005).

[285] L. Bultel, C. Roux, E. Siebert, P. Vernoux, and F. Gaillard, Solid State Ionics **166**, 183 (2004).

[286] S. Bonanni, K. Ait-Mansour, M. Hugentobler, H. Brune, and W. Harbich, European physical Journal **xx**, Submitted (2010).

[287] R. Shigeishi and D. A. King, Surf Sci **75**, L397 (1978).

[288] S. Kunz, F. F. Schweinberger, V. Habibpour, M. Rötgen, C. Harding, M. Arenz, and U. Heiz, Journal of Physical Chemistry C **114**, 1651 (2010).

[289] C. Xia, M. Hugentobler, Yongdan-Li, C. Comninellis, and W. Harbich, Electrochem Commun **12**, 1551 (2010).

[290] C. Xia, M. Hugentobler, Y. Li, C. Comninellis, and W. Harbich, In preparation (2010).

[291] I. Horcas, R. Fernandez, J. M. Gomez-Rodriguez, J. Colchero, J. Gomez-Herrero, and A. M. Baro, Review of Scientific Instruments **78**, 013705 (2007).

[292] S. Wendt, J. Matthiesen, R. Schaub, E. K. Vestergaard, E. Laegsgaard, F. Besenbacher, and B. Hammer, Phys Rev Lett **96**, 066107 (2006).

[293] A. Kolmakov and D. W. Goodman, Surf Sci **490**, L597 (2001).

Remerciements

J'aimerais remercier tout les personnes autour de moi qui m'ont aidé pour la réalisation de cette thèse. Je ne suis pas la première personne à le souligner: une thèse n'est jamais un travail d'un seul homme mais d'un ensemble de personnes. Chacun et chacune contribue à sa façon sur un plan technique, administratif ou, plus important, sur un plan humain.

Tout d'abord, un grand merci au Dr. Wolfgang Harbich, mon directeur de thèse, qui m'a donné la possibilité de réaliser mon travail de diplôme et ma thèse dans son groupe de recherche. Cette collaboration de plus de 5 ans me laisse de très bons souvenirs. Son positivisme et ses encouragements m'ont donné de l'énergie dans les moments difficiles.

Merci à mes collègues de groupe, Raphael Vallotton, Régis Stephan, Simon Bonanni, Kamel Ait-Mansour, Chun Xia et Stefan Minniberger et aux nombreux diplômés et stagiaires: Antoine Sautier, Fabian Bircher et Julia Sester. J'aimerais remercier spécialement Raphael Vallotton. C'est lui qui m'a initié aux secrets de la machine et qui m'a guidé dans mes premières années de thèse. On a aussi passé des heures ensemble en dehors du travail, notamment sous l'eau, dans les montagnes ou en vélo. Les sorties matinales en peau de phoque avant d'aller travailler sont des très bons souvenirs. Merci aussi à Prof. René Monot qui a eu la gentillesse de relire mon travail et de me donner des feedbacks.

Un grand merci à tous le Staff technique et administratif de l'institut, notamment l'atelier mécanique avec Gilles Grandjean, Philippe Zürcher, Philippe Guex, Olivier Haldimand, Michel Longchamp et Claude Amendola (avec qui j'ai fait de nombreuses courses à pied, merci!). Les électroniciens et informaticiens Martial Doy, José Grandjean, Philippe Cuanillon, Philippe Cordey et Primo Locatelli. Merci aussi au secrétariat, Florence Choulat et Chantal Roulin pour leur disponibilité. Un grand merci à Claire-Lise Bandelier pour la préparation de nombreuses figures pour cette thèse. Merci aussi aux anciens collaborateurs, Michel Fazan et André Schläfli, les bonnes âmes dans les couloirs!

184

Curriculum Vitae

Nom:	Michael HUGENTOBLER
Date de naissance:	24 novembre 1980
Lieu d'origine:	Braunau (TG)
Nationalité	Suisse
Adresse:	Rue du Simplon 26, 1006 Lausanne

1995-1999	Gymnase en section scientifique, Kreuzlingen
2000	Etudes de physique à l'École Polytechnique Fédérale de Zurich (ETHZ)
2001-2005	Etudes de physique à l'École Polytechnique Fédérale de Lausanne (EPFL)
2006	Master en physique sous la direction du Dr. W. Harbich *"Controlled implantation of size selected metal and semi-conductor clusters in graphite (HOPG)"*
2006-2010	Assistant-doctorant à l'Institut of Condensed Matter Physics (ICMP) de l'EPFL. Travail de doctorat sous la direction du Dr. W. Harbich.

Publications

M. Limat and G. Fóti and M. Hugentobler and R. Stephan and W. Harbich, *Electrochemically stable gold nanoclusters in HOPG nanopits*, Catal. Today **146**, 378 (2009)

C. Xia, M. Hugentobler, Y. Li, C. Comninellis, W. Harbich, *Quantifying electrochemical promotion of induced bipolar Pt particles supported on YSZ*, Electrochem. Comm. **12**, 1551-1554 (2010)

M. Hugentobler, S. Bonanni, A. Sautier, W. Harbich *Morphology and stability of Au nanoclusters in HOPG nanopits of well defined depth*, Eur. Phys. J. D **accepted**

C. Xia, M. Hugentobler, Y. Li, C. Comninellis, W. Harbich, *Electrochemical promotion of CO combustion over non-percolated Pt particles supported on YSZ using a novel bipolar configuration*, Electrochem. Comm. **in press**

S. Bonanni, K. Ait-Mansour, M. Hugentobler, H. Brune, W. Harbich *An experimental setup combining a highly sensitive detector for reaction products with a mass-selected cluster source and a low-temperature STM for advanced surface and catalysis measurements* Eur. Phys. J. D **submitted**

M. Hugentobler, S. Bonanni, C. Xia, W. Harbich *Particle-enhanced local etching and oxygen dissociation on Au nanoparticles stabilized in prestructured HOPG* Eur. Phys. J. D **submitted**

R. Vallotton, R. Stephan, M. Hugentobler, H. Brune, W. Harbich, *Stability of size-selected Au_n clusters on rutile TiO$_2$(110)-(1×2)*, **to be published**

C. Xia, M. Hugentobler, Y. Li, C. Comninellis, W. Harbich, *Charge tunes catalytic activity : Pt on Yttria Stabilized Zirconia (YSZ)*, **to be published**